

**Quinol Oxidation and Transmembrane Electron Transfer  
in *E. coli* Nitrate Reductase A**

by

Justin Gerald Fedor

A thesis submitted in partial fulfilment of the requirements for the degree of

Doctor of Philosophy

Department of Biochemistry

University of Alberta

© Justin Gerald Fedor, 2015

## Abstract

Approximately one third of the *E. coli* and human proteomes consist of membrane proteins. Among these proteins are oxidoreductases, which fulfil central roles in the bioenergetic processes of cells, function as pathogenicity factors in microorganisms and their dysfunction is responsible for many inherited diseases in humans. They also find utility in industrial applications such as solar cells, biosensors and carbon sequestration. Unfortunately, many membrane-bound oxidoreductases, or the organisms in which they are found, are not easy to work with, and so our understanding of them relies on the ability to extrapolate from more easily tractable systems – Nitrate reductase (NarGHI) is such a system.

NarGHI is a Molybdenum-containing enzyme expressed in *E. coli* when nitrate is available for anaerobic cellular respiration. Molybdoenzymes are widely found across the tree of life where they generally perform oxygen-transfer redox reactions. Bacterial respiratory diversity is largely due to the variety of molybdoenzymes they encode for, enabling a variety of terminal electron acceptors to be utilized for cellular respiration. Molybdoenzymes also largely facilitate the global biogeochemical Nitrogen cycle. Importantly, humans have four types of molybdoenzymes, which are active in drug metabolism, the catabolism of nucleotides, the processing of S-containing amino acids, and sulfite detoxification. Deficiencies in molybdoenzymes has serious health effects. The study of molybdoenzymes is therefore a critical and active area of research, for which NarGHI represents an excellent model system.

Since it was first discovered, NarGHI has been keenly studied. It is not only an important enzyme in bacterial metabolism, but it is also a pathogenicity factor of certain microbes, and the principles of its structure and function are applicable to many human enzymes. NarGHI is a menaquinol:nitrate oxidoreductase that faces the cytoplasm from the plasma membrane. NarI is the membrane subunit in which quinol oxidation occurs, and NarG binds the molybdenum cofactor where nitrate is reduced. Quinol oxidation occurs at the periplasmic aspect of NarI and the electrons are transferred across the membrane via two *b*-type hemes. Electrons are subsequently transferred to NarG via NarH, which binds four iron-sulfur clusters. Overall, the electron transfer relay in NarGHI functions like a wire measuring ~100 Å long. This molecular wire feature is more the rule than the exception when it comes to integral membrane oxidoreductases. By understanding electron transfer in NarGHI, we can better understand transmembrane and long-distance electron transfer in numerous other enzymes. The process of quinol oxidation is also widely applicable to many enzymes in humans and bacteria, as quinone pool coupling is nearly universal and the basic principles of quinone chemistry are similar between disparate systems. However, while much has been learned about electron transfer and quinone binding in NarGHI, much remains to be understood.

It has been the aim of this thesis to further probe the functioning of the membrane subunit, NarI. Specifically I sought to examine two key aspects of NarI function: 1) to probe the spectroscopic and electrochemical properties of the hemes and how these properties relate to transmembrane electron transfer; and 2) to gain a greater understanding of the mechanism by which NarI catalyses menaquinol

oxidation.

The findings of this thesis can be summarized in the following points:

- 1) The occupancy of the quinol oxidation site (Q-site) of NarI by quinones influences the EPR spectroscopic and electrochemical properties of the heme adjacent to the Q-site (heme  $b_D$ ).
- 2) The redox characteristics of the NarI hemes and the adjacent iron-sulfur cluster of NarH facilitate transmembrane electron transfer in a controlled manner.
- 3) Quinol oxidation proceeds via a protonated intermediate, where its binding to NarI requires the Q-site be deprotonated.
- 4) The deprotonation of inbound quinol is catalysed by a partially conserved lysine (Lys86), and that the property of Lys86 that is most important is its ionisability.
- 5) The Q-site of NarI requires that Lys86 undergo a conformational change in order to facilitate quinol deprotonation. This is hinted at by an engineered second-site rescuer mutation which restores quinol oxidase activity in a catalytically dead variant of Lys86 (Lys86Ala).

## Preface

The research conducted in this thesis is my own original work. The publications of which I have contributed are listed below, those references marked with an (\*) represent a significant body of my work and have been included as chapters in this thesis.

\*Fedor, J.G., Rothery R.A., Weiner, J.H. (Submitted) A NarI<sup>Met156Lys</sup> variant of *Escherichia coli* nitrate reductase A restores quinol oxidase activity of a NarI<sup>Lys86Ala</sup> mutation. *Archives of Biochemistry and Biophysics* (ABBI-15-614)

\*Fedor, J.G., Rothery, R.A., Weiner, J.H. (Submitted) Quinol oxidation progresses through a neutral semiquinone in *Escherichia coli* nitrate reductase A. *Biochimica et Biophysica Acta – Bioenergetics* (BBABIO-15-258)

\*Fedor, J.G., Ma, Yi Ke, Giraldi, K.S., Rothery, R.A., Weiner, J.H. (Submitted) Quinol oxidation and proton egress in *Escherichia coli* nitrate reductase A. *Biochimica et Biophysica Acta – Bioenergetics* (BBABIO-15-235)

Duca, M., Weeks, J., Fedor, J.G., Weiner, J.H., Vincent, K.A. (2015) Combining noble metals and enzymes for relay cascade electrocatalysis of nitrate reduction at neutral pH. *ChemElectrochem*. doi:10.1002/celc.201500166

\*Fedor, J.G., Rothery, R.A., Weiner, J.H. (2014) A new paradigm for electron transfer through *Escherichia coli* nitrate reductase A. *Biochemistry*, 53, 4549-4556

\*Fedor, J.G., Rothery, R.A., Giraldi, K.S., Weiner, J.H. (2014) Q-site occupancy defines heme heterogeneity in *Escherichia coli* nitrate reductase A. *Biochemistry*, 53, 1733-1741

Magalon, A., Fedor, J.G., Walburger, A., Weiner, J.H. (2011) Molybdenum enzymes in bacteria and their maturation, *Coordination Chemistry Reviews*, 255, 1159-1178

## Acknowledgements

A thesis project is not the work of a single person, but requires the input and support of many. It is for this reason I would first like to thank my supervisor Dr. Joel Weiner for welcoming me to his lab as a project student and later as a graduate student. His perspicacity, guidance and encouragement have allowed me to succeed and his devotion and love for science is inspiring.

Second, I must thank Dr. Richard Rothery, whose scientific and editorial inputs have been of considerable quantity and quality. Whether it was an EPR experiment, a modified growth protocol or liquid nitrogen ice cream, he has always been an advocate of the true scientific mentality of “just try it out.” I will truly miss our lab ski trips, death marches and Friday afternoon “beer O'clock” celebrations.

Throughout the years I have had the pleasure of mentoring several terrific summer/project students: Nicholas Chua, Kelly Ma and Karissa Giraldi. Each has made significant contributions to the work reported herein and for this, and their friendship, I owe them a debt of gratitude.

The Weiner lab and the U of A Department of Biochemistry has always been, for me, a stimulating and fun place to work. I am truly grateful to have made many friends and to have had the pleasure of working with many great people. I must also express immense thanks for the funding provided by the Canadian Institutes for Health Research, Alberta Innovates Health Solutions and the Killam Trust.

Last but not least, I am infinitely indebted to my family and close personal friends. Thank you so much Mom, Dad, Bryce, Cole, Auntie June, Terry Pearson, Grandma, Chuen Wei Leong, David Kramer, Kristen Lusk, Brewster Laxton, Kelly Robinson, James Rodway, Angela Fung, and Roshani Payoe. You guys were there to cheer me up on the worst days and celebrate with me the best days. More importantly, however, I am truly grateful for your unwavering support and inveterate love.

# Table of Contents

<b>Abstract</b> .....	<b>ii</b>
<b>Preface</b> .....	<b>v</b>
<b>Acknowledgements</b> .....	<b>vii</b>
<b>List of Tables</b> .....	<b>x</b>
<b>List of Figures</b> .....	<b>xi</b>
<b>List of Abbreviations</b> .....	<b>xiv</b>
<b>1. General Introduction</b> .....	<b>1</b>
1.1. Basic Bioenergetics.....	2
1.1.1. Thermodynamic Fundamentals.....	2
1.1.2. Eukaryotic Respiratory Pathways.....	5
1.1.2.1. Mitochondrial Physiology.....	5
1.1.2.2. Mechanisms for Generating PMF.....	7
1.1.3. Bacterial Respiratory Diversity.....	9
1.1.3.1. <i>E. coli</i> Respiratory Pathways.....	9
1.1.3.2. Quinones in <i>E. coli</i> Respiratory Diversity.....	12
1.1.3.3. Regulation of <i>E. coli</i> Respiration.....	13
1.1.4. Intraprotein Electron Transfer.....	16
1.1.5. Redox Cofactors.....	18
1.1.5.1. Iron-Sulfur Clusters.....	18
1.1.5.2. Heme.....	20
1.1.5.3. Mono-Nuclear Molybdenum Cofactor.....	23
1.1.5.4. Quinones.....	25
1.2. <i>E. coli</i> Nitrate Reductase A (NarGHI).....	29
1.2.1. The Nitrogen Cycle.....	29
1.2.2. The Physiology of Bacterial Nitrate Reductases.....	31
1.2.3. NarGHI Structure and Function.....	33
1.2.3.1. NarG.....	35
1.2.3.2. NarH.....	38
1.2.3.3. NarI.....	40
1.2.4. NarGHI Maturation.....	45
1.3. Thesis Research Objectives.....	46
<b>2. Q-site Occupancy Defines Heme Heterogeneity in <i>E. coli</i> NarGHI</b> .....	<b>47</b>
2.1. Introduction.....	48

2.2. Materials and Methods.....	50
2.3. Results.....	53
2.4. Discussion.....	60
2.5. Supplementary Material.....	66
<b>3. A New Paradigm for Electron-Transfer Through <i>E. coli</i> NarGHI.....</b>	<b>67</b>
3.1. Introduction.....	68
3.2. Materials and Methods.....	70
3.3. Results and Discussion.....	72
3.4. Summary.....	84
3.5. Supplementary Material.....	85
<b>4. Quinol Oxidation Progresses Through a Neutral Semiquinone in <i>E. coli</i> NarGHI.....</b>	<b>89</b>
4.1. Introduction.....	90
4.2. Materials and Methods.....	93
4.3. Results.....	96
4.4. Discussion.....	100
<b>5. A Mechanism for Menaquinol Deprotonation in <i>E. coli</i> NarGHI.....</b>	<b>106</b>
5.1. Introduction.....	107
5.2. Materials and Methods.....	109
5.3. Results.....	113
5.4. Discussion.....	119
5.5. Supplementary Material.....	124
<b>6. A NarI<sup>Met156Lys</sup> Variant of <i>E. coli</i> NarGHI Restores Quinol Oxidase Activity of a NarI<sup>Lys86Ala</sup> Mutation.....</b>	<b>127</b>
6.1. Introduction.....	128
6.2. Materials and Methods.....	131
6.3. Results and Discussion.....	135
6.4. Conclusion.....	142
6.5. Supplementary Material.....	143
<b>7. Conclusions and Future Directions.....</b>	<b>144</b>
7.1. Heme Electrochemical and Biophysical Characteristics.....	145
7.2. Quinol Oxidation by NarI.....	148
<b>8. References.....</b>	<b>152</b>

## List of Tables

<b>Table 2.1</b>	NarI variant PBH <sub>2</sub> :NO <sub>3</sub> <sup>-</sup> oxidoreductase activities.	56
<b>Table 3.1</b>	Cooperative (C) and Noncooperative (NC) fitting parameters for redox titrations of nitrate reductase preparations as seen in Figure 3.3.	74
<b>Supplementary Table 3.1</b>	Previously reported midpoint potentials for the hemes and [3Fe-4S] cluster for vesicle preparations of <i>E. coli</i> nitrate reductase A pertinent to this study.	85
<b>Table 4.1</b>	Fitting parameters for the low potential semiquinone EPR signals of NarI( $\Delta$ GH) and NarGHI enriched vesicles.	95
<b>Table 5.1</b>	The <i>in vivo</i> and <i>in vitro</i> activity of NarGHI Lys86 variants.	114
<b>Table 5.2</b>	The rate constants, $k_{\text{fast}}$ and $k_{\text{slow}}$ , for heme reduction of NarGHI <sup>Lys86</sup> variants by 0.35 mM menadiol.	117
<b>Supplementary Table 5.1</b>	Fitting parameters for pre-steady state heme reduction by menadiol of NarGHI-enriched vesicles of wild-type, K86H, and K86E as depicted in Figure 5.3.	125
<b>Table 6.1</b>	The <i>in vivo</i> and <i>in vitro</i> activity of NarGHI Lys86 and M156 variants.	138
<b>Supplementary Table 6.1</b>	Fitting parameters for pre-steady state heme reduction by menadiol.	143

## List of Figures

<b>Figure 1.1</b>	Mitochondrial oxidative phosphorylation.	6
<b>Figure 1.2</b>	<i>E. coli</i> formate-nitrate redox loop.	7
<b>Figure 1.3</b>	The Q-cycle of complex III (cytochrome <i>bc</i> <sub>1</sub> ).	8
<b>Figure 1.4</b>	<i>E. coli</i> respiratory diversity.	10
<b>Figure 1.5</b>	Metabolic context of the formate nitrate redox loop.	11
<b>Figure 1.6</b>	Heme cofactor structural diversity and axial coordination.	21
<b>Figure 1.7</b>	Molybdenum-containing cofactors.	23
<b>Figure 1.8</b>	The quinones of <i>E. coli</i> and quinone chemistry overview.	26
<b>Figure 1.9</b>	The global biogeochemical nitrogen cycle.	30
<b>Figure 1.10</b>	<i>E. coli</i> nitrate reductase A (NarGHI).	33
<b>Figure 1.11</b>	The electron transfer relay and cofactors of NarGHI.	34
<b>Figure 1.12</b>	Mo-bisPGD and FS0 of NarG.	35
<b>Figure 1.13</b>	The coordination of FS1-4 of NarH.	39
<b>Figure 1.14</b>	The architecture of NarI.	40
<b>Figure 1.15</b>	The Q-site of NarI in stereo.	43
<b>Figure 1.16</b>	Covariance analysis of conserved Q-site residues.	44
<b>Figure 1.17</b>	Maturation of NarGHI.	45
<b>Figure 2.1</b>	The Q-site of NarI with pentachlorophenol bound.	49
<b>Figure 2.2</b>	Effects of growth conditions and quinones on heme <i>b</i> <sub>D</sub> EPR line shape are apparent in redox-poised oxidized heme spectra of NarGHI hemes <i>b</i> <sub>P</sub> ( <i>g</i> = 3.75) and <i>b</i> <sub>D</sub> ( <i>g</i> = 3.0 – 3.4).	54
<b>Figure 2.3</b>	The effects of HOQNO binding on heme <i>b</i> <sub>D</sub> EPR spectra.	57

<b>Figure 2.4</b>	Redox titrations and pH dependence of the components of heme $b_D$ .	59
<b>Figure 2.5</b>	Summary of Q-site occupancy on the heme $b_D$ EPR spectrum.	65
<b>Supplementary Figure 2.1</b>	Spectral contributions of cytochromes $bd$ and $bo$ to the NarI heme signals.	66
<b>Supplementary Figure 2.2</b>	Anaerobic growth assays of LCB79 in glycerol-nitrate media for pVA700-G65A and pVA700-K86A variants.	66
<b>Figure 3.1</b>	Transmembrane electron-transfer relay of NarGHI comprising hemes $b_D$ and $b_P$ and FS4 and their representative EPR spectral features.	69
<b>Figure 3.2</b>	Thermodynamic model for NarGHI hemes $b_D$ , $b_P$ and FS4 depicted schematically.	71
<b>Figure 3.3</b>	Fits for the redox titrations of hemes $b_D$ , $b_P$ and FS4.	76
<b>Figure 3.4</b>	Electron-transfer across the plasma membrane from $b_D$ to FS4 using the old and new paradigm for the transmembrane electron-transfer relay of NarGHI.	82
<b>Figure 3.5</b>	Summary of energetics of electron flow through $b_D$ , $b_P$ , FS4 system	84
<b>Supplementary Figure 3.1</b>	Three-center redox model for NarGHI.	86
<b>Supplementary Figure 3.2</b>	Two-center redox model for NarI( $\Delta$ GH).	86
<b>Supplementary Figure 3.3</b>	Residual plots for the fits depicted in Figure 3.3.	88
<b>Figure 4.1</b>	The electrochemical transitions of quinones, with the physiologically relevant pathway from oxidized quinone through semiquinone to quinol indicated in black.	90
<b>Figure 4.2</b>	The quinone binding site of NarGHI with the Q-site inhibitor pentachlorophenol (PCP) bound.	91
<b>Figure 4.3</b>	Structure of (demethyl)menaquinol-8.	92

<b>Figure 4.4</b>	Representative EPR spectra of the maximal intensity semiquinone signals for NarI( $\Delta$ GH) and NarGHI.	96
<b>Figure 4.5</b>	pH dependence of the NarGHI MSQ.	97
<b>Figure 4.6</b>	pH dependence of the NarI( $\Delta$ GH) DMSQ.	98
<b>Figure 4.7</b>	Midpoint potential data from 31 redox titrations of nitrate reductase-associated naphthoquinones.	99
<b>Figure 5.1</b>	The quinol binding site and proton egress pathways of <i>E. coli</i> NarGHI.	108
<b>Figure 5.2</b>	Naphthoquinol substrates of NarGHI.	115
<b>Figure 5.3</b>	Pre-steady state kinetics of heme reduction.	116
<b>Figure 5.4</b>	$k_{\text{fast}}$ pH dependence of heme reduction by 0.35 mM menadiol.	118
<b>Figure 5.5</b>	Proposed mechanism of menaquinol oxidation by NarI.	123
<b>Supplementary Figure 5.1</b>	A representative anaerobic growth assay of <i>E. coli</i> strain LCB79 complemented with pVA700 encoding NarGHI variants on glycerol:nitrate media.	124
<b>Supplementary Figure 5.2</b>	$k_{\text{slow}}$ pH dependence of heme reduction by 0.35 mM menadiol.	126
<b>Figure 6.1</b>	The quinol binding site and Lys86 proton egress pathway within the NarI subunit of <i>E. coli</i> NarGHI.	130
<b>Figure 6.2</b>	Anaerobic growth assay on glycerol:nitrate media of <i>E. coli</i> LCB79 complemented with pVA700 encoding NarGHI variants.	137
<b>Figure 6.3</b>	Pre-steady state kinetics of heme reduction of 1 mg mL <sup>-1</sup> NarGHI with 0.35 mM menadiol at pH 7.0.	139
<b>Figure 6.4</b>	pH dependence of $k_{\text{fast}}$ and $k_{\text{slow}}$ parameters for pre-steady state heme reduction of NarGHI by menadiol.	140

## List of Abbreviations

**ADP** – adenosine 5'-diphosphate

**Anammox** – anaerobic ammonium oxidation

**Arc/ArcAB** – anoxic respiration control two-component regulatory system

**ATP** – adenosine 5'-triphosphate

**$b_D$**  – *b*-heme distal to NarGH

**$b_P$**  – *b*-heme proximal to NarGH

**BV** – benzyl viologen

**C** – cooperative

**CHES** – N-cyclohexyl-2-aminoethanesulfonic acid

**Cyd/CydAB** – cytochrome *bd* quinol oxidase (low oxygen)

**Cyo/CyoABCD** – cytochrome *bo* quinol oxidase (high oxygen)

**DDM** – dodecylmaltoside

**DMQH<sub>2</sub>** – demethylmenaquinol

**DMQ** – demethylmenaquinone

**DMSO** – dimethylsulfoxide

**DMSQ** – demethylmenasemiquinone

**$\Delta\Psi$**  – transmembrane electric charge differential

**$\Delta p$**  – transmembrane electrochemical differential (proton motive force)

**$\Delta pH$**  – transmembrane pH differential

**$e^-$**  – electron

***E. coli*** – *Escherichia coli*

**$E^{\circ'}$**  – standard biochemical reduction potential

**$E_1$**  – quinone to semiquinone reduction potential

**$E_2$**  – semiquinone to quinol reduction potential

**$E_h$**  – applied potential

**$E_{m,x}$**  – reduction potential at pH X

**EDTA** – ethylenediaminetetraacetic acid

**EPR** – electron paramagnetic resonance  
**ESEEM** – Electron Spin Echo Envelope Modulation  
**FdnGHI** – nitrate-associated formate dehydrogenase  
**FeS** – Iron-sulfur cluster  
**FNR** – fumarate and nitrate reductase regulator  
**FS4** – [3Fe-4S] of NarH  
**GPF** – glycerol-peptone-fumarate  
**GTP** – guanosine 5'-triphosphate  
**HALS** – highly anisotropic low spin  
**H-bond** – hydrogen bond  
**HOQNO** – 2-*n*-heptyl 4-hydroxyquinoline-N-oxide  
**HYSCORE** – hyperfine sublevel correlation  
**IPTG** – isopropyl-1-thio- $\beta$ -D-galactopyranoside  
**ISC** – iron-sulfur cluster biogenesis system  
**MES** – 2-(N-morpholino)ethanesulfonic acid  
**Mo** – molybdenum  
**Mo-bisPGD** – molybdo-bis(pyranopterin guanine dinucleotide)  
**Moco** – molybdenum cofactor  
**MOPS** – 3-(N-morpholino)propanesulfonic acid  
**MQ** – menaquinone  
**MQH<sub>2</sub>** – menaquinol  
**MSQ** – menasemiquinone  
**MWP** – microwave power  
**NAD(P)<sup>+</sup>** – nicotinamide adenine dinucleotide (phosphate) (oxidized)  
**NAD(P)H** – nicotinamide adenine dinucleotide (phosphate) (reduced)  
**Nap/NapAB** – periplasmic dissimilatory nitrate reductase  
**Nar A/Z** – respiratory membrane-bound nitrate reductases  
**NarGHI** – respiratory nitrate reductase A  
**NarI( $\Delta$ GH)** – NarI subunit expressed in the absence of NarGH and NarJ  
**NarJ** – dedicated chaperone for NarGHI

**NarK** – nitrate/nitrite antiporter  
**NarXL/NarQP** – nitrate/nitrite two-component regulatory systems  
**NarZYV** – respiratory nitrate reductase Z  
**Nas** – cytosolic assimilatory nitrate reductase  
**NC** – non-cooperative  
**Ndh** – NADH:ubiquinone oxidoreductase (non-proton pumping)  
**N-side** – negative side of energy conserving membrane  
**Nuo(A-N)** – NADH:quinone oxidoreductase (proton pumping)  
**P-side** – positive side of energy conserving membrane  
**PB** – plumbagin (oxidized)  
**PBH<sub>2</sub>** – plumbagin (reduced)  
**PCP** – pentachlorophenol  
**PDB** – protein databank  
**PFL** – pyruvate-formate lyase  
**PMF** – proton motive force  
**Q** – quinone  
**QH<sub>2</sub>** – quinol  
**Q-pool** – quinone pool  
**Q-site** – quinone binding site  
**Q<sub>i</sub>-site** – inside facing quinone binding site of cytochrome *bc<sub>1</sub>*  
**Q<sub>o</sub>-site** – outside facing quinone binding site of cytochrome *bc<sub>1</sub>*  
**SDS-PAGE** – sodium dodecylsulfate polyacrylamide gel electrophoresis  
**SQ** – semiquinone  
**SUF** – sulfur mobilization FeS biogenesis system  
**TM** – transmembrane helix  
**TMAO** – trimethylamine N-oxide  
**UQ** – ubiquinone  
**UQH<sub>2</sub>** – ubiquinol  
**USQ** – ubisemiquinone  
**UV-vis** – ultraviolet-visible

# 1. General Introduction

## 1.1. Basic Bioenergetics

### 1.1.1. Thermodynamic Fundamentals

In his book, *What is Life?* <sup>1</sup>, Erwin Schrödinger succinctly stated that “living matter evades the decay to equilibrium.” To assemble and maintain living matter requires the input and conversion of usable energy – metabolism. Otherwise, the organism will eventually succumb to the second law of thermodynamics and reach that final equilibrium. Metabolism is the sum of all chemical processes in a cell, and includes catabolism (processes releasing energy, such as digestion and macromolecular degradation) and anabolism (processes that require energy, such as building macromolecules). Rather than try to use an impossibly convoluted system of chemical bartering, where every catabolic reaction is directly coupled to every other anabolic reaction, primordial life settled on a form of energetic currency: adenosine 5'-triphosphate (ATP). The hydrolysis of ATP to yield ADP (adenosine 5'-diphosphate) and inorganic phosphate releases substantial energy if the concentration of ATP is maintained at a sufficiently high level relative to ADP. When the ATP:ADP ratio is maintained at 1000:1 (10 orders of magnitude from equilibrium), ATP hydrolysis releases 57 kJ mol<sup>-1</sup> of energy, as in the cytoplasm of human cells <sup>2</sup>. Even in the cytoplasm of *E. coli* and the mitochondrial matrix, where ATP:ADP ratios are only about 10:1, the hydrolysis of ATP releases 46 kJ mol<sup>-1</sup> <sup>2,3</sup>. Thus, hydrolysis of ATP can be used to power endergonic chemical processes, where the energy available is a function of the mass action ratio ( $\Gamma$ ) of reactants and products, given by **equation 1.1**:

$$\Delta G = \Delta G^{\circ} + 2.3RT \cdot \log_{10} \Gamma \quad (1.1)$$

The problem then becomes maintaining the ATP:ADP ratio.

Chemiosmosis was a term first coined by Peter Mitchell in 1961 <sup>4</sup>. It was known that phosphate containing 'high energy' compounds are the energy source for many processes in the cell, ATP. The only mechanism known at the time for generating such compounds was substrate level phosphorylation, a direct coupling of an

exergonic chemical reaction to the endergonic process of phosphorylation. An interesting hint at the mechanisms involved in generating the vast majority of ATP was that this phosphorylation was associated with membrane proteins. It was also widely known that there is an electrical potential across almost all cell membranes, such as the plasma membrane of eukaryotes and prokaryotes, as well as the inner membranes of mitochondria and the thylakoid membrane of chloroplasts. It was in his 1961 paper that Peter Mitchell proposed the idea that redox reactions catalysed by membrane bound proteins were coupled to the net deposition of protons on one side of the membrane, which generates a proton gradient <sup>4</sup>. Being positively charged, the proton gradient imbues the membrane with a charge and pH differential which can be dissipated in a controlled manner by other enzymes to drive forward endergonic chemical reactions. One such example he proposed was the reverse action of an ATP hydrolase, which could energetically afford to phosphorylate ADP by dissipating the proton gradient in a controlled fashion. It was for this work that Mitchell won the 1978 Nobel Prize in chemistry <sup>5</sup>.

Central to the mechanism of chemiosmosis is an energy conserving membrane. The plasma membranes of bacteria, and inner membranes of chloroplast thylakoids and mitochondria are largely sealed against leakage of ions <sup>2</sup>. Embedded within these membranes are two kinds of proton pumps sharing the same orientation. The periplasmic side of the bacterial membrane, the inter membrane space of mitochondria and the lumen (interior) of chloroplast thylakoids are imbued with a positive charge due to the accumulation of protons and is therefore termed the P-side. The opposite face of the membrane has a relatively negative charge and is called the N-side. Because there is a concentration difference of protons ( $\Delta pH$ ) and a gradient of charge ( $\Delta \Psi$ ) due to concentration differences of ions, the sum of the two is termed the transmembrane electrochemical gradient or proton motive force ( $\Delta p$ ), which Mitchell defined in terms of Volts. The equation for calculating  $\Delta p$  from  $\Delta pH$  and  $\Delta \Psi$  is therefore:

$$\Delta p = \Delta \Psi - \frac{2.3RT}{F} \Delta pH \quad (1.2)$$

At a temperature ( $T$ ) of 37°C (310 K), and substituting in for Faraday's constant ( $F$ ) and the universal gas constant ( $R$ ) (96 485.3 C mol<sup>-1</sup> and 8.3415 V C K<sup>-1</sup> mol<sup>-1</sup>, respectively) <sup>6</sup>, **equation 1.2** simplifies to:

$$\Delta p = \Delta \Psi - 61 \Delta pH \quad (1.3)$$

Where  $\Delta \Psi$ ,  $\Delta pH$  and  $\Delta p$  are measured as the P-side minus N-side and therefore  $\Delta \Psi$  and  $\Delta p$  are typically positive, whereas  $\Delta pH$  is negative <sup>2</sup>. The exact values of these parameters depends on various conditions and whether one is observing the membrane potential of a thylakoid or mitochondrial/bacterial membrane. The mitochondrial  $\Delta p$  (~180 mV) is mostly made up of a  $\Delta \Psi$ , typically 150 mV <sup>7,8</sup>, and the measured  $-\Delta pH$  is ~0.5 <sup>8</sup>, though it has been measured as high as 0.9 <sup>9</sup>. This electrochemical gradient ( $\Delta p$ ) imposes a force upon charged particles, specifically protons, hence the term 'proton motive force' (PMF). Work can be done by tapping the PMF in order to pump substrates across the membrane against their electrochemical gradient, powering the motion of flagella, or for the action of ATP synthase <sup>2,4</sup>.

Responsible for generating and maintaining the PMF are oxidoreductases, which catalyse the exergonic ('downhill') electron transfer between two compounds – from the lower potential compound to the higher potential compound. The difference in reduction potentials of the redox couples ( $\Delta E_h$ ) determines the amount of energy released:

$$\Delta G = nF \Delta E_h \quad (1.4)$$

where  $\Delta E_h = E_h A - E_h B$  in the reaction  $A^{ox} + B^{red} \leftrightarrow A^{red} + B^{ox}$ , and  $n$  is the electron stoichiometry of the redox reaction, typically  $n = 1$ . The  $E_h$  for a given redox couple ( $A^{ox}/A^{red}$  or  $B^{ox}/B^{red}$ ) is dependent on its standard reduction/midpoint potential ( $E^\circ/E_{m,7}$ ), the temperature, and the ratio of the concentrations of oxidized and reduced forms, as given by the Nernst equation <sup>6,10</sup>:

$$E_h = E_m + \frac{RT}{nF} \ln \left( \frac{[X^{ox}]}{[X^{red}]} \right) \quad (1.5)$$

Which at 25°C simplifies to:

$$E_h = E_m + \frac{59 \text{ mV}}{n} \log_{10} \left( \frac{[X^{\text{ox}}]}{[X^{\text{red}}]} \right) \quad (1.6)$$

The release of redox energy can then be coupled to the transfer of protons up their concentration gradient to the P-side of the membrane. This is accomplished either by vectorial proton transport, where there is an actual pumping of protons across the membrane; or scalar proton transport, where there is a net consumption of protons on the N-side of the membrane and deposition of protons on the P-side. ATP synthase is an example of the former; in the absence of a membrane potential, ATP synthase catalyses the hydrolysis of ATP and pumps protons across the membrane <sup>2</sup>. However, there are many other examples of proton pumps, and examples of both mechanisms of PMF generation will be explored further in the following sections (see **Section 1.1.1.2**).

## 1.1.2. Eukaryotic Respiratory Pathways

### 1.1.2.1. Mitochondrial Physiology

Respiration in eukaryotes is catalysed in the mitochondria, the endosymbiotic bacterial vestiges that specialize in the chemiosmotic production of ATP from oxidation of pyruvate <sup>11</sup>. Through co-evolution, the size of the mitochondrial genome has almost completely been transferred to the nuclear genome. Of the 37 genes remaining in the mammalian mitochondrial genome, 13 encode for integral membrane subunits of complexes I, III, IV and V (**Figure 1.1**). Since these 13 polypeptides only account for 1% of the mitochondrial proteome, significant and complex coordination between the two genomes is required for mitochondrial biogenesis <sup>2</sup>.

Past the porin-filled outer membrane of mitochondria lies the convoluted inner membrane – a sealed dielectric slab with a voltage of about +150 mV. Within this membrane are embedded a series of five protein complexes, four of which constitute

the electron transfer relay. These four oxidoreductases catalyse sequential redox reactions, terminating with the reduction of oxygen, in order to build up and maintain the PMF. The fifth complex, ATP synthase, dissipates the gradient to make ATP. Housing its own transcription and translation machinery, the mitochondrial matrix is the spatial location of the pyruvate dehydrogenase complex, citric acid cycle, and fatty acid and amino acid oxidation <sup>11</sup>. These catabolic pathways release copious amounts of reducing equivalents, mostly in the form of NADH, which in turn is oxidized by the electron transfer relay of the inner membrane.

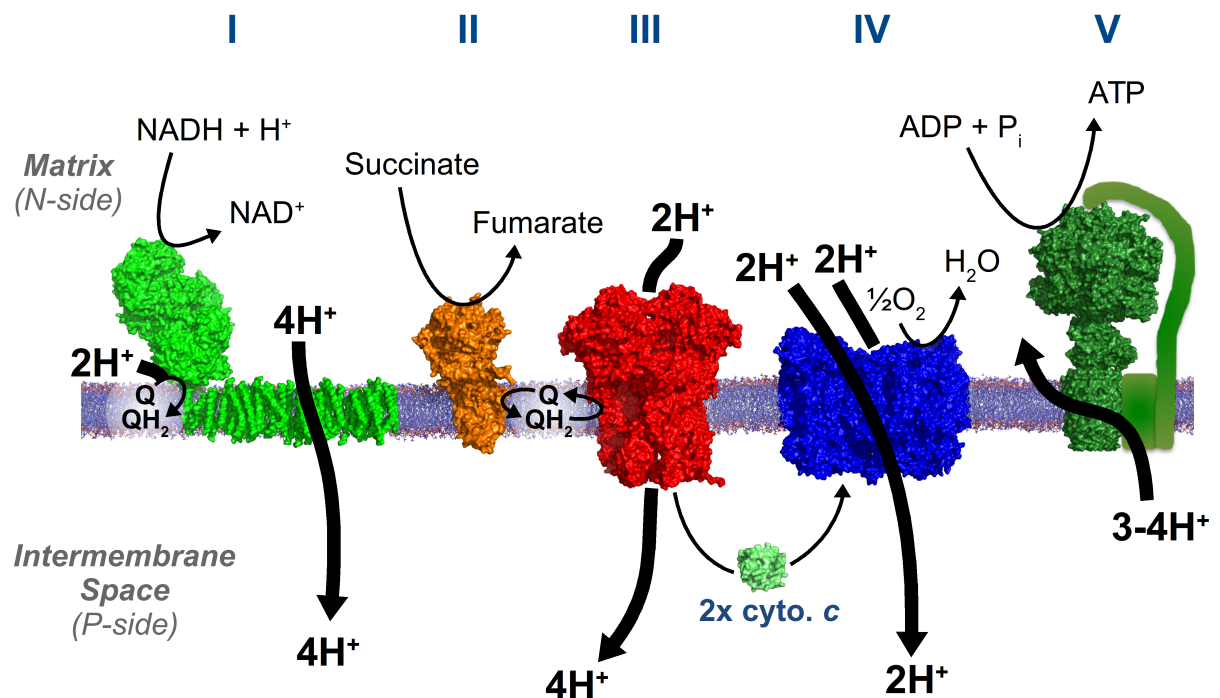
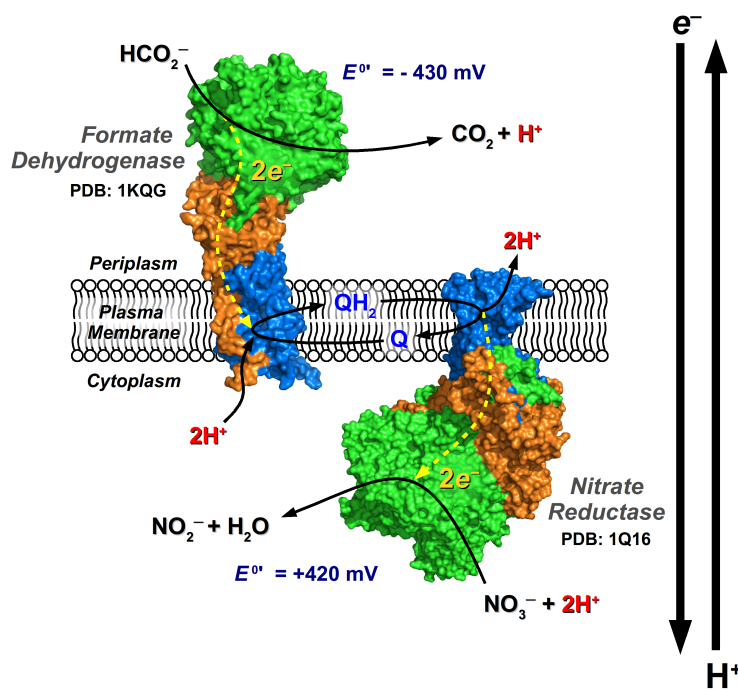


**Figure 1.1: Mitochondrial oxidative phosphorylation.** The four oxidoreductase complexes of the electron transfer chain are: (I) NADH:ubiquinone oxidoreductase, (II) succinate dehydrogenase, (III) cytochrome *bc*<sub>1</sub>, (IV) cytochrome oxidase. Complex V, ATP synthase, dissipates the proton gradient in order to power the phosphorylation of ADP. Note the 'L' shape of complex I, where the peripheral domain contains all the redox centers and the membrane domain is solely responsible for proton pumping.

### 1.1.2.2. Mechanisms for Generating PMF

As mentioned above, there are two principle mechanisms by which a protein complex can contribute to the proton gradient. Firstly, the protein complex can pump protons directly. The simplest case is bacteriorhodopsin, which pumps protons across the membrane of some archaea by undergoing a series of conformational changes upon absorbing light<sup>12</sup>. Complex I of oxidative phosphorylation also pumps protons directly. It is an “L”-shaped complex comprised of two subdomains, as seen in **Figure 1.1**. The peripheral domain contains all the redox cofactors (flavin mononucleotide, 8-10 FeS clusters, and the Q-site), and makes contact with one end of the membrane domain, protruding into the matrix to form the iconic “L”-shape. The membrane domain of *E. coli* complex I consists of 7 subunits, three of which are homologs of



$\text{Na}^+/\text{H}^+$  antiporter proteins. By a mechanism not yet completely understood the redox chemistry of the peripheral domain is coupled to concerted conformational changes of the membrane domain to pump  $4\text{H}^+ / 2\text{e}^-$ <sup>13,14</sup>.

The second major mode of contributing to a proton gradient is exemplified by bacterial redox loops. Here, quinone and substrate chemistry contribute to

**Figure 1.2: *E. coli* formate-nitrate redox loop.** The redox loop composed of formate dehydrogenase (FdHnGHI), nitrate reductase (NarGHI) and the Q-pool is representative of bacterial respiration<sup>18,19</sup>. The oxidation of formate and reduction of nitrate is a highly exergonic process, which is coupled to the generation of a proton gradient.

the proton gradient. Topology of the complexes and position of their Q-sites with respect to the membrane determines the capacity of redox loops to contribute to PMF<sup>15</sup>. The first atomically resolved redox loop is the formate-nitrate couple, depicted in **Figure 1.2**<sup>16–19</sup>. Quinone reduction on the cytoplasmic face, as in the periplasmic-facing formate dehydrogenase (FdnGHI), involves uptake of two protons from the cytoplasm; concurrent with deposition of a proton into the periplasm from formate oxidation. The quinol protons are then deposited into the periplasm by quinol oxidation on the periplasmic face of the membrane by the cytoplasmic-facing nitrate reductase (NarGHI), which also consumes two cytoplasmic protons upon nitrate reduction<sup>20,21</sup>. A further contributing factor is electron flow, which in the case of the formate-nitrate redox loop is from the periplasm into the cytoplasm (P- to N- side), where the negative charge of formate in the periplasm is lost upon its oxidation. Consequently, the formate-nitrate redox loop has a measured stoichiometry of  $4H^+/2e^-$ <sup>15</sup>.

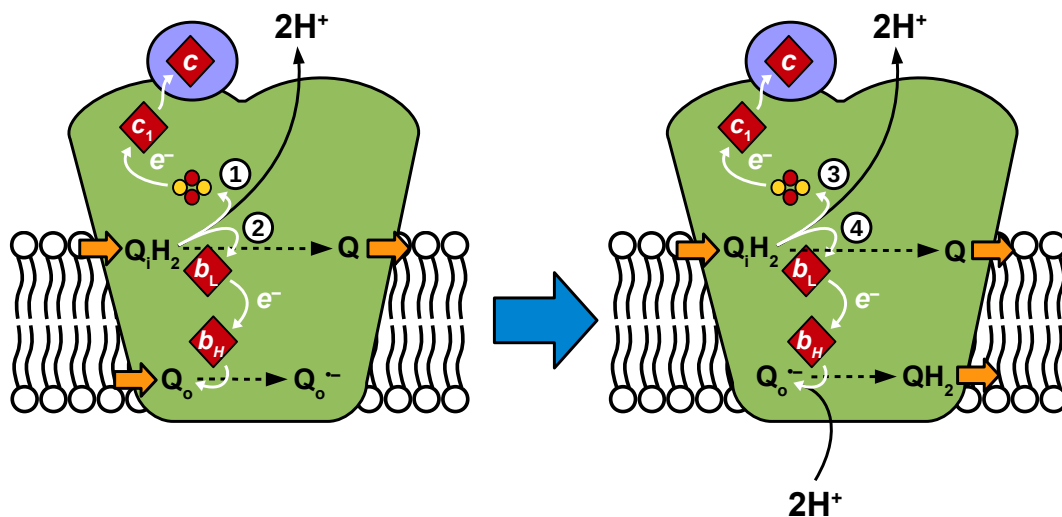


**Figure 1.3: The Q-cycle of complex III (cytochrome *bc*<sub>1</sub>).** The Q-cycle is depicted in two phases and for only a single monomeric unit of complex III, the first phase represents oxidation of the first quinol bound to the Q<sub>i</sub>-site and generation of the anionic semiquinone in the Q<sub>o</sub>-site. The second phase represents the oxidation of the second quinol at Q<sub>i</sub> and the formation of fully reduced quinol at Q<sub>o</sub>. White arrows denote electron transfer, black arrows proton translocation, and orange arrows show binding/unbinding of quinone. Note that each phase reduces one cytochrome *c*, and that movement of the Rieske subunit is not depicted.

An additional example of this topology-dependent scalar proton-translocating system is the Q-cycle of complex III, as outlined in **Figure 1.3**. The cytochrome  $bc_1$  complex couples the oxidation of the quinone pool to the reduction of cytochrome  $c$  in mitochondria and many bacteria (but not *E. coli*)<sup>2,22</sup>. The problem here is that cytochrome  $c$  can only accept one electron, but quinol is a two electron carrier. In order to circumvent this issue, complex III has two Q-sites;  $Q_o$  is on the P-side of the membrane and  $Q_i$  is on the N-side. Transmembrane electron transfer between the two occurs via two  $b$ -type hemes. The  $Q_o$  site is therefore involved in electron bifurcation, where the first electron travels through the Rieske [2Fe-2S] cluster and cytochrome  $c_1$  to cytochrome  $c$ , and the second electron is used to reduce  $Q_i$ . Upon reduction, the Rieske protein very rapidly moves away from  $Q_o$  by 20 Å, thus gating electron transfer. It therefore takes two rounds of quinol oxidation at  $Q_o$  to fully reduce one quinone at  $Q_i$ . The process of quinol oxidation by  $Q_o$  releases two protons onto the P-side of the membrane, and quinone reduction at  $Q_i$  consumes 2 protons from the N-side. Overall, the oxidation of two ubiquinol at  $Q_o$ , and the reduction of one ubiquinone at  $Q_i$ , yields a final stoichiometry of  $4H^+/2e^-$ <sup>2,11,22</sup>.

### 1.1.3. Bacterial Respiratory Diversity

#### 1.1.3.1. *E. coli* Respiratory Pathways

*E. coli* is a facultative anaerobe with the ability to thrive in a variety of environments, switching between aerobic respiration, anaerobic respiration, or mixed-acid fermentation. As a common feature of bacteria in general, this biochemical flexibility is attributable to the highly branched organization of bacterial respiratory pathways, where multiple electron sources can be oxidized by a diverse selection of electron acceptors, as depicted in **Figure 1.4**<sup>2,23,24</sup>. These enzyme complexes are associated in so-called 'redox loops' where a dehydrogenase is coupled to a reductase by the quinone pool, exemplified by the fumarate-nitrate redox loop of **Section 1.1.1.2**. *E. coli* lacks the cytochrome  $c$  present in mitochondrial oxidative

phosphorylation and so the oxidases are coupled directly to the Q-pool<sup>2,4,23,24</sup>. While 15 dehydrogenases/hydrogenases and 13 reductases/oxidases are theoretically available to form redox loops, the set of these active at any one time is transcriptionally regulated by oxygen, nitrate and other effectors so that only certain combinations of electron donors and acceptors are ever utilized<sup>21,25,26</sup>. These respiratory redox loops are believed to exist largely as supramolecular complexes which can be further regulated spatio-temporally<sup>27-30</sup>.

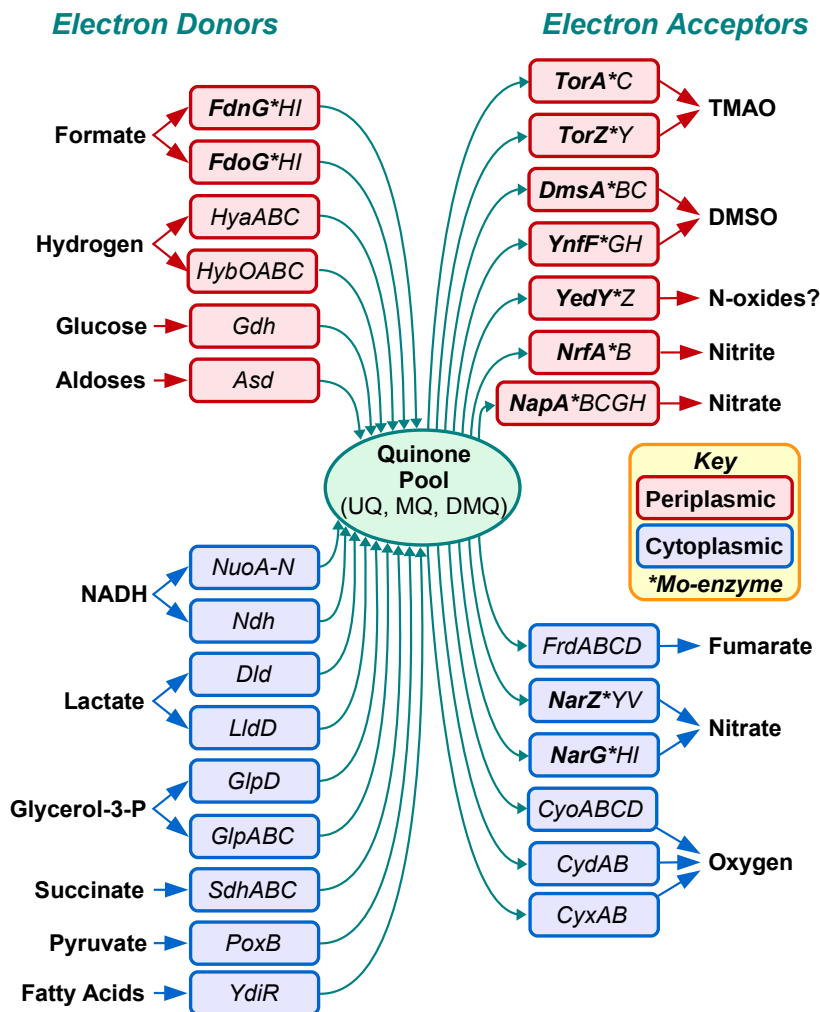


**Figure 1.4: *E. coli* respiratory diversity.** The central role of the quinone pool is highlighted and topology of the various enzyme complexes is depicted. Enzymes containing Moco at the active site are bolded. Figure adapted from reference 24.

The basis for which electron donors and acceptors are utilized is their availability and reduction potential. The more potent an electron donor (reductant) is, the more favourably it is utilized, since it can potentially contribute more significantly to PMF generation. This is clear from the  $\Delta p$  generated by *E. coli* under various conditions. Fermentative conditions only support a  $\Delta p$  of -100 mV, insufficient for ATP production by oxidative phosphorylation. Under aerobic conditions, however, a  $\Delta p$  of -160 mV is possible, and anaerobic conditions with nitrate as a terminal electron acceptor support a  $\Delta p$  of -140 mV<sup>3</sup>.

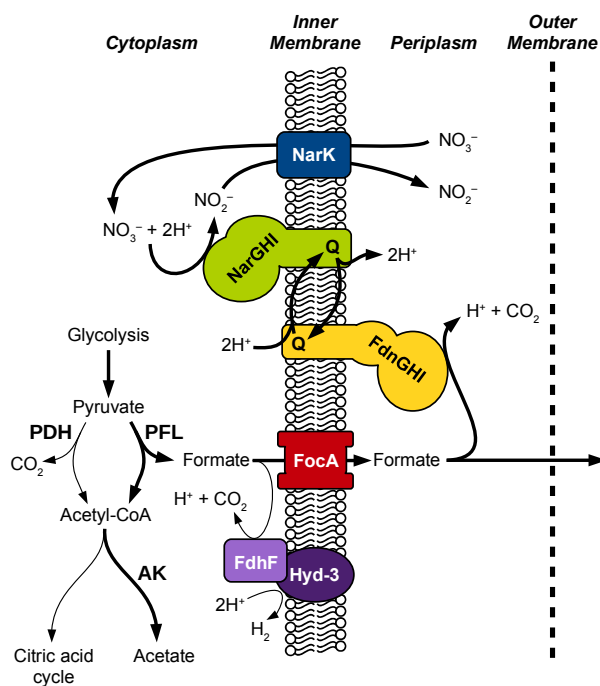


**Figure 1.5: Metabolic context of the formate nitrate redox loop.** Formate is significantly produced under anaerobic conditions as pyruvate dehydrogenase (PDH) activity diminishes and pyruvate-formate lyase (PFL) activity increases. In the presence of nitrate, formate-hydrogen lyase complex (FdhF/Hyd-3) is down-regulated so most formate is pumped out of the cell via FocA. Nitrite/Nitrate exchange is possible through activity of NarK. Under anaerobic/high-nitrate conditions, the citric acid cycle is down-regulated and ATP synthesis is possible through acetate kinase (AK).

NADH ( $E^{\circ} = -320$  mV) is the primary electron donor for respiration but glycerol-3-phosphate ( $E^{\circ} = -190$  mV), succinate ( $E^{\circ} = +30$  mV), lactate ( $E^{\circ} = -190$  mV) and fatty acids are also sources of electrons for aerobic respiration<sup>21,26</sup>. Under anaerobic conditions, formate ( $E^{\circ} = -420$  mV) becomes a significant source of electrons due to the increased expression of pyruvate-formate lyase (PFL), and diminished flux through the citric acid cycle, see **Figure 1.5**<sup>31</sup>. Excess formate is either exported out of the cell (FocA) or, in the absence of any electron acceptor (fermentative growth), its

oxidation is coupled to the generation of hydrogen (FdhF-Hyd3) <sup>32</sup>. In the presence of nitrate, however, the nitrate-linked formate dehydrogenase (FdnGHI) is up-regulated and FdhF is down-regulated <sup>33,34</sup>. At the same time there is an increased expression of the nitrate/nitrite antiporter (NarK) and nitrate reductase (NarGHI) <sup>31</sup>. The formate-nitrate redox loop therefore represents a significant generator of PMF in the anaerobic respiration of *E. coli* <sup>17,31,33</sup>.

Electron acceptors are also utilized according to a hierarchy based on oxidizing strength <sup>21</sup>. Oxygen ( $E^{\circ} = +820$  mV), for instance, is the most oxidizing terminal electron acceptor available and therefore represses the expression of enzymes involved in anaerobic respiration and fermentation <sup>21,35</sup>. Nitrate ( $E^{\circ} = +420$  mV), the optimal anaerobic electron acceptor, inhibits the expression of anaerobic respiratory enzymes of less oxidizing substrates: TMAO ( $E^{\circ} = +130$  mV), DMSO ( $E^{\circ} = +160$  mV), fumarate ( $E^{\circ} = +30$  mV) <sup>21,26</sup>.

In the case where multiple isoenzymes exist for a substrate, the  $H^+/e^-$  ratio for a given enzyme is selected for at the transcriptional level in order to maximize not the efficiency but the rate of PMF generation (growth rate) <sup>21,36</sup>. For instance most dehydrogenases acting under aerobic conditions – such as NADH:quinone oxidoreductase (Ndh) – do not contribute to PMF generation by proton pumping, but the coupled cytochrome *bo* quinol oxidase (CyoABCD) does. This system ensures maximal flux through the respiratory pathway rather than maximal efficiency in redox:PMF energy conversion <sup>21,35,36</sup>. In oxygen limited or anaerobic conditions, the proton-pumping NADH:quinone oxidoreductase (NuoA-N) is coupled to the non-protonmotive cytochrome *bd* quinol oxidase (CydAB), which has a higher affinity for  $O_2$  but slower turnover compared to cytochrome *bo* <sup>21,35,37</sup>.

### **1.1.3.2. Quinones in *E. coli* Respiratory Diversity**

*E. coli* synthesizes three respiratory quinone species: ubiquinone (UQ,  $E^{\circ} = +110$  mV), demethylmenaquinone (DMQ,  $E^{\circ} = +40$  or  $-9$  mV) and menaquinone

(MQ,  $E^{\circ} = -80$  mV) (**Figure 1.8**)<sup>2,38,39</sup>. Due to their respective reduction potentials, ubiquinone is ideally suited for mediating electron transfer when oxygen is the terminal electron acceptor. Under anaerobic conditions, however, only lower potential oxidants are available and so the two low potential quinones, MQ and DMQ, are utilized<sup>21,40</sup>.

The composition of the Q-pool is a reflection of the ambient oxidizing conditions of the cell; where the Q-pool is largely comprised of UQ under aerobic conditions (65%) and MQ/DMQ comprise 2-4% and 32%, respectively<sup>40,40-42</sup>. Upon shifting to anaerobiosis, MQ concentrations rise 20 fold as UQ concentration falls 8 fold. DMQ concentration, on the other hand, only changes by 1.5 – 2 fold, indicating a role for DMQ in facilitating a smooth aerobic-anaerobic transition<sup>41</sup>. Even in the presence of all quinones, partitioning is possible by the intrinsic affinity for the various enzyme complexes with particular quinones. The NADH:quinone oxidoreductases and quinol oxidases mostly utilize ubiquinone, whereas TMAO, DMSO and fumarate reductases utilize DMQ and MQ<sup>21,42-44</sup>. NarGHI has been shown to utilize all three quinones, though some experiments indicate that NarGHI does not utilize DMQ<sup>40,43,45</sup>.

### 1.1.3.3. Regulation of *E. coli* Respiration

As already indicated, the choice of electron donor, and particularly electron acceptor, is predicated by a hierarchy of use based on availability and redox potency. Two regulatory pathways exist in *E. coli* for the oxygen-dependent control of respiratory gene expression. The anoxic respiration control (ArcAB) pathway is most active under micro-aerobic conditions (10-20% O<sub>2</sub>), while the fumarate and nitrate reductase regulator (FNR) is active in the absence of oxygen (0-10% O<sub>2</sub>)<sup>46</sup>. These two pathways control the flow of carbon, and thus electrons, across the central metabolic pathways of the cell<sup>21</sup>.

ArcAB is a two-component regulatory system where ArcB is membrane bound

and senses the oxidation state of the Q-pool <sup>47</sup>. ArcB stimulation occurs with a constant rate, but deactivation occurs as a function of the concentration of oxidized UQ <sup>47</sup>. Upon activation by decreasing levels of oxidized UQ, ArcB autophosphorylates via an N-terminal histidine kinase domain and subsequently transfers the phosphate onto the effector protein, ArcA <sup>26</sup>. In the phosphorylated state, ArcA binds to its respective DNA operator sequences with higher affinity, repressing *cyoABCD*, *nuoA-N* and succinate dehydrogenase (*sdhABC*), but activating *cydAB*, *cyxAB*, *focA-pfl* and hydrogenase I (*hya*) <sup>26,31,46</sup>.

FNR is an activator of genes associated with anaerobiosis: *narGHI*, *dmsABC*, *nirB*, *frdABCD*, *fdnGHI*, *pfl*, *glpA*. It also acts to repress genes associated with aerobic metabolism, such as *cyoABCDE*, *cydAB*, *ndh*, *sdhABC* <sup>26</sup>. FNR is a direct sensor of cytoplasmic oxygen and shows significant similarity to the cyclic-AMP receptor protein, a regulatory component of catabolite repression in *E. coli* <sup>48</sup>. It consists of an N-terminal sensory domain and a C-terminal helix-turn-helix DNA-binding domain <sup>49</sup>. In its activated form, two monomers come together and coordinate an inserted [4Fe-4S] cluster, which is oxygen labile <sup>50-52</sup>. In the presence of oxygen the [4Fe-4S] cluster is degraded to a [2Fe-2S] cluster, resulting in homo-dimer monomerization. In low or rapidly changing oxygen conditions, the monomers are able to reform the [4Fe-4S] cluster by rapidly re-associating, made possible by lingering Cys-persulfides from the preceding breakdown. However, under greater oxygen tensions the [2Fe-2S] clusters are entirely lost and rapid re-dimerization is not possible <sup>51,53</sup>. Apo-FNR re-acquires its [4Fe-4S] cluster by the ISC FeS cluster biogenesis machinery (**Section 1.1.4.1**).

Nitrate, being the preferred oxidant of anaerobically growing *E. coli*, is a major gene regulator in bacteria through the homologous two-component regulatory systems NarXL and NarQP, which both function much like ArcAB. NarX and NarQ are membrane-bound sensor histidine kinases, which upon stimulation autophosphorylate and activate the response regulator proteins NarL and NarP through phospho transfer reactions <sup>54,55</sup>. The two systems have appreciable cross-talk, resulting in a convoluted regulatory mechanism <sup>54,56</sup>. In the presence of high nitrate

levels, NarX acts as a NarL kinase; whereas in the presence of nitrite, NarX dephosphorylates phospho-NarL<sup>57,58</sup>. NarQ, on the other hand, acts as a kinase in the presence of nitrite and low nitrate levels<sup>54,57</sup>. Phospho-NarL up-regulates expression of *narGHJI*, *narK*, *narXL*, *fdnGHI*, *nuoA-N*, meanwhile down-regulating the expression of fumarate and DMSO reductases, the periplasmic nitrate reductase (*napFDAGHBC*), and the nitrite reductases (*nrfA-G*, *nirBDC*)<sup>31,55</sup>. Accumulation of phospho-NarP only activates the nitrite reductases<sup>54,55</sup>. All known NarL and NarP regulon targets are also controlled by FNR, and thus this convoluted system of regulation functions to finely tune respiratory enzyme expression according to fluctuating nitrate and nitrite levels<sup>55,59</sup>.

Molybdenum-containing enzymes have been deemed “the Swiss army knife” of the cell, since they are particularly important for conferring anaerobic respiratory diversity and flexibility in prokaryotes, as depicted in **Figure 1.4** and discussed in **Section 1.1.4.3**. Molybdenum-containing enzymes bind an organo-metallic cofactor known generally as molybdenum cofactor (Moco). Biosynthesis of Moco is a multi-step pathway that is regulated by the ModE and FNR transcription factors upon sensing molybdate and anoxia, respectively<sup>48,60–62</sup>. Both Mo-bound ModE and FNR activation increase expression of the *moaABCDE* (Moco biosynthesis) operon and molybdoenzyme structural genes, ensuring the appropriate conditions (anoxia) and prerequisites (Mo) are present for Moco production<sup>48,60</sup>. Mo-ModE also down-regulates expression of molybdate transporters (*modABCD*)<sup>62,63</sup>. An interesting additional form of control are highly conserved Moco-responsive riboswitches; mRNA aptamer elements found upstream of the encoding gene which bind Moco directly as it accumulates in the cell<sup>64</sup>. These riboswitches down-regulate Moco biosynthesis genes (*moaABCDE*) and molybdate transporters, but are also found in the mRNA encoding DMSO reductase, formate dehydrogenase, TMAO reductase, nitrate reductase and aldehyde oxidase, where Moco binding increases their expression<sup>65</sup>.

### 1.1.4. Intraprotein Electron Transfer

The redox cofactors within proteins are rarely directly adjacent to each other and can be up to 14 Å apart, normally having protein and/or solvent between them<sup>66</sup>. The mechanism by which electrons can jump across such gaps is via the phenomenon of tunnelling<sup>6,67,68</sup>. According to quantum theory, an electron's wave function on a donor cofactor has a non-zero probability of existing on the adjacent acceptor cofactor. The energetic barrier of having the electron move between cofactors is overcome by its quantum mechanical nature, where it can spontaneously appear on the acceptor<sup>2,6,68</sup>. The lack of temperature dependence, even down to 5 K, is evidence that tunnelling is the process by which electrons are transferred<sup>67,69</sup>. The protein medium composition and density between redox centers has significant impact on electron transfer rates. Over a fixed distance, electron transfer rates can differ by 3 orders of magnitude<sup>70</sup>. The three main factors that determine the rate of electron transfer are:

- 1) *The inter-center distance.* There is an exponential decay of the electron's wavefunction with distance, which translates into an exponential decay in rates of electron transfer with distance. The decay constant for this behaviour represents the coupling efficiency between redox centers and is determined by the packing density of the intermediary protein medium; the value of  $\beta = 1.4 \text{ \AA}^{-1}$  has been found to be a good first approximation for this constant, but due to the inhomogeneity of proteins the precise value can vary significantly<sup>66,71</sup>. The inter-center distance is taken as the edge-to-edge separation between cofactors and is almost always <14 Å, greater than this and electron transfer can become rate limiting<sup>66,72</sup>.
- 2) *The reduction potential difference of cofactors expressed in free energy terms ( $\Delta G^\circ$ )*<sup>2,73</sup>. As mentioned in **Section 1.1.1**, electrons are spontaneously transferred from low potential to high potential (low  $E_m$  to high  $E_m$ ):  
$$\Delta G^\circ = -nF \Delta E_m$$
. The ways in which cofactor potentials can be modulated

is detailed in later sections. The presence of adjacent cofactors and their oxidation state can have a significant effect on the energetics of electron transfer, i.e. redox cooperativity <sup>74</sup>.

- 3) *The reorganization energy of the system.* The reorientation of dipoles and movement of charged groups within the protein and solvent, changes in metal-coordination bond lengths and concomitant proton transfers all require movement of nuclei, which requires energy – the reorganization energy ( $\lambda$ ). Proteins serve to provide a low reorganization energy environment, due to low polarizability, where  $\lambda < 1.6$  eV, but typically  $\lambda = 0.9 \pm 0.2$  eV <sup>75,76</sup>.

For his work on how electron transfer rates depend on reorganization energy and the free energy change, R.A. Marcus was awarded the 1992 Nobel prize in chemistry <sup>68,77,78</sup>. The Marcus relation is given by **equation 1.7**:

$$\Delta G^\ddagger = \frac{(\Delta G^\circ + \lambda_o)^2}{4\lambda_o} \quad (1.7)$$

Where the activation energy barrier ( $\Delta G^\ddagger$ ) depends on the standard free energy change ( $\Delta G^\circ$ ) and standard reorganization energy ( $\lambda_o$ ). In turn, the electron transfer rate ( $k_{et}$ ) is a function of the activation energy, temperature and a pre-exponential factor ( $A$ ):

$$k_{et} = A \cdot \exp\left(\frac{-\Delta G^\ddagger}{RT}\right) \quad (1.8)$$

An interesting consequence of this relation is that the fastest rates of electron transfer are when  $-\Delta G^\circ = \lambda_o$ . Any higher or lower driving force, and electron transfer occurs more slowly – in proteins, individual electron transfer steps are in the range of 0 to 100 mV (0 to  $-10$  kJ mol<sup>-1</sup>) <sup>2</sup>. Also, the larger a reorganization energy, i.e. a larger required nuclear deviation between pre- and post- electron transfer states, slows electron transfer as well. Fortunately, FeS clusters and hemes have very low reorganization energies, only varying by a factor of 2-3 <sup>2</sup>.

Electron transfer rates can be predicted empirically (for exergonic redox steps)

by **equation 1.9**<sup>66,79</sup>:

$$\log_{10} k_{et} = 13.0 - (1.2 - 0.8\rho)(r - 3.6) - 3.1(\Delta G + \lambda)^2/\lambda \quad (1.9)$$

The fraction of volume between redox cofactors that is in van der Waals contact is given by the weighting factor  $\rho$ , where a value of 1 represents fully packed protein medium ( $\beta = 0.9 \text{ \AA}^{-1}$ ) and 0 represents no packing and thus vacuum ( $\beta = 2.8 \text{ \AA}^{-1}$ ).  $r$  is the inter-center distance, where optimal electron transfer occurs at van der Waals contact ( $3.6 \text{ \AA}$ ,  $k_{et} = 10^{13} \text{ s}^{-1}$ ).

### 1.1.5. Redox Cofactors

Cofactors are relatively small compounds required for proteins, RNA and even DNA molecules to perform their function<sup>80-82</sup>. In the case of enzymes, an inactive apo-enzyme is converted into the active holo-enzyme by incorporation of the necessary cofactor. These cofactors play roles as catalytic centers, for conducting electrons through proteins, for redox sensing, and as structural components. For redox chemistry, nature exploits several organic cofactors (flavins and quinones), metallic cofactors containing Fe, Ni, Mg, Mn and Cu, and organo-metallic cofactors (hemes, Mo/W-pterin cofactors, FeMoco of nitrogenase). By far the most prevalent of the metal-containing cofactors are heme and heme-like compounds (chlorins and chlorophylls) and iron-sulfur clusters<sup>81</sup>. For the purposes of this thesis we will discuss only the cofactors relevant to nitrate reductase: hemes, FeS clusters, molybdenum cofactors and quinones.

#### 1.1.5.1. Iron-Sulfur Clusters

Iron-sulfur (FeS) clusters are among the most ancient protein-bound cofactors. Their ubiquitous use across all domains of life and likely presence as inorganic components of Earth's environment 4.2 billion years ago suggests they played a crucial role in the origin of life<sup>83</sup>. FeS proteins are extremely widespread, with roles in

cellular metabolism<sup>84–89</sup>, gene regulation and expression<sup>53,90–94</sup>, and DNA repair and synthesis<sup>95,96</sup>. As protein bound prosthetic groups, FeS clusters exist as various stoichiometries of iron and inorganic sulfur, where the most common are [1Fe], [2Fe-2S], [3Fe-4S], and [4Fe-4S]. FeS clusters are also found as components of more complex cofactors, such as the FeMo cofactor at the active site of nitrogenase<sup>81,97</sup>. Regardless of the number of iron ions, FeS clusters act as 1 e<sup>-</sup> carriers, where individual iron ions can be in the +2, +2.5 and +3 oxidation states<sup>81,97</sup>. As an example, a [3Fe-4S] cluster, as in NarH of nitrate reductase, goes from a reduced state configuration of 2Fe<sup>2.5+</sup>/1Fe<sup>3+</sup>, to 3Fe<sup>3+</sup> in the oxidized state<sup>19,97</sup>. Most frequently, proteins bind FeS clusters by coordination of the iron ions by cysteines, but coordination by serine, arginine and histidine is also possible – as in the 2His/2Cys coordinated [2Fe-2S] cluster of the Rieske protein in cytochrome *bc*<sub>1</sub> and the 1His/3Cys [4Fe-4S] cluster of NarG in nitrate reductase<sup>19,97,98</sup>. The reduction potentials of FeS clusters vary considerably, from that of *Azotobacter vinelandii* ferredoxin I (-650 mV)<sup>99</sup> to the high-potential iron-sulfur protein of *Rhodospirillum rubrum* (+350 mV)<sup>100</sup>. Proteins evolve to tune the potential of an FeS cofactor by the type of cluster coordinated, the geometry and nature of coordinating ligands, and the surrounding electrostatic environment<sup>73,81,97,101</sup>.

Since FeS clusters are prone to oxidative damage, and can catalyse the formation of reactive oxygen species (namely hydroxyl radicals), it is prudent that the cell sequester FeS clusters within protein interiors. It is for these reasons that specific biosynthetic machinery has evolved for FeS protein biosynthesis<sup>102,103</sup>. The biogenesis of FeS clusters, regardless of the organism, occurs in two phases: assembly and transfer<sup>104,105</sup>. Bacteria encode for three such systems, each usually in their own operons. The NIF (nitrogen fixation) system is unique to nitrogen-fixing bacteria for the maturation of nitrogenase, which converts N<sub>2(g)</sub> into bioavailable NH<sub>3(aq)</sub><sup>104,106,107</sup>. The ISC (iron-sulfur cluster) system is a general 'housekeeping' system used under normal conditions for the biogenesis of FeS clusters, and is related to the mitochondrial system used by eukaryotes<sup>104,105,108</sup>. Finally, the SUF (sulfur mobilization) system is used in conditions of low iron availability or oxidative

stress, and is found in bacteria, archaea and plastids<sup>104,109,110</sup>. Bacteria may have one, two or all three systems, and NUF has been demonstrated to replace both the ISC and SUF systems of *E. coli* under anaerobic conditions, demonstrating their interchangeability<sup>104,111</sup>. Non-photosynthetic eukaryotic FeS cluster biogenesis occurs in the mitochondria, where a system very similar to the bacterial ISC machinery generates all cellular FeS clusters<sup>112,113</sup>. Highly conserved among eukaryotes are the 'ISC-export machinery', which exports FeS clusters from the mitochondria into the cytoplasm, and the 'cytosolic FeS protein assembly machinery', which is responsible for generating all cytosolic and nuclear FeS proteins<sup>105,112,113</sup>.

FeS cluster biogenesis is a complex process requiring three ingredients: sulfur, iron, and electrons<sup>104,105,113</sup>. Sulfur is derived from free L-cysteine, which is converted to alanine by the cysteine desulfurase (IscS – bacterial, NFS1 – mitochondrial)<sup>1</sup>. Iron, being a highly reactive metal, is obtained as Fe<sup>3+</sup> bound to iron donors or carrier proteins (IscX, CyaY, IscA, frataxin). Electrons are required for FeS clusters to chemically form, and are supplied by ferredoxin/ferredoxin reductase, which reduces both the Fe<sup>3+</sup> and the extracted sulfur (S<sup>0</sup>). A scaffold protein (IscU, ISCU) acts as a conformationally flexible platform onto which all three ingredients come together to produce transiently-bound [2Fe-2S] or [4Fe-4S] clusters. The FeS cluster is then transferred and inserted into target apo-proteins in an ATP-dependent fashion utilizing a chaperone/co-chaperone pair (HscA/HscB, HSPA9/HSC20) and sometimes requiring a carrier protein (IscA) or further sets of proteins in eukaryotes<sup>104,105,113</sup>. While the general mechanism for FeS cluster biogenesis has been elucidated, many questions remain.

#### **1.1.5.2. Heme**

Hemes are organo-metallic cofactors which, similar to FeS clusters, function as 1 e<sup>-</sup> carriers; cycling through the ferric (+3) and ferrous (+2) states. The basic

---

1 Proteins from the bacterial ISC and mitochondrial machinery are indicated in brackets, where the mitochondrial protein is indicated by an underscore.

structure of heme includes a porphyrin ring which coordinates a central iron ion via the pyrrole nitrogens. The porphyrin ring can be adorned with various functional groups and chemical modifications – such as farnesylation, formylation, hydroxylation and acetylation – to give rise to the diverse set of hemes; those most commonly encountered in respiration are hemes *a*, *b*, *c*, *d* and *o* (**Figure 1.6**)<sup>97,114</sup>. Hemes exhibit oxidation state dependent UV-vis absorbance spectra, and it is thanks to this property that led to their discovery as “cellular pigments” around the turn of the 20<sup>th</sup> century<sup>2,115–117</sup>. It is by their reduced-*minus*-oxidized peak position in the 550-630 nm range (the  $\alpha$ -peak) which allows their differentiation. In the case of *b*-hemes, as in NarGHI, this is around 560 nm<sup>2,97,118</sup>.

Proteins containing at least one heme are known as hemoproteins and those associated with respiration are known as cytochromes. Hemoproteins function in oxygen transport<sup>119,120</sup>, electron transfer<sup>114,121</sup>, sensing NO, O<sub>2</sub> and CO<sup>122</sup>, enzyme

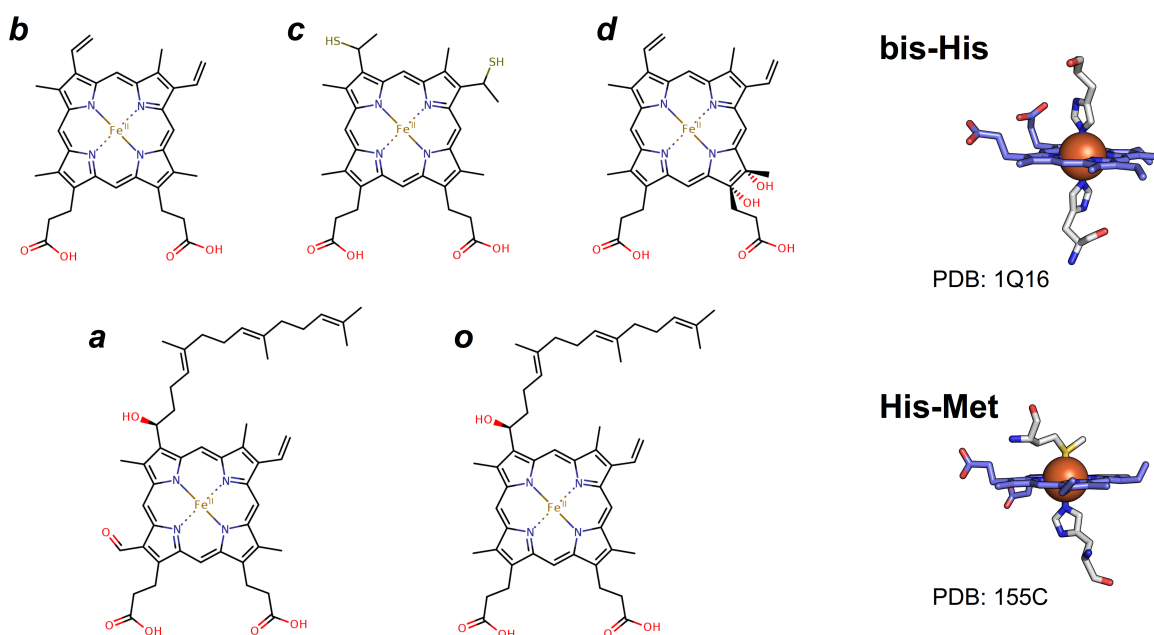


**Figure 1.6: Heme cofactor structural diversity and axial coordination.** Heme *b* (protoporphyrin IX) is the basic model heme, on which chemical modifications results in hemes *a*, *c*, *d* and *o*. Cytochrome heme axial coordination most commonly occurs via bis-His or His-Met coordination. Note the nearly perpendicular arrangement of the imidazole planes in the bis-His coordinated heme. Atoms colored according to CPK convention.

regulation <sup>123,124</sup>, and oxidative reactions <sup>125</sup>. Hemoproteins can bind their hemes via four main interactions: 1) mono- or bis- coordination of the central heme iron by histidine or methionine (see **Figure 1.6**); 2) polar contacts of protein side chains with the heme propionates; 3) van der Waals and hydrophobic interactions with the porphyrin; and, 4) in the case of *c*-cytochromes, the cysteines of conserved CxxCH motifs form one or two thioether linkages between the thiols of *c*-type hemes <sup>81,97,126,127</sup>. The identities and numbers of ligands, the coordination geometry, heme 'ruffling' and distortion, solvent exposure, redox-Bohr effects, and the various other interactions of the protein and adjacent cofactors with the heme determine its spectroscopic and electrochemical properties <sup>8,73,127–135</sup>. Through manipulation of these various factors, hemoproteins can tune their heme potentials over a 1 V range (-550 mV to +450 mV) <sup>97,133,134,136</sup>.

Due to the mixing of Fe<sup>2+</sup> *d*-orbitals with the π-orbitals of the conjugated porphyrin ring, the electron added upon heme reduction is spread out over the entire heme system, including the propionates and axial ligands <sup>137–139</sup>. Functionally, this spreading of electron density over the entire cofactor effectively decreases the distance between hemes, which facilitates rapid electron transfer <sup>72,137</sup>. The delocalization of charge also makes hemes particularly useful for transferring electrons across membranes; *b*-cytochromes in particular are central components in the aerobic respiration of mitochondria (cytochrome *bc*<sub>1</sub> <sup>22</sup>), photorespiration in chloroplasts (cytochrome *b<sub>6</sub>f* <sup>140</sup>) and bacterial anaerobic respiration (NarGHI <sup>19</sup> and FdnGHI <sup>18</sup>). The ability for hemes to delocalize charge also makes them ideal cofactors for storing electrons, as in mitochondrial cytochrome *c* and the multi-heme cytochromes of many bacteria and archaea <sup>134,137,141</sup>.

Depending on the organism there is one of two ways for heme biosynthesis to proceed. The starting materials used are succinyl-CoA and glycine in animals, fungi and α-proteobacteria, or glutamate in most bacteria, archaea and plants <sup>142</sup>. The two pathways converge at the first committed step of heme biosynthesis, which is the creation of δ-aminolevulinic acid <sup>143</sup>. In a series of condensation, decarboxylation and

oxidation reactions, the final Fe<sup>2+</sup> insertion by ferrochelatase yields Fe-protoporphyrin IX (heme *b*)<sup>81,142,143</sup>. Heme *b* is then either directly incorporated into *b*-type cytochromes or used as a template for synthesis of hemes *a*, *c*, *d* and *o*<sup>81,114</sup>.

### 1.1.5.3. Mono-Nuclear Molybdenum Cofactor

Molybdenum (Mo) is an essential trace element for plants, animals and prokaryotes and the only 2<sup>nd</sup> row transition metal utilized in biochemistry<sup>62</sup>. It is a component of the active site cofactors of well over 50 enzymes, which themselves play diverse roles in metabolism and the biogeochemical cycles of sulfur, nitrogen

(Section 1.2.1) and carbon<sup>62,144</sup>. In

humans, four molybdoenzymes are known, having roles in sulfite and N-hydroxy-cytosine detoxification, purine metabolism, and pro-drug activation<sup>62,145</sup>.

Deficiency of Mo and Mo-containing cofactor (Moco) in humans is characterized by progressive neurological damage, which in most cases leads to early childhood death. The fatal effects of Moco deficiency are mainly the result of the toxic accumulation of sulfite<sup>146</sup>.

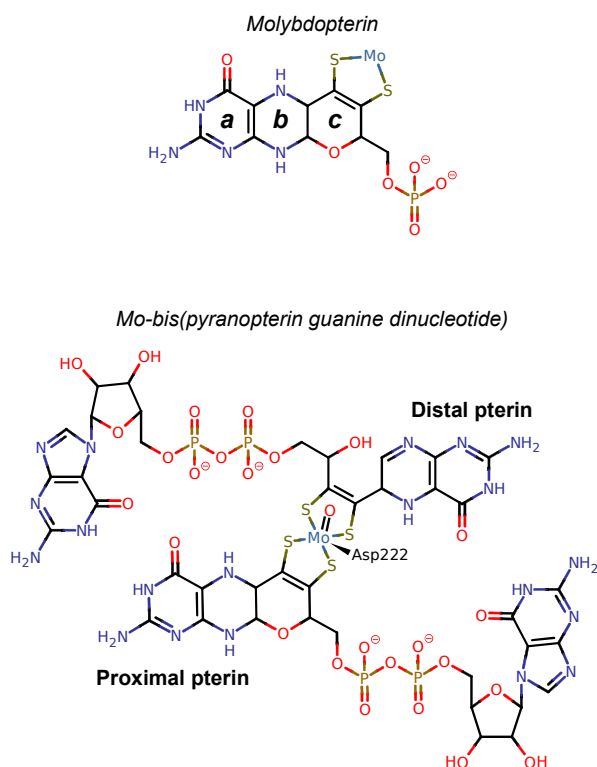


### Figure 1.7: Molybdenum-containing cofactors.

Molybdopterin is the most basic pterin and is comprised of the (a) pyrimidine, (b) pyrazine and (c) pyran rings. The two pterins of NarGHI Mo-bis(pyranopterin guanine dinucleotide) are identified by their proximity to FS0, of which the distal pterin has an open pyran ring. Atoms colored by CPK convention.

Apart from the Fe-Mo cofactor of nitrogenase<sup>147</sup> and the Cu-Mo cofactor of *Desulfovibrio gigas* orange protein<sup>148</sup>, Mo is found coordinated in Moco as a single ion by tricyclic organic cofactors

called pterins (pyranopterin). The basic pyranopterin structure is shown in **Figure 1.7** where the pyrimidine, pyrazine and pyran rings are indicated <sup>81</sup>. The two dithiolene sulfurs act as ligands to the Mo, and the coordination sphere is completed by a combination of oxo, hydroxo, sulfido or amino acid (Ser, Cys, Se-Cys and Asp) ligands. The Mo itself cycles between the +IV/+V/+VI oxidation states in order to catalyse oxo-transfer or hydroxylation reactions, for which these enzymes have broad reactivity (xanthine, DMSO, formate, ethylbenzene, nitrate, selenate, chlorate, sulfur, arsenic, and others) <sup>62,149</sup>. Mononuclear molybdoenzymes (those binding Moco) are classified into four families based on their pterin structure and active site Mo coordination sphere: the xanthine oxidase, DMSO reductase, sulfite oxidase and aldehyde oxidase families <sup>62,150</sup>. The pyranopterin phosphate is left unmodified in eukaryotic molybdoenzymes and bacterial sulfite oxidases, but bacterial DMSO reductases and xanthine oxidases are modified by the addition of guanosine monophosphate and cytosine monophosphate, respectively <sup>149</sup>.

The DMSO reductase family, of which *E. coli* nitrate reductase is a member, is found only in prokaryotes and represents the most diverse family in terms of function <sup>62,151</sup>. This family is characterized by binding Mo with two pyranopterins, each modified by addition of guanosine monophosphate at the pyranopterin phosphate – named Mo-bis(pyranopterin guanine dinucleotide) or Mo-bisPGD (**Figure 1.7**) <sup>62</sup>. The Mo<sup>VI</sup> coordination sphere is completed by an oxygen or sulfur ligand and either a hydroxo or amino acid (Ser, Cys, Se-Cys, Asp) ligand <sup>149</sup>. In *E. coli* nitrate reductase (NarGHI), the Mo<sup>VI</sup> coordination sphere is completed by an oxygen/Asp or bidentate Asp ligand <sup>19,152,153</sup>. A further modification of the NarG Moco is the open state of the pyran ring of the distal pterin, similar to the Moco of ethylbenzene dehydrogenase of *Aromatoleum aromaticum*, also a DMSO reductase family enzyme <sup>19,154</sup>.

*E. coli* has five known operons involved in Moco metabolism (*moa*, *mob*, *mod*, *moe*, and *mog*) encoding a total of 15 proteins <sup>155</sup>. Biosynthesis of the basic pyranopterin cofactor involves a highly conserved and complex pathway involving three main steps <sup>62,149</sup>: 1) the cyclization of a guanosine 5'-triphosphate (GTP) to

produce cyclic pyranopterin monophosphate (MoaA, MoaC); 2) production of the dithiolenes by sulfuration (MoaD/MoaE, MoeB), a process that shares a common enzyme with FeS cluster production (IscS); and 3) incorporation of molybdate (MogA, MoeA). The dimerization of pyranopterin and addition of two additional guanosine nucleotides (MobA) is required for the biosynthesis of NarG-bound Moco, which in total requires 9 proteins and 5 ATP equivalents. Due to the high lability of Moco, system specific chaperones are required to transfer and insert Moco into the correct apo-enzyme<sup>62,149,156</sup>.

While much has been learned with regards to ligand control of Mo electrochemistry, less is known about what role the pterin plays in determining the functionality of Moco as a whole. This includes the significance of pyranopterin conformation/oxidation state and the function and consequences of an open pyran ring.

#### 1.1.5.4. Quinones

Quinones are essential mobile electron carriers of energy conserving membranes, where they serve as  $2\text{H}^+/2\text{e}^-$  mediators in respiratory and photosynthetic pathways<sup>2</sup>. Their presence as respiratory components is nearly universal across the tree of life, being absent only in most obligate fermentative bacteria (*Lactobacillus*, *Streptococcus*) and methanogenic archaea of the order *Methanosarcinales*<sup>157,158</sup>. *E. coli* produces three different quinone species, where the concentrations of each varies with culture aeration (see **Section 1.1.3.2**). Ubiquinone ( $E_{m,7} = +100$  mV) (**Figure 1.8**) is found in mitochondria and is the major respiratory quinone of *E. coli* under aerobic conditions<sup>40,41,157</sup>.

The core of a quinone is the aromatic head group which consists of either one ring (benzoquinones) or two rings (naphthoquinones). While there are many forms of quinones in nature, those involved in respiration are 1,4-hydroxyquinones (**Figure 1.8**), which are rendered highly lipophilic by addition of poly-isoprenoid (or phtyl)

tails. The length of these tails, in terms of the number of isoprene units, depends on the organism and varies most commonly between 6 and 10, where human ubiquinone contains 10 isoprenoid units and quinones of *E. coli* have 8<sup>157,158</sup>. In the membrane, quinone tails localize to the mid-plane region whereas the head groups localize close to the polar head group region of the bilayer, where interactions with water are possible<sup>159,160</sup>.

Quinones can cycle through three oxidation states, fully reduced quinols (having 1,4-hydroxyls), one electron reduced semiquinone radicals (mono-protonated or anionic), or the fully oxidized quinones (1,4-ketones) (**Figure 1.8**). In turn, each oxidation state can have three protonation states where each protonation and reduction can be characterized by a  $pK_a$  and reduction potential:  $E_1$  for the

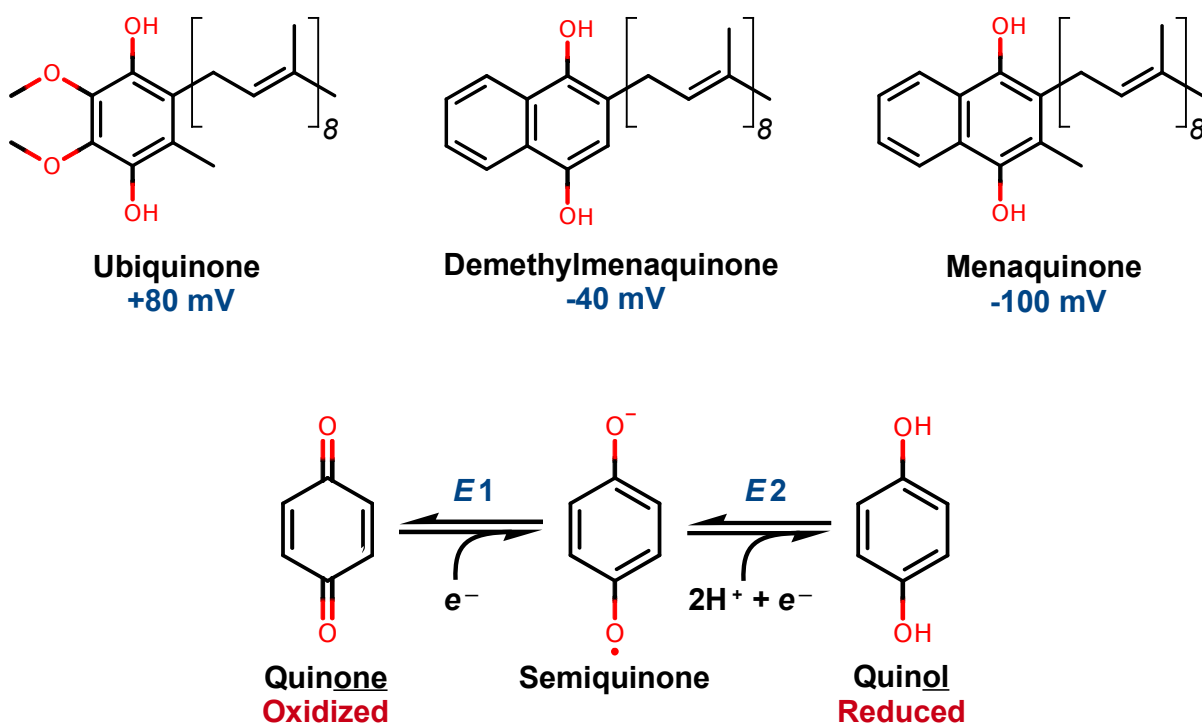


**Figure 1.8: The quinones of *E. coli* and quinone chemistry overview.** *E. coli* synthesizes three quinones: ubiquinone (UQ), menaquinone (MQ) and its biosynthetic intermediate demethylmenaquinone (DMQ). Quinol is a  $2e^-/2H^+$  carrier, as such quinone reduction is characterized by two reduction potentials ( $E_1$ ,  $E_2$ ) and proceeds through a semiquinone radical intermediate. Atoms colored according to CPK convention.

quinone/semiquinone couple and  $E_2$  for the semiquinone/quinol couple, where a quinone's  $E_m = (E_1 + E_2)/2$ . In a biological context, the most stable forms for the three oxidation states are  $\text{QH}_2$  (reduced and fully protonated),  $\text{Q}^{\bullet-}$  (anionic semiquinone) and  $\text{Q}$  (oxidized and deprotonated)<sup>2,158</sup>. Two main factors influence the intrinsic electrochemical properties of quinones: the number of rings and the addition of electron withdrawing or donating groups to the quinone ring(s). Case in point, naphthoquinones generally have lower potentials than benzoquinones due to the greater resonance stabilization afforded by the second aromatic ring. In a rough sense, the addition of electron-donating groups ( $-\text{OCH}_3$ ,  $-\text{CH}_3$ ,  $-\text{OH}$ ,  $-\text{NH}_3$ ) raises the  $\text{QH}_2$   $\text{pK}_a$  and lowers the  $E_m$  ( $\text{Q}/\text{QH}_2$ ), while addition of electron-withdrawing groups ( $-\text{NO}_2$ ,  $-\text{COOH}$ ) have the opposite effect<sup>161–163</sup>. Quinone properties are further tuned by the surrounding medium (protein), where the electrostatic environment and hydrogen bonding (geometry and partner identity) not only modifies the electron density over the quinone ring, but also influences the orientation of quinone functional groups (methoxyls, for instance) with respect to the quinone ring<sup>161,162,164,165</sup>.

Since the semiquinone intermediate is a radical, various aspects of quinone electrochemistry and the nature of its surrounding environment can be determined by EPR. In a redox titration of the semiquinone radical, where the concentration (EPR signal intensity) of semiquinone is plotted as a function of the ambient reduction potential, a bell-shaped curve results. The center of the titration peak is determined by the  $E_m$  value, and the width of the titration curve is a function of the difference between  $E_1$  and  $E_2$ . The titration curve width reports on the stability ( $K_s$ ) of a semiquinone, where  $K_s = 10^{((E_1 - E_2)/59)}$ <sup>166,167</sup>. Using pulsed EPR and electron-nuclear double resonance techniques the immediate environment of protein-bound semiquinones can be probed<sup>168–172</sup>.

While >1000 structures exist for many of the >50 quinone-binding proteins, there appears to be no universally identifiable protein sequence or motif for Q-sites<sup>173</sup>. Attempts to find such motifs have been made, however, with partial success. The  $\text{Q}_A$  and  $\text{Q}_B$  sites of bacterial reaction centers and photosystem II, as well

as cytochrome *bc*<sub>1</sub>/*b*<sub>6</sub>*f* Q<sub>i</sub> sites, are roughly predictable by the motif: aliphatic-(X)<sub>3</sub>-H-(X)<sub>2-3</sub>-(L/T/S) <sup>173</sup>. The Q<sub>o</sub> site of cytochrome *bc*<sub>1</sub> complexes, on the other hand, exhibits a conserved PEWY motif that provides structure features of the Q<sub>o</sub> site <sup>174</sup>. In agreement with these motifs, quinone binding often involves an acidic residue and a basic residue (His or Lys), which facilitate proton transfer <sup>173,175,176</sup>. Some examples include *E. coli* nitrate reductase (His66) and fumarate reductase (C-Glu29 and B-Lys228) <sup>170,177,178</sup>, yeast cytochrome *bc*<sub>1</sub> Q<sub>o</sub> (Glu272 and His161) <sup>174,179</sup>, and *Desulfovibrio vulgaris* membrane-bound cytochrome-*c* quinol dehydrogenase (Asp89 and Lys82) <sup>175</sup>. Interactions between the quinone, including ubiquinone methoxy groups, and the protein can be via any amino acid capable of making hydrogen bonds or backbone amides (Ser264 of photosystem II Q<sub>B</sub>, and Tyr130 of polysulfide reductase) <sup>180,181</sup>, and these interactions can include intermediary waters <sup>182</sup>. In order to facilitate efficient electron transfer, Q-sites are found in close proximity (<14 Å) to redox-active prosthetic groups, such as hemes and FeS clusters <sup>173,175</sup>. Quinone binding is often through a residue ligand of these adjacent metal centers, such as His66-heme *b*<sub>D</sub> of nitrate reductase or His161-Rieske [2Fe-2S] cluster of cytochrome *bc*<sub>1</sub> <sup>170,183-185</sup>. In the case of hemes, a propionate group often interacts directly with the quinone, as in *E. coli* nitrate reductase and formate dehydrogenase <sup>18,183,186</sup>. These hemes often contribute to a second feature common of Q-sites: proton transfer pathways. Since quinone reduction and quinol oxidation involve the uptake and release of protons, respectively, quinone binding sites are located near the interfacial regions of the bilayer <sup>175</sup>. Furthermore, since Q-sites are still within hydrophobic portions of protein interiors, as well as being within the membrane, there needs to be a way for the protein to channel these protons to the aqueous milieu, where they are often used to contribute to PMF. As such, Q-site associated proton transfer pathways have been identified in many proteins: nitrate reductase <sup>19</sup>, cytochrome *b*<sub>6</sub>*f* <sup>187</sup>, formate dehydrogenase <sup>18</sup>, respiratory complex I <sup>13,14</sup>, cytochrome *bc*<sub>1</sub> <sup>188</sup>, and the bacterial reaction center Q<sub>B</sub>-site <sup>189</sup>.

The biosynthesis of the quinone head group and isoprenoid tail occurs along separate pathways before being linked together by a prenyltransferase. The tail

derives from sequential condensations of isopentenyl diphosphate to dimethylallyl diphosphate, and the head group of menaquinone and ubiquinone is ultimately derived from chorismate via the shikimate pathway, involving the *men/mqn* and *ubi* operons<sup>158,190</sup>. Following condensation of the head and tail, further modifications are required, such as decarboxylation, methylation and hydroxylation<sup>39,158</sup>. Methylation of UQ and MQ is catalysed by UbiE, where upon knocking it out results in only demethylmenaquinone, the precursor to menaquinone<sup>42,191</sup>. MQ biosynthesis occurs mainly by a soluble complex of enzymes, whereas UQ biosynthesis occurs within a membrane-bound enzyme complex<sup>158</sup>. Regulation of quinone biosynthesis is not yet known, but it has been shown that the machinery to make MQ is present in *E. coli* under aerobic conditions and is activated post-translationally by changes in substrate concentration and increased flux through the quinone biosynthesis pathway<sup>41,192</sup>.

## 1.2. *E. coli* Nitrate Reductase A (NarGHI)

### 1.2.1. The Nitrogen Cycle

Nitrogen is an essential component of proteins, nucleic acids and even carbohydrates and lipids. It is the fourth most common element in the human body, at 3.3%(w/w), and constitutes ~75% (w/w) of our atmosphere<sup>193</sup>. Despite this, N<sub>2</sub> is unavailable to most organisms due to its inertness and is often a limiting nutrient in the primary photosynthetic production of Earth's ecosystems. NH<sub>4</sub><sup>+</sup> and NO<sub>3</sub><sup>-</sup> constitute the major bioavailable forms of nitrogen, made naturally available by prokaryotes via the nitrogen cycle (see **Figure 1.9**). Humans, however, are currently the largest source of bioavailable nitrogen by means of the Haber-Bosch process for production of ammonia fertilizers<sup>194,195</sup>. Certain species of bacteria and archaea are capable of fixing N<sub>2</sub> and, by means of symbiosis, so are some eukaryotes (legumes and termites). Nitrogenase is a highly conserved [Mo-Fe<sub>7</sub>-S<sub>9</sub>] cofactor-containing enzyme which, with the energy of ~16 ATP, is capable of ripping the triple N<sub>2</sub> bond apart to produce ammonia – a process known as nitrogen fixation<sup>196</sup>. Ammonia can

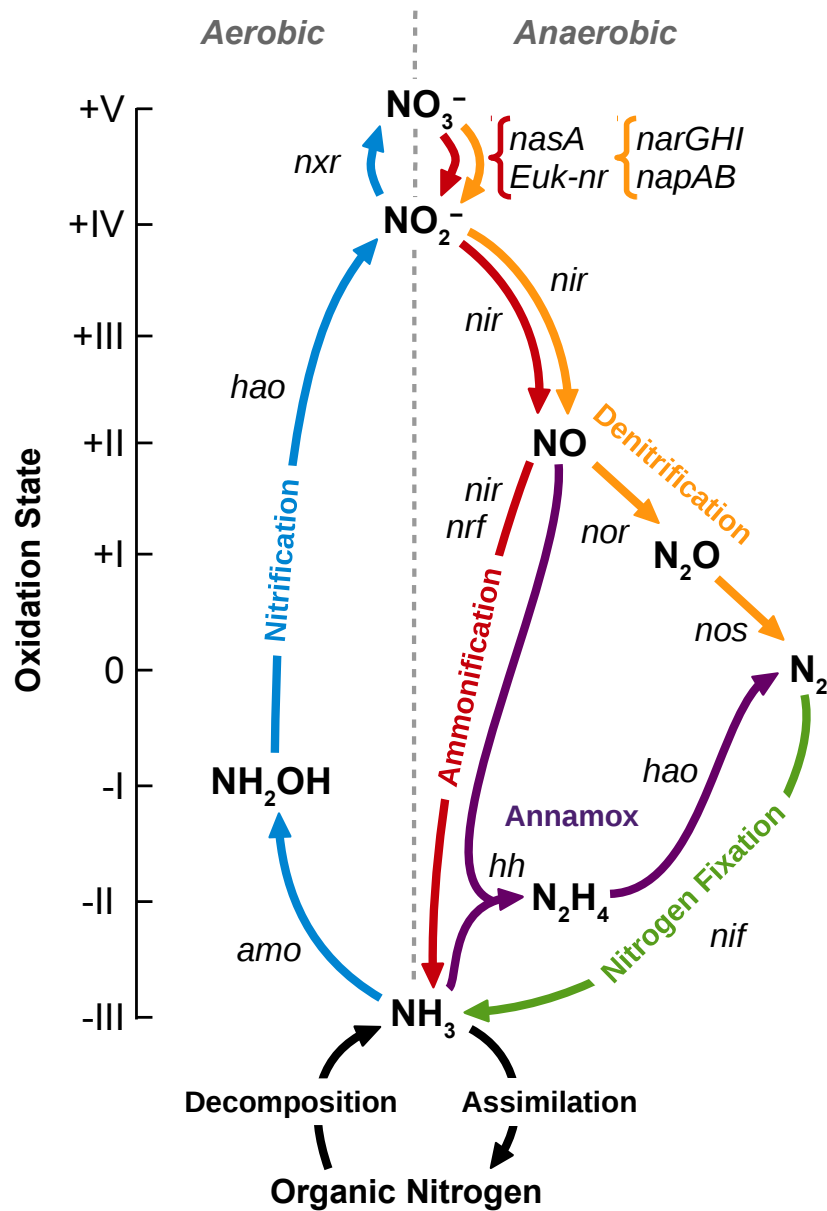


**Figure 1.9: The global biogeochemical nitrogen cycle.** Bacteria catalyse the interconversions of nitrogenous compounds via the action of several enzymes: assimilatory cytoplasmic nitrate reductase (*nasA*), Eukaryotic (plant) nitrate reductase (*Euk-nr*), respiratory nitrate reductase (*narGHI*), dissimilatory periplasmic nitrate reductase (*napAB*), nitrite reductases (*nir*), nitric oxide reductase (*nor*), nitrous oxide reductase (*nos*), cytochrome c nitrite reductase (*nrf*), hydrazine hydrolase (*hh*), hydrazine oxidoreductase (*hao*), nitrogenase (*nif*), ammonia mono-oxygenase (*amo*), nitrite oxidoreductase (*nxr*). Note that certain conversions occur only aerobically or anaerobically, as indicated by the center dotted line. Figure adapted from reference 194.

then be assimilated into complex biological matter, or be produced through decomposition. In the presence of oxygen, specific prokaryotes are capable of converting  $\text{NH}_4^+$  into  $\text{NO}_3^-$  via the process of nitrification, whereby the electrons released from this oxidative process are used for chemoautotrophic growth in the absence of light <sup>194</sup>. Nitrate dissimilation occurs through nitrate respiration, ammonification or denitrification. In the process of denitrification, bacterial and plant nitrate reductases can convert  $\text{NO}_3^-$  to  $\text{N}_2$ , along the way producing a significant amount of the greenhouse gas  $\text{N}_2\text{O}$  <sup>197,198</sup>. Alternatively,  $\text{NO}_3^-$  can be converted to  $\text{NH}_4^+$  by over 60 genera of prokaryotes and some eukaryotes (fungi and protozoa) <sup>197,199</sup>. This process of ammonification begins with nitrate reductases (NarGHI, NapAB) and goes through  $\text{NO}_2^-$  and  $\text{NO}$  before yielding  $\text{NH}_4^+$  <sup>194</sup>. The pathway by which a bacterial community utilizes  $\text{NO}_3^-/\text{NO}_2^-$  (ammonification vs denitrification) depends on the initial concentrations of  $\text{NO}_3^-$  and  $\text{NO}_2^-$ : higher initial concentrations of  $\text{NO}_3^-$  favour ammonification, whereas higher  $\text{NO}_2^-$  concentrations result in greater flux through the denitrification pathway <sup>200</sup>. An additional pathway that can be used by anaerobic bacteria to generate energy is called anaerobic ammonium oxidation (anammox). This process is catalysed by a group of bacteria known as planctomycetes, which oxidize  $\text{NH}_4^+$  with  $\text{NO}$  to produce  $\text{N}_2$  <sup>201</sup>.

### 1.2.2. The Physiology of Bacterial Nitrate Reductases

Nitrate reductases have essential biological functions in facilitating nitrogen utilization for growth (assimilation), generating proton motive force (respiration), and maintaining redox balance in the cell by eliminating excess reducing equivalents (denitrification). The reaction catalysed by all nitrate reductases is:  $\text{NO}_3^- + 2\text{H}^+ + 2\text{e}^- \leftrightarrow \text{NO}_2^- + \text{H}_2\text{O}$  ( $E^{\circ} = +420 \text{ mV}$ ) <sup>202</sup>. Bacteria can encode for three types of nitrate reductases, while a eukaryotic nitrate reductase is encoded by fungi and plants <sup>203,204</sup>. Despite all nitrate reductases being molybdoenzymes, the bacterial nitrate reductases are members of the DMSO reductase family and bind Mo-bisPGD; whereas the eukaryotic assimilatory nitrate reductases are members of the sulfite oxidase family,

binding molybdopterin instead (see **Figure 1.7** and **Section 1.1.5.3**)<sup>202</sup>.

The three bacterial nitrate reductase systems include the cytoplasmic assimilatory nitrate reductases (NasCA, NarB), the periplasmic dissimilatory nitrate reductase (Nap) and the respiratory membrane-bound nitrate reductases (NarGHI, NarZYV). Assimilatory nitrate reductases are cytoplasmic enzymes whose composition and electron donors differ between species, though the system can be broadly divided into two types: NasCA and NarB<sup>202,204,205</sup>. NasCA uses NAD(P)H as an electron donor and NarB is reduced by either ferredoxin or flavodoxin. The regulation of Nas is complex and species specific, though generally NH<sub>4</sub><sup>+</sup> acts as a negative regulator, and NO<sub>3</sub><sup>-</sup> and NO<sub>2</sub><sup>-</sup> are positive regulators of Nas. *E. coli* does not encode for either Nas system<sup>202,204</sup>.

The Nap system is widespread among Gram negative bacteria, where 11 genes are encoded in four types of operon, genomically and on plasmids<sup>202</sup>. Depending on the organism, regulation of Nap may or may not be dependent on oxygen or nitrogen. In *E. coli* Nap is encoded by the *napFDAGHBC* operon, where expression is induced by low O<sub>2</sub> and low nitrate conditions (<1 mM)<sup>206</sup>. In almost all cases, Nap functions as a soluble heterodimer, NapAB, and therefore does not directly contribute to the proton motive force<sup>207-209</sup>. However, several *nap* genes encode for membrane-anchored proteins (NapC,G,H) which allows Q-pool coupling of NapAB to respiratory dehydrogenases<sup>205,210</sup>. It is through these electrogenic dehydrogenases by which Nap can contribute to respiration. Due to its high nitrate affinity, Nap serves a particularly important role in respiration under nitrate- and/or carbon-limiting conditions<sup>208</sup>. It is for this reason that Nap can be viewed as a pathogenicity factor<sup>211</sup>. Nap also serves to maintain cellular redox balance by removing excess reducing equivalents (NADPH/NADH) by reducing nitrate.

*E. coli* encodes two Nar systems which are highly conserved in sequence and even similar in terms of the properties of their cofactors, Nar A (NarGHI) and Nar Z (NarZYV)<sup>212,213</sup>. NarGHI (encoded by the *narKGHJI* operon) is the primary respiratory nitrate reductase of *E. coli* and is most highly expressed under anaerobic and high

nitrate conditions ( $\geq 10$  mM) <sup>206</sup>. NarZYV (encoded by the *narUZYWV* operon), on the other hand, is only expressed at low levels during stationary phase and is unaffected by oxygen or nitrate concentration. Its function is believed to facilitate respiration on nitrate during aerobic, stress-associated conditions <sup>214–216</sup>. NarGHI is particularly important for bacterial survival, as nitrate is the preferred electron acceptor in the absence of oxygen (see **Section 1.1.3.1**). During an inflammatory response, immune cells release NO and  $O_2^-$ . These two compounds react to produce peroxynitrite, a potent bactericide, which can then decompose to  $NO_3^-$  <sup>217</sup>. In the case of patients with irritable-bowel disease, the inflammatory response results in elevated production of  $NO_3^-$ . *Enterobacteriaceae*, such as *E. coli*, can utilize this source of  $NO_3^-$  to support elevated levels of growth, with serious implications for host-associated gut flora communities in the colon <sup>218,219</sup>. NarGHI also plays a role in the pathogenicity of tuberculosis. The ability for *Mycobacterium tuberculosis* to survive in human macrophages is largely attributed to NarGHI, whereby macrophage produced  $NO_3^-$  can be utilized to promote growth <sup>206,220,221</sup>. The resulting accumulated  $NO_2^-$  in turn stimulates *M. tuberculosis* dormancy by inhibiting growth, enhancing ATP synthesis and regulating the expression of 120 genes needed for adaptation to acid, hypoxia, iron limitation and oxidative/nitrosative stress <sup>206,222,223</sup>. Nitrate reductases therefore not only have important roles in bacterial metabolism, but also human health.

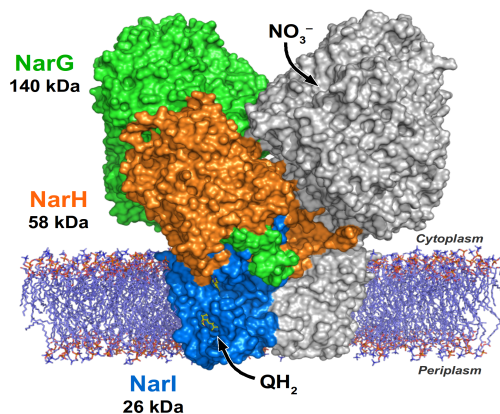


**Figure 1.10: *E. coli* nitrate reductase A (NarGHI).** The dimeric unit of NarGHI is depicted where one heterotrimer is shaded in blue (NarI), orange (NarH) and green (NarG). The location of the Q-site and NarG substrate tunnel are indicated. Generated from PDB ID 1Q16 <sup>19</sup>.

### 1.2.3. NarGHI Structure and Function

Nitrate Reductase A (NarGHI), as depicted in **Figure 1.10**, has been identified

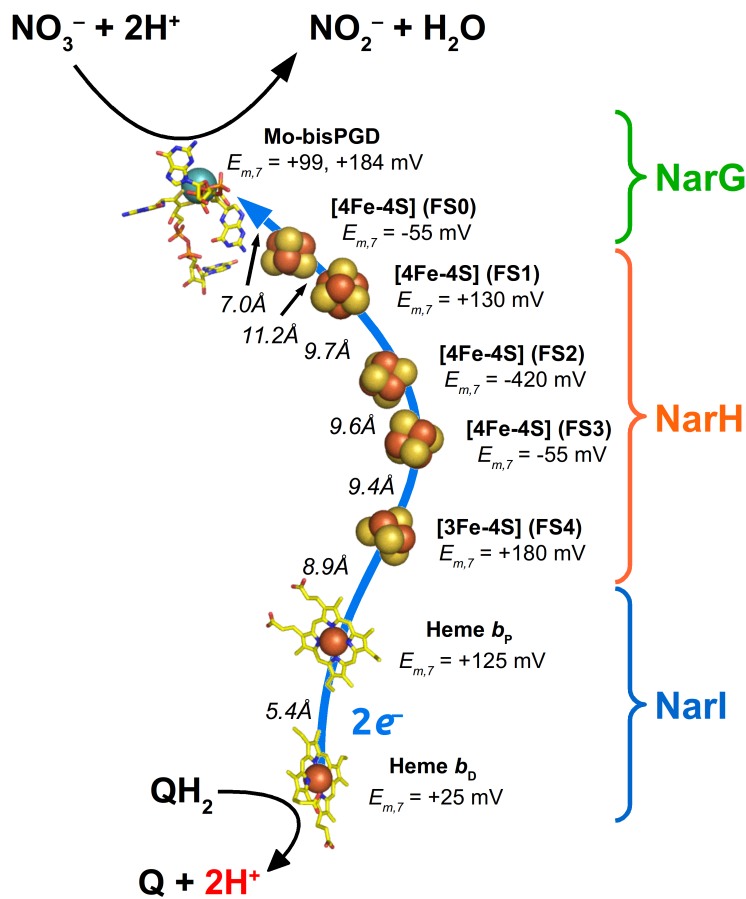


**Figure 1.11: The electron transfer relay and cofactors of NarGHI.** Cofactor midpoint potentials ( $E_m$ ) and edge-to-edge distances are shown. Adapted from reference 19.

and isolated in many organisms, but most of what we know about it comes from the *E. coli* enzyme which has been the subject of study for over 40 years<sup>205,224</sup>. Functionally, NarGHI is a dimer of heterotrimers and can be isolated as such by treatment of isolated inner membrane vesicles with mild detergents; the interaction surface between NarGHI heterotrimers is approximately 11,450 Å<sup>2</sup>,<sup>17,19</sup>. The soluble dimer, NarGH, is cytoplasmic facing and can be extracted from the membrane anchor subunit, NarI, by heat treatment<sup>225–228</sup>. The entire dimeric NarGHI complex is about 0.5 MDa in size and incorporates into its structure a variety of redox cofactors as well as structural lipids<sup>17,19,229</sup>. The full electron transfer pathway and complement of cofactors was finally determined by the solving of the crystal structures of NarGHI and NarGH at 1.9 Å and 2.0 Å, respectively, by two independent groups<sup>19,152</sup>. In total there are ten crystal structures of wild-type and variants of NarGHI, including two with a bound Q-site inhibitor (pentachlorophenol). It is clear from these structures that electrons from quinol oxidation, which occurs adjacent to the distal heme of NarI, are transferred to the nitrate reductase site (Moco) of NarG via its nearly 100 Å-long electron transfer relay:

$b_D \rightarrow b_P \rightarrow FS4 \rightarrow FS3 \rightarrow FS2 \rightarrow FS1 \rightarrow FS0 \rightarrow Mo\text{-bisPGD}$  (**Figure 1.11**). NarI, the membrane anchor subunit, binds the two hemes; NarH binds FS1-4; and NarG, the catalytic subunit, coordinates the FS0 and Mo-bisPGD cofactors. The next sections explore the structure and function of these subunits in greater detail.

### 1.2.3.1. NarG

NarG (140 kDa) is the catalytic subunit and as such binds the Mo-bisPGD cofactor ( $E_{m,8}^{VI/V} = +184$  mV,  $E_{m,8}^{V/IV} = +99$  mV) as well as a [4Fe-4S] cluster (FS0) ( $E_{m,8} = -55$  mV)<sup>230–232</sup>. NarG is organized into four conserved domains which surround Moco, and shares similar structure and cofactor content to the *E. coli* NapA enzyme<sup>151,152,233–235</sup>. Due to its sensitivity to hydrolysis, Moco is buried deep within NarG, whereby  $NO_3^-$  gains access to the Mo atom via a narrow, deep binding funnel supplied by a fifth conserved domain<sup>151,236</sup>. NarG is inhibited at Moco by the binding of azide and thiocyanate, and is capable of reducing chlorate to toxic chlorite<sup>237–239</sup>.

The two pterins of Moco are identified as P and Q, where the FS0-proximal Q-pterin mediates electron transfer from FS0 to Mo, as depicted in **Figure 1.12**. As opposed to the Q-pterin, which is tricyclic, the P-pterin is bicyclic (an open pyran ring) as in the ethylbenzene dehydrogenase from *Aromatoleum aromaticum* (see **Figure 1.7**)<sup>19,152,154</sup>. Functionally, the role of this bicyclic pterin is unknown, but it may play a role in proton transfer and Moco redox chemistry<sup>240–242</sup>. Generally, pterin cofactor oxidation state/conformation and protein-pterin interactions of molybdoenzymes appear to play an active role in tuning the Mo electrochemistry (ligand non-innocence)<sup>241,243</sup>. Mutagenesis studies have indicated that the protein environment around the

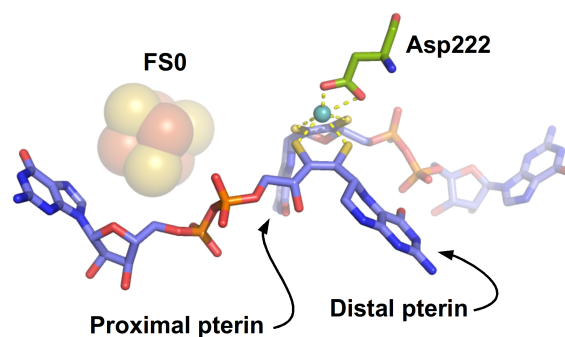


**Figure 1.12: Mo-bisPGD and FS0 of NarG.**

The positions of FS0 relative to the two pterins of NarG Moco is depicted, as is the bidentate coordination of Mo by Asp222. Based on PDB ID 1Q16<sup>19</sup>.

pterin indeed tunes the redox properties of Mo, and the reduction potential correlates with NarGHI activity both *in vivo* and *in vitro* <sup>240</sup>.

The Mo ion itself is directly coordinated by six ligands in a distorted trigonal prismatic geometry, where the dithiolene sulfurs of the two pyranopterins provide four ligands <sup>19,152</sup>. Asp222, which contributes to the Mo coordination sphere, is highly conserved across all NarG proteins from bacteria and archaea <sup>152</sup>. In the NarGH structure, Asp222 provides a single carboxylate oxygen to the coordination sphere of Mo, which is also coordinated by an oxo (=O) ligand <sup>152</sup>. On the other hand, the NarGHI structures show Asp222 coordinates Mo in a bi-dentate fashion, with no oxo ligand present, as in **Figure 1.12** <sup>19,183,244</sup>. It has been proposed that these two structures represent two different oxidation states of the Mo, where NarGHI has been radiolytically reduced, whereas NarGH remains oxidized <sup>62,245</sup>. NarGHI also exhibits two forms of Mo<sup>V</sup> EPR spectrum, a low-pH form with splittings indicating a strongly associated proton, and a high-pH form with only a weakly coupled proton. The two forms interconvert with a complicated pH dependence <sup>153,237,246</sup>. It has been proposed that the low-pH/reduced form is due to Mo coordination by an oxo ligand and monodentate Asp222, whose other carboxylic oxygen is hydrogen bonded with the conserved His546 <sup>152</sup>. This low-pH coordination of Mo grants it high reactivity with NO<sub>3</sub><sup>-</sup> and the ability to bind anions <sup>237</sup>. The high-pH form may represent the deprotonation of His546, releasing Asp222 to swing into a bi-dentate coordination of Mo, blocking NO<sub>3</sub><sup>-</sup> from binding <sup>152</sup>.

Protein film voltammetry studies of the *E. coli* and *Paracoccus pantotrophus* NarGH dimer have given yet further insight into the mechanism of NarGHI <sup>239,247</sup>. Both enzymes exhibit two kinetic activities: a high potential activity (-25 mV) which is pH dependent with a pK<sub>a</sub> of 7.8, and a low potential activity (-400 mV) which does not vary with pH in the 5-9 range <sup>239,247</sup>. Inhibition studies with azide determined that NO<sub>3</sub><sup>-</sup> binds more tightly to the Mo<sup>V</sup> state of NarGHI than to the Mo<sup>IV</sup> state <sup>239</sup>. However, NO<sub>3</sub><sup>-</sup> reduction proceeds more quickly through the Mo<sup>IV</sup>-bound state, where NO<sub>3</sub><sup>-</sup> binding and H<sub>2</sub>O release are nearly simultaneous. This suggests that NarGHI exhibits two

routes for nitrate reduction, one for low concentrations of nitrate (slower turnover but high affinity for  $\text{NO}_3^-$ ) and one for high concentrations of nitrate (lower  $\text{NO}_3^-$  affinity but faster turnover) <sup>239</sup>. Electrochemical and structural studies of periplasmic nitrate reductase and formate dehydrogenase suggests that such active site heterogeneity and flexibility is a common feature for DMSO reductase family enzymes, like nitrate reductase <sup>235,239,247–250</sup>.

The FS0 cluster ( $E_{m,7} = -55$  mV) of NarG is coordinated by the  $\text{H}^{49}\text{xxxC}^{53}\text{xxC}^{57}(\text{x})_n\text{C}^{92}\text{PR}^{94}$  motif, which differs from the more prototypical motif of other [4Fe-4S]-coordinating prokaryotic nitrate reductases:  $\text{CxxCxxC}(\text{x})_n\text{CxK}$  <sup>235</sup>. It is because of the coordination by a His, instead of a fourth Cys, that it was initially believed that NarG did not bind an FeS cluster, which was supported by the failure of initial attempts to detect FS0 by EPR. Upon solving the structure and subsequent EPR studies it was apparent that NarG does coordinate a [4Fe-4S] cluster, but with a high-spin state, different from typical [4Fe-4S] clusters, being visible at 9-12 K around  $g = 5.02$  and  $5.55$  <sup>19,152,231,244,251,252</sup>. FS0 has two primary functions in NarG: 1) it constitutes part of the electron transfer pathway through NarGHI; and 2) its insertion into NarG is a required pre-requisite step to Moco insertion by the dedicated chaperone NarJ <sup>244,252,253</sup>.

It has long been known that NarGHI undergoes reductive activation, where an initial reduction of the enzyme is required for attainment of full activity <sup>239,254–257</sup>. Activation can be achieved by direct voltammetry, or reaction with low potential viologens and endogenous quinol substrates <sup>239,255,256</sup>. It was determined that with prolonged exposure to these electron sources the FeS relay became progressively reduced and EPR detected  $\text{Mo}^{\text{V}}$  intensity diminished <sup>255,256</sup>. In order to explain the reductive activation of NarGHI, three hypotheses have been put forth: 1) the oxidation state of the electron transfer relay of NarGHI (i.e. the FeS clusters) determines the rate; 2) the molybdenum coordination sphere/environment undergoes redox-dependent changes; or 3) the oxidation state of the pterin cofactor itself changes. While no direct evidence exists for the third possibility, and due to the slow rate and

temperature dependence of activation, mechanisms 1) and 3) are not likely <sup>257</sup>. The mechanism for reductive activation therefore likely represents a conformational change of the enzyme, most likely in the proximity of Mo. This, however, requires further work.

While much has been learned about the mechanism of nitrate reduction by NarG, many questions remain: what is the physical meaning and origin of the two pH and kinetic forms of NarGHI? What role does the pterin play in NarG function? what conformational changes are required during turnover? and, What is the mechanism for the reductive activation of NarGHI?

### 1.2.3.2. NarH

NarH (58 kDa) acts as a scaffold for the coordination of four FeS clusters, three [4Fe-4S] clusters (FS1, FS2, FS3) and a [3Fe-4S] cluster (FS4) adjacent to NarI, as depicted in **Figure 1.11**. This linear arrangement of FeS clusters acts as a 'wire' to facilitate electron transfer between the active sites of NarI and NarG, where the distance between each FeS cluster is well below the 14 Å limit for efficient electron transfer <sup>19,71</sup>. FeS cluster coordination occurs through conserved ferredoxin-like motifs (Cys groups I-IV in **Figure 1.13**) by the consensus sequence: C<sub>A</sub>X<sub>2</sub>C<sub>B</sub>X<sub>2-11</sub>C<sub>C</sub>X<sub>3</sub>C<sub>D</sub>P <sup>258</sup>. Here the first 3 cysteines of a motif (C<sub>A-C</sub>) plus the fourth of an adjacent motif (C<sub>D</sub>) coordinate one [4Fe-4S] cluster. FS4 is rendered a [3Fe-4S] cluster by degeneration of a Cys in Cys group III to Trp (NarI<sup>Trp220</sup>) <sup>19,258</sup>.

NarH is believed to have originated as a fusion of the bacterial 2[4Fe-4S] ferredoxins <sup>151,259</sup>. Each FeS cluster is coordinated by three blocks of core sequence which structurally form two core domains, labelled as domains A and B in **Figure 1.13** <sup>151</sup>. These core domains are structurally conserved, aligning with an RMSD of 1.8 Å over 157 residues of the corresponding subunit of formate dehydrogenase (FdnH) <sup>18,19,151</sup>. However, NarH is 220 residues longer than FdnH due to three additional surface subdomains which function to insulate the FeS clusters from oxidative

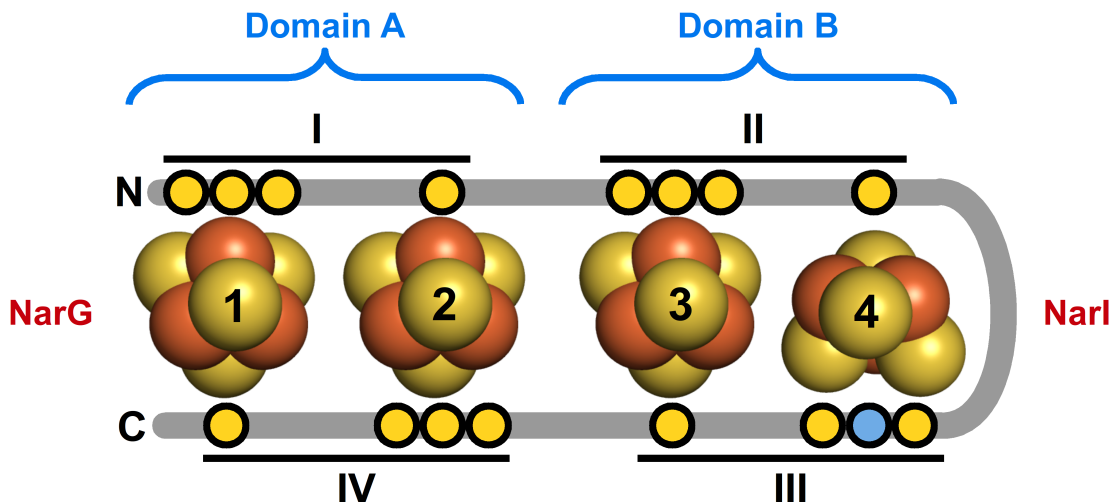


**Figure 1.13: The coordination of FS1-4 of NarH.** The NarH polypeptide is represented by the thick grey line and cysteine and tryptophan residues are depicted as yellow and blue circles, respectively. Individual Cys groups are highlighted by the line and roman numeral identification. Domains A and B represent the two core ferredoxin-like domains of NarH. The relative positions of NarG and NarI are indicated. Note that FS1-3 are [4Fe-4S] clusters and FS4 is a [3Fe-4S] cluster. Adapted from reference 59.

damage<sup>18,19,151</sup>. The redox properties of the clusters suggests that electron transfer through NarH is largely energy conserving: FS4  $E_{m,8} = +180$  mV to FS1  $E_{m,8} = +130$  mV, however FS2 ( $E_{m,8} = -420$  mV) imposes a redox barrier<sup>258</sup>. Such low potential FeS centers are a common feature of electron transfer relays, as found in nitrate reductase Z, succinate dehydrogenase, fumarate reductase, formate dehydrogenase-N and DMSO reductase<sup>213,260-264</sup>. The purpose of these clusters remains unknown, though they may help regulate electron transfer kinetics under nitrate-limiting circumstances<sup>151</sup>, though such endergonic electron transfer steps seem to pose no major restriction on electron transfer kinetics<sup>263</sup>. There are none-the-less examples where NarH variants influence the redox properties of the electron transfer relay, and consequently enzyme kinetics. In the NarH<sup>Cys26Ala</sup> variant, FS2 is converted to a [3Fe-4S] cluster and the  $E_m$  is raised by ~600 mV, the effect of which is significantly diminished turnover with menaquinol (26% of wild-type)<sup>59,258</sup>. The NarH<sup>Cys16Ala</sup> variant, which converts FS1 into a [3Fe-4S] cluster (PDB ID 3EGW,

unpublished), exhibits significantly slowed NarH FeS re-oxidation and even a kinetically stabilized semiquinone <sup>265</sup>. The  $E_m$  of this cluster in NarGHI<sup>Cys16Ala</sup> has not been characterized. It has similarly been found that the FS0  $E_m$  of NarG<sup>Arg94Ser</sup> is decreased by 115 mV, and consequently exhibits 30% wild-type activity <sup>244</sup>.

While it is tempting to interpret such mutagenesis studies as having effects only on the redox properties of the adjacent cluster or modulating preferred electron tunnelling pathways, the fact remains that packing density as well as small conformational deviations throughout the protein can result and have significant effects on the thermodynamics and kinetics of electron transfer. Furthermore, due to electrostatic interactions, the modulation of cofactor reduction potentials can consequently modulate the redox properties of adjacent centers. The determinants of FeS cluster  $E_m$  and the function of very low potential clusters in an electron transfer relay requires further work.

### 1.2.3.3. NarI

NarI (26 kDa) functions as the membrane anchor subunit and the site of Q-pool coupling <sup>17,238,266</sup>. It is comprised of five transmembrane helices (TM I-V) which are tilted by 30° relative to the membrane normal, as seen in **Figure 1.14**. The two *b*-type hemes are bound to NarI via bis-His coordination by helices II and V, where His66 (TM II) and His187 (TM V) coordinate  $b_D$ , and His56 (TM II) and His205 (TM V) coordinate  $b_P$  <sup>19,267,268</sup>. The  $b_D$  and  $b_P$  nomenclature specifies

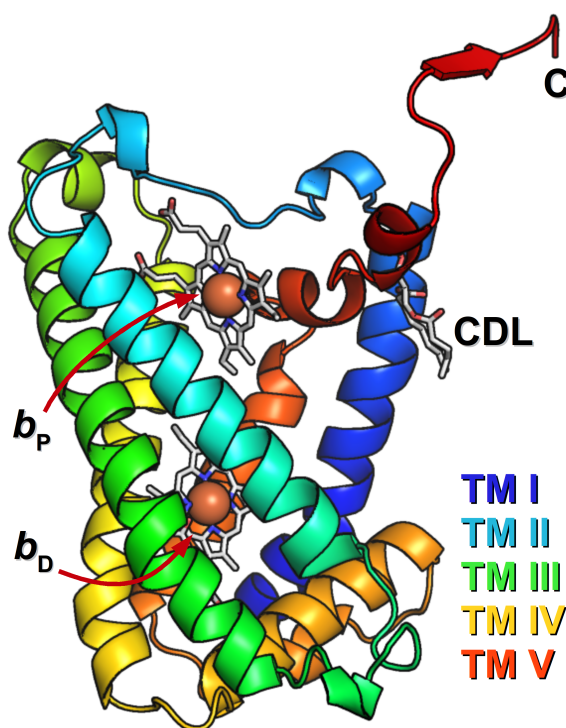


**Figure 1.14: The architecture of NarI.**

Highlighted are the five transmembrane (TM) helices, the C-terminus, the two hemes and the binding of a cardiolipin (CDL) fragment. Based on PDB ID 3EGW.

the proximity of each heme to the NarGH dimer – heme  $b_D$  (+25 mV) is distal and heme  $b_P$  (+125 mV) is proximal (see **Figure 1.11**)<sup>19,183,269,270</sup>. In addition to the four conserved heme ligand histidines, there are several highly conserved Gly residues which are involved in accommodating the hemes<sup>271</sup>. Heme  $b_P$  binding is also facilitated by a set of conserved hydrogen bonds and electrostatic interactions with Arg112, Arg202, Ser39, Ser40 in NarI, and Arg221 in NarH. This contrasts with the considerably more hydrophobic environment of heme  $b_D$  where less extensive stabilization of the propionates occurs, however its propionates contribute to a hydrogen bonding network that leads to the periplasm from the Q-site. It is this difference in environment that is responsible for the ~100 mV difference in  $E_m$  and redox-Bohr effect ( $E_m$  pH dependence) of the two hemes<sup>19,271</sup>. In accordance with the “positive inside rule,” the cytoplasmic face of NarI is enriched in five conserved and several less well conserved Arg residues. The C-terminus of NarI forms a horizontal  $3_{10}$ -helix which faces the cytoplasm, where a number of highly conserved residues (Tyr213, Arg216, Arg222) interact with NarG and NarH. Binding of NarGH to NarI is therefore accomplished via a number of intermolecular hydrogen bonds and conserved salt bridges with NarH and NarG<sup>19,271</sup>. Additionally, the NarGHI heterotrimer appears to be stabilized by the tight binding of a cardiolipin molecule through hydrophobic interactions of the acyl chains and hydrophobic residues in NarI, and the phosphodiester head groups are stabilized by interactions with NarG-Arg6, NarH-Arg218 and NarI-Tyr28<sup>229</sup>.

Both hemes of NarI exhibit highly anisotropic EPR signals where their  $g_z$  values are centered at 3.76 and 3.36, for  $b_P$  and  $b_D$  respectively<sup>268</sup>. The origin of these highly anisotropic EPR signals lies with the near perpendicular arrangement of the imidazole rings of the axial coordinating histidines, as depicted in **Figure 1.6**<sup>272–274</sup>. As a consequence of this arrangement, the NarI heme EPR signals are sensitive to any changes in the bis-His coordination angle. For instance, upon loss of NarGH, hemes  $b_D$  and  $b_P$  report a conformational change by a shift in their  $g_z$  values to 3.15 and 2.92, respectively<sup>270,275</sup>. This change in solvent exposure and heme coordination is accompanied by a modulation of heme  $b_P$  and  $b_D$   $E_{m,7}$  values (-178 mV and +37 mV,

respectively)<sup>270</sup>. Likewise, the heme  $b_D$  EPR signal is also sensitive to the binding of Q-site inhibitors 2-*n*-heptyl-4-hydroxyquinoline-N-oxide (HOQNO), stigmatellin and pentachlorophenol (PCP), shifting to  $g_z = 3.50, 3.31$  and  $3.45$ , respectively<sup>183,270,275</sup>.

Prior to solving the crystal structure of NarGHI, it was predicted that NarI may have two Q-sites<sup>265,276</sup>. However, with two crystal structures available with the potent Q-site inhibitor PCP bound it is evident that there is but a single Q-site, located adjacent heme  $b_D$  and between TM II and TM III<sup>183</sup>. Fluorescence quench titrations with the fluorescent menasemiquinone analog HOQNO, kinetics studies, and site directed mutagenesis overwhelmingly corroborate the existence of only a single Q-site<sup>270,277–281</sup>. That there is only a single Q-site adjacent heme  $b_D$  and near the periplasm is bioenergetically consistent with a measured  $2H^+/2e^-$  stoichiometry for NarGHI<sup>20</sup>. Furthermore, EPR spectroscopy has demonstrated that all three types of semiquinones (UQ, DMQ, MQ) are bound to the same Q-site, and that they form a weak in-plane hydrogen bond to N $\delta$  of His66<sup>45,170,282</sup>. Apparent from the crystal structures of PCP-bound enzyme, a heme  $b_D$  propionate also forms a hydrogen bond with the phenolic oxygen of PCP, as demonstrated in **Figure 1.15** where MQ-1 has been modeled in place of PCP<sup>183</sup>. The importance of the heme for quinol binding and electron transfer is apparent from mutagenesis studies, where NarI<sup>His66Tyr</sup> and NarI<sup>His187Tyr</sup> results in the loss of heme  $b_D$  and renders the enzyme unable to reduce quinol substrates or bind HOQNO<sup>278,283</sup>. NarI<sup>His66Tyr</sup> also exhibits greater flexibility and disorder around the Q-site, according to the crystal structure (PDB ID 1Y5L)<sup>183</sup>.

While much of what is known about quinone binding is based on EPR spectroscopy of the semiquinone intermediates and structural data of PCP bound, the mechanism by which quinol is oxidized is still under investigation. Apart from heme  $b_D$ /His66, Lys86 is a highly conserved residue in NarI although its position relative to the quinone may suggest no active role in quinol oxidation<sup>19,271</sup>. However, the variant NarGHI<sup>Lys86Ala</sup> exhibits a severely diminished activity (14% of wild-type), an  $IC_{50}$  for PCP of  $2.5 \mu M$  (wild-type  $IC_{50}^{PCP} = 0.4 \mu M$ ) and an undetectable affinity for HOQNO (wild-type  $IC_{50}^{HOQNO} = 1.5 \mu M$ )<sup>183</sup>. EPR also confirms altered binding of HOQNO and

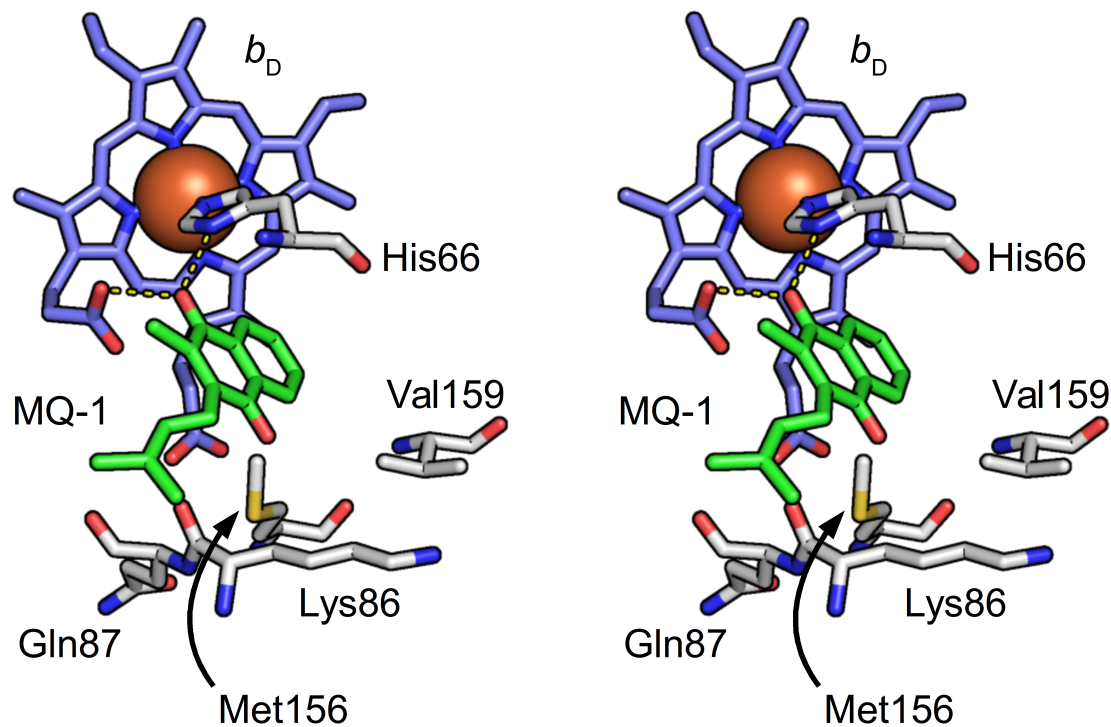


**Figure 1.15: The Q-site of NarI in stereo.** Menaquinone-1 (MQ-1) has been modeled in place of PCP bound to the Q-site, based on PDB ID 1Y4Z<sup>183</sup>. Hydrogen bonds between the heme  $b_D$  propionate and His66 are shown by dotted yellow lines. The position of residues involved in the covariance analysis are shown in stick representation and labelled.

PCP to the Q-site based on the difference in heme  $b_D$   $g_z$  value shift compared to wild-type, and slightly modified heme  $b_P$  and  $b_D$  potentials<sup>183,284</sup>. NarI<sup>Lys86Ala</sup> also renders NarGHI incapable of stabilizing semiquinones<sup>284</sup>. It is therefore indisputable that Lys86 is required for quinol oxidase activity and binding.

Additional details with regards to the function of NarI are revealed upon investigation of a sequence alignment of 313 sequences with <90% sequence identity. In addition to Lys86, Gln87, Met156 and Leu159 are conserved residues that line the Q-site. However, by correlating the occurrence of these residues and their natural variants with the type of quinones comprising the Q-pool of the respective source organism, a trend appears, as summarized in **Figure 1.16**. In organisms that utilize menaquinones only, Tyr, His, Arg and Ile are the residues of choice for positions 86, 87, 156 and 159, respectively. However, in organisms able to synthesize

ubiquinone, such as *E. coli*, the preferred residues at these positions are Lys86, Gln87, Met156 and Leu159. From the alignments and looking for residue covariance, it is apparent that in 99.6% of sequences a basic residue occupies either position 86 or 156 in NarI, but 0% of the time does a basic residue occupy both positions. This agrees with structural data showing residues Met156 and Lys86 facing in towards the bound PCP<sup>183</sup>. Invariably, position 87 is a polar (83% Gln) or protonatable (15% His) residue, which corresponds to position 156 occupancy by a basic residue (15% Arg) or a hydrophobic residue (82.9% Met/Leu/Ile/Phe/Ala). It therefore seems apparent that the Q-site of *E. coli* NarI is especially accommodating to ubiquinones. This is supported by the fact that PCP, which more closely resembles ubiquinone, is a more potent inhibitor of NarI than HOQNO, a naphthoquinone analog<sup>183</sup>. However, kinetics studies of menaquinone and ubiquinone analogs, as well as studies using bacterial strains capable of producing only certain quinones, have not definitively shown what is the preferred substrate for NarGHI, though menasemiquinone is more highly stabilized than ubisemiquinone<sup>40,45,265,276</sup>. It will however be necessary to conduct site directed mutagenesis studies based on this analysis to demonstrate whether these residues largely determine the quinone preference of species-specific NarGHI enzymes.

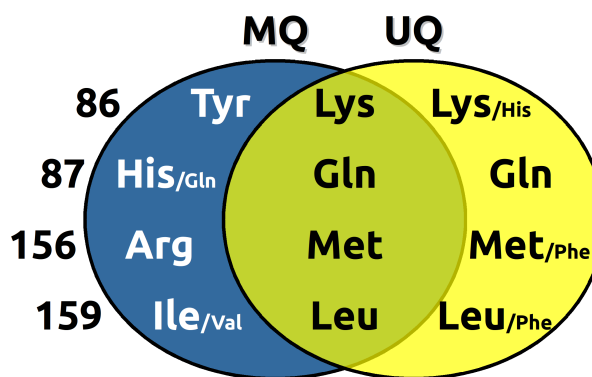


**Figure 1.16: Covariance analysis of conserved Q-site residues.** Correlation of the type of quinone produced by the respective organism, menaquinone (MQ) or ubiquinone (UQ), with the presence of certain Q-site residues. In the case where variants exist as a significant proportion of sequences, the minor variant is given in smaller font.

Further experiments are also required to determine how the binding of reduced and oxidized quinones differs from the semiquinone intermediates and what are the roles for the various conserved/semi-conserved residues that line the Q-site. It also remains to be determined what role, if any, conformational changes play in quinol



absence of NarJ leads to an inactive apo-form of NarGH associating with NarI<sup>231,285</sup>. NarG obtains its Moco via direct interaction with a transient multi-protein complex of Moco biosynthetic proteins and NarJ<sup>253</sup>. Release of NarG may proceed via a conformational dependent deprotonation event of NarJ<sup>Glu119</sup>, which diminishes the affinity for NarJ to NarG<sup>1-15</sup> by 100 fold. It is hypothesized that correct folding of NarG may initiate this deprotonation event<sup>290</sup>.

Incorporation of FeS clusters into NarGH is independent of NarJ and occurs via the Isc FeS biogenesis system, which requires the FeS carrier proteins IscA and ErpA as well as the FeS biosynthetic scaffold protein IscU<sup>291</sup>. NarI is co-translationally inserted into the inner membrane by the SecYEG system<sup>292</sup>. The mechanism by which the two hemes are inserted into NarI are not yet known. Interestingly, the absence of NarJ leads to the loss of heme *b<sub>P</sub>* from NarI, indicating a role for NarJ in final stabilization ('proof-reading') of NarGHI<sup>252</sup>. It is possible that interaction of NarJ with a rigidly bound cardiolipin represents the final stage in NarGHI maturation<sup>229</sup>.

### 1.3. Thesis Research Objectives

*E. coli* NarGHI plays critical roles in the anaerobic respiration of bacteria, where it can be regarded as a pathogenicity factor, and is a key enzyme in the global biogeochemical nitrogen cycle. In light of its significance, NarGHI has been the subject of research for several decades, yet much of its function awaits elucidation. For my thesis research I focused on the membrane subunit, NarI. Specifically I examined the functioning of the quinol oxidation site and the importance of key residues contained therein. I also sought to better understand transmembrane electron transfer through NarI via its two hemes by probing their biophysical and electrochemical properties.

## 2. Q-site Occupancy Defines Heme Heterogeneity in *E. coli* NarGHI

**A version of this chapter has been previously published:**

J.G. Fedor, R.A. Rothery, K.S. Giraldi, J.H. Weiner, Q-Site occupancy defines heme heterogeneity in *Escherichia coli* nitrate reductase A (NarGHI), *Biochemistry*. **53** (2014) 1733–1741. doi:10.1021/bi500121x

**Acknowledgements:**

The authors would like to thank Francesca Sebastian and Nicholas Chua for their fantastic technical support.

## 2.1. Introduction

Nitrate reductase A (NarGHI) from *Escherichia coli* is a membrane-bound quinol:nitrate oxidoreductase that is expressed under anaerobic conditions in the presence of nitrate<sup>293</sup>. It functions as a terminal reductase, coupling quinol oxidation to nitrate reduction, and contributes to the generation of a proton electrochemical potential across the cytoplasmic membrane<sup>294</sup>. NarGHI comprises a catalytic subunit (NarG, 140 kDa), an electron-transfer subunit (NarH, 58 kDa), and a membrane anchor subunit (NarI, 26 kDa). NarG contains a molybdo-bis(pyranopterin guanine dinucleotide) (Mo-bisPGD) cofactor that is the site of nitrate reduction, as well as a single tetranuclear iron-sulfur ([4Fe-4S]) cluster known as FS0. NarH contains three [4Fe-4S] clusters (FS1-FS3) and one trinuclear iron-sulfur cluster ([3Fe-4S], FS4). NarI anchors the NarGH subunits to the inside of the cytoplasmic membrane and contains two hemes *b*, that are proximal (*b<sub>P</sub>*) and distal (*b<sub>D</sub>*) to the NarGH subunits, respectively. Overall, these subunits provide a molecular scaffold for an electron-transfer relay connecting the site of quinol oxidation adjacent to heme *b<sub>D</sub>* in NarI (the Q-site) with the Mo-bisPGD of NarG<sup>19,295</sup>. NarGHI is a robust enzyme that is readily expressed to levels approaching spectroscopic purity in *E. coli* cytoplasmic membrane preparations, rendering it an excellent system for studying redox cofactor spectroscopy and electrochemistry<sup>85,213,232,269,270,296</sup>. Although the overall architecture of the enzyme has been defined by X-ray crystallography, the factors controlling reactivity at the Mo-bisPGD and Q-sites are far from being fully understood.

The redox properties and reduction potentials of the NarGHI cofactors have been extensively studied using a combination of spectroscopic<sup>269</sup> and potentiometric methods<sup>270,296</sup>. In general, electrons flow in the overall thermodynamically down hill direction from menaquinol (MQ) or ubiquinol (UQ), through the two hemes of NarI, the four FeS clusters of NarH, and then through the single [4Fe-4S] cluster of NarG to the Mo-bisPGD cofactor where nitrate is reduced to nitrite. One of the hemes of NarI, heme *b<sub>D</sub>* is in close juxtaposition to the Q-site identified by protein crystallography<sup>183</sup>. Elements of the heme, including one of this propionate groups and one of its iron-

coordinating His residues (His66), directly participate in hydrogen-bonding interactions with the bound Q-site inhibitor pentachlorophenol (PCP) observed in one of the available structures (PDB ID 1Y4Z) (Figure 2.1) This results in the EPR spectrum and reduction potential of heme  $b_D$  being exquisitely sensitive to the presence of quinol analog inhibitors in the Q-site. NarGHI is able to oxidize both major quinol species found in the *E. coli* cytoplasmic membrane <sup>40</sup>: ubiquinol dominates under oxidizing and oxic conditions, whereas menaquinol dominates under reducing and anoxic conditions. This raises the question of how the composition of the quinol pool impacts the spectroscopic and functional properties of heme  $b_D$ .

The two hemes of NarI exhibit highly anisotropic low spin (HALS) spectra with reported  $g_z$  values of approximately 3.76 and 3.36 for heme  $b_P$  and  $b_D$ , respectively <sup>270</sup>. Heterogeneity of heme  $b_D$  has been reported in a mutant unable to synthesize Mo-bisPGD <sup>252</sup>, resulting in the appearance of two components, with a  $g_z$  values of approximately 3.35 and 3.21. Arias-Cartin *et al.* <sup>297</sup> also reported that heme  $b_D$  can exist in two forms, one with a  $g_z$  of approximately 3.20 and the other with a  $g_z$  of approximately 3.35. Extraction of hydrophobic components using dodecylmaltoside (DDM) resulted in diminution of the  $g = 3.20$  component and retention of the  $g = 3.35$  component. These effects were interpreted to arise from the DDM-induced leaching of a tightly-bound cardiolipin molecule from the membrane intrinsic region of NarGHI. In this chapter, we test the alternative hypothesis that

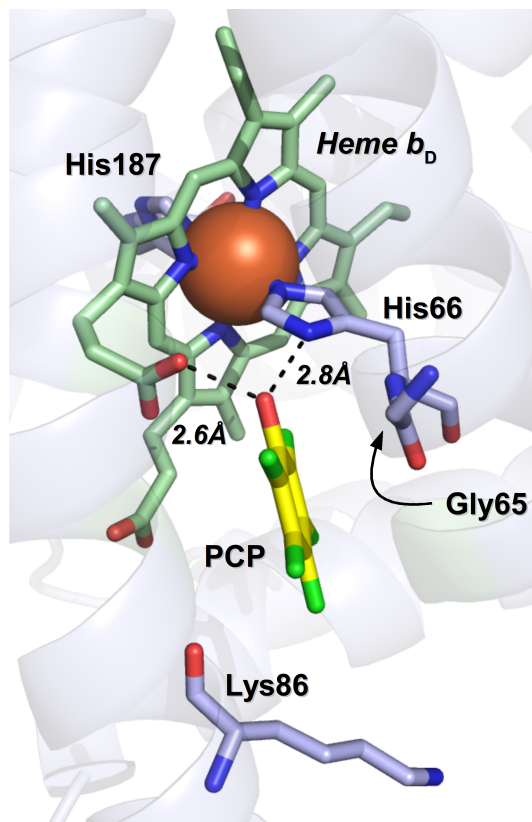


**Figure 2.1: The Q-site of NarI with pentachlorophenol bound.**

Coordinating heme  $b_D$  are His187 and His66, which also hydrogen bonds with bound PCP and semiquinone. Image generated using PyMol and PDB ID 1Y4Z <sup>183, 374</sup>.

quinone composition and binding are the determinants of heme  $b_D$  heterogeneity. We present evidence that the two components arise from specific quinone-bound and quinone-free populations of NarGHI within the *E. coli* inner membrane.

## 2.2. Materials and Methods

*Bacterial strains, plasmids, membrane vesicle preparation* – Wild-type NarGHI was overexpressed in *E. coli* strains LCB79 (*araD139*  $\Delta$ (*lacI*-POZYA-*argF*) *rpsL*, *thi*,  $\Phi$ 79(*nar-lac*))<sup>298</sup>, the cardiolipin-deficient strain S330 (W3110 *ksgB1 lpp-2 pgsA30::kan*)<sup>299</sup>, the naphthoquinone (menaquinone, demethylmenaquinone) deficient strain JCB4111 (JCB4011  $\Delta$ *menBC*)<sup>209</sup>, the ubiquinone deficient JCB4211 (JCB4011  $\Delta$ *ubiCA*)<sup>209</sup>, and the cytochrome deficient strains JW0723 (W3110  $\Delta$ *cydB*) and JW0421 (W3110  $\Delta$ *cyoB*)<sup>300</sup>. The expression vector used was pVA700 (*tacP*, *rrnB*, *lacI*<sup>Q</sup>, *amp*<sup>r</sup>, *narGHJI*)<sup>258</sup>. Growth of LCB79, JCB4111 and JCB4211 was supplemented with 100 mg L<sup>-1</sup> streptomycin, 50 mg L<sup>-1</sup> kanamycin for S330, JW0723, JW0421, and 100 mg L<sup>-1</sup> ampicillin was added to cultures of all strains bearing the pVA700 expression vector. Cell growth in 2 L batches of Terrific Broth<sup>301</sup> was performed as previously described<sup>270</sup>. Fermenter growths were conducted in 5 L or 10 L batches in either fermenter broth, or glycerol-peptone-fumarate (GPF) (anaerobic growth)<sup>302</sup> at pH 7.0 using 2 M NaOH and 1 M HCl for pH adjustments<sup>183</sup>. The GPF was supplemented with 4 mM KNO<sub>3</sub>, 0.003% (w/v) leucine and 0.003% (w/v) threonine. Fermenter broth contains 12 g L<sup>-1</sup> tryptone, 24 g L<sup>-1</sup> yeast extract, 5 g L<sup>-1</sup> NaCl, 0.56% (v/v) glycerol, and 200 mg L<sup>-1</sup> thiamine hydrochloride; note: overnight precultures of fermenter broth use 0.4% (v/v) glycerol. Inoculation was accomplished with 10% (v/v) overnight cultures grown at 37°C, 225 rpm in flasks containing Terrific or fermenter broth<sup>183</sup>. When the OD<sub>600</sub> reached 0.5 (Anaerobic, GPF culture) or 2.0 (micro-aerobic, FB cultures), 1 mM of isopropyl-1-thio- $\beta$ -D-galactopyranoside (IPTG) was added to induce NarGHI expression from pVA700<sup>183</sup>. Stir speed, post-induction incubation temperature, and aeration rates are detailed in

the legend of **Figure 2.2**. The buffer system used for vesicle preparations contained 5 mM EDTA and at pH 6.0, 7.0, 8.0 and 9.0 respectively, are: 100 mM 2-(N-morpholino)ethanesulfonic acid (MES), 100 mM 3-(N-morpholino)propanesulfonic acid (MOPS), 100 mM Tricine, and 100 mM N-cyclohexyl-2-aminoethanesulfonic acid (CHES). The processing of the cells has been previously outlined <sup>270</sup> and included the addition of 0.2 mM phenylmethylsulfonyl fluoride prior to emulsiflexing 3-5 times. Throughout the processing procedure 100 mM MOPS, 5 mM EDTA buffer (pH 7.0) was used until the final two resuspensions, where the appropriate buffer for pH poisoning was used. All samples were resuspended to  $\sim 30 \text{ mg mL}^{-1}$ , flash frozen as aliquots in liquid nitrogen, and stored at  $-80^\circ\text{C}$ .

*Redox potentiometry and EPR spectroscopy* – Redox titrations were conducted under argon at  $25^\circ\text{C}$  in the pH specific buffers mentioned above, as previously described <sup>270,278,303</sup>. Redox titrations require the inclusion of  $25 \mu\text{M}$  each of the following redox mediators (dyes), prepared as 50 mM aqueous stock solutions: quinhydrone (+287 mV), 2,6-dichlorophenolindolphenol (+217 mV), 1,2-naphthoquinone (+125 mV), toluylene blue (+115 mV), phenazine methosulfate (+80 mV), thionine (+60 mV), methylene blue (-11 mV), resorufin (-50 mV), indigo trisulfonate (-80 mV), indigo carmine (-125 mV), anthraquinone-2-sulfonic acid (-225 mV), phenosafranin (-255 mV), neutral red (-329 mV) <sup>278</sup>. All samples were taken in 3 mm I.D. quartz EPR tubes, rapidly frozen using liquid nitrogen-chilled ethanol and stored at  $-70^\circ\text{C}$  prior to use. EPR spectra were acquired as previously described <sup>270</sup> using a Bruker Elexsys E500 series X-band EPR spectrometer (9.38 GHz) with an ESR-900 flowing helium cryostat, a temperature of 10-12K, 10  $G_{pp}$  modulation amplitude at 100 kHz. All potentials are relative to the standard hydrogen electrode, and unless otherwise mentioned the depicted spectra are poised at approximately +280 mV. See figure legends for microwave power (MWP) levels used. Baseline correction for Gaussian deconvolution analysis was conducted by using a derivative Lorentzian line shape, which gave superior fits to 3<sup>rd</sup>-5<sup>th</sup> order polynomial baselines as well as derivative Gaussian line shapes <sup>304</sup>. The area normalized equation used for derivative

Lorentzian baseline correction is:

$$\frac{dY}{dx} = -S \left( \frac{2L^2(x-x_0)}{L^2 + (x-x_0)^2} \right) + Dx + A \quad (2.1)$$

Where  $S$  is a scale factor and is equal to half the peak-to-peak amplitude,  $L$  is the line width at half-peak-height,  $x_0$  is the  $x$ -intercept of the derivative,  $D$  is the linear slope and  $A$  is the linear  $y$ -intercept. This satisfactorily simulates the interfering portion of the “junk” iron signal at  $g = 4.3$  that causes the extreme extent of the baseline at low field ( $g < 3.75$ )<sup>305</sup>. Baseline correction and Gaussian deconvolution was conducted by non-linear least squares fitting via the Levenberg-Marquadt method using Matlab (version R2013b, The MathWorks Inc., Natick, Massachusetts).

*Enzyme assays* – The Lowry procedure for protein concentration determination was modified to include 1% (w/v) SDS for solubilization of membrane proteins<sup>306,307</sup>. Quinol:nitrate oxidoreductase assays were conducted using the quinol analog plumbagin (PBH<sub>2</sub>)<sup>277</sup>. Stock solutions of which were prepared with 100% anhydrous ethanol at concentrations of 20 mM PBH<sub>2</sub> then were stored at -20°C. Zinc powder was used as a reductant where ~70 mg Zn<sup>0</sup> and 1.7 mL PBH<sub>2</sub> solution were added to a 2 mL HPLC vial followed by addition of 60 μL 5 M HCl<sub>(aq)</sub>. The vials were then sealed with a rubber septum and shielded from light with aluminum foil. The assay buffer consists of 100 mM MOPS, 5 mM EDTA, 4 mM KNO<sub>3</sub>, 30 mM glucose at pH 7.0 and was degassed on a vacuum line for ≥1 hour prior to use. Individual assays were conducted in 1.0 cm two-sided acryl cuvettes fitted with two-holed tight-fitting Teflon stoppers and a stir bar. In order to ensure anaerobic conditions, 5 μL of ≥200 U mg<sup>-1</sup> low catalase activity (≤0.1 U mg<sup>-1</sup>) glucose oxidase solution (Sigma Aldrich G0543) was added to the cuvette; it was topped up with reaction buffer, and then the stopper was inserted such that no air bubbles remained in the cuvette (this volume was determined to be 2.98 ± 0.04 mL). Typically, 10-20 μL of a 1:1 to 1:5 dilution of protein sample (~30 mg mL<sup>-1</sup>) was added via Hamilton syringe, and then the blank measurement was taken. The reaction was initiated by addition via Hamilton

syringe of 50  $\mu\text{L}$  of  $\text{PBH}_2$  to give a final concentration of 0.33 mM. The Q-site independent (nonspecific) reductant benzyl viologen (BV) was used to monitor nitrate reduction activity independent of quinol oxidation activity. The assay was conducted similar to the  $\text{PBH}_2:\text{NO}_3^-$  assay, however an aqueous stock solution of 6.1 mM BV was prepared and a 20 mM solution (1 M Tris, pH 9.0) of sodium dithionite was used to reduce the BV. To stoppered cuvette filled with buffer, vesicles and 50-100  $\mu\text{L}$  of dithionite was added 100  $\mu\text{L}$  BV. Assays were conducted on an HP8453 diode array spectrophotometer equipped with a HP 89090A Peltier temperature controller/cuvette stirrer set to a stir rate of 200 rpm, 25°C. Baseline correction of  $A_{419}$  minus the average( $A_{695}-A_{700}$ ) was used for rate calculation of the  $\text{PBH}_2:\text{NO}_3^-$  assay. The relevant chemical parameters for  $\text{PBH}_2$ :  $\lambda_{\text{max}} = 419 \text{ nm}$ ,  $\epsilon_{419} = 3.95 \text{ mM}^{-1} \text{ cm}^{-1}$  and BV:  $\lambda_{\text{max}} = 570 \text{ nm}$ ,  $\epsilon_{570} = 7.8 \text{ mM}^{-1} \text{ cm}^{-1}$  <sup>277</sup>.

## 2.3. Results

### Growth Conditions Influence Heme $b_D$ Heterogeneity

**Figure 2.2A(i)** shows a representative EPR spectrum of the NarGHI hemes in redox-poised oxidized membranes derived from cells grown on rich media with essentially no aeration <sup>270</sup>. This spectrum exhibits a sharp peak at approximately  $g = 3.75$  arising from heme  $b_P$  and a broad peak centered at approximately 3.34 that arises from heme  $b_D$ . A minor peak at  $g = 2.97$  can be assigned to the cytochrome *bo* ubiquinol:oxygen oxidoreductase (see **Supplementary Figure 2.1**)<sup>a</sup>. We investigated the effect of growth-culture aeration by recording heme EPR spectra of NarGHI-containing membranes from cells grown at high (**Figure 2.2A(ii)**), intermediate (**Figure 2.2A(iii)**), and low (**Figure 2.2A(iv)**) levels of culture aeration. These three spectra exhibit heterogeneity comprising two peaks centered at  $g = 3.34$  and  $g = 3.18$ , with diminishing intensity of the latter feature with decreasing aeration.

---

a For the sake of clarity,  $g$ -values observed in this work will be quoted throughout. Minor differences in  $g$ -values between contributions likely arises from subtle differences in preparations and instrument calibrations.

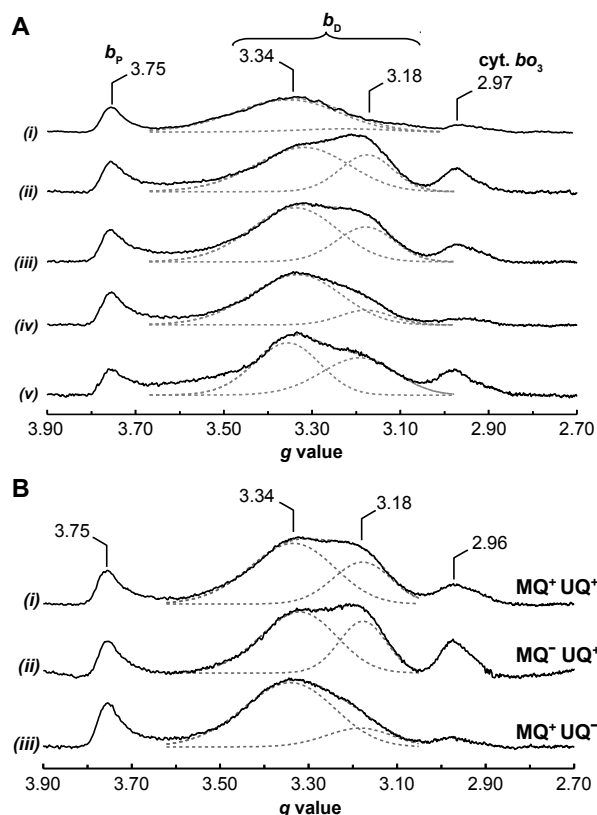


**Figure 2.2: Effects of growth conditions and quinones on heme  $b_D$  EPR line shape are apparent in redox-poised oxidized heme spectra of NarGHI hemes  $b_P$  ( $g = 3.75$ ) and  $b_D$  ( $g = 3.0 - 3.4$ ).** The  $g$ -value labels indicate the average maximum  $g$ -value over the range of applied potentials. **(A)** Effects of growth conditions (oxygenation) on heme  $b_D$  heterogeneity. **Spectrum (i)** is of pH 7 membranes obtained from 2 L batches of cells grown overnight at 30°C at very low agitation in 6 L non-baffled Erlenmeyer flasks. **Spectra (ii-iv)** depict the effect of aerobic to increasingly more anaerobic growth conditions: **(ii)**: 10 L vessel, 2 L min<sup>-1</sup> aeration and 500 rpm impeller stir rate, pH 7 membranes; **(iii)**: 5 L vessel, 500 rpm stirring, <1 L min<sup>-1</sup> aeration, pH 8 membranes; **(iv)**: 10 L vessel, 200 rpm stirring, no aeration, pH 8 membranes. **Spectrum (v)** is of NarGHI expressed in a cardiolipin deficient strain (S330), flask grown, pH 7 membranes. The sample **spectra (i-v)** were respectively poised at: +266, +279, +292, +274, +278 mV. **(B)** Effects of MQ and UQ on the heme  $b_D$  EPR signal. **(i)**: 10 L vessel, 2 L min<sup>-1</sup> aeration and 500 rpm impeller stir rate, pH 7 LCB79/pVA700 membranes poised at +279 mV; **(ii)**: NarGHI expressed in a menaquinone-deficient strain (JCB4111/pVA700) grown in a 5 L vessel, 500 rpm stirring, <1 L min<sup>-1</sup> aeration, pH 8 membranes poised at +280 mV; **(iii)**: NarGHI expressed in a ubiquinone-deficient strain (JCB4211/pVA700) grown in a 10 L vessel, 200 rpm stirring, no aeration, pH 8 membranes poised at +281 mV. Spectra were collected at 10 K and 4 mW (17 dB) MWP, except **(i)** which was collected at 10 dB MWP.

It has been suggested that heme  $b_D$  heterogeneity is due to a mixture of enzyme with and without a tightly bound cardiolipin<sup>297</sup>. In this context, the heme  $b_D$  EPR signal heterogeneity has been interpreted such that the  $g = 3.18$  signal is due to cardiolipin-bound enzyme, and the  $g = 3.34$  signal is due to cardiolipin-free enzyme<sup>297</sup>. To test if cardiolipin does indeed contribute to the heterogeneity, nitrate reductase was expressed semiaerobically in an *E. coli* strain deficient in its biosynthesis as well as for phosphatidylglycerol (*E. coli* S330)<sup>299</sup>. As shown the **Figure 2.2A(v)**, both heme  $b_D$  components are still observed in membranes from the cardiolipin-deficient strain. It is therefore unlikely that cardiolipin plays a role in heme  $b_D$  heterogeneity in NarGHI.

### **Influence of Q-site structure and occupancy on heme $b_D$ EPR spectra**

*E. coli* synthesizes two major types of lipophilic quinones that shuttle electrons from dehydrogenases to reductases within the cytoplasmic membrane. These comprise UQ-8 and MQ-8 which predominate under oxidizing and reducing conditions, respectively<sup>21,40,308,309</sup>. NarGHI is able to bind and oxidize both major quinol species at its Q-site<sup>42,43</sup>. Given that the heme  $b_D$  heterogeneity appears to decrease with decreasing aeration during cell growth and is not eliminated in the absence of cardiolipin, we speculated that it may be related to the composition of quinones within the *E. coli* cytoplasmic membrane. Alternative binding modes for the two quinones, which have already been shown to bind to the same Q-site in NarI<sup>183,282</sup>, may account for the two different conformations seen in the EPR spectra of heme  $b_D$ .

To test whether heme  $b_D$  heterogeneity reflects the differential binding of MQ and UQ, NarGHI was expressed in a strain incapable of producing naphthoquinones MQ/DMQ (MQ<sup>-</sup>UQ<sup>+</sup>): JCB4111 ( $\Delta menBC$ ), and a strain incapable of producing UQ (MQ<sup>+</sup>UQ<sup>-</sup>): JCB4211 ( $\Delta ubiCA$ ). *E. coli* JCB4211 ( $\Delta ubiCA$ ) can only grow under micro-aerobic/anaerobic conditions, and *E. coli* JCB4111 ( $\Delta menBC$ ) is unable to grow under anaerobic conditions. The heterogeneity observed in the EPR spectra of heme  $b_D$  in **Figure 2.2B** is similar to that in **Figure 2.2A**; however, in the MQ<sup>+</sup>UQ<sup>-</sup> strain the heterogeneity is greatly reduced, with a much lower contribution from the  $g = 3.18$

component. There is no significant effect on signal position of either component, and the difference in heterogeneity can be explained by the differing growth conditions necessary for cultivating membranes from the two strains. The most aerobically grown cultures (MQ<sup>-</sup>UQ<sup>+</sup>) exhibit the greatest heterogeneity while the most anaerobically grown cultures (MQ<sup>+</sup>UQ<sup>-</sup>) the least heterogeneity. The MQ<sup>+</sup>UQ<sup>+</sup> culture, being grown less aerobic than MQ<sup>-</sup>UQ<sup>+</sup>, exhibited intermediate heterogeneity. In general, there is a correlation between a lack of UQ/anaerobic growth conditions and a decreased intensity of the  $g = 3.18$  component.

### Quinone site variants and their effects on heme $b_D$

To probe the potential involvement of quinone binding in determining heme  $b_D$  heterogeneity further, we investigated several Q-site variants of two conserved residues, Lys86 and Gly65, and the effect of the Q-site inhibitor HOQNO on their heme  $b_D$  EPR spectra<sup>183,271</sup>. HOQNO is a menasemiquinone analog and Q-site inhibitor, which, when added to membranes containing wild-type NarGHI, elicits a collapse of the  $g = 3.18$  and  $g = 3.33$  components into a single HOQNO-bound form with a peak at  $g = 3.52$  (**Figure 2.3A**). NarI-Lys86 is a highly conserved residue, and it has previously been shown that mutation of this residue to an alanine significantly diminishes quinol:nitrate oxidoreductase activity and menasemiquinone stability<sup>183,284</sup>. Furthermore, the redox-poised heme  $b_D$  EPR spectrum manifests as a single peak centered at  $g = 3.27$ - $3.28$  (see **Figure 2.3A**)<sup>284</sup>. Addition of HOQNO to membranes

Narl variant	$\mu\text{mol BV mg}^{-1} \text{ min}^{-1}$	$\mu\text{mol PBH}_2 \text{ mg}^{-1} \text{ min}^{-1}$	PBH <sub>2</sub> /BV	Growth on NO <sub>3</sub> <sup>-</sup>
Wild-Type	63.6	3.37	53 (100%)	+++
G65A	21.5	0.79	38 (69%)	++
K86A	30.3	0.25	8 (16%)	-

**Table 2.1: NarI variant PBH<sub>2</sub>:NO<sub>3</sub><sup>-</sup> oxidoreductase activities** The activities of the PBH<sub>2</sub> and BV oxidation and nitrate reduction for the NarI variants tested are represented as mean values of at least triplicate experiments with standard errors less than 10%. Anaerobic growth on glycerol:nitrate is depicted in **Supplementary Figure 2.2**.

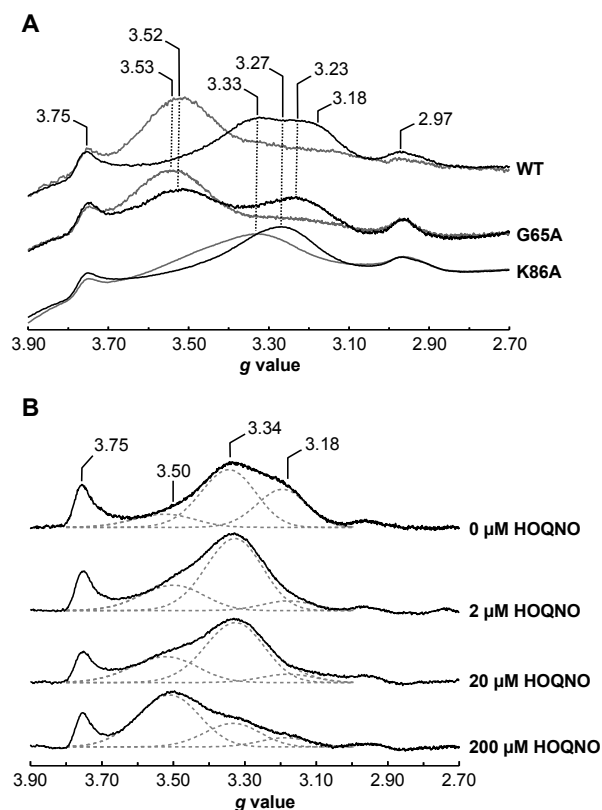


**Figure 2.3: The effects of HOQNO binding on heme  $b_D$  EPR spectra. (A)** HOQNO binding to Q-site variants K86A and G65A. Black lines represent spectra of oxidized membranes, grey lines represent spectra of DCPIP-oxidized membranes treated with 0.5 mM HOQNO. **(B)** HOQNO titration of the heme  $b_D$  EPR signal. The spectra obtained are pH 8 membranes redox-poised to about +280 mV. All the membranes were prepared from flask-grown cultures under standard growth conditions (see Materials and Methods) and contain an approximate concentration of 60-70  $\mu$ M of NarGHI. Spectra were collected at 10 K and 4 mW (17 dB) MWP.

containing the K86A variant elicits a minor shift of the heme  $b_D$  peak from  $g = 3.27$  to  $g = 3.33$ . The K86A variant does not support growth and has diminished quinol:nitrate oxidoreductase activity (**Table 2.1**). NarI-Gly65 is another highly conserved residue lining the Q-site of NarGHI<sup>183</sup>, and we generated a G65A variant. This retains two heme  $b_D$  components in its EPR spectrum at  $g = 3.23$  and  $g = 3.52$ , which collapse into a single  $g = 3.53$  peak of greater intensity upon treatment with HOQNO (**Figure 2.3A**). It is notable that the G65A is able to support growth and retains significant quinol:nitrate oxidoreductase activity (**Table 2.1**).

### **Effect of HOQNO on the heme $b_D$ spectrum is concentration-dependent**

What is unclear from the HOQNO-binding experiments outlined earlier is whether both components are equally sensitive to inhibitor binding. **Figure 2.3B** shows the effects of titrating HOQNO into oxidized wild-type NarGHI membranes. First the  $g = 3.18$  component collapses concomitant with a rise in the  $g = 3.50$  component. In the presence of higher concentrations of HOQNO the signal at  $g = 3.34$  begins to shift to  $g = 3.50$ . This, therefore, indicates the  $g = 3.18$  conformation of NarI has a greater ability to bind HOQNO compared to the  $g = 3.34$  conformation.

### **Redox potentiometry of the $g = 3.34$ and $g = 3.18$ components of NarI heme $b_D$**

The biophysical characteristics of hemes are known to be influenced by the surrounding protein environment. In the case of heme  $b_D$  there appears to be two distinct environments that are resolvable by EPR spectroscopy. Given the link between quinone pool composition/growth conditions and the intensity of the  $g = 3.18$  component (**Figure 2.2B**), we speculated that investigating the pH dependence of the reduction potentials of the two components may shed light on their origins. The  $g = 3.18$  and  $g = 3.34$  components titrate with reduction potentials of +25 mV and -35 mV at pH 8.0, respectively (**Figure 2.4A**). The integrated intensity of the spectrum encompassing both peaks titrates with reduction potentials of +25 mV (25%) and -35 mV (75%). When titrations are carried out at a range of pH values between 6.0 and 9.0, the  $g = 3.18$  and 3.34 components exhibit dependencies of  $-59 \text{ mV pH}^{-1}$  and  $-40 \text{ mV pH}^{-1}$ , respectively (**Figure 2.4B**). These observations suggest that the form of NarI giving rise to the  $g = 3.18$  peak has an ionizable group in the vicinity of heme  $b_D$  that is tightly coupled to the pH of the aqueous milieu (heme reduction results in the uptake of one proton per electron), whereas the  $g = 3.34$  form is more weakly coupled.

Examination of redox-poised EPR spectra at either end of the pH range of **Figure 2.4C** reveals that the  $g = 3.18$  component is favored under acidic conditions, collapsing to the  $g = 3.34$  conformation at higher pH. The single integration of the

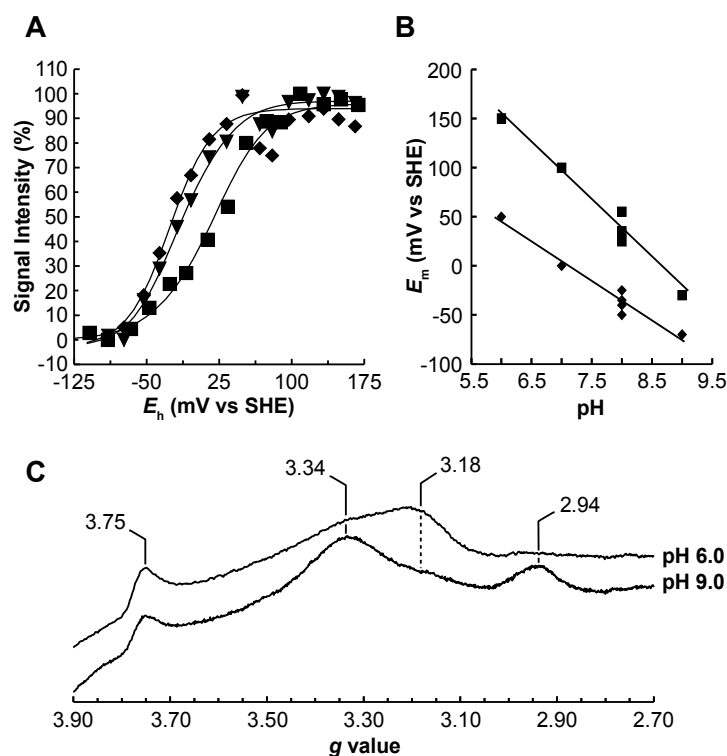


**Figure 2.4: Redox titrations and pH dependence of the components of heme  $b_D$ .**

(A) Redox titration at pH 8 of  $\Delta cydB/pVA700$  membranes. The  $g = 3.18$  titration (■) was fit with  $E_{m,8}$  components of +25 mV (81%) and -35 mV (15%). The  $g = 3.34$  titration (◆) was fit with a single  $E_{m,8}$  of -35 mV. Inverted triangles (▼) represent the data obtained by single integration of the heme  $b_D$  signal with baseline correction fit with  $E_{m,8}$  components of -35 mV (75%) and +25 mV (25%). Integrated intensity values and baseline subtraction was done with the software Xepr. The single-component titrations were obtained by doing three-point dropline subtraction at  $g = 3.81$  and  $3.05$ . Fits are modeled with the Nernst equation scaled for average maximum intensity and with an electron stoichiometry of  $n = 1$ . The EPR spectra for the titration were obtained at 12 K and 4 mW (17 dB) MWP. (B) Reduction potential pH dependence of heme  $b_D$  for the two heme  $b_D$  components. The pH dependence of the  $g = 3.18$  component (■) is approximately  $-59 \text{ mV pH}^{-1}$ , while the  $g = 3.34$  component (◆) is approximately  $-40 \text{ mV pH}^{-1}$ . (C) Two spectra from a single membrane preparation split into two redox titrations at pH 6.0 and pH 9.0 each poised at +289 mV and +292 mV, respectively. The increase in pH is concomitant with a decrease in the  $g = 3.18$  component and the  $g = 3.75$  heme  $b_P$  signal, and an increase in the  $g = 3.34$  and the appearance of a  $g = 2.94$ . Using the software Xepr, a 5<sup>th</sup> order polynomial baseline correction and integration was conducted on the signals. For  $g = 3.75$ , pH 6 area = 29 and pH 9 area = 19. For  $g = 3.3 + g = 3.18$ : pH 6 area = 195 and pH 9 area = 181. For  $g = 2.94$ , pH 6 area = 2 and pH 9 area = 42. The EPR spectra were acquired at 4 mW (17 dB) MWP 10 K.

entire heme  $b_D$  EPR signal shows interconversion of the two forms with no significant difference, with the pH 6 signal having an area of 181 and the pH 9 signal, an area of 195. Heme  $b_P$ , however, decreases in intensity upon alkalization: 29 at pH 6 to 19 at pH 9. This is concomitant with an increase in the  $g = 2.94$  component under more alkaline conditions.

## 2.4. Discussion

Although the two hemes of NarI have EPR spectra well resolved from each other, interpretation of the heme  $b_D$  EPR properties is complicated by the presence of components appearing at  $g = 3.34$  and  $g = 3.18$  (**Figure 2.2B**). Furthermore, we observed that these two components are dependent upon growth conditions, the composition of the quinone pool, and ambient pH (**Figure 2.2** and **Figure 2.4**). Membranes from cells grown at high aeration exhibit more heme  $b_D$  heterogeneity, and we established that this can be attributed to multiple subpopulations of NarGHI by recording EPR spectra of membrane samples lacking the two well-characterized *E. coli* quinol:oxygen oxidoreductases that also contain HALS  $b$ -type hemes (**Supplementary Figure 2.1**).

Recently, it has been proposed that the two components of heme  $b_D$  arise from cardiolipin-bound versus cardiolipin-free states, corresponding to the  $g = 3.18$  and  $g = 3.34$  peaks, respectively <sup>297</sup>. The cardiolipin head group binds to a region within the complex where all three subunits converge and is stabilized by the conserved residues NarG-Tyr9, NarG-Arg6, NarH-Arg218 and NarI-Tyr28. Given that maturation of NarGHI is highly-coordinated and involves a dedicated chaperone (NarJ) and sequential insertion of its prosthetic groups <sup>244,252</sup>, it is unlikely that a significant proportion of the mature enzyme would be assembled without the structurally-important cardiolipin. It is also unlikely that another anionic phospholipid (phosphatidylglycerol) binds in its place since the S330 strain is defective in phosphatidylglycerol and cardiolipin biosynthesis ( $\Delta pgsA$ ) <sup>299</sup>. In either case, the

protein structure indicates a fatty acyl chain of cardiolipin is located within 4 Å of His66. It has been proposed that this interacts with and ensures the proper orientation of His66 to ensure effective quinone binding <sup>297</sup>. However, the contact surface is small, since the cardiolipin acyl chain lies perpendicular to the His66 imidazole plane and would have a weak van der Waals interaction with it at best. Critically, when NarGHI is expressed in cells deficient in cardiolipin biosynthesis, the EPR spectrum of heme  $b_D$  still shows a clear heterogeneity, as seen in **Figure 2.2A(v)**. As reported by us <sup>183</sup> and Arias-Cartin *et al.* <sup>297</sup>, the presence of increasing concentrations of detergent clearly decreases the observed heterogeneity of the heme  $b_D$  EPR signal. Preparation in Thesit ( $C_{12}E_9$ ) <sup>183</sup> and high concentrations of dodecylmaltoside (DDM) collapse the  $g = 3.18$  signal <sup>297</sup>. However it is known that detergent binding can have effects on the structure and function of membrane proteins <sup>310–312</sup>. Furthermore, even at high concentrations of DDM (0.15%) a 1:1 molar amount of cardiolipin was found to remain bound to NarGHI, likely the tightly bound cardiolipin molecule implicated in modulating heme  $b_D$  conformation <sup>297</sup>. So interpretation of data obtained for detergent solubilized NarGHI is complicated at best and may result in physiologically irrelevant results.

As an alternative explanation for the heme  $b_D$  heterogeneity, we focused on the role of Q-site occupancy and quinone binding for several reasons. Firstly, it has been previously shown that the EPR spectrum of heme  $b_D$  is exquisitely-sensitive to the binding of the Q-site inhibitors 2-*n*-heptyl-4-hydroxyquinoline-N-oxide (HOQNO), pentachlorophenol (PCP) and stigmatellin <sup>270,275</sup>. Herein we show that binding of HOQNO collapses the heterogeneity in the heme  $b_D$  EPR signal (**Figure 2.3**). Second, the heterogeneity is dependent upon growth conditions (**Figure 2.2A**), as are the membrane concentrations of menaquinone and ubiquinone <sup>21,313</sup>. Third, the extent of heterogeneity is quinone-dependent, with the  $g = 3.18$  component inversely correlated with the availability of UQ and aerobicity of growth conditions (**Figure 2.2B**). Finally, we observed that the heterogeneity is sensitive to Q-site variants of Lys86 and Gly65 (see **Figure 2.3A**). Collectively, these observations clearly indicate a role for Q-site occupancy/structure in heme  $b_D$  heterogeneity.

The first possibility is that each component corresponds to the binding of either of the two major types of quinone. This would be logical given that the unique binding characteristics of each inhibitor (HOQNO, PCP or stigmatellin) elicit specific shifts in position of the heme  $b_D$   $g_z$ . However, because the two components are present when either MQ or UQ are present (**Figure 2.2B**), the heterogeneity is not due to the binding of one quinone versus the other. Therefore, these two components may be due to alternative binding modes of quinones, which has been proposed for *E. coli* succinate:quinone oxidoreductase (SdhCDAB)<sup>314</sup>, or one component corresponds to a Q-site free of quinone and the other to quinone-bound. We have previously observed that binding of the Q-site inhibitor PCP modulates the  $g_z$ -value of heme  $b_D$  as well as the dihedral angle observed in crystal structures<sup>183</sup>, whereas HOQNO has an even larger effect on the spectrum. The correlation between  $g_z$  value and bis-His coordination dihedral angle is well documented, with a larger “more strained”  $g_z$  value (more anisotropic) resulting from a more perpendicular bis-His interplanar angle, and a more parallel “relaxed” orientation giving a lower  $g_z$  value (less anisotropic)<sup>274</sup>. Since NarGHI preferentially uses MQ, which binds it with a higher affinity over ubiquinone, and better stabilizes menaquinone over ubiquinone, one therefore expects the component corresponding to the occupied Q-site conformation to correlate most closely with the presence of MQ<sup>265,282,297</sup>. In the case where MQ is absent (**Figure 2.2B**), we observe the most heterogeneity and greatest contribution from the  $g = 3.18$  component. When both MQ and UQ are present, the heterogeneity is reduced, and the  $g = 3.34$  component becomes more prominent. Finally, when *ubiCA* is knocked out, as in JCB4211, the MQ content was found to actually be enhanced by 30% compared to wild-type *E. coli* (MQ<sup>+</sup>UQ<sup>+</sup>)<sup>315</sup>, and consequently the heme heterogeneity is at its lowest extent, with the  $g = 3.34$  component being greatly dominant. Therefore, we propose that the  $g = 3.34$  component is due to an occupied Q-site, especially by MQ, which modulates the His66 coordination geometry of heme  $b_D$  via a previously characterized hydrogen bond<sup>168,170</sup>. *Ipsa facto*, the  $g = 3.18$  component is due to a unoccupied Q-site conformation of NarI. This is supported by experiments such as that depicted in **Figure 2.3B**, wherein increasing concentrations

of HOQNO collapse the  $g = 3.18$  component prior to the  $g = 3.34$  component. The collapse of the  $g = 3.18$  component occurs at concentrations less than  $2 \mu\text{M}$  HOQNO (~1:35 moles of HOQNO to NarGHI) whereas the shift in  $g = 3.34$  to  $3.50$  begins occurring at about a molar ratio of 2:7, with complete conversion accomplished with addition of excess HOQNO (20:7). This is interpreted such that empty Q-sites are occupied by the inhibitor prior to displacement of quinone from occupied sites.

To probe the involvement of the Q-site in defining heme  $b_D$  properties further, we looked at the effects of variants of the Q-site residues Gly65 and Lys86. Gly65 is a highly conserved residue in NarI and has a role in defining Q-site functionality<sup>183</sup>. The G65A variant retains substantial quinol:nitrate oxidoreductase activity and is able to support respiratory growth on nitrate, whereas the K86A variant has diminished activity and is unable to support growth (**Table 2.1** and **Supplementary Figure 2.2**). The G65A variant exhibits an EPR spectrum where the  $g_z$ -values for the two components of the heme  $b_D$  signal are more divergent than in the wild-type enzyme (**Figure 2.3A**). The  $g = 3.18$  component exhibits a minor shift to  $g = 3.23$ ; however, the  $g = 3.34$  component shifts to  $g = 3.52$ . In the presence of HOQNO, the G65A variant exhibits similar behavior to the wild-type: diminution of the “relaxed”  $g = 3.23$  component and a shift of the  $g = 3.52$  “strained” component to  $g = 3.53$  with a concomitant increase in intensity (**Figure 2.3A**). The K86A variant has decreased quinol:nitrate oxidoreductase activity and is unable to support anaerobic growth on nitrate (**Table 2.1**)<sup>183</sup>. HOQNO elicits only a minor effect on the heme  $b_D$  spectrum in membrane samples, shifting it from  $g = 3.27$  to  $g = 3.33$  (**Figure 2.3A**), with no evidence of two components in the unbound form. These observations suggest that the  $g = 3.27$  feature of the K86A variant EPR spectrum is equivalent to the  $g = 3.18$  feature of the wild-type spectrum, and reflects an unoccupied Q-site. Overall, these observations support the hypothesis that heme  $b_D$  heterogeneity is linked to Q-site occupancy.

With heme  $b_D$  demonstrating two subpopulations, it is likely that these two conformations exhibit different redox properties, since we have previously observed that HOQNO and stigmatellin modulate heme  $b_D$  reduction potential by  $\Delta E_{m,7} +100$  mV

and +30 mV, respectively <sup>270</sup>. Redox characterization (**Figure 2.4A**) of the two components was carried out by expressing NarGHI in a cytochrome *bd* deficient strain in order to eliminate the interfering *b*<sub>559</sub> signal, see **Supplementary Figure 2.1**. The “free” (*g* = 3.18) component titrates with an *E*<sub>m,8</sub> of +25 mV while the *E*<sub>m,8</sub> of the “occupied” component at *g* = 3.34 is -35 mV. A titration of the first integral heme *b*<sub>D</sub> signal can be fit with a -35 mV component (75%) and a +25 mV component (25%). **Figure 2.4B** shows that over the pH range tested the “free” component consistently titrates at a higher potential than the “occupied” state. The pH dependence calculated in the present study for the “occupied” heme *b*<sub>D</sub> conformation of -40 mV pH<sup>-1</sup> is within agreement of the previously reported value of -36 mV pH<sup>-1</sup> <sup>278</sup>, and a redox-Bohr effect of -59 mV pH<sup>-1</sup> was calculated for the “free” conformation. This difference between the two conformations of NarI is likely due to the modulation of His66 and/or heme *b*<sub>D</sub> propionate *pK*<sub>a</sub> upon quinone binding. Quinone and quinone-analog binding alters the electrostatic environment of the heme and therefore is expected to modulate heme reduction potential, which would explain the different redox-Bohr effect we observe for the two conformations as well as the modulation of reduction potential when quinol analogs are present. For example, the reduction potentials of hemes and the protonation state of their propionates are known to be coupled, with reduced heme having a higher *pK*<sub>a</sub> than oxidized heme. In the case of cytochrome *c*<sub>551</sub>, the *pK*<sub>a</sub> shifts from 5.9 in the oxidized state to 7.0 in the reduced state <sup>316,317</sup>, and for surfactant micelles of hemin (diaquo heme *b*) in tetrahydrofuran, the heme propionates exhibit a *pK*<sub>a</sub> of 6.5 in the ferric form and 7.5 in the ferrous form <sup>318</sup>. We also observe a pH dependence for the heterogeneity: **Figure 2.4C** shows that the *g* = 3.18 form is favored at low pH, whereas a high pH collapses this component to the *g* = 3.34 conformation. Therefore, the Q-site “occupied” conformation seems to be favored at high pH and the “free” conformation at low pH. This pH dependence of stabilization of the two conformations may be tied to the heme propionates themselves or the Lys86 residue, as its mutation to an alanine results in only a single conformer being favored at pH 8 (**Figure 2.3A**). Because of the structural flexibility and chemical nature of lysine, Lys86 plays a role in stabilizing two apparent conformations of NarI. In the

wild-type/G65A enzyme, these two conformations correspond to quinone bound ( $g = 3.33/3.52$ ) and quinone free ( $g = 3.18/3.23$ ) NarI. Therefore, the binding of quinones and Q-site inhibitors to NarI modulates the electrochemical ( $E_m$  and  $pK_a$ ) and  $g_z$ -value of heme  $b_D$  in a Lys86 dependent manner. The exact role of Lys86 and quinol binding/oxidation is still a very active area of investigation in the field.

In conclusion, we have observed that the heterogeneity exhibited in EPR signals of heme  $b_D$  of *E. coli* nitrate reductase A is dependent upon growth conditions. Heterogeneity does not arise from effects of cardiolipin binding, but most probably arises from differences in Q-site occupancy, where these differences can modulate heme  $b_D$  EPR signal position (**Figure 2.5**), reduction potential, and pH dependence of reduction potential. Our work indicates that careful analysis of redox titrations of NarGHI should be done in membranes prepared from cells grown very micro-aerobically and preferably in a cytochrome *bd* deletion strain.

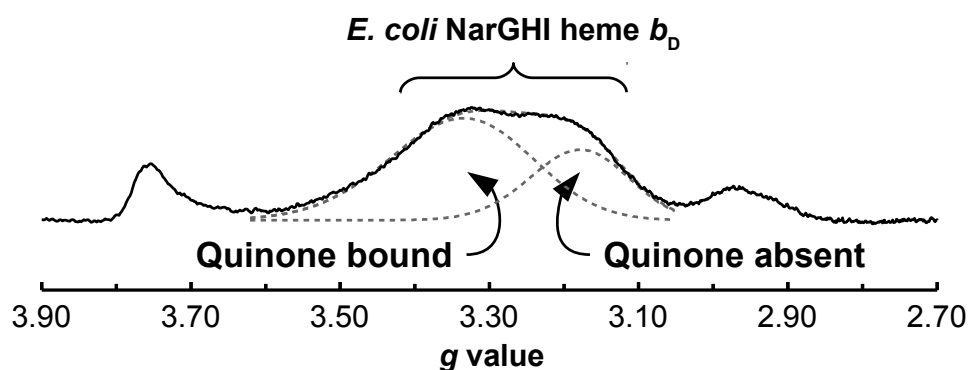
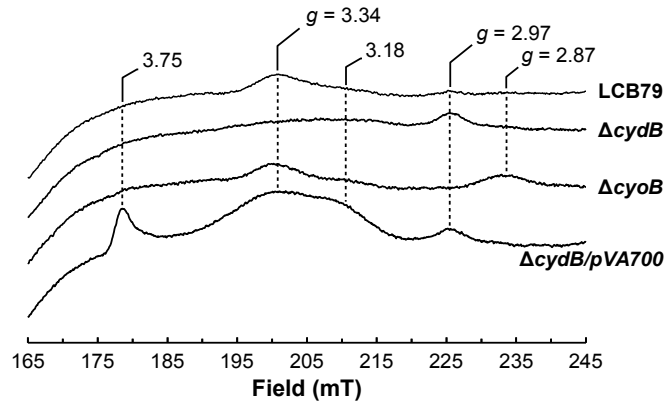


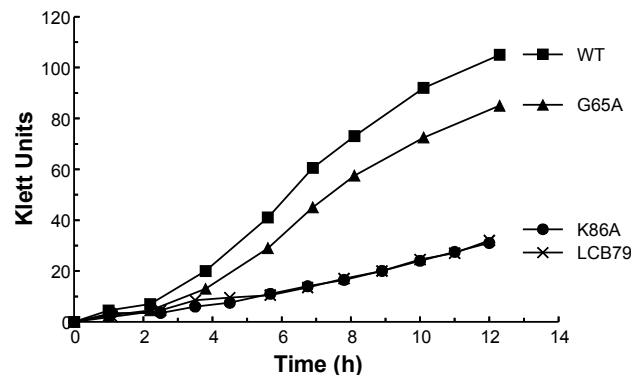
**Figure 2.5: Summary of Q-site occupancy on the heme  $b_D$  EPR spectrum.**

## 2.5. Supplementary Material

The figures included demonstrate the results of the cytochrome *bd* and *bo* deletions on NarGHI EPR heme spectra as well as anaerobic growth curves for NarGHI, NarGHI-K86A, NarGHI-G65A, and the background strain LCB79.



**Supplementary Figure 2.1: Spectral contributions of cytochromes *bd* and *bo* to the NarI heme signals.** Presented are pairs of spectra, the NarGHI-enriched and background membranes prepared from the indicated strains. LCB79 contains both cytochromes *bd* and *bo*,  $\Delta cydB$  lacks *cydB* of cytochrome *bd* and  $\Delta cyoB$ , lacks *cyoB* of cytochrome *bo*. The membranes were oxidized for 5 min at 23°C with 2 mM DCPIP and the spectra collected at 10 K and 4 mW (17 dB) MWP.



**Supplementary Figure 2.2: Anaerobic growth assays of LCB79 in glycerol-nitrate media for pVA700-G65A and pVA700-K86A variants.** The growth assay was conducted as previously described in **Materials and Methods** using minimal salts medium<sup>302</sup> with 50 mM KNO<sub>3</sub>.

### 3. A New Paradigm for Electron-Transfer Through *E. coli* NarGHI

**A version of this chapter has been previously published:**

J.G. Fedor, R.A. Rothery, J.H. Weiner, A new paradigm for electron transfer through *Escherichia coli* nitrate reductase A, *Biochemistry*. **53** (2014) 4549–4556. doi:10.1021/bi500394m.

**Acknowledgements:**

The authors would like to thank Francesca Sebastian and Shannon Murphy for technical assistance as well as the rest of the Weiner Lab for their helpful comments and discussions.

### 3.1. Introduction

*Escherichia coli* nitrate reductase A (NarGHI) is a membrane-bound quinol:nitrate oxidoreductase that is expressed under anaerobic conditions in the presence of nitrate<sup>293</sup>. The enzyme functions as a terminal reductase where quinol oxidation is coupled to nitrate reduction, resulting in a net deposition of protons into the periplasm, which contributes to the transmembrane electrochemical gradient<sup>294</sup>. NarGHI comprises a nitrate-reducing subunit (NarG, 140 kDa), an electron-transfer subunit (NarH, 58 kDa), and a quinol oxidase subunit (NarI, 26 kDa). Overall the subunits form an electron-transfer relay connecting the quinol oxidation activity of NarI to the nitrate reductase activity of NarG. NarI anchors NarGH to the cytoplasmic side of the inner membrane and binds two *b*-type hemes, one proximal (*b<sub>P</sub>*) to NarGH and the other distal (*b<sub>D</sub>*) from it. Electron-transfer commences at the Q-site and proceeds through the two hemes (*b<sub>D</sub>* then *b<sub>P</sub>*) of NarI, a [3Fe-4S] cluster (FS4), three [4Fe-4S] clusters (FS1-FS3) located in NarH, and a final [4Fe-4S] cluster (FS0) and a molybdo-bis(pyranopterin guanine dinucleotide) (Mo-bisPGD) cofactor located in NarG which forms the site of nitrate reduction<sup>19,295</sup>. Each cofactor in the electron-transfer relay has been demonstrated to be critical for electron-transfer and catalysis<sup>19,258,278,319</sup>. As a model system for studying biological electron-transfer, NarGHI presents the advantages of robustness and being readily overexpressed in *E. coli*<sup>85,213,232,269,270,296</sup>.

The redox properties and reduction potentials of the NarGHI cofactors have been extensively studied using a combination of spectroscopy<sup>269</sup> and redox potentiometry<sup>270,296</sup>. EPR spectra of the hemes, FS0, FS4 and the Mo-bisPGD are well resolved from each other, whereas those of the remaining FeS centers in NarH are complicated by spin-spin interactions<sup>258,319</sup>. EPR spectra of hemes *b<sub>D</sub>* and *b<sub>P</sub>* exhibit *g<sub>z</sub>*-values of approximately 3.35 and 3.75, respectively (see **Figure 3.1**). Analysis via potentiometric titrations indicates that heme *b<sub>D</sub>* has an  $E_{m,7}$  (reduction potential at pH 7) of  $+14 \pm 12$  mV and heme *b<sub>P</sub>* has an apparent  $E_{m,7}$  of approximately  $+118 \pm 8$  mV (see **Supplementary Table 3.1** and the references therein). However,

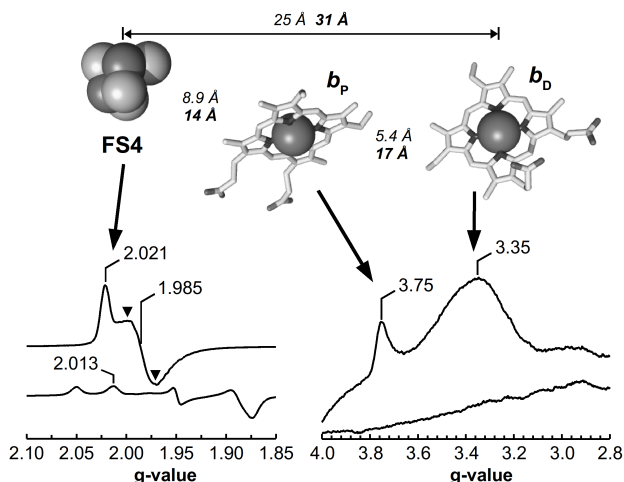


**Figure 3.1: Transmembrane electron-transfer relay of NarGHI comprising hemes  $b_D$  and  $b_P$  and FS4 and their representative EPR spectral features.**

The distances between cofactors are given as edge-to-edge (*italics*) and center-to-center (**bold**). Representative pH 7.0 EPR spectra (9.47 GHz) at 12 K of FS4 (10 dB) and hemes  $b_D$  ( $g_z = 3.35$ ) and  $b_P$  ( $g_z = 3.75$ ) (17 dB) fully oxidized (+286 mV) and fully reduced (-67 mV for hemes and -8 mV for FeS). The inverted triangles denote the intensity measurement for the FS4 signal at  $g = 1.997$  and 1.973. Image generated using PyMol<sup>374</sup> and PDB ID 1Q16<sup>19</sup>.

3.35, 3.50, 3.45 and 3.31 for unbound, HOQNO-, PCP- and stigmatellin-bound enzyme, respectively<sup>183,270,275</sup>. The  $g_z$  value of heme  $b_P$ , however, is unaltered in each case, and a crystal structure of the PCP-bound form and a model of the HOQNO-bound enzyme reveal no significant structural perturbations around heme  $b_P$ <sup>183</sup>. Furthermore, enzyme kinetics, EPR and binding assays are consistent with the presence of a single Q-site in close juxtaposition to heme  $b_D$ <sup>170,183,265,268,270,275–279,282–284</sup>. Interestingly though, HOQNO binding influences the apparent reduction potentials of both hemes; with that of heme  $b_D$  increasing from about +20 to +120 mV and that of heme  $b_P$  decreasing from about +120 to +60 mV<sup>278</sup>. The anomalies described above

the redox properties of hemes  $b_P$  and  $b_D$  and the adjacent [3Fe-4S] cluster (FS4), herein termed the transmembrane electron-transfer relay, display several abnormalities, which can be seen in **Table 3.1 (rows “NC”)**. Firstly, the fits to the titration data of FS4 exhibit two components, the origin of which remains unknown<sup>278</sup>. Second, fits to the redox titration of heme  $b_D$  are optimal with reduction occurring with a physically-impossible substoichiometric number of electrons ( $n$  often approaching 0.6)<sup>270</sup>. Finally, the binding of Q-site inhibitors, such as the menaquinone analog 2-*n*-heptyl-4-hydroxyquinoline-N-oxide (HOQNO), pentachlorophenol (PCP), and stigmatellin, perturbs the local environment of heme  $b_D$  as manifested by altered  $g_z$  values:  $g_z$

indicate that our understanding of transmembrane electron flow through NarGHI is substantially incomplete.

In this chapter, we demonstrate a model describing electronic interactions among the three prosthetic groups of the transmembrane electron-transfer relay of NarGHI that explains their apparently anomalous behaviors. This model also describes a mechanism for enhanced electron-transfer against a transmembrane electrochemical potential and possibly a mechanism for gated electron flow into NarGHI.

## 3.2. Materials and Methods

*Bacterial strains, plasmids, membrane vesicle preparation* – Wild-type NarGHI was overexpressed in *E. coli* strain LCB79 (*araD139*  $\Delta(lacI-POZYA-argF)$  *rpsL*, *thi*,  $\Phi79(nar-lac)$ )<sup>298</sup>. The expression vector used was pVA700 (*tacP*, *rrnB*, *lacI<sup>q</sup>*, *amp<sup>r</sup>*, *narGHJI*)<sup>258</sup>. The vector pCD7 (*tacP*, *rrnB*, *lacI<sup>q</sup>*, *amp<sup>r</sup>*, *narI*) was used to express NarI( $\Delta$ GH)<sup>268</sup>. Growth in flasks and vesicle preparation methods were conducted as previously described and the inner membrane fraction was obtained via differential ultracentrifugation (40 000 rpm, 1.5 hrs) using a 55% (w/v) sucrose step gradient as previously described<sup>270</sup>. The buffer system used for vesicle preparation was 100 mM MOPS, 5 mM EDTA (pH 7.0).

*Redox potentiometry and EPR spectroscopy* – Redox titrations were conducted under argon at 25°C in 100 mM MOPS and 5 mM EDTA at pH 7.0 as previously described<sup>270,303</sup>. The titrations are conducted in the reducing direction with several points taken in the oxidizing direction as well. We do not find any appreciable hysteresis in the titrations. Titrations in the presence of HOQNO, PCP, and stigmatellin were conducted using inhibitor concentrations of 0.5 mM, 1 mM and 0.3 mM, respectively. All samples were prepared in 3 mm inner diameter quartz EPR tubes, rapidly frozen using liquid nitrogen-chilled ethanol, and stored under liquid nitrogen prior to use.

EPR spectra were acquired as previously described <sup>270</sup> using a Bruker ESP300 spectrometer (9.47 GHz) with ESR-900 flowing helium cryostat, a temperature of 12 K, 19 G<sub>pp</sub> modulation amplitude at 100 kHz at 20 mW microwave power for the stigmatellin and 100 mW microwave power for the HOQNO titrations. The wild-type and PCP-bound spectra were recorded using a Bruker Eleksys E500 series X-band EPR spectrometer (9.38 GHz) with ESR-900 flowing helium cryostat, a temperature of 12 K, 10 G<sub>pp</sub> modulation amplitude at 100 kHz, with 20 mW microwave power. All potentials mentioned are relative to the standard hydrogen electrode. All FS4 data were acquired at 10 dB, with signal intensity taken from  $g = 1.997$  minus the trough intensity at  $g = 1.973$ .

*Fitting and modeling of redox titration data* – To model the redox interactions in the system comprising hemes  $b_D$  and  $b_P$  and FS4, we used a model diagrammatically depicted in **Figure 3.2A** and mathematically outlined in **Supplementary Figure 3.1** <sup>10,320</sup>. For applying the model to the data, we assigned center **A** as heme  $b_D$ , **B** as  $b_P$  and **C** as FS4. To model the system comprising just the two hemes, a simplified

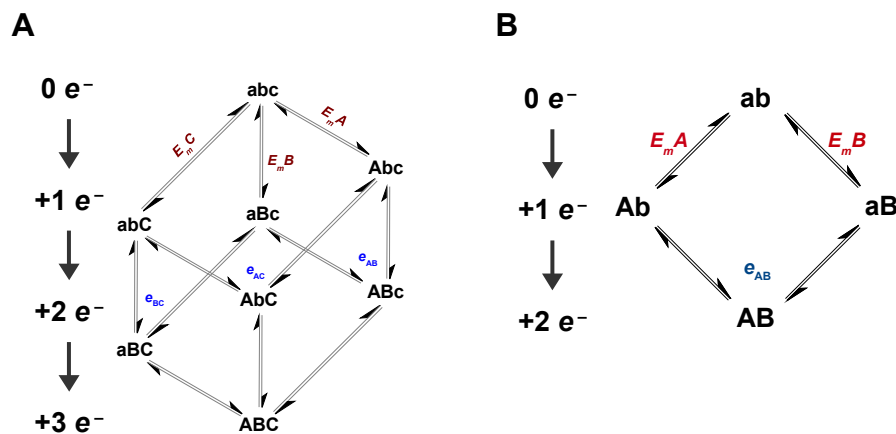


**Figure 3.2: Thermodynamic model for NarGHI hemes  $b_D$ ,  $b_P$  and FS4 depicted schematically.**  $E_m$  is the given reduction potential of the given cofactor A, B, or C, and the interaction potentials are depicted as the variables  $e_{AB}$ ,  $e_{BC}$ ,  $e_{AC}$  for interactions between the specified cofactors. Lower case letters (a, b, c) indicate an oxidized state, whereas uppercase letters denote reduction by a single electron, where  $A = b_D$ ,  $B = b_P$ ,  $C = FS4$ . See the text for a full description of the model, the specific equations used can be found in **Supplementary Figure 3.1**.

model was used where just  $E_mA$ ,  $E_mB$  and  $e_{AB}$  were used, **Figure 3.2B**.

In applying this model to the data, we assume there are no interactions between the hemes or FS4 with the other centers in NarGHI, including bound quinone species, and only interactions between adjacent centers are considered. Matlab (version R2013b, The MathWorks Inc., Natick, Massachusetts) was used to do nonlinear least-squares fitting of the model to the data by reducing the sum of squared residuals between theoretical fits and experimental data points, where the reduction and interaction potentials, baseline, and scale were allowed to vary. The maximum and baseline of the titration curves were limited to vary by  $\pm 5\%$ . The qualities of fits were calculated in MatLab to yield the correlation coefficients, as well as 95% confidence intervals and standard errors in the modeled parameters. In each case, fits achieved a correlation coefficient of  $\geq 98\%$ . The raw data for the K86A, stigmatellin, HOQNO and NarI( $\Delta$ GH) titrations used in this study were previously published but reprocessed and reanalyzed<sup>270</sup>.

### 3.3. Results and Discussion

#### Sample and data considerations

EPR is an excellent technique for the study of electron-transfer relays containing cofactors with well-resolved spectral features. The oxidized hemes of the NarGHI transmembrane electron-transfer relay are readily resolved, with heme  $b_P$  having a  $g_z$  of approximately 3.75 and heme  $b_D$  having a  $g_z$  of approximately 3.35. The spectrum of oxidized FS4 is also well resolved from the other centers of the enzyme and comprises a peak ( $g_z$ ) at  $g = 2.02$  and a peak-trough ( $g_{xy}$ ) immediately upfield at  $g = 1.99$ . However, before their behavior in the potential domain can be thoroughly analyzed, the homogeneity of these signals needs to be established. The  $g = 3.75$  peak of heme  $b_D$  is clearly resolved from signals of other moieties that might impact our analyses (**Figure 3.1**), as there are no signals in this region in membranes lacking NarGHI<sup>252,268,284,321</sup>. FS4 is more complicated, because FS1 can interfere with the signal interpretation as can the presence of extraneous background FeS clusters.

It has previously been shown, however, that NarH-FS4 is by far the predominant species and that only at low potentials does FS1 begin to interfere<sup>232,258,270,278</sup>. The nearest signal due to FS1 appears at  $g = 2.013$ , and the background signal exhibits a peak at 2.02, which overlaps with the dominant signal of FS4 at 2.021. These forms of signal interference can be mitigated by measuring the FS4 signal intensity at  $g = 1.997$  minus the trough intensity at 1.973, as depicted by the inverted black triangles in **Figure 3.1**.

Interpretation of the Heme  $b_D$  EPR signal poses the most significant challenge. Heme  $b_D$  often manifests as having two subpopulations with  $g_z$  values of  $\sim 3.35$  and  $\sim 3.2$ , which we propose are due to differential Q-site occupancies<sup>321</sup>; whereas others have suggested the subpopulations arise from differential cardiolipin occupancies<sup>297</sup>. Under anaerobic or micro-aerobic conditions, the  $g_z$  feature of the heme  $b_D$  spectrum manifests as a single peak at  $g = 3.35$  (**Figure 3.1**)<sup>268,270,321</sup>. When present, these two subpopulations do exhibit different apparent reduction potentials, and thus simple signal integration is not feasible<sup>321</sup>. However, the two subpopulations collapse into one signal, albeit with a shifted  $g_z$ , upon inhibitor binding. In the case of HOQNO, PCP, and stigmatellin binding the  $g_z$  value for heme  $b_D$  shifts from 3.35 to 3.50, 3.45 and 3.31, respectively<sup>183,270,275</sup>. Likewise, the NarGHI<sup>K86A</sup> Q-site variant exhibits a homogeneous heme  $b_D$  EPR signal at  $\sim 3.3$ , but it also exhibits reduced quinol oxidase activity and is unable to bind HOQNO or stabilize a semiquinone radical<sup>183,284,321</sup>. Using the inhibitor-bound states also addresses the possibility, and likely inevitability, of interactions of the adjacent heme ( $b_D$ ) with the bound quinone species, particularly the stable anionic semiquinone<sup>231,282</sup>. For the above reasons we focus our analyses herein on the more homogeneous inhibitor-bound states and the NarGHI<sup>K86A</sup> Q-site variant.

### **Redox titrations of FS4 and hemes $b_D$ and $b_P$**

The basic Nernst equation is normally applied to analyze redox titration data (**Figure 3.3A - dashed lines**)<sup>10</sup>. However, close examination of previous titrations reveals a couple of redox titration anomalies for components of the NarGHI

		$E_m^{a,c}$ Heme $b_D$ (mV)	$E_m^{a,c}$ Heme $b_P$ (mV)	$E_m^{a,b}$ [3Fe-4S] (mV)	$e^d$ $b_D-b_P$ (mV)	$e^d$ $b_P$ -[3Fe-4S] (mV)
Wild-type	NC1	+2 ± 5	+128 ± 5	+163 ± 5	0	0
	NC2	+2 ± 5	+129 ± 5 ( $n = 0.64$ )	+186 ± 5 (75%) +83 ± 18 (25%)	0	0
	C	+3 ± 4	+163 ± 5	+181 ± 4	0	-50 ± 7
K86A	NC1	+12 ± 8	+88 ± 2	+182 ± 4	0	0
	NC2	+12 ± 8	+88 ± 2	+195 ± 3 (84%) +85 ± 16 (16%)	0	0
	C	+15 ± 3	+131 ± 8	+186 ± 3	0	-45 ± 9
+ 0.5 mM HOQNO	NC1	+109 ± 6	+51 ± 5	+174 ± 5	0	0
	NC2	+106 ± 5 ( $n = 0.6$ )	+52 ± 8 ( $n = 0.8$ )	+196 ± 6 (74%) +105 ± 19 (26%)	0	0
	C	+120 ± 4	+142 ± 9	+182 ± 4	-49 ± 7	-46 ± 10
+ 0.3 mM Stigmatellin	NC1	+35 ± 2	+115 ± 6	+167 ± 7	0	0
	NC2	+35 ± 2	+115 ± 5 ( $n = 0.56$ )	+197 ± 4 (70%) +94 ± 10 (30%)	0	0
	C	+58 ± 6	+166 ± 4	+187 ± 3	-27 ± 8	-62 ± 5
+ 1 mM PCP	NC1	-38 ± 3	+73 ± 2	+178 ± 3	0	0
	NC2	-38 ± 3	+73 ± 2	+190 ± 2 (89%) +88 ± 16 (11%)	0	0
	C	-38 ± 2	+120 ± 7	+184 ± 2	0	-49 ± 7
pCD7	NC	+40 ± 3	-180 ± 5	N.A.	0	N.A.
	C	+39 ± 3	-180 ± 4	N.A.	0	N.A.

**Table 3.1: Cooperative (C) and Noncooperative (NC) fitting parameters for redox titrations of nitrate reductase preparations as seen in Figure 3.3.** *a* –  $E_m$  values correspond to reduction potentials at pH 7. *b* – The noncooperative values represent macroscopic  $E_m$  values, where the percentage denotes the contribution of the single component in multi-component fits. *c* – Unless specified, fits were generated using electron stoichiometries of  $n = 1$ . *d* –  $e$  is the cooperative component of the system and quantifies the interactions between the two specified adjacent cofactors. MatLab modeled fits are represented as mean ± standard error. N.A. = Not applicable.

transmembrane electron-transfer relay. (i) To adequately fit the titration data for FS4, two components of  $E_m$  (+186 mV and +83 mV) are required (**Table 3.1**), essentially in agreement with published values<sup>232,270,278</sup>. Compare the fits in **Figure 3.3** for FS4, where the broadly dashed lines represent idealized Nernstian fits ( $n = 1$  and one component) and the finely dashed lines are fits where two  $n = 1$  components are utilized. The residuals (**Supplementary Figure 3.3**) clearly show that FS4 is better fit by two components rather than a single component. (ii) While previously published titration data for heme  $b_P$  utilized  $n = 1$  fits<sup>270</sup>, the curves can be better modeled with an apparent electron stoichiometry significantly below unity. Again, this can be seen in **Figure 3.3** (and **Table 3.1**) where the broadly dashed lines represent idealized Nernstian fits ( $n = 1$ ) and the more finely dashed lines are modified models where the apparent  $n$  is  $< 1$  (see residuals in **Supplementary Figure 3.3**). Critically, this behavior is dependent upon the variant studied, the presence of Q-site inhibitors, and the subunit composition of the preparation studied. For example, data obtained from the NarGHI<sup>K86A</sup> variant, wild-type enzyme in the presence of PCP, and from the NarI subunit expressed by itself (NarI( $\Delta$ GH)) can be fit to  $n = 1$  Nernstian curves – see **Table 3.1** and **Figure 3.3B, D, and F**.<sup>270,284</sup> In contrast to the behavior of heme  $b_P$ , reduction of heme  $b_D$  is well-described by  $n = 1$  fits. The heme  $b_D$  titrations depicted in panels **A, B, and D** of **Figure 3.3** do have a minor extraneous component modeled at  $+157 \pm 2$  mV, which has been attributed to the overlapping spectrum of heme  $b_{558}$  of cytochrome  $bd$ <sup>268,320–322</sup>.

A further peculiarity of the NarGHI transmembrane electron-transfer relay is that the Q-site inhibitor HOQNO elicits an apparent inversion of the reduction potentials of the two hemes, and has a modest effect on the lower-potential component of FS4 – shifting it from approximately +83 mV to +105 mV (**Figure 3.3C and Table 3.1**). Interestingly, this is accompanied by the titration of heme  $b_P$  taking on a more ideal  $n = 1$  behavior while heme  $b_D$  exhibits an apparent  $n = 0.6$  fit (**Table 3.1**).

Together, these observations could be explained by NarI containing multiple quinone binding sites or that HOQNO-binding induces structural changes in the enzyme and consequently shifts the  $E_m$  for both hemes. However, we and others

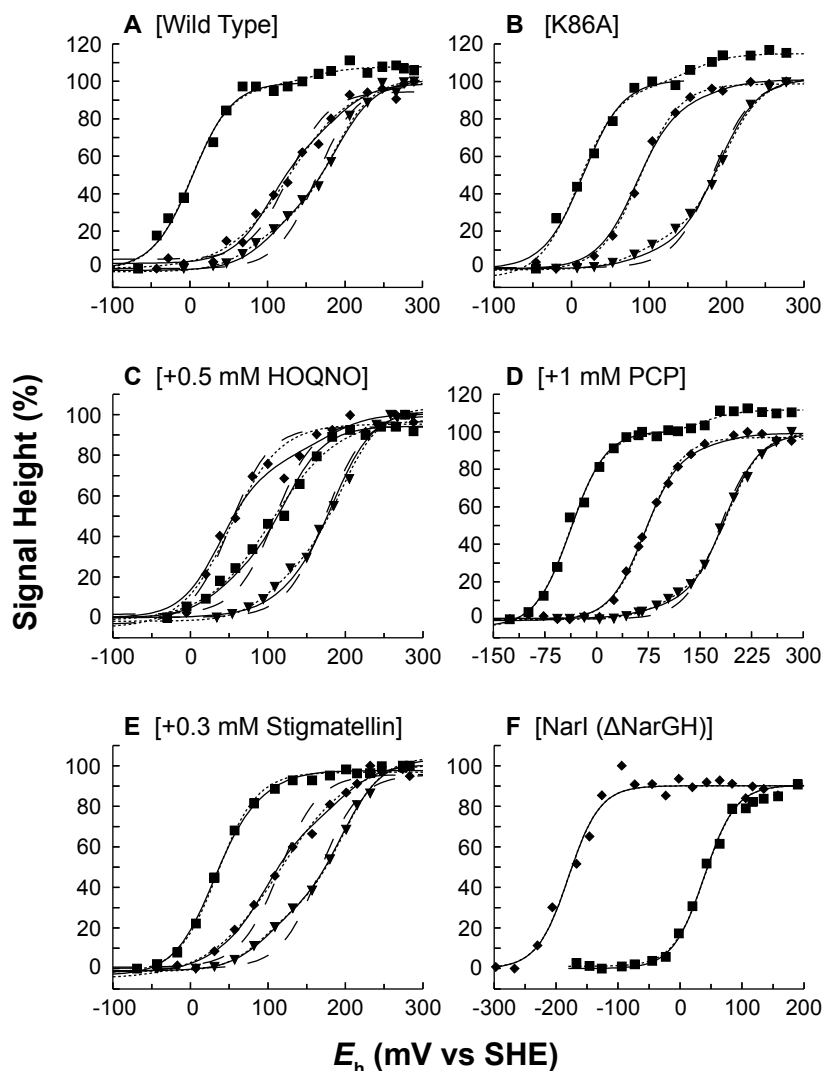


**Figure 3.3: Fits for the redox titrations of hemes  $b_D$  (■),  $b_P$  (◆) and FS4 (▼).** Broadly dashed lines (— — —) denote “standard” Nernstian fits in which a single  $n = 1$  component is modeled. Finely dashed lines (- - - -) denote modified Nernstian fits where either two components or apparent  $n$ -values  $< 1$  are used as the model. Solid lines (—) denote fits by the cooperative models depicted in **Figure 3.2**. See **Table 3.1** for the respective fitting parameters used. The applied potential ( $E_h$ ) is relative to the standard hydrogen electrode and the signal intensities are normalized to 100%. Titrations **A**, **B** and **D** include fits of +160, +156 and +155 mV, respectively, in order to account for the contaminating  $b_{558}$  of cytochrome  $bd$  in the membrane preparations. The redox titrations correspond to vesicle preparations of: **(A)** wild-type NarGHI, **(B)** NarGHI<sup>K86A</sup>, **(C)** NarGHI supplemented with 0.5 mM HOQNO, **(D)** NarGHI in the presence of 1 mM PCP, **(E)** NarGHI supplemented with 0.3 mM stigmatellin, **(F)** NarI( $\Delta$ GH) membranes.

have shown by HOQNO fluorescence quench titrations, EPR spectroscopy, and X-ray crystallography that there is only a single quinol binding site in the enzyme, found adjacent to heme  $b_D$ , which binds both menaquinone and ubiquinone as well as Q-site inhibitors PCP, HOQNO and stigmatellin<sup>170,183,270,282,284</sup>. Furthermore, a crystal structure with PCP bound to NarI has been determined<sup>183</sup> and modeling HOQNO into the position taken by PCP reveals that there are no significant actual or predicted conformational changes in the vicinity of heme  $b_P$  elicited by inhibitor binding. It is thus unlikely that the redox behavior of heme  $b_P$  and FS4 in the HOQNO-bound state is due to a second Q-site or inhibitor-binding induced changes in conformation. There is also no published evidence for appreciable redox-dependent conformational changes in NarGHI. Thus, the non-ideal redox behavior of NarGHI is unlikely to be due to redox-dependent conformational changes. We therefore posit that the underlying cause is the existence of anti-cooperative redox interactions between the cofactors.

### **Modeling redox cooperativity**

It is known that surface charges as well as charged residues and dipole moments within proteins influence the reduction potentials of embedded cofactors, which are analogous to the factors that influence the  $pK_a$  values of amino acid residues<sup>81,323</sup>. Because reduction of a cofactor can readily change its overall charge, it can also elicit electrostatic effects on adjacent cofactors, thereby modulating their reduction potentials<sup>74,134</sup>. This is manifested in the observation of positive ( $n > 1$ ) or negative ( $n < 1$ ) cooperativity. For a system exhibiting positive cooperativity, reduction of a cofactor *increases* the electron affinity (increases  $E_m$ ) of adjacent cofactors. Conversely, negative cooperativity (anti-cooperativity) is such that reduction of one cofactor decreases the electron affinity (reduces  $E_m$ ) of the others. Thus, cooperativity is a plausible explanation for the observation of non-Nernstian redox chemistry within the transmembrane electron-transfer relay of NarGHI. A notable example of an anti-cooperative redox interaction is that between hemes  $b_{558}$  and  $b_{595}$  of *E. coli* cytochrome *bd*, wherein apparent  $n$ -values of 0.7 – 0.9 were required for satisfactory

fits using standard Nernstian models. Similar quality fits were obtained by modeling an anti-cooperative interaction of -32 mV between these two cofactors<sup>320</sup>.

To explain the anomalous behavior of the NarGHI transmembrane electron-transfer relay, we applied a three-center model with pairwise interactions between adjacent centers. The thermodynamic model for the transmembrane electron-transfer relay, consisting of  $b_D$ ,  $b_P$  and FS4, is depicted schematically in **Figure 3.2A** (see **Supplementary Figure 3.1** for mathematical details). In the scheme,  $E_m$  is the midpoint potential of the given center (A)  $b_D$ , (B)  $b_P$ , or (C) FS4, and the interaction potentials are depicted as variables  $e_{AB}$ ,  $e_{BC}$ ,  $e_{AC}$ , denoting an interaction between the specified centers. Lowercase letters (a, b, c) indicate an oxidized state, whereas uppercase letters (A, B, C) denote reduction by a single electron. To prevent over-parameterization of the fittings we looked only at pairwise interactions of adjacent centers, therefore  $e_{AC}$  was fixed at 0 mV. This is reasonable if the cooperativity is purely electrostatic, because the inverse distance dependence of electrostatic interaction energy would ensure the long-range interaction between centers FS4 and  $b_D$  (edge-to-edge distance of  $\sim 25$  Å) would be negligible in comparison to the much more proximal pairwise interactions ( $b_P$ -FS4 distance of 8.9 Å ;  $b_D$ - $b_P$  distance of 5.4 Å) (see **Figure 3.1**)<sup>19</sup>. As a reminder, the heme  $b_D$  titrations depicted in panels **A**, **B** and **D** of **Figure 3.3** do have a minor extraneous component modeled at  $+157 \pm 2$  mV, which is due to heme  $b_{558}$  of cytochrome  $bd$ , and consequently this high-potential component of the titrations of  $b_D$  was not included in the cooperativity model<sup>268,320-322</sup>.

### Applying the model to the redox titrations of hemes $b_D$ , $b_P$ and FS4

**Table 3.1** summarizes the fitting parameters used for the noncooperative and cooperative models for the inhibitor-free, HOQNO-bound, PCP-bound, and stigmatellin-bound states of NarGHI, and the corresponding redox titrations are depicted in **Figure 3.3**, wherein **broadly dashed lines** represent single component standard Nernstian fits where  $n = 1$ . The **finely dashed lines** represent multi-component Nernstian fits or fits where the apparent  $n$ -value is less than one. The

**solid lines** represent fits derived from the cooperative model depicted in **Figure 3.2A** (see **Supplementary Material** for additional details). The residuals are plotted in **Supplementary Figure 3.3**.

We favor the cooperative model over those invoking multiple components and apparent  $n$ -values  $<1$  because similar quality fits are obtained using fewer parameters. For example, the multiple-component fit for the wild-type inhibitor-free bound enzyme has seven degrees of freedom, whereas the cooperative fit has only five. However, it does appear that certain sections of the titrations, particularly the low potential end of FS4 titrations, are better fit with the modified Nernstian models than the cooperative model. Our model utilizes only pair-wise interactions and does not take into account interactions with other cofactors within the protein, including the bound quinone. We have found that modeling the interaction between  $b_D$ -FS4 gave slightly better fits (data not shown), however the increased number of parameters resulted in greatly diminished confidence in the fits, and as a consequence, we decided to look at only adjacent pair-wise interactions. Therefore, the model has the ability to account for multiple components for FS4 and shallower titration slopes for  $b_D$  (and  $b_P$  in the HOQNO-bound state) but is not sophisticated enough to account for all the more subtle effects we observe in the redox titrations of the transmembrane electron-transfer relay.

The most evident pairwise interaction is between heme  $b_P$  and FS4, with an average between all samples of  $-50 \pm 7$  mV. This interaction manifests as substoichiometric apparent  $n$ -values for heme  $b_P$  and multiple apparent redox components for FS4 titrations and it has previously been suggested that a mutual redox interaction is responsible for this behavior <sup>278</sup>. However, there is a weaker apparent interaction between the two hemes despite the distances between  $b_D$ - $b_P$  being similar to the separation of FS4 and  $b_P$ ; see **Figure 3.1**. One reasonable explanation for this would be that the charge density is higher in iron-sulfur clusters than in hemes, because the electron density of reduced hemes is known to extend over the entire porphyrin macrocycle <sup>137,139</sup>. In order to eliminate the supposed effects of the FS4- $b_P$  interaction on heme  $b_P$  line shape, we re-examined the published EPR

spectra of NarI expressed in the absence of NarGH where heme  $b_P$  undergoes a  $g$ -value shift from 3.75 to 2.92 and a decrease in  $E_{m,7}$  of  $>100$  mV<sup>270</sup>. With the large divergence in reduction potentials between the two hemes, no obvious redox interaction was discerned and the  $b_P$ - $b_D$  interaction was therefore set to zero. In agreement with the hypothesis that the non-ideal redox titration curve of heme  $b_P$  is due to redox interactions with heme  $b_D$  and FS4, we observe only single-component  $n = 1$  Nernstian redox titrations of the two hemes, **Figure 3.3F**.

In the case of  $b_D$ - $b_P$  interaction, there is a dependence of interaction energy on the apparent difference in reduction potentials. In most cases, the difference in  $E_m$  values for heme  $b_D$  and  $b_P$  are divergent enough such that the titration curve effects indicative of redox cooperativity, such as slope shallowing or multiple apparent components, are not present, and therefore, an interaction potential was not measurable. The two instances where this was not the case are the titrations of the HOQNO- and stigmatellin- bound states. In the stigmatellin titration, a  $b_D$ - $b_P$  interaction potential of -27 mV was determined and the corresponding divergence in  $E_m$  values of the two hemes was  $\sim 100$  mV. Contrast this with the wild-type inhibitor-free heme  $E_m$  difference of 160 mV. In the HOQNO titration, the heme  $E_m$  difference is a mere 20 mV and the magnitude of the inter-heme interaction (-49 mV) approaches that of the  $b_P$ -FS4 interaction (-50 mV).

Fitting redox titrations of the transmembrane electron-transfer relay to the model presented also gives us an alternative perspective on the effects of HOQNO binding. Previously, HOQNO was thought to modify the  $E_m$  values of hemes  $b_D$  and  $b_P$  such that heme  $b_D$  exhibits an  $E_m$  higher than that of  $b_P$ . This is concurrent with HOQNO eliciting a significant shallowing of the titration curve of  $b_D$ <sup>270</sup>. Utilizing the cooperative model, heme  $b_P$  does experience an increase in its  $E_m$ ; however it remains lower than that of heme  $b_D$ . This is expected because HOQNO binds adjacent to, and therefore changes the  $g_z$ -value, of heme  $b_D$  and not  $b_P$ , and models based on the PCP-bound structure indicate a lack of HOQNO-induced conformational changes in NarI<sup>183,270,275</sup>. In the context of cooperativity, the  $E_m$  of heme  $b_P$  is only diminished by 20 mV, however the heme  $b_D$  reduction potential and  $b_D$ - $b_P$  interaction

are modulated upon HOQNO binding. The interaction potential between the two hemes varies significantly between the inhibited states of the enzyme, but as the  $E_m$  of heme  $b_P$  and FS4 remains largely unchanged, so too does the interaction energy between these two centers. Similar phenomena are observed in the PCP and stigmatellin titrations where principally the  $E_m$  of heme  $b_D$  is influenced. Again, this is consistent with a single Q-site and the conformational integrity of NarI, regardless of whether inhibitors are bound or absent. Modulation of the  $b_D$ - $b_P$  interaction may be due to the effects of inhibitor binding on the electrostatic environment around and between these two hemes. Additionally, or alternatively, as the  $E_m$  values of the hemes become more divergent, it becomes more difficult to determine the magnitude of their interaction and therefore their effect on one another.

### **Functional consequences of redox anti-cooperativity in NarGHI**

The phenomenon of redox anti-cooperativity in NarGHI would explain the two-phase reoxidation kinetics previously observed for NarGHI, particularly in the presence of HOQNO where the slower reoxidation phase becomes significantly more pronounced (see ref <sup>278</sup> for details). That is, HOQNO predominantly modulates the heme  $b_D$   $E_m$  and  $b_D$ - $b_P$  interaction, such that the macroscopic  $E_m$  of  $b_P$  appears lower than that of  $b_D$ . It is the anti-cooperative  $b_D$ - $b_P$  interaction and the increased  $b_D$  reduction potential which slows electron transfer through NarI.

Redox interactions within NarGHI may actually have implications in the broader context of bacterial respiration. Due to the orientation of NarGHI in the membrane, electron flow through NarI is from the P-side of the membrane (heme  $b_D$ ) to the N-side (heme  $b_P$ ) and therefore is against the transmembrane potential,  $\Delta\Psi$ , which is approximately -130 mV in nitrate respiring *E. coli* <sup>3</sup>. Considering the previously reported values of +14 mV and +118 mV for hemes  $b_D$  and  $b_P$ , respectively, the  $\Delta E$  of +104 mV is insufficient to overcome the transmembrane potential (see **Figure 3.4A**). However, **Figure 3.4B** demonstrates that when considering the values modeled herein of +3 mV for  $b_D$  and +163 mV for  $b_P$ , the resultant  $\Delta E$  of +160 mV is sufficiently compensatory for the transmembrane potential. Similarly, the presence of

a membrane potential has shown to have large effects on electron transfer and distribution between hemes  $b_{556}$  and  $b_{562}$  of cytochrome  $bc_1$ <sup>2,324</sup>.

It is also possible that the major functional consequence of electrostatic interactions in the transmembrane electron-transfer relay may be to gate electron flow

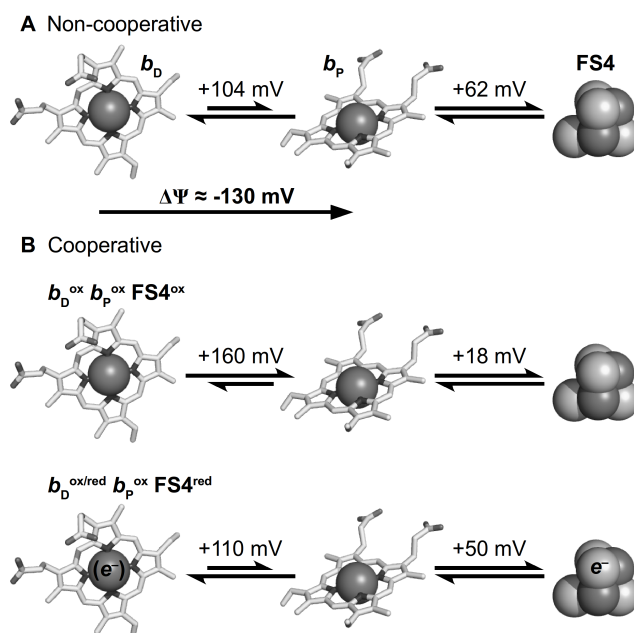


**Figure 3.4: Electron-transfer across the plasma membrane from  $b_D$  to FS4 using the old and new paradigm for the transmembrane electron-transfer relay of NarGHI.** The equilibrium arrows between  $b_D$  and  $b_P$  indicate the direction of favourable electron transfer when  $\Delta\Psi$ , -130 mV, is considered<sup>3</sup>. **A** depicts the current paradigm of electron-transfer through the transmembrane electron-transfer relay using the average published  $E_{m,7}$  values for  $b_D$ ,  $b_P$ , FS4 of +14 mV, +118 mV, +180 mV, as mentioned in the text. **B** depicts the thermodynamics of electron-transfer through the transmembrane electron-transfer relay where the revised potentials and interactions are considered where the potentials used for  $b_D$ ,  $b_P$ , FS4,  $e_{bD-bP}$ ,  $e_{bP-FS4}$  are: +3 mV, +163 mV, +181 mV, 0 mV, -50 mV. Three states are considered: the first in which the system is fully oxidized and the second/third where FS4 is reduced or FS4 and  $b_D$  are reduced. When FS4 is reduced the apparent  $E_m$  of  $b_P$  becomes diminished by 50 mV to +113 mV. This results in mildly unfavourable electron flow across the membrane and increased electron residence on heme  $b_D$ , the effects of which may include tighter binding of the semiquinone and thus blocked entrance of further reducing equivalents into NarGHI.

through NarI. **Figure 3.4B** shows the energetics of transmembrane electron-transfer when the system is either fully oxidized (top) or when FS4 (and  $b_D$ ) is reduced (bottom). The reduction of FS4 brings the inter-heme electron-transfer potential, that is from  $b_D$  to  $b_P$ , from +160 mV to +110 mV, due to the lowering of the  $E_m$  of  $b_P$  by  $b_P$ -FS4 anti-cooperativity (-50 mV). When  $\Delta\Psi$  is taken into account, the  $\Delta E$  for transmembrane electron transfer goes from +30 mV when FS4 is oxidized, to -20 mV when FS4 is reduced. Consequently, during steady-state turnover of the enzyme and upon reduction of FS4,  $b_D$  has a greater propensity to remain reduced. It has been previously shown that reduction of NarI decreases the  $K_m$  for HOQNO from 0.34  $\mu\text{M}$  to 0.07  $\mu\text{M}$ , thus ensuring tighter binding of HOQNO, and supposedly the semiquinone intermediate.<sup>278</sup> Such an effect has been observed for cytochrome  $bc_1$ , where  $Q_o$ -site semiquinone stability is directly coupled to  $b_{562}$  reduction (the adjacent heme) and semiquinone stability increases further when  $b_{566}$  is reduced<sup>324</sup>. By more tightly binding and stabilizing the semiquinone, the enzyme may physically prevent entry of further reducing equivalents. Therefore, by decreasing the potential for transmembrane electron-transfer under nitrate-limiting conditions, the anti-cooperativity within NarI may facilitate more effective usage of the Q-pool by diverting quinol to the other terminal reductases, such as those for DMSO, TMAO and fumarate reductase.

A further consideration is that the model addresses only part of the entire NarGHI electron-transfer relay that comprises eight cofactors (two hemes, five FeS clusters, and a molybdenum cofactor) and the reactants. The span of reduction potentials in NarGHI is rather large (-400 to +200 mV), but with the number of cofactors present, the midpoint potential overlap is considerable<sup>19</sup>. Also, redox cooperativity would have significant implications for quinol binding and oxidation as well as semiquinone stabilization. Therefore, to have a complete thermodynamic picture of NarGHI, it would be necessary to extend the current model to include all other redox cofactors, including quinone and nitrate binding and redox transitions. One example is the very low potential [4Fe-4S] cluster FS2 in NarH which has a measured  $E_{m,7}$  of -420 mV, it may be that the measured  $E_m$  is so low due to

electrostatic interactions with adjacent reduced cofactors and that the microscopic midpoint potential is actually higher than measured <sup>213</sup>.

### 3.4. Summary

In summary, we have shown that the non-ideal Nernstian redox titration curves for hemes  $b_D$ ,  $b_P$  and FS4 in the Q-site inhibitor bound state can be modeled as arising from anti-cooperative electrostatic interactions between these cofactors. We were able to satisfactorily fit the redox titrations with a model that includes  $E_m$  values and pairwise interactions between adjacent cofactors. Importantly, by modeling NarGHI redox cofactor thermodynamics in the frame of redox cooperativity, we obtain values significantly different from those previously reported, particularly for heme  $b_P$ , providing an alternative perspective on electron-transfer thermodynamics in the NarGHI system (**Figure 3.5**), and shedding light on inhibitor binding effects and a functional role for these electrostatic interactions in electron-transfer through NarI in the presence of an electrochemical gradient.

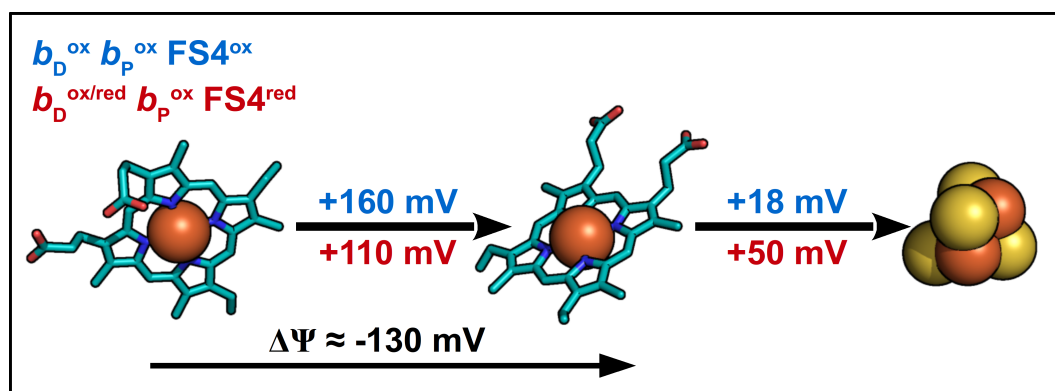


**Figure 3.5: Summary of energetics of electron flow through  $b_D$ ,  $b_P$ , FS4 system**

### 3.5. Supplementary Material

The supplementary figures include the equations utilized in modeling the redox titrations as well as the plotted residuals of the titrations depicted in **Figure 3.3**.

Titration Details	$b_D E_m^a$ (mV)	$b_P E_m^a$ (mV)	FS4 $E_m^{a,b}$ (mV)	pH <sup>d</sup>	Spectroscopic Technique	Reference
NarGHI	+17	+122	—	7.0	optical	269
	—	+110	—	7.0	EPR	268
	—	—	+180 (69%) +95 (31%)	8.0	EPR	232
	+20	+120	+195 (70%) +95 (30%)	7.0	EPR	270
	+28	+125	—	7.0	optical	270
	-5	+108	+185 (70%) +100 (30%)	7.0	EPR	271
	-15	+110	+180	6.5	EPR	297
	-35 <sup>c</sup>	—	—	8.0	EPR	321
NarGHI +0.5 mM HOQNO	+120	+60	+200 (70%) +110 (30%)	7.0	EPR	270
	+100	+40	—	7.0	optical	270
NarGHI + 0.3 mM Stigmatellin	+50	+120	+200 (70%) +105 (30%)	7.0	EPR	270
NarI( $\Delta$ GH)	+37	-178	—	7.0	EPR	270
	+30	-178	—	7.0	EPR	271
NarGHI-K86A	+40	+80	—	7.5	EPR	284

#### Supplementary Table 3.1: Previously reported midpoint potentials for the hemes and [3Fe-4S] cluster for vesicle preparations of *E. coli* nitrate reductase

**A pertinent to this study** **a** – All cited potentials were derived from  $n = 1$  Nernstian fits. **b** – The percent contribution to the titration of the respective components is indicated in parentheses. **c** – This is specifically the potential for the  $g = 3.34$  component of heme  $b_D$ . **d** – Further pH titration data can be found in reference 271.

### The thermodynamic models for NarGHI hemes $b_D$ , $b_P$ and FS4

$$\begin{aligned}
 p_1 &= 1 \\
 p_2 &= \exp\left(\frac{nF}{RT} \cdot (E_m A - E_h)\right) \\
 p_3 &= \exp\left(\frac{nF}{RT} \cdot (E_m B - E_h)\right) \\
 p_4 &= \exp\left(\frac{nF}{RT} \cdot (E_m C - E_h)\right) \\
 p_5 &= \exp\left(\frac{nF}{RT} \cdot (E_m A + E_m B + e_{AB} - 2 \cdot E_h)\right) \\
 p_6 &= \exp\left(\frac{nF}{RT} \cdot (E_m A + E_m C + e_{AC} - 2 \cdot E_h)\right) \\
 p_7 &= \exp\left(\frac{nF}{RT} \cdot (E_m B + E_m C + e_{BC} - 2 \cdot E_h)\right) \\
 p_8 &= \exp\left(\frac{nF}{RT} \cdot (E_m A + E_m B + E_m C + e_{AB} + e_{AC} + e_{BC} - 3 \cdot E_h)\right)
 \end{aligned}$$

$$[abc] = \frac{p_1}{\sum_{i=1}^8 p_i}$$

$$[abc] = \frac{p_4}{\sum_{i=1}^8 p_i} \quad [aBc] = \frac{p_3}{\sum_{i=1}^8 p_i} \quad [Abc] = \frac{p_2}{\sum_{i=1}^8 p_i}$$

$$[aBC] = \frac{p_7}{\sum_{i=1}^8 p_i} \quad [AbC] = \frac{p_6}{\sum_{i=1}^8 p_i} \quad [ABC] = \frac{p_5}{\sum_{i=1}^8 p_i}$$

$$[ABC] = \frac{p_8}{\sum_{i=1}^8 p_i}$$

$$[a] = [abc] + [aBc] + [Abc] + [ABC]$$

$$[b] = [abc] + [Abc] + [aBC] + [AbC]$$

$$[c] = [abc] + [Abc] + [aBc] + [ABC]$$

**Supplementary Figure 3.1: Three-center redox model for NarGHI.** As diagrammed in Figure 3.2A and used for fits A-E of Figure 3.3, see next page for description.

$$\begin{aligned}
 p_1 &= 1 \\
 p_2 &= \exp\left(\frac{nF}{RT} \cdot (E_m A - E_h)\right) \\
 p_3 &= \exp\left(\frac{nF}{RT} \cdot (E_m B - E_h)\right) \\
 p_4 &= \exp\left(\frac{nF}{RT} \cdot (E_m A + E_m B + e_{AB} - 2 \cdot E_h)\right)
 \end{aligned}$$

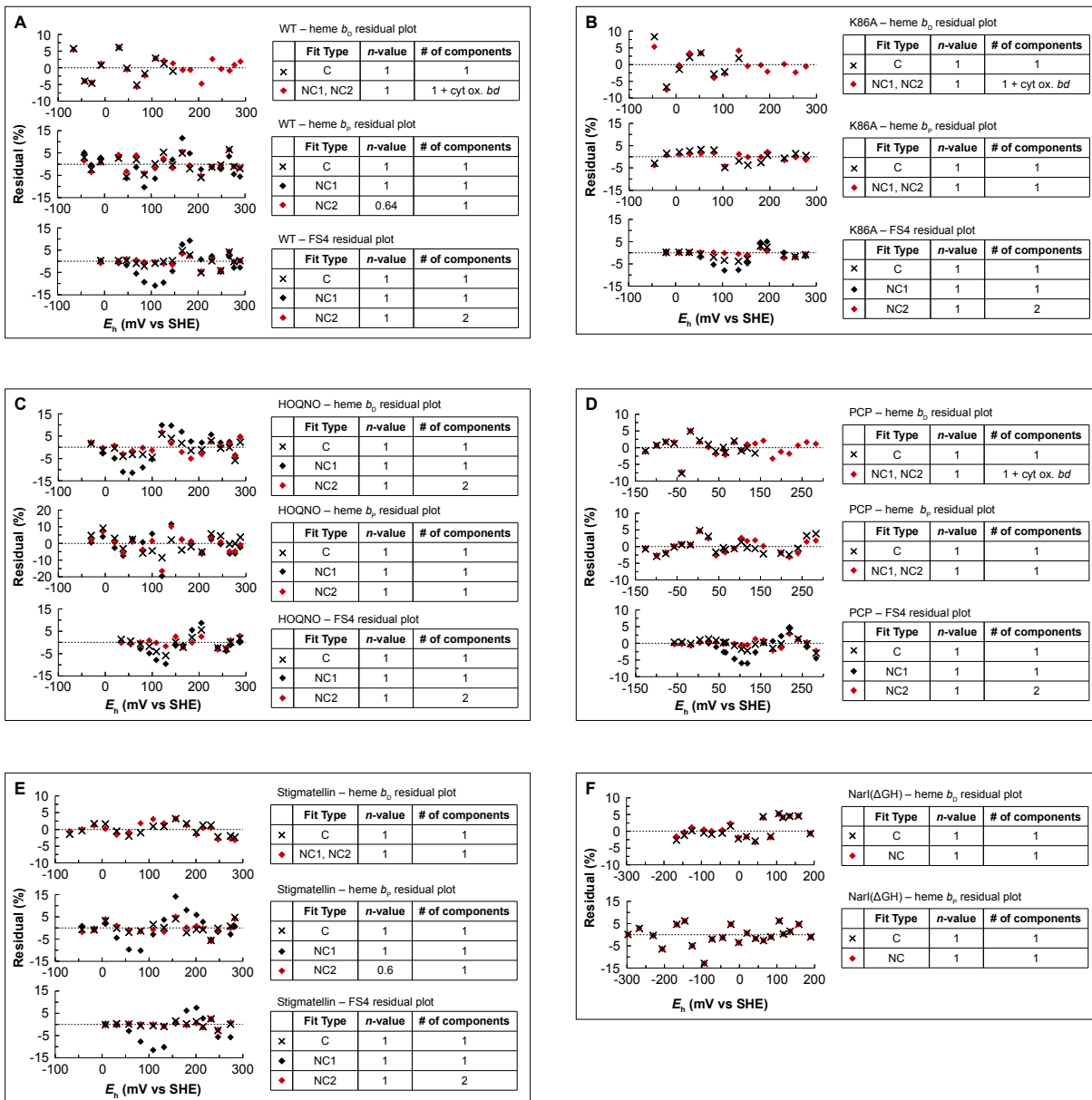
$$[ab] = \frac{p_1}{\sum_{i=1}^4 p_i} \quad [Ab] = \frac{p_2}{\sum_{i=1}^4 p_i} \quad [aB] = \frac{p_3}{\sum_{i=1}^4 p_i} \quad [AB] = \frac{p_4}{\sum_{i=1}^4 p_i}$$

$$[a] = [ab] + [aB] \quad [b] = [ab] + [Ab]$$

**Supplementary Figure 3.2: Two-center redox model for NarI( $\Delta$ GH).** As diagrammed in Figure 3.2B and used for fit F of Figure 3.3, see next page for description.

## Description of redox models

The constants used in the equations in **Supplementary Figures 3.1** and **3.2** are:  $R$ , the universal gas constant ( $8.314 \text{ V} \cdot \text{C} \cdot \text{K}^{-1} \cdot \text{mol}^{-1}$ ), Faraday's constant ( $F$ ) ( $96485.3 \text{ C} \cdot \text{mol}^{-1}$ ), the absolute temperature ( $T$ ) of 295 K, and  $n$  is the electron stoichiometry for each individual redox reaction ( $n = 1$ ).  $E_h$  is the applied potential,  $E_m$  values are the midpoint potentials of the generic cofactors A, B, C, and the interaction potentials are depicted as the variables  $e_{AB}$ ,  $e_{BC}$ ,  $e_{AC}$  respectively denoting an interaction between the specified cofactors, all in Volts (as outlined in **Figure 3.2**). The probability of finding a given configuration of the system – as described in the square brackets – is given by the middle portion of equations. Lower case letters (a,b,c) indicate an oxidized state, whereas uppercase letters denote reduction by a single electron, where  $A = b_D$ ,  $B = b_P$ ,  $C = \text{FS4}$ . The last block of equations are used to simulate the titration for the given cofactor, taking into account microstates of the system where only the oxidized (EPR visible) state of the given cofactor is considered<sup>10,320</sup>.



**Supplementary Figure 3.3: Residual plots for the fits depicted in Figure 3.3.**

Each panel (A-F) contains an individual plot of the residuals as a function of applied potential ( $E_h$ ) for each cofactor. Each plot is identified by the accompanying legend table to its right. Within the tables, “C” denotes the cooperative model fit and “NC” denotes noncooperative fits. For instances where there is an apparent  $n$ -value other than unity or more than one Nernstian component is used to make a fit, both the modified noncooperative fit as well as an idealized noncooperative fit ( $n = 1$ ; 1 component) is given for comparison. The panels are: (A) WT, (B) K86A, (C) HOQNO-bound, (D) PCP-bound, (E) Stigmatellin-bound, (F) NarI( $\Delta$ GH).

## 4. Quinol Oxidation Progresses Through a Neutral Semiquinone in *E. coli* NarGHI

**A version of this chapter has been submitted for publication:**

Justin G. Fedor, Richard A. Rothery, Joel H. Weiner. Quinol oxidation progresses through a neutral semiquinone in *Escherichia coli* nitrate reductase A. *Biochimica et Biophysica Acta. – Bioenergetics* (BBABIO-15-258)

### **Acknowledgements:**

We would like to thank Dr. Arno Siraki for providing us with TEMPOL and Shannon Murphy for technical assistance. We would also like to thank Dr. Andrei Astashkin for his helpful comments regarding EPR.

## 4.1. Introduction

Quinones are lipophilic  $2e^-/2H^+$  carriers found in the plasma membrane of prokaryotes and the mitochondrial inner membrane and thylakoid membranes of eukaryotes where they are crucial for coupling dehydrogenases to reductases and oxidases <sup>158</sup>. *Escherichia coli* (*E. coli*) is a facultative anaerobe and synthesizes ubiquinone (UQ,  $E_{m,7} \approx +110$  mV) as well as menaquinone (MQ,  $E_{m,7} \approx -70$  mV) and demethylmenaquinone (DMQ,  $E_{m,7} = +36$ ) <sup>2,21,38,325</sup>. The concentrations and relative ratios of UQ, DMQ and MQ vary according to the aeration of *E. coli* cultures. Aerobic respiration favors UQ [60% UQ, 37% DMQ, 3% MQ] whereas naphthoquinones predominate under anaerobic conditions where their lower reduction potentials are better suited to reducing lower potential electron acceptors (nitrate, DMSO, TMAO, fumarate, etc) <sup>21</sup>. Specifically, anaerobic growth on fumarate favors MQ [10% UQ, 16% DMQ, 74% MQ] <sup>41</sup> and growth on nitrate favors DMQ [0% UQ, 70% DMQ and 30% MQ] <sup>21,39,40,313</sup>.

The evaluation of electron paramagnetic resonance (EPR) spectral parameters of semiquinone (SQ) intermediates using multiple microwave wavelengths and pulsed techniques, such as ESEEM (Electron Spin Echo Envelope Modulation) and HYSCORE (Hyperfine Sublevel Correlation), can provide significant detail on binding orientation, magnetic couplings, and hydrogen bonding (H-bonding) partners <sup>166,167,176,326-330</sup>. Furthermore, by conducting redox titrations of the SQ radical over a

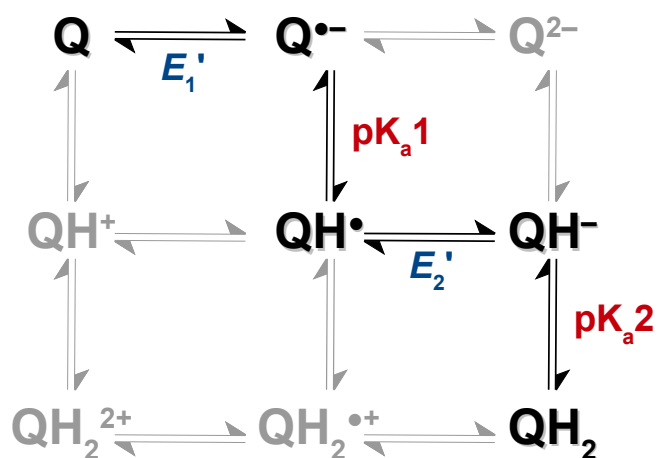


**Figure 4.1: The electrochemical transitions of quinones, with the physiologically relevant pathway from oxidized quinone through semiquinone to quinol indicated in black.** Redox transitions ( $E_1', E_2'$ ) are indicated in blue along the horizontal and protonation events ( $pK_{a1}, pK_{a2}$ ) are labelled in red as vertical transitions.

range of both applied potential and poised sample pH, one can determine  $pK_a$  values and reduction potentials ( $E_1'$ ,  $E_2'$ ) of the quinol to quinone transitions (see **Figure 4.1**)<sup>166,167,326</sup>. This information provides the basis for elucidating the mechanism of SQ stabilization and enzyme catalysed quinol/quinone redox chemistry.

*E. coli* nitrate reductase A (NarGHI) is a highly studied and structurally characterized<sup>19,152,183</sup> enzyme and excellent model system for looking at transmembrane electron and proton transfer<sup>132,278,279</sup>, quinol oxidase mechanism, oxidoreductase maturation<sup>240,252,290,297</sup>, and aspects related to organometallic cofactor function<sup>232,240,254</sup>. It is expressed under low oxygen but high nitrate levels and can oxidize and stabilize the semiquinones of UQ, MQ, and DMQ<sup>45,170,282,293</sup>. NarI is the location of the quinol oxidation site (Q-site) and also binds two *b*-type hemes – *b<sub>D</sub>* is distal to NarGH and *b<sub>P</sub>* is proximal. Electron transfer proceeds via *b<sub>D</sub>*, *b<sub>P</sub>* and a relay of one [3Fe-4S] and four [4Fe-4S] clusters in NarGH and finally to the molybdenum cofactor (Mo-bis(pyranopterin guanine dinucleotide) in NarG where nitrate reduction occurs<sup>19</sup>.

**Figure 4.2** shows the crystal structure of the quinone analog pentachlorophenol (PCP) bound to the Q-site of NarI, and adjacent to heme *b<sub>D</sub>* (PDB ID 1Y4Z and 1Y5N)<sup>183</sup>. There is a short H-bond between the hydroxyl group of PCP and propionate D of

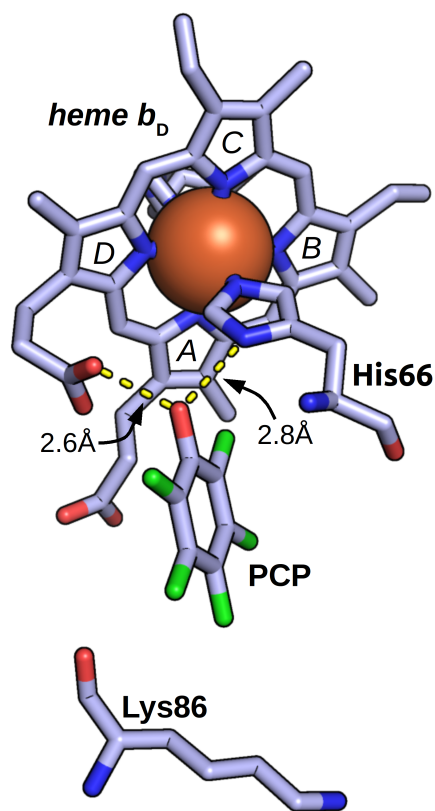


**Figure 4.2: The quinone binding site of NarGHI with the Q-site inhibitor pentachlorophenol (PCP) bound.** The pyrole rings of heme *b<sub>D</sub>* are indicated as per the assignment in the crystal structure (PDB ID 1Y4Z)<sup>183</sup>. Carbons are colored grey, nitrogens blue, oxygens red and chlorines as green. Image created with PyMol<sup>374</sup>.

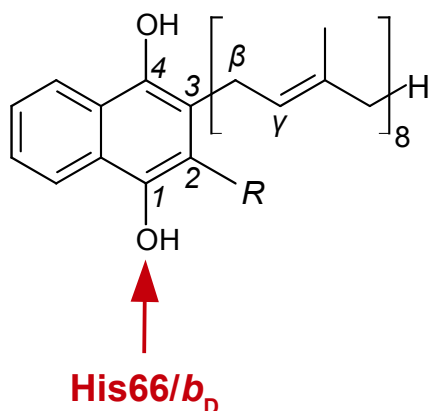


**Figure 4.3: (Demethyl)menaquinol-8**

**structure.** For menaquinol-8, R = -CH<sub>3</sub>; for demethylmenaquinol R = -H. The numbers of relevant carbons in the naphthoquinone head group as well as the  $\beta$  and  $\gamma$  carbons of the first isoprenoid unit are indicated.

heme  $b_D$ , which reflects a similar interaction of propionate D and the O1 of the quinone, as per the numbering in **Figure 4.3**. X-ray crystallography as well as ESEEM and HYSCORE demonstrate that His66 not only acts as an axial ligand for heme  $b_D$  but also forms a weak in-plane H-bond (1.6Å) with the bound MSQ, DMSQ, and USQ <sup>45,168,170,176,183,270,282,284</sup>. Additionally, a recent study by our lab of the pre-steady state reduction of the hemes by menadiol has implicated the heme  $b_D$  propionate D in deprotonating the SQ O1 <sup>331</sup>. However, while considerable work has gone into determining

SQ binding mode and quinol oxidation, many questions remain before we have a fully descriptive view of quinol binding and oxidation in NarGHI.

In this study we investigated the pH dependence of the low-potential SQ radical and determined the factors governing its stability in membranes enriched in NarGHI or NarI( $\Delta$ GH). Membranes enriched in NarI( $\Delta$ GH) have a greater concentration of NarI, and thus Q-sites, with the expectation of yielding better SQ EPR signals <sup>270</sup>, and it has been previously demonstrated that the SQ  $E_m$  is only slightly perturbed (by approximately +30 mV) in NarI( $\Delta$ GH) relative to the radical stabilized in NarGHI, and that the EPR signals are similar, apart from partially resolved splittings ( $\sim$ 11 G or 4 G<sub>pp</sub>) in the NarI( $\Delta$ GH) SQ EPR signal (see **Figure 4.4**) <sup>284</sup>. Our results indicate not only that the SQ bound to NarGHI and NarI( $\Delta$ GH) is neutral, but also that quinone binding to NarI is dependent on the protonation state of an ionizable residue with a pK<sub>a</sub> of approximately 7.

## 4.2. Materials and Methods

*Bacterial strains, plasmids, membrane vesicle preparation* – Wild-type NarGHI was overexpressed in *E. coli* strain LCB79 (*araD139*  $\Delta$ (*lacI*-POZYA-*argF*) *rpsL*, *thi*,  $\Phi$ 79(*nar-lac*))<sup>298</sup>, which is deficient in *narGHJI*, complemented with the plasmid pVA700 (*tacP*, *rrnB*, *lacI*<sup>q</sup>, *amp*<sup>r</sup>, *narGHJI*)<sup>268</sup>. For overexpression of NarI alone the plasmid pCD7 (*tacP*, *rrnB*, *lacI*<sup>q</sup>, *narI*) was used<sup>268</sup>.

*Cell culturing and preparation of membrane vesicles* – The cells were cultured in 2 L batches of Terrific Broth<sup>301</sup> in 6 L non-baffled Erlenmeyer flasks containing 100 mg L<sup>-1</sup> ampicillin, 100 mg L<sup>-1</sup> streptomycin and a 10% inoculum of an overnight stationary culture. Growth conditions for the expression culture included low aeration (100 rpm shaking) at 30°C overnight and induced with 1 mM IPTG. For NarI( $\Delta$ GH) enriched membranes, LCB79/pCD7 was cultured identically to LCB79/pVA700, except for the use of 6 L baffled flasks, a higher aeration (150 rpm), and a 4 hour incubation at 37°C<sup>278</sup>. Harvested cells were then rinsed and suspended in 100 mM MOPS, 5 mM EDTA, pH 7 and supplemented with the serine protease inhibitor phenylmethanesulfonyl fluoride (PMSF) at a final concentration of 0.2 mM. Crude membranes were obtained after 3-4 passages through an Emulsiflex followed by differential centrifugation and a 55% (w/v) sucrose bed step to obtain NarGHI-enriched inner membrane vesicles, as detailed previously<sup>270,321</sup>. Membranes were diluted to a final concentration of about 30 mg mL<sup>-1</sup> and stored at -70°C.

*Determination of protein and heme concentration* – Protein concentrations of NarGHI and NarI-enriched inner membrane vesicles was determined by the method of Lowry<sup>307</sup>, but with the inclusion of 1% (w/v) SDS for solubilization of membrane proteins<sup>306</sup>. Heme content was determined at pH 7.0 by measuring the reduced-minus-oxidized intensity of the alpha band at 559 nm minus  $A_{575}$ . The extinction coefficient of  $\epsilon_{559-575} = 14.8 \text{ mM}^{-1} \text{ cm}^{-1}$  was used to calculate the concentration of NarI-bound heme *b* and agrees with previously published values for heme *b*<sub>559</sub><sup>332</sup>.

*Redox potentiometry and EPR spectroscopy* – Redox titrations were conducted under

an argon atmosphere, as previously described<sup>270,303</sup>, and with the following redox dyes: 2,6-dichlorophenolindolphenol (+217 mV), 1,2-naphthoquinone (+125 mV), toluylene blue (+115 mV), phenazine methosulfate (+80 mV), thionine (+60 mV), methylene blue (-11 mV), resorufin (-50 mV), indigo trisulfonate (-80 mV), indigo carmine (-125 mV), anthraquinone-2-sulfonic acid (-225 mV), phenosafranine (-255 mV), neutral red (-329 mV)<sup>270,303</sup>. In addition to 5 mM EDTA, the buffers used were 100 mM MES (pH 6.0), 100 mM MOPS (pH 7.0), 100 mM Tricine (pH 8.0), and 100 mM CHES (pH 9.0). EPR samples were taken every 10-20 mV by transferring 200  $\mu$ L into 3.0 mm (ID) quartz EPR tubes, frozen in liquid nitrogen chilled ethanol and stored at  $\sim$ 63 K. All potentials reported are relative to the standard hydrogen electrode. EPR spectra of the semiquinone was acquired using a Bruker Elexsys E500 series X-band EPR spectrometer (9.43 GHz) with a Bruker SHQE microwave cavity and a Bruker ER4131 Variable Temperature Unit utilizing liquid nitrogen to maintain a temperature of 225 K. To ensure the  $\text{Nar}(\Delta\text{GH})$  semiquinone signals were not saturated a power attenuation of 40 dB (0.02 mW) with a field modulation of 2  $G_{\text{pp}}$  at 100 kHz was used and 5 scans were averaged. Aqueous TEMPOL (4-Hydroxy-2,2,6,6-tetramethylpiperidine 1-oxyl) was used as a standard ( $\epsilon_{429.9} = 13.4 \pm 0.6 \text{ M}^{-1} \text{ cm}^{-1}$ ) for spin quantification of the semiquinone and EPR spectra were acquired under identical conditions to the semiquinone, except for a larger sweep width<sup>304,333</sup>. Fitting of the data was conducted using Matlab (version 2014b, The MathWorks Inc., Natick, MA) and a model where the electrochemistry of the quinone, **equations 4.1-4.3**<sup>166,167</sup>, as well as pH-dependence of Q-site occupancy, **equation 4.4**<sup>334</sup>, are considered.

$$[\text{SQ}] = \frac{Q_{\text{occ}}}{\left[1 + 10^{(E_n - E_1)/59} + 10^{(E_2 - E_n)/59}\right]} \quad (4.1)$$

Where [SQ] is the concentration of the semiquinone,  $Q_{\text{occ}}$  is the Q-site occupancy,  $E_n$  is the applied potential (mV),  $E_1$  is the potential for the Q/SQ transition and  $E_2$  is the SQ/QH<sub>2</sub> transition. For a given pH,  $E_1$  and  $E_2$  are in turn governed by **equations 4.2** and **4.3**.

$$E_1 = E_1' + (2.3 RT/F) \log_{10} (1 + 10^{pK_{a1} - pH}) \quad (4.2)$$

$$E_2 = E_2' + (2.3 RT/F) \log_{10} \frac{(1 + 10^{pK_{a2} - pH})}{(1 + 10^{pH - pK_{a1}})} \quad (4.3)$$

Where  $E_1'$  is the  $Q/Q^{\cdot-}$  transition and  $E_2'$  is the  $QH^{\cdot}/QH^-$  transition and  $pK_{a1}$  governs the equilibrium for  $Q^{\cdot-}/QH^{\cdot}$  and  $pK_{a2}$  governs the equilibrium for  $QH^{\cdot}/QH_2$ .

$$Q_{occ} = \frac{LH_{occ}(10^{-pH}) + L_{occ}(10^{-pK_{a}Nar})}{10^{-pH} + 10^{-pK_{a}Nar}} \quad (4.4)$$

In the simplest case, the pH dependence of Q-site occupancy can be viewed as being dependent on a single protonatable residue within the protein with a particular  $pK_a$  ( $pK_aNar$ ) with parameters denoting the Q-site occupancy when this residue is protonated ( $LH_{occ}$ ) and deprotonated ( $L_{occ}$ ). Least squares fitting was conducted using a MatLab script that utilized a Trust-Region-Reflective algorithm. Iterative fits were conducted using a set value of  $E_1' - E_2'$  (quinone stability) and allowing the parameters  $E_m'$ ,  $pK_{a1}$ ,  $pK_{a2}$ ,  $LH_{occ}$ ,  $L_{occ}$  and  $pK_aNar$  to float within a generously set range of bounds. Using this procedure a global minimum for each set of titrations was

Parameter	MSQ NarGHI	DMSQ + MSQ NarI( $\Delta$ GH)
$E_m'$ (mV)	-125 $\pm$ 2	-138 $\pm$ 5
$E_1' - E_2'$ (mV)	-40 $\pm$ 10	26 $\pm$ 7
$pK_{a1}$	8.71 $\pm$ 0.06	9.2 $\pm$ 0.1
$pK_{a2}$	7.30 $\pm$ 0.09	8.41 $\pm$ 0.09
$L_{occ}$ (Q/Nar)	0.16 $\pm$ 0.02	0.142 $\pm$ 0.008
$LH_{occ}$ (Q/Nar)	0.034 $\pm$ 0.005	0.075 $\pm$ 0.005
$pK_aNar$	6.9 $\pm$ 0.1	7.1 $\pm$ 0.1

**Table 4.1: Fitting parameters for the low potential semiquinone EPR signals of NarI( $\Delta$ GH) and NarGHI enriched vesicles** The fitting parameters for MSQ-NarGHI are for **Figure 4.5** and those for DMSQ-NarI( $\Delta$ GH) correspond to **Figure 4.6**.

determined. The values for the parameters as well as their fitting error (standard error) are summarized in **Table 4.1**.

### 4.3. Results

To ensure consistency between membrane samples for individual redox titrations of NarGHI and NarI( $\Delta$ GH), we prepared three batches of membranes per set, pooled them, then split them evenly and poised the samples at pH values of 6.0, 7.0, 8.0 or 9.0. Lowry and heme optical assays used for normalization of the EPR data confirmed equivalent protein concentrations between the split samples. **Figure 4.5** depicts a representative set of titrations of MSQ at four pH values of NarGHI-enriched membranes. As expected for protein-bound semiquinones, the signal intensity increases with increasing pH<sup>166,167</sup>. However, pH 9.0 has a lower signal intensity than expected and a similar titration width compared to pH 8.0. This phenomenon was consistently observed not only for NarGHI but also for NarI( $\Delta$ GH) samples (**Figure 4.6**). To account for this, a pH dependence for Q-site occupancy was included in the model (see **equation 4.4**). The SQ redox titrations for all pH values were simultaneously fit for the quinone parameters  $E_m'$ ,  $E_1'-E_2'$ ,  $pK_{a1}$ ,  $pK_{a2}$  and

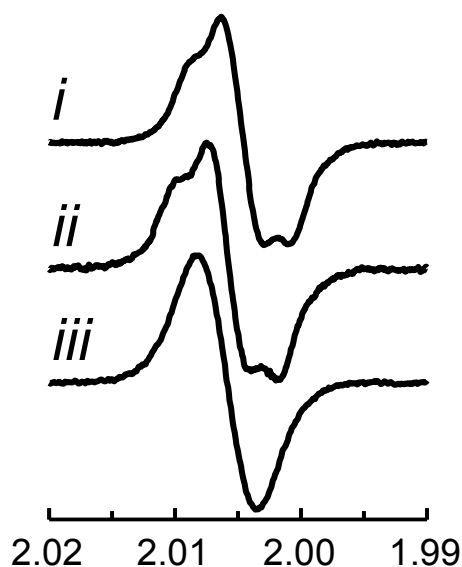


**Figure 4.4: Representative EPR spectra of the maximal intensity semiquinone signals for NarI( $\Delta$ GH) and NarGHI.** (i) NarI( $\Delta$ GH)-enriched membranes [-82 mV; 225 K; 2.0 Gpp modulation amplitude; 30 dB (0.2 mW)], (ii) more aerobically derived NarGHI-enriched membranes [-87mV; 150 K; 3.0 Gpp modulation amplitude; 30 dB (0.2 mW)], and (iii) anaerobically derived NarGHI-enriched membranes [-120 mV; 150 K; 2.83 Gpp modulation amplitude; 30 dB (0.2 mW)].

the Q-site parameters  $L_{occ}$ ,  $LH_{occ}$ , and  $pK_aNar$ , see Methods section for more details. **Table 4.1** summarizes the fitting parameters which gave a fit with an adjusted coefficient of determination (adjusted  $R^2$ ) of 0.94 and 0.95 for NarGHI and NarI( $\Delta$ GH), respectively. **Figure 4.7** summarizes the  $E_1$ ,  $E_2$  and  $E_m$  values of NarGHI MSQ and NarI( $\Delta$ GH) DMSQ titrations as well as the simulated  $E_m$  curves from the fitting results. All available experimental semiquinone  $E_m$  values for nitrate reductase are also included in **Figure 4.7**.

Overall, the SQ bound to NarI( $\Delta$ GH) ( $E_{m,7} = -32$  mV) titrates with an  $E_{m,7}$  30 mV higher than MSQ bound to NarGHI ( $E_{m,7} = -61$  mV) (**Figure 4.7A**), and the partially resolved splittings in the EPR spectra are consistent with this quinone being a DMQ

45,284

The values for  $pK_{a1}$  and  $pK_{a2}$  we report in **Table 4.1** are similar to those

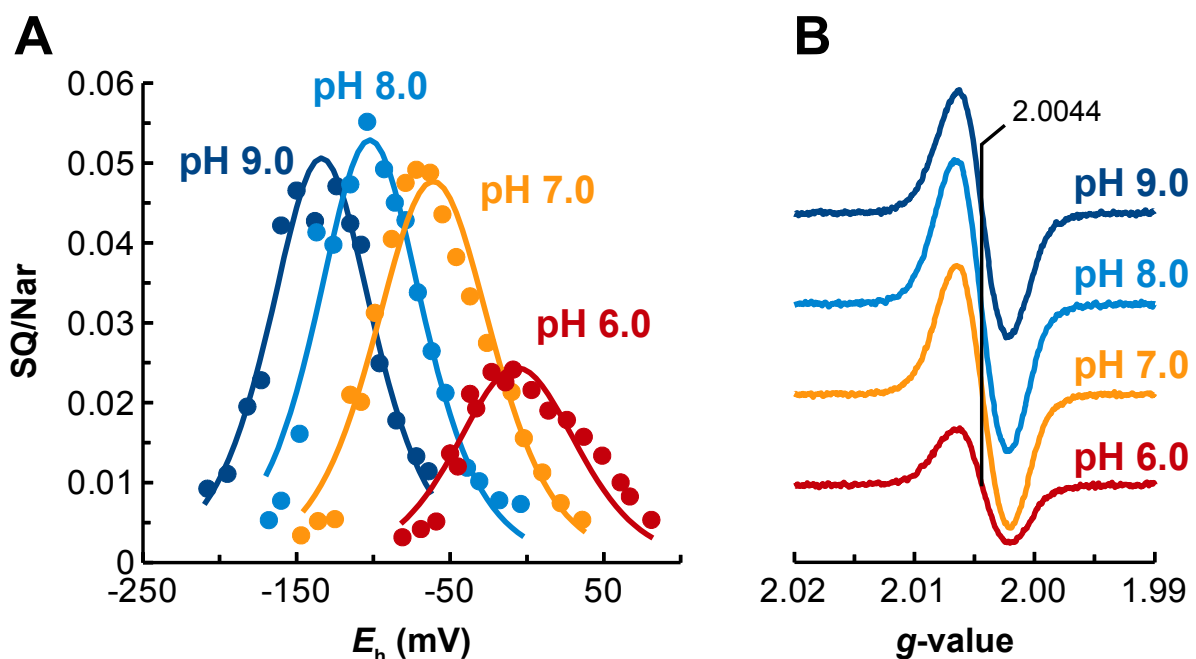


**Figure 4.5: pH dependence of the NarGHI MSQ.** (A) A representative set of titrations of NarGHI-enriched membranes from micro-aerobically grown cells at pH values 6.0, 7.0, 8.0 and 9.0. The resultant fitting parameters are found in **Table 4.1**. (B) Representative maximal intensity NarGHI-associated MSQ X-band EPR signals at various pH values. The spectra are normalized to heme concentration and the poised potentials for samples at pH 6, 7, 8 and 9 are -9 mV, -72 mV, -104 mV and -150 mV, respectively. Spectra were acquired as described in Methods and Materials.

reported for USQ bound to *E. coli* cytochrome *bd*<sup>167</sup> and cytochrome *bo*<sub>3</sub><sup>166</sup>, however in the case of NarGHI and NarI( $\Delta$ GH), the  $pK_{a1}$  is greater than  $pK_{a2}$ , whereas in cytochromes *bd* and *bo*<sub>3</sub>, the opposite is the case. Using the  $pK_a$  parameters for NarGHI, it is expected that at pH 7.0, 2% of the semiquinone is anionic (deprotonated) and 98% is neutral (protonated), indicating that the semiquinone is coupled to an exchangeable proton, as previously demonstrated by pulsed EPR<sup>45,168</sup>. The  $E_{m,7.5}$  of -83 mV is within experimental error of the previously published value of -95 mV however the  $K_{Stab}$  at pH 7.5 we report, 2.3-5.9, is smaller than the previously reported value range of 33-158<sup>45,281</sup>. We also report a pH dependence of Q-site occupancy with a  $pK_{aNar} \sim 7$ , where in the set of titrations depicted in **Figure 4.5** ( $pK_{aNar} = 7.0$ ) the occupancy goes from a maximal value at pH 9 of 16% MQ/NarI to a minimal value at pH 6 of 5% MQ/NarI. The Q-site occupancy at pH 7.5 is expected to be 13% MQ/NarI, which is within the range reported by Rendon et al., (10-15%)<sup>45</sup>.

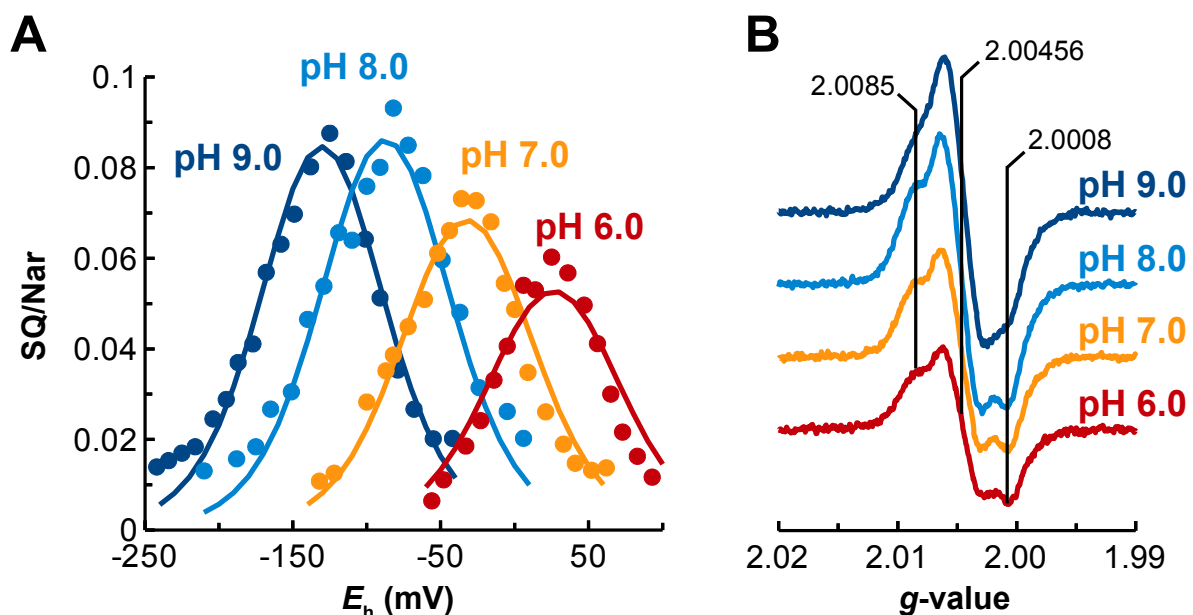


**Figure 4.6: pH dependence of the NarI( $\Delta$ GH) DMSQ.** (A) A representative set of titrations of NarI( $\Delta$ GH)-enriched membranes from aerobically grown cells at pH values 6.0, 7.0, 8.0 and 9.0. The resultant fitting parameters are found in **Table 4.1**. (B) Representative maximal intensity NarI( $\Delta$ GH)-associated DMSQ X-band EPR signals from pH 6 to 9. The spectra are normalized to heme concentration and the poised potentials for samples at pH 6, 7, 8 and 9 are +25 mV, -36 mV, -82 mV, and -125 mV. Spectra were acquired as described in Methods and Materials.

The pH dependence of the MSQ and the Q-site occupancy results in a maximal amount of EPR visible semiquinone at around pH 8.0 where the measured maximum SQ/Nar ratio is 5.5%.

In the system comprising NarI( $\Delta$ GH) and DMQ, interpretation of the semiquinone is more complex due to contributions from both DMQ and MQ. However, large degrees of splitting were observed indicating this system mostly represents NarI with DMQ bound, which is consistent with the highly aerated cultures from which these membranes are derived. The  $pK_{a1}$  and  $pK_{a2}$  values were both slightly higher than seen for MQ-NarGHI and the stability of the semiquinone was notably higher in this system, 15-23. The  $E_{m,7.5}$  of -61 mV is within experimental error of the reported value of -74 mV and we determined similar  $pK_{aNar}$  and occupancy levels as the NarGHI system (**Table 4.1**). In the NarGHI enriched membranes we did not observe any obvious changes in SQ EPR spectra over the pH range tested (**Figure 4.5B**),

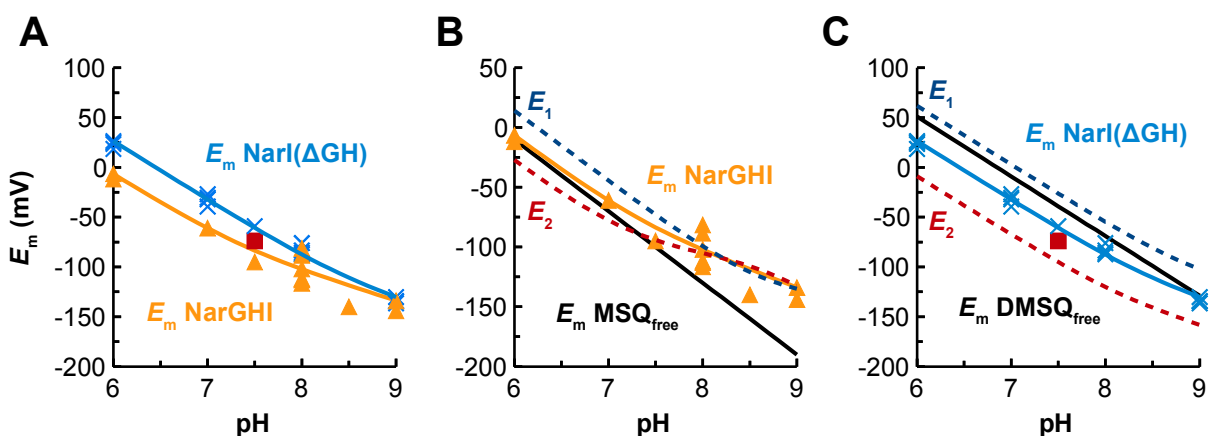


**Figure 4.7: Midpoint potential data from 31 redox titrations of nitrate reductase-associated naphthosemiquinones.** Simulation-derived fits of  $E_m$  for DMSQ and MSQ based on fitting parameters from **Figures 4.5 and 4.6** and **Table 4.1**. Blue 'X's represent  $E_m$  values of NarI( $\Delta$ GH)-associated SQ (one literature value at pH 7.5)<sup>281</sup>, the red square (■) corresponds to a literature value for the  $E_m$  of NarGHI-associated DMSQ<sup>45</sup>, and yellow triangles (▲) correspond to NarGHI-associated semiquinone  $E_m$  values (two literature values at pH 7.5 and 8.5)<sup>281,282</sup>. **(A)**  $E_m$  trends with respect to the data set. **(B)** MSQ-NarGHI  $E_1$ ,  $E_2$  and  $E_m$  pH dependence. **(C)** DMSQ-NarI( $\Delta$ GH)  $E_1$ ,  $E_2$  and  $E_m$  pH dependence.  $E_1$  trends are indicated by blue dashed lines (- - -) and  $E_2$  trends by red dashed lines (- - -).

however for NarI( $\Delta$ GH) we observed a diminished degree of splitting with increasing pH, as seen in **Figure 4.6B**, and a minor central g-value shift from  $2.00456 \pm 0.00006$  (pH 6-8) to  $2.0044 \pm 0.0001$  at pH 9.0 (P-value 0.00297), indicating a change in structure of NarI and/or a change in semiquinone binding mode.

Overall the pH-dependence of the semiquinone suggests that it is bound to NarGHI and NarI( $\Delta$ GH) as a neutral (protonated) form, based on the  $pK_a$  values being  $>7$ . Furthermore, while the occupancy states are dependent on the individual preparations, the  $pK_a$ Nar is consistently measured as being  $7.1 \pm 0.2$  over 4 sets of pH-series redox titrations.

## 4.4. Discussion

### Hypothetical origin for the observed splitting in DMSQ EPR spectra

The EPR signals that we observed exhibit a splitting on the order of  $4 G_{pp}$  (11 MHz) (**Figure 4.4**) for both the NarI( $\Delta$ GH) and aerobically-derived NarGHI membrane samples, which are similar to those recently reported for NarGHI-bound DMSQ ( $\sim 15$  MHz)<sup>45</sup>. These splittings were shown to be due to a non-exchangeable proton<sup>45</sup> and based on the pattern and extent of splitting we propose that the origin lies with the two  $\beta$ -methylene protons of the isoprenoid tail. The reason this splitting is not observed in MSQ radicals of NarGHI is due to the presence of the C3 methyl group, whose three extra hydrogens further split the semiquinone EPR signal by  $\sim 5.5$  MHz, thus rendering the signal devoid of obvious splittings at X-band frequencies, as is the case for NarGHI-bound MSQ<sup>168</sup>. Even more significantly, it has been reported that the presence of a methyl group at position C3 in quinones can influence the orientation of the isoprenoid tail in solution<sup>335,336</sup>. If one examines the dihedral angle for  $C\gamma$ - $C\beta$ - $C2$ - $C3$  (**Figure 4.3**) the energetic boundary in going from a perpendicular to parallel conformation of the isoprenoid tail with a C3 methyl group present is  $\sim 6$  kcal mol<sup>-1</sup> but only 1.4 kcal mol<sup>-1</sup> in the absence of a C3 methyl<sup>336</sup>. The quinone head conformation with respect to the isoprenoid tail in turn influences the

isotropic component of the hyperfine coupling constant ( $a_{\text{iso}}$ ), an EPR parameter that quantifies the degree of splitting in the spectrum. When the C $\beta$ -C $\gamma$  is perpendicular to the quinone ring the  $a_{\text{iso}}$  is expected to be 2.0-3.5 MHz, but in the parallel conformation the  $a_{\text{iso}}$  would be 7-8 MHz or greater. Using the McLachland relation,<sup>335,337</sup> in order to account for the 11 MHz splitting we observe the spin density on C2 would have to be 37% for a perpendicular conformation of the isoprenoid tail, but would be a much more reasonable 12% if the isoprenoid were parallel to the naphthoquinone head group. It is therefore conceivable that due to the relative shallowness of the Q-site in NarGHI, the isoprenoid tail of the bound quinone is more free to adopt multiple conformations, such as a more parallel orientation with respect to the naphthoquinone head group, which would produce the large splittings observed for DMSQ in NarGHI.

### Electrochemistry of the semiquinones of NarGHI and NarI( $\Delta$ GH)

In this study we have electrochemically determined that the semiquinone exists predominantly in a protonated (neutral) state with a  $pK_a$  of 8.7. This is in agreement with previous experiments where the critical NarI<sup>Lys86</sup> residue was subjected to site directed mutagenesis studies. We found that not only was His able to substitute for Lys, but anionic residues Glu and Asp were also able to substitute for Lys<sup>331</sup>. This suggests the bound semiquinone is neutral, which appears to be the case, supporting the mechanism we recently outlined<sup>331</sup>.

Throughout the pH range examined, the  $E_m$  of NarGHI-bound MQH<sub>2</sub>/MQ is above the Q-pool  $E_m$  of MQ, as seen in **Figure 4.7B**, where a  $E_{m,7}$  is taken as -70 and a -59 mV pH<sup>-1</sup> dependence is applied. One can calculate the relative affinity for NarGHI for reduced vs oxidized quinone by examining the deviation of the  $E_m$  QH<sub>2</sub>/Q from the expected pool  $E_m$  as per **equation 4.5**<sup>338</sup>.

$$\frac{K_d MQH_2}{K_d MQ} = 10^{\left(\frac{E_m^{\text{bound}} - E_m^{\text{pool}}}{-30}\right)} \quad (4.5)$$

A deviation above the free value indicates preferential binding of  $\text{QH}_2$  and below indicates a preference for binding Q. Therefore, NarGHI has only a slight preference to bind  $\text{MQH}_2$  over MQ with a  $K_d\text{MQH}_2/K_d\text{MQ}$  ratio of 0.5 at pH 7, which is in line with  $\text{MQH}_2$  being the substrate and MQ being the product of NarGHI. Additionally, we report a  $K_{\text{Stab}}$  at pH 7.5 for MSQ of 2.3, which is much lower than the previously reported value of  $\sim 70$ <sup>281</sup> but is in line with the DMSQ of NarGHI  $K_{\text{Stab}}$  at pH 7.5 of 2.5<sup>45</sup>. The value we report puts the NarGHI-MSQ stability more in line with those of other menasemiquinones, such as  $K_{\text{Stab}}$  17 for menadione bound to cytochrome *bd* (pH 9.0)<sup>167</sup> and  $K_{\text{Stab}}$  1.5 for menaquinone bound to quinone-fumarate reductase mutant E29L (pH 8)<sup>339</sup>.

The  $K_{\text{Stab}}$  for DMSQ bound to NarI( $\Delta$ GH) is  $\sim 14$  at pH 7.5 and similar to what has been reported for DMQ bound to NarGHI. The reported  $E_{m,7}$  for free DMQ is reported as either -9 or +36 mV, both values significantly greater than the  $E_{m,7}$  of -138 mV reported herein<sup>38,325</sup>. Using an  $E_{m,7}$  for DMQ of -9 mV, the pH 7.5  $K_d\text{DMQH}_2/K_d\text{DMQ}$  ratio is 5.3 for NarI( $\Delta$ GH) and 15 for DMQ-bound NarGHI<sup>45</sup>. This indicates a preferential binding of oxidized DMQ to both NarGHI and NarI( $\Delta$ GH). The origin of the electrochemical differences between DMQ-bound to NarI( $\Delta$ GH) versus NarGHI is likely related to deviations in the structure of NarI when expressed in the absence of NarGH and the fully active complex. This structural difference is evident from the  $g_z$  value shifts for heme  $b_D$  (3.36 and 3.15) and  $b_P$  (3.76 and 2.92) for NarGHI and NarI( $\Delta$ GH), respectively<sup>270</sup>. The origin of the difference in redox-specific binding affinities for DMQ versus MQ, however, is likely due to the different electrochemical properties of the bound quinones to NarI, as clearly shown from the different  $pK_a$  and  $E_m$  values reported here, and possibly slightly different modes of binding (i.e. isoprenoid tail orientation).

### **pH dependent binding of semiquinones to NarI**

Semiquinones bound to proteins typically exhibit an exponential dependence of SQ concentration on pH, where the SQ stability increases with increasing pH. This

behavior has been observed for semiquinones bound to cytochromes *bd*<sup>167</sup> and *bo*<sub>3</sub><sup>166</sup> of *E. coli* as well as the antimycin-insensitive semiquinone of the *bc*<sub>1</sub> complex<sup>326</sup>. We observed an increasing intensity of the semiquinone EPR signal from pH 6-8, but a decreasing intensity from pH 8-9. In order to account for this behavior we included in our model a pH dependence for total quinone occupancy of the Q-site. The modeled  $pK_a$ Nar was found to be ~7 for both NarGHI and NarI( $\Delta$ GH). The origin of the  $pK_a$ Nar of 7.1 can be limited to His66, Lys86 and heme *b*<sub>D</sub> propionate D (see **Figure 4.1**).

It is very unlikely that  $pK_a$ Nar is due to NarI<sup>Lys86</sup>. While reports exist of lysine residues with  $pK_a$  values near 7<sup>340</sup>, a  $pK_a$  of  $\geq 9.7$  was predicted for Lys86 by subjecting NarGHI to  $pK_a$  analysis by PROPKA3.1<sup>341,342</sup>. Furthermore, a  $pK_a$  of  $>10$  was recently determined by pre-steady state kinetics of heme reduction by menadiol and was assigned to Lys86<sup>331</sup>. This is in agreement with the lack of interactions between Lys86 and the bound quinone by X-ray crystallography and EPR<sup>19,168,170,183</sup>.

The alternatives are His66 and heme *b*<sub>D</sub> propionate D. **Figure 4.1** shows that in crystal structures where the Q-site inhibitor pentachlorophenol (PCP) is bound (PDB IDs 1Y4Z and 1Y5N) both propionate D and His66 are within H-bonding distance of the PCP phenolic oxygen, 2.6 Å and 2.8 Å respectively<sup>183</sup>. In particular, there is continuous electron density (at  $1\sigma$ ) of the PCP phenol and propionate D<sup>183</sup>. Importantly, PCP has been demonstrated to very closely approximate the binding mode of quinones, particularly UQ, as in the structure of polysulfide reductase (PsrABC) with PCP, UQ and MQ bound<sup>181</sup>. While <sup>14</sup>N ESEEM and HYSCORE has been able to verify the interaction of the semiquinone with His66<sup>45,170,282</sup>, the interaction of the quinol/semiquinone and propionate D is based solely on crystallography<sup>183</sup>.

A proper estimate for the  $pK_a$  of His66 was not obtainable with PROPKA3.1, however due to the absence of adjacent positive charges it is unlikely to exhibit a  $pK_a$  close to 7. The histidine/histidinyI  $pK_a$  is 14 and drops by ~2-3 pH units upon ligation to iron, with further modification by the protein environment such that *b*-heme axial

His  $pK_a$ s have been reported in the 8-11 range <sup>81,184,343,344</sup>.

Heme propionates often exhibit  $pK_a$  values near 7 <sup>316–318,343,345</sup> and the involvement of heme propionates in proton-coupled electron transfer has been reported in a number of systems, including heme *a* of cytochrome *c* oxidase <sup>138</sup> and quinol:fumarate reductase from *Wolinella succinogenes* <sup>186</sup>. PROPKA analysis of NarGHI predicts  $pK_a$  values of 5.86 and 7.70 for heme  $b_D$  propionates D and A, respectively <sup>341,342</sup>. We have recently reported a kinetically determined  $pK_a$  of 5.8 from the pre-steady state reduction of the NarI hemes by menadiol <sup>331</sup> and attributed this  $pK_a$  to heme  $b_D$  propionate D. The difference in  $pK_a$  likely arises because of the different conditions of the two techniques, including the inclusion of the mild detergent Thesit in the kinetics study and/or redox mediators in the EPR study, as well as the fact that the two values are derived kinetically versus thermodynamically. Propionate D exhibits the physiologically relevant  $pK_a$  of ~7. The O1 hydroxyl of the incoming quinol would be facing the deprotonated propionate D and an additional H-bond between His66 and its protonated N $\delta$  would be made to O1. The heme  $b_D$  propionate D can then readily transfer the proton from the quinol O1 to the periplasm via the adjacent H-bonding network <sup>183,331</sup>.

Furthermore, due to the redox-Bohr effect, the  $pK_a$  values of both heme propionates and their axial histidinate ligands exhibit oxidation-state dependent  $pK_a$  values, where upon reduction of the heme,  $pK_a$  values for the propionates or axial histidines can increase by 1 pH unit or more <sup>317,318,343,346–348</sup>. Previous work in our lab has demonstrated that heme  $b_D$  exhibits a pH-dependent  $E_m$  of  $-40 \text{ mV pH}^{-1}$  and  $-60 \text{ mV pH}^{-1}$  for  $g_z$  3.34 and 3.18, respectively <sup>278,321</sup>. No  $pK_a$  values could be gleaned from these pH dependence experiments which indicates a complicated pH dependence of the heme due to several ionizable residues in proximity to the heme <sup>343</sup>. The quinone itself is a likely contributor of the pH dependence of heme  $b_D$  <sup>321</sup>. The oxidation state dependent protonation of propionate D may be responsible for the effect where upon reduction of NarGHI the fluorescent semiquinone analog HOQNO binds to the Q-site with an almost 5 fold lower  $K_d$  ( $K_d^{\text{ox}} = 0.34 \text{ }\mu\text{M}$ ;  $K_d^{\text{red}} = 0.07 \text{ }\mu\text{M}$ ) <sup>278</sup>.

This would have probable applicability for proton uptake from the quinol by NarI and its subsequent deposition into the periplasm.

The observation of pH-dependent semiquinone binding to NarGHI is in agreement with previous work regarding Q-site occupancy. Depending on the ambient pH and Q-site occupancy, heme  $b_D$  exhibits heterogeneity in its  $g_z$  EPR spectrum, where two major components are evident:  $g_z$  3.18 and 3.34. We believe the  $g_z$  3.18 component arises from a conformation of the Q-site in which quinone is absent and the  $g_z$  3.34 component arises when quinone is bound<sup>321</sup>. This heterogeneity was found to diminish at high pH where the  $g_z$  3.34 component – the quinone bound conformation – was favored, which agrees with the finding that Q-site occupancy is greatest at high pH. This also correlates with a change in the line shape of the DMSQ EPR signal in NarI( $\Delta$ GH) (**Figure 4.5B**).

To summarize the electrochemical properties of the bound MSQ to NarGHI and DMSQ to NarI( $\Delta$ GH), we found that the semiquinones are predominantly neutral under equilibrium conditions with the  $pK_a$  for the  $Q^{\bullet-}/QH^{\bullet}$  of both being  $\sim 9$ . Furthermore, we noted a pH dependence of quinone binding to the Q-site and report a  $pK_a$ Nar of 7.1 which we assign to propionate D of heme  $b_D$ . Taking into account redox-Bohr effects, this neutral value  $pK_a$  of the Q-site has implications in quinol oxidation and semiquinone stabilization as well as proton release to the periplasm via a proton conduction pathway adjacent to, and partially consisting of, the heme  $b_D$  propionates<sup>183</sup>.

## 5. A Mechanism for Menaquinol Deprotonation in *E. coli* NarGHI

**A version of this chapter has been submitted for publication:**

Justin G. Fedor, Yi Ke Ma, Karissa S. Giraldi, Richard A. Rothery and Joel H. Weiner.  
Quinol Oxidation and Proton Egress in Escherichia coli Nitrate Reductase A.  
*Biochimica et Biophysica Acta – Bioenergetics* (BBABIO-15-235)

**Acknowledgements:**

We would like to thank Francesca Sebastian and Shannon Murphy for technical assistance.

## 5.1. Introduction

In the anaerobic environments of the soil, human gut, and the tissues invaded by pathogenic bacteria, alternative reductases become vital for microbial survival<sup>21,218,219,349–351</sup>. Under anaerobic high-nitrate conditions, *Escherichia coli* couples the oxidation of formate and hydrogen, respectively by formate dehydrogenase N and hydrogenase, to the reduction of nitrate to nitrite by nitrate reductase A (NarGHI) through the quinone pool<sup>17–19,40</sup>. NarGHI faces the cytoplasm and functions as a dimer of heterotrimers<sup>17,226,352</sup>. NarG coordinates a [4Fe-4S] cluster and the molybdo-bis(pyranopterin guanine dinucleotide) (Mo-bisPGD) cofactor – the site of nitrate reduction. NarI is the integral membrane anchor subunit that contains two bis-His coordinated *b*-type hemes, one distal (*b<sub>D</sub>*) and one proximal (*b<sub>P</sub>*) to NarGH. The quinol oxidation site (Q-site) is located adjacent to heme *b<sub>D</sub>* and x-ray crystallography as well as HYSCORE demonstrate that His66 not only acts as an axial ligand for heme *b<sub>D</sub>* but also forms a weak in-plane hydrogen bond (H-bond) with the bound quinol/semiquinone<sup>45,168,170,176,183,270,282,284</sup>. Finally, NarH coordinates one [3Fe-4S] and three [4Fe-4S] centers, and functions to transfer electrons from NarI to NarG.

Apparent from the crystal structures of NarGHI is the presence of a series of conserved water molecules that form a channel leading to the interior of NarI and which lie adjacent to heme *b<sub>D</sub>* (**Figure 5.1**)<sup>353</sup>. These participate in H-bonding interactions with the conserved hydrophilic/ionizable residues Thr143, Ser147, His150, Ser154, Gln87, Asp 152 and the heme *b<sub>D</sub>* propionates<sup>19,183</sup>. This H-bonding network leads from the heme *b<sub>D</sub>* propionate groups to the periplasmic surface of NarI. In lieu of a quinone-bound structure of NarGHI, models for quinone binding have been based on structures of the wild-type (PDB ID 1Y4Z) and the NarGHI<sup>K86A</sup> variant (PDB ID 1Y5N) with the potent Q-site inhibitor pentachlorophenol (PCP) bound<sup>183</sup>. It is evident from these structures that the phenolic oxygen of PCP forms a strong H-bond (inter-oxygen distance: 2.6 Å) to the heme *b<sub>D</sub>* propionate attached to the D-pyrrole of the heme (**Figure 5.1**). This is supported by the observation of continuous electron density between the two at  $1\sigma$ <sup>183</sup>. Thus, we predict that there is a continuous

H-bonding network leading from the C1-OH of the bound quinol to the periplasm, and that this network provides a framework for a mechanism of C1-OH deprotonation.

Elucidation of the mechanism of C4-OH deprotonation is less tractable than that of C1-OH deprotonation. There is a conserved water molecule at the periplasmic limit of the Q-site which participates in H-bonds with the backbone carbonyl oxygens of Thr72 and Gly69. In all but one of the available wild-type crystal structures the terminal amine nitrogen (N $\zeta$ ) of Lys86 is 5.9 Å from the predicted position of the C4-

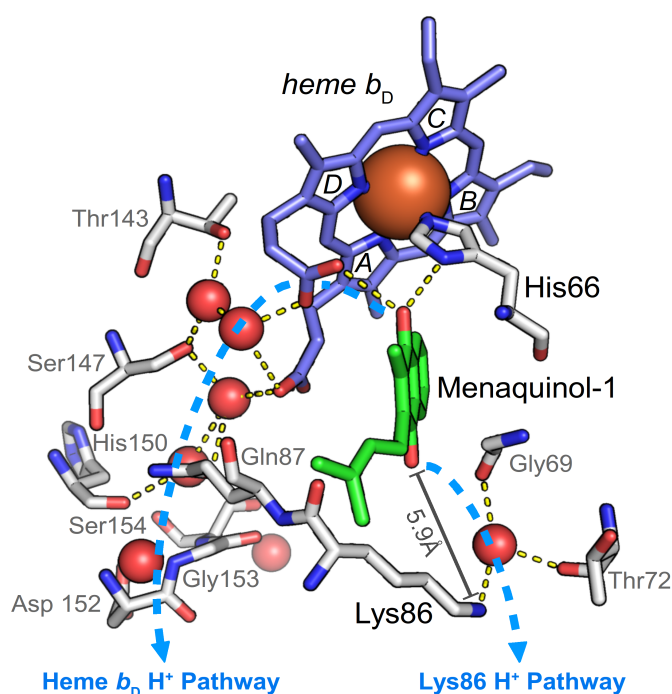


**Figure 5.1: The quinol binding site and proton egress pathways of *E. coli* NarGHI.** The image was generated using PyMOL based on the wild-type crystal structure with the Q-site inhibitor pentachlorophenol (PCP) bound (PDB ID 1Y4Z) but with menaquinol-1 (green) modeled in its place and PyWater to determine crystallographically conserved waters (80%)<sup>183, 353, 374</sup>. Heme  $b_D$  is bis-His coordinated, where one of the ligands, His66, also H-bonds with the phenolic oxygen of PCP and the O1 of the bound quinone. Heme  $b_D$  propionates are identified according to the pyrrole ring of the heme they are bonded to, i.e. propionates D and A. Crystallographically conserved waters are depicted as red spheres and H-bonding interactions are depicted as dashed yellow lines. Residues critical in forming the H-bonding networks are represented as sticks and labelled. The two main pathways of proton egress are highlighted by the bold dashed arrow lines and labelled.

OH of the bound quinol. Also, the lysine N $\zeta$  does not interact directly with the observed semiquinone intermediates of ubiquinone, menaquinone or demethylmenaquinone<sup>45,168,183,282</sup>. However, the NarGHI<sup>K86A</sup> variant exhibits severely impaired quinol:nitrate turnover activity using the hydroxylated menaquinol analog plumbagin as substrate, dropping from 68 s<sup>-1</sup> for the wild-type to 10 s<sup>-1</sup> for the NarGHI<sup>K86A</sup> variant. Further, in this variant menadiol:nitrate reductase activity is completely lost and juglone:nitrate reductase activity is only 2% of that observed for the wild-type<sup>183,284</sup>. The NarGHI<sup>K86A</sup> variant has an increased IC<sub>50</sub> for PCP – 2.5  $\mu$ M *versus* 0.4  $\mu$ M for wild-type – and is unable to bind the quinone inhibitor HOQNO (2-*n*-heptyl-4-hydroxyquinoline-N-oxide) or stabilize semiquinones<sup>183</sup>. As previously proposed the void between PCP and Lys86 suggests that Lys86 may have multiple conformational states, and indeed the weaker electron density and slightly elevated crystallographic temperature factor (B-factor) around the terminus of Lys86 suggests conformational flexibility in the structure<sup>19,183</sup>. Taken together, this line of evidence indicates a role for Lys86 in the initial steps of quinol oxidation and binding. Herein we test the hypothesis that Lys86 abstracts a proton from the quinol C4-OH. We posit that through its conformational flexibility, Lys86 is able to alternately interact with the quinol as well as a set of polar residues and a conserved water which allows conduction of the proton into the aqueous milieu of the periplasm.

## 5.2. Materials and Methods

*Materials* – Quinol analogs plumbagin (5-hydroxy-2-methyl-1,4-naphthoquinol) and menadiol (2-methyl-1,4-naphthoquinone) were obtained from Sigma Aldrich, as was the low catalase glucose oxidase from *Aspergillus niger* (Sigma-Aldrich G0543). Thesit<sup>R</sup> (Polyoxyethylene 9-dodocyl ether) was purchased from Fluka and stored at -80 °C after being rigorously degassed as a 10% (w/v) solution.

*Bacterial strains, plasmids, membrane vesicle preparation* – Wild-type NarGHI was overexpressed in the *E. coli* strain LCB79 (*araD139*  $\Delta$ (*lacI-POZYA-argF*) *rpsL*, *thi*,

$\Phi 79(nar-lac)$  <sup>298</sup>, which is deficient in *narGHJI*, transformed with the plasmid pVA700 (*tacP*, *rrnB*, *lacI<sup>q</sup>*, *amp<sup>r</sup>*, *narGHJI*) <sup>268</sup>.

*Cell culturing and preparation of membrane vesicles* – The cells were cultured in 2 L batches of Terrific Broth <sup>301</sup> in 6 L non-baffled Erlenmeyer flasks containing 100 mg L<sup>-1</sup> ampicillin, 100 mg L<sup>-1</sup> streptomycin and a 10% inoculum of an overnight stationary culture. Growth conditions for the expression culture included low aeration (100 rpm shaking) at 30°C overnight and protein overexpression was induced with 1 mM IPTG <sup>278</sup>. Cells were harvested by centrifugation, were washed by re-suspension in 100 mM MOPS and 5 mM EDTA pH 7.0 and re-centrifugation. The cell pellet was re-suspended in 100 mM MOPS, 5 mM EDTA, pH 7.0 and supplemented with the serine protease inhibitor phenylmethanesulfonyl fluoride (PMSF) at a final concentration of 0.2 mM. Crude membranes were obtained after 3-4 passages through an Emulsiflex, followed by differential centrifugation and a 55% (w/v in 100 mM MOPS and 5mM EDTA, pH 7.0) sucrose bed step to obtain NarGHI-enriched inner membrane vesicles, as detailed previously <sup>270,321</sup>. Membranes were diluted to a final concentration of about 30 mg mL<sup>-1</sup> and stored at -70°C.

*Determination of protein and heme concentration* – Protein concentrations of the NarGHI and NarI-enriched inner membrane vesicles were determined by a modified Lowry method, which included 1% (w/v) SDS for solubilization of membrane proteins <sup>306</sup>. Heme content was determined by measuring the difference between the absorbance in reduced-*minus*-oxidized spectra of the  $\alpha$ -band at 559 nm *minus* the absorbance at 575 nm. A NarGHI specific extinction coefficient of  $\epsilon_{559-575} = 14.8 \text{ mM}^{-1} \text{ cm}^{-1}$  agrees with previously published values for heme  $b_{559}$  <sup>332</sup>.

*Anaerobic growth assays* – The strain *E. coli* strain LCB79 was used as a host and the cells were grown at 37°C in tightly sealed 125 mL Klett flasks on glycerol-nitrate (GN) media supplemented with 100 mg L<sup>-1</sup> Ampicillin, 100 mg L<sup>-1</sup> Streptomycin, 0.003% (w/v) leucine and threonine, since LCB79 is auxotrophic for threonine and leucine. GN media contains 40 mM KH<sub>2</sub>PO<sub>4</sub>, 60 mM K<sub>2</sub>HPO<sub>4</sub>, 15 mM (NH<sub>4</sub>)<sub>2</sub>SO<sub>4</sub>, 187  $\mu$ M MgSO<sub>4</sub>, 2.5  $\mu$ M Fe<sub>2</sub>(SO<sub>4</sub>)<sub>3</sub>, 6.8  $\mu$ M CaCl<sub>2</sub>, 0.05% (w/v) casamino acids,

0.75  $\mu\text{M}$  thiamine hydrochloride, 0.7% (v/v) glycerol, and 40 mM  $\text{KNO}_3$ . Absorbance was measured over time with a Klett spectrophotometer equipped with a red filter. Growth was determined in independent assays with at least four replicates and the ensemble of data was fit with a modified Gompertz model <sup>354</sup>.

$$y = A \exp\left(-\exp\left(\frac{\mu_m e}{A}(\lambda - t) + 1\right)\right) \quad (5.1)$$

where  $A$  is the stationary phase absorbance,  $\mu_m$  is the maximum specific growth rate ( $\text{h}^{-1}$ ) and  $\lambda$  is the lag phase duration (h).

*In vitro activity assays* – For monitoring quinol:nitrate activity, the menaquinol analog plumbagin (5-hydroxy-2-methyl-1,4-naphthoquinol) was used and the assays were carried out as previously described using an HP 8453 UV/Vis spectrophotometer equipped with an HP89090A Peltier temperature controller/cuvette stirrer <sup>277,321</sup>. Briefly, the assays were conducted in 3 mL teflon stoppered acryl cuvettes with inclusion of a stir bar and the buffer consisted of vacuum degassed 100 mM MOPS, 5 mM EDTA, 4 mM  $\text{KNO}_3$ , 30 mM glucose and 0.01% (w/v) Thesit. Stock ethanolic solutions of 20 mM plumbagin were reduced in the presence of  $\sim 70$  mg of  $\text{Zn}^0$  and 190 mM  $\text{HCl}_{(\text{aq})}$  in sealed 2 mL HPLC vials, which were protected from light. Reactions were carried out at  $25^\circ\text{C}$  and included 5  $\mu\text{L}$  of a  $\geq 200$   $\text{U mg}^{-1}$  low catalase ( $\leq 0.1$   $\text{U mg}^{-1}$ ) glucose oxidase ( $24.1$   $\text{mg mL}^{-1}$ ) (Sigma-Aldrich G0543) and 50  $\mu\text{L}$  of plumbagin solution. The reactions included 0.01 – 0.05  $\text{mg mL}^{-1}$  of sample per cuvette,  $\sim 0.4$   $\text{mg mL}^{-1}$  in the case of empty-vector ( $\Delta\text{NarGHI}$ ) control vesicles. Plumbagin  $\lambda_{\text{max}} = 419$  nm,  $\epsilon_{419} = 3.95$   $\text{mM}^{-1} \text{cm}^{-1}$  <sup>277</sup>.

*Pre-steady state kinetics of heme reduction assays* – Stopped-flow kinetics experiments were performed with an Applied Photophysics SX-18MV stopped-flow spectrophotometer equipped with a photodiode array and using Xscan software (Applied Photophysics Ltd. Leatherhead, UK). The pathlength was 1 cm and the instrument dead time was determined to be  $1.12 \pm 0.04$  ms. The buffer systems used consisted of 100 mM Citrate (pH 5.25), 100 mM MES (pH 6.0), 100 mM MOPS (pH

7.0), 100 mM Tricine (pH 8.0, pH 8.64) or 100 mM CHES (pH 9.0, pH 9.47) and 5 mM EDTA, 30 mM glucose, 0.01% Thesit. Added in small batches of degassed buffer was 0.5  $\mu\text{L}$  per mL of  $\geq 200 \text{ U mg}^{-1}$  low catalase ( $\leq 0.1 \text{ U mg}^{-1}$ ) glucose oxidase ( $24.1 \text{ mg mL}^{-1}$ ) (Sigma-Aldrich G0543). Stock 20 mM ethanolic menadiol (2-methyl-1,4-naphthoquinone) was reduced by HCl/Zn<sup>0</sup>, as described above. The buffer was degassed fully on a vacuum line for several hours prior to use and degassed buffer was used to dilute the NarGHI-enriched vesicle samples to  $2 \text{ mg mL}^{-1}$  and menadiol to 0.7 mM and to flush the system thoroughly before experiments. The mixing ratio was 1:1 and thus the final concentrations of protein and menadiol upon mixing were  $1 \text{ mg mL}^{-1}$  and 0.35 mM, respectively. The oxidation state of the hemes of NarI was monitored by measuring the absorbance at 558 nm *minus* that at 575 nm, utilizing the oxidized sample as a reference, for 10 s or 100 s using logarithmic sampling at 23°C. Typically the first 3-4 ms of data was discarded due to mixing artifacts and a (-0.0012 s, 0.0) time correction was added to account for the fact that fully oxidized NarGHI was used as the blank. Using Matlab (version 2014b, The MathWorks Inc., Natick, MA) the signal traces were fit to a two-component exponential decay, as in **equation 5.2**, while a single component was sufficient for the negative control membranes.

$$A_{559-575} = A_1 \exp(-k_{fast} t) + A_2 \exp(-k_{slow} t) + P \quad (5.2)$$

Where  $A_1$  and  $A_2$  are initial points and  $P$  is final plateau reached, both in absorbance units, and  $k_{fast}$  and  $k_{slow}$  are rate constants ( $\text{s}^{-1}$ )<sup>279,283</sup>. The pH dependence of the observed rate constants for wild-type, NarGHI<sup>K86E</sup> and NarGHI<sup>K86H</sup> were modeled using **equation 5.3**<sup>334</sup>.  $\text{H}_2\text{A} \leftrightarrow \text{HA}^- + \text{H}^+$ ;  $K_1 = [\text{HA}^-][\text{H}^+][\text{H}_2\text{A}]^{-1}$



$$k_{obs} = \frac{[\text{H}^+]^2 L_{\text{H}_2\text{A}} + [\text{H}^+] K_1 L_{\text{HA}^-} + K_1 K_2 L_{\text{A}^{2-}}}{K_1 K_2 + [\text{H}^+] K_1 + [\text{H}^+]^2} \quad (5.3)$$

Where  $L_{\text{H}_2\text{A}}$ ,  $L_{\text{HA}^-}$ , and  $L_{\text{A}^{2-}}$  are the rate constants for the various protonation states of the system,  $L_{\text{H}_2\text{A}}$  and  $L_{\text{A}^{2-}}$  were set to zero while  $L_{\text{HA}^-}$  was allowed to float. Data was fit

for the first 0.5 or 2 s using Matlab.

## 5.3. Results

### ***Selection of NarI<sup>Lys86</sup> variants***

In order to test the hypothesis that NarI<sup>Lys86</sup> is involved in quinol deprotonation, we generated and characterized several variants of Lys86: Ala, Met, Arg, Glu, Asp, His, Gln, Asn and Tyr. Of these residues Tyr and His are natural variants of Lys86, and in an alignment of 254 NarI sequences that share <70% sequence identity, Lys86, His86 and Tyr86 occurred with frequencies of 26%, 10% and 58%, respectively. Alignments were conducted with MAFFT alignment software using sequences obtained via Uniprot<sup>355,356</sup>. Residues His, Glu and Asp are ionizable under physiological conditions and therefore would facilitate direct proton transfer whereas Gln, Asn and Tyr can only facilitate proton transfer via H-bond formation to bound water molecules. Being charged residues, Arg and Glu/Asp address the possibility that the role of NarI<sup>Lys86</sup> is for electrostatic stabilization of the semiquinone. Finally, Ala and Met (being of similar dimensions and flexibility to Lys) were chosen as variants expected to lack functionality.

Based on SDS-PAGE, Lowry and heme optical assays, substitutions of Lys86 do not have a significant effect on the expression or assembly of NarGHI. We also do not expect any large changes in structure for any of the variants since no significant deviations were noted in the crystal structure of NarGHI<sup>K86A</sup><sup>183</sup>.

### ***In vivo and in vitro activity of Lys86 variants***

We assessed the *in vivo* function of the Lys86 variants by monitoring their ability to support anaerobic cell growth on a minimal glycerol-nitrate (GN) medium<sup>298</sup>. The host strain for these experiments (*E. coli* LCB79) lacks the *narGHJI* operon, ensuring that the observed plasmid complemented growth was largely NarGHI-

dependent. Residual growth observed in the host strain was due to the expression of periplasmic nitrate reductase, NapAB<sup>208</sup>. The growth curves, seen in **Supplementary Figure 5.1**, were fit with a modified Gompertz equation (**equation 5.1**) and the maximal growth rates ( $\mu_m$ ) for the variants are tabulated in **Table 5.1**. The variants with ionizable residues substituted for Lys86 (NarGHI<sup>K86H</sup>, NarGHI<sup>K86D</sup> and NarGHI<sup>K86E</sup>) supported growth rates similar to that of the wild-type. Variants of residues with side chains of similar size to Lys supported moderate growth (NarGHI<sup>K86M</sup>, NarGHI<sup>K86R</sup>) and polar/small residue variants of Lys86 grew only marginally better than the host strain (NarGHI<sup>K86A</sup>, NarGHI<sup>K86N</sup>, NarGHI<sup>K86Q</sup> and NarGHI<sup>K86Y</sup>).

<b>Variant</b>	<b>Growth Assay<sup>a</sup></b> $\mu_m$ (h <sup>-1</sup> )	<b>Plumbagin:NO<sub>3</sub><sup>-b</sup></b> $\mu\text{mol min}^{-1} \text{nmol heme}^{-1}$
Wild-type	15.4 ± 0.3	3.2 ± 0.1
Asp	16.4 ± 0.7	ND
His	13.8 ± 0.4	2.8 ± 0.1
Glu	10.7 ± 0.3	2.0 ± 0.1
Met	8.5 ± 0.2	0.43 ± 0.01
Arg	7.4 ± 0.1	1.32 ± 0.03
Gln	6.6 ± 0.1	0.52 ± 0.02
Asn	5.6 ± 0.5	ND
Tyr	5.4 ± 0.2	0.43 ± 0.2
Ala	5.0 ± 0.1	0.190 ± 0.005
Negative Control	4.2 ± 0.1	0.073 ± 0.006

**Table 5.1: The *in vivo* and *in vitro* activity of NarGHI Lys86 variants.** The maximal growth rates ( $\mu_m$ ) and specific activity for PBH<sub>2</sub>:NO<sub>3</sub><sup>-</sup> activity. The negative control in the growth assays was untransformed LCB79 while the negative control in the PBH<sub>2</sub>:NO<sub>3</sub><sup>-</sup> activity assays is the activity of  $\Delta$ NarGHI vesicles – vesicles lacking NarGHI. There is four or more replicates and at least biological duplicates of each variant in the growth assay. The PBH<sub>2</sub>:NO<sub>3</sub><sup>-</sup> activity assays were performed in at least triplicate with biological replicates of two or more, depending on the variant. **a** – The mean ± standard error of fitting the Gompertz model to the aggregated data points. **b** – The mean ± standard deviation. ND – Not Determined.

The hydroxylated naphthoquinone plumbagin (PBH<sub>2</sub>;  $E_{m,7}$  = -40 mV) was used as a soluble menaquinol analog to measure *in vitro* steady-state enzyme activities for the Lys86 variants, tabulated in **Table 5.1**<sup>277</sup>. The chemical structures of menaquinol and plumbagin are shown in **Figure 5.2**, the main differences between them being the lack of a long poly-isoprenoid tail and the mono-hydroxylation of the naphthoquinone ring of plumbagin, which increases its solubility relative to menaquinol-8<sup>277</sup>. In

agreement with the *in vivo* growth assays, the most active variants in terms of PBH<sub>2</sub>:NO<sub>3</sub><sup>-</sup> oxidoreductase activity are NarGHI<sup>K86H</sup> (88% of wild-type) and NarGHI<sup>K86E</sup> (63% of wild-type) also supporting substantial activity. Contrary to the growth assay, NarGHI<sup>K86R</sup> exhibited greater PBH<sub>2</sub>:NO<sub>3</sub><sup>-</sup> activity than NarGHI<sup>K86M</sup>, 41% and 13% wild-type respectively. The remaining variants exhibited very low activity ( $\leq 16\%$  wild-type).

The anaerobic growth assays and PBH<sub>2</sub>:NO<sub>3</sub><sup>-</sup> oxidoreductase activity assays suggest that an ionizable residue is required at position 86 in *E. coli* NarI for effective quinol oxidation/binding to occur and that neither the positive charge of Arg nor the similar bulk of the side chains of Met or Tyr are able to support quinol:nitrate oxidoreductase activity.

### Pre-steady state kinetics of heme reduction

To further probe the mechanism of quinol oxidation, we examined the pre-steady state kinetics of quinol-dependent (menadiol;  $E_{m,7}$  = -13 mV) heme reduction using a stopped flow apparatus coupled to a diode array spectrophotometer<sup>279,283,357</sup>.

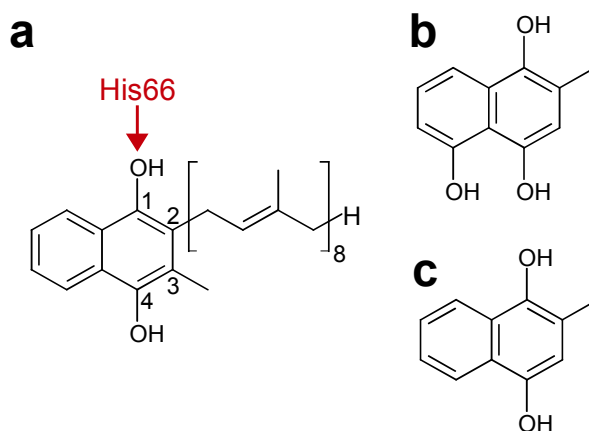


**Figure 5.2: Naphthoquinol substrates of NarGHI.** **a** Menaquinol-8 ( $E_{m,7}$  = -74 mV) is the natural substrate of NarGHI in *E. coli* where as **b** plumbagin ( $E_{m,7}$  = -40 mV), **c** menadiol ( $E_{m,7}$  = -13 mV) are its much more soluble derivatives<sup>21, 277, 357</sup>.

Oxidized NarGHI at 1 mg mL<sup>-1</sup> was used as a time zero blank and the absorbance of the  $\alpha$  peak (559 nm) *minus* that of the background at 575 nm was measured with respect to time. The resulting data trace was fit to a double exponential equation which yields two kinetic constants:  $k_{\text{fast}}$  and  $k_{\text{slow}}$ , for the fast and slow phases of quinol-dependent heme reduction, respectively (see **equation 5.2**). Previously, the stopped flow data for NarI heme reduction was interpreted as having four kinetic phases and an intermediate observed at 390 nm was attributed to the menadiol radical <sup>279</sup>. However, we did not observe such an intermediate under the conditions used in our study. Since these and the previously reported stopped flow assays were conducted in the absence of nitrate, NarGHI builds up charge. Particularly on these short time scales charge builds up on the hemes due to the electron transfer barrier imposed by the low reduction potential of the FS2 [4Fe-4S] cluster of NarH (-420 mV) <sup>213</sup>. We therefore interpreted the kinetic data such that  $k_{\text{fast}}$  represents the initial reduction by the first reducing equivalents of menadiol: menadiol  $\rightarrow$  menadione + 2H<sup>+</sup> + 2e<sup>-</sup>.  $k_{\text{slow}}$  constitutes the subsequent reductions of NarGHI as well as interference

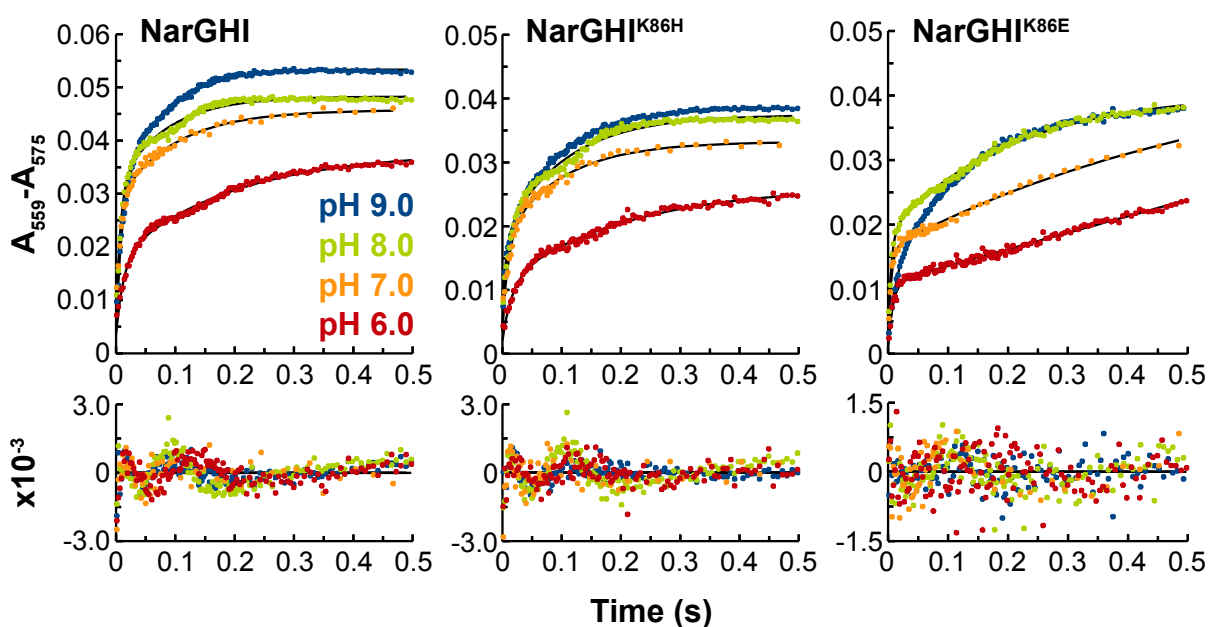


**Figure 5.3: Pre-steady state kinetics of heme reduction.** 1 mg mL<sup>-1</sup> membranes enriched in wild-type NarGHI, NarGHI<sup>K86H</sup> and NarGHI<sup>K86E</sup> was reduced by 0.35 mM menadiol at pH values 6.0, 7.0, 8.0 and 9.0 and monitored by stopped flow kinetics. The data is fit using **equation 2** and the resultant fitting parameters can be found in **Supplementary Table 5.1**.

by the reduction of background cytochromes<sup>332</sup>, photo-reduction of the hemes<sup>358</sup> and a more complex pH-dependence of active site regeneration, i.e. more protonatable residues involved in this step of the reaction. This makes  $k_{\text{slow}}$  more difficult to interpret without a full kinetic and thermodynamic model of NarGHI and hence our focus on  $k_{\text{fast}}$ .

We first investigated the kinetics of heme reduction for the wild-type and Lys86 variants at pH 7.0, and representative traces and fits are shown in **Figure 5.3** and the kinetic data is summarized in **Table 5.2**. Our analysis herein focuses on the initial rapid phase of quinol-dependent heme reduction,  $k_{\text{fast}}$ , as this parameter is more likely to be specifically sensitive to variant-dependent variations in quinol deprotonation (for  $k_{\text{slow}}$  values, see **Table 5.2**). The NarGHI<sup>K86H</sup> variant has a  $k_{\text{fast}}$  of  $101 \pm 12 \text{ s}^{-1}$ , which is nearly identical to that of the wild-type ( $k_{\text{fast}} = 125 \pm 20 \text{ s}^{-1}$ ). NarGHI<sup>K86E</sup>, however, exhibits a  $k_{\text{fast}}$  nearly twice that of wild-type,  $219 \pm 38 \text{ s}^{-1}$ . The other variants, NarGHI<sup>K86M</sup>, NarGHI<sup>K86Q</sup>, NarGHI<sup>K86Y</sup> and NarGHI<sup>K86A</sup>, are characterized by very low  $k_{\text{fast}}$  values of  $< 15 \text{ s}^{-1}$ . Once again, the ionizable His and Glu variants of Lys86 have

Variant	pH 7 $k_{\text{fast}}$ ( $\text{s}^{-1}$ )	pH 7 $k_{\text{slow}}$ ( $\text{s}^{-1}$ )
Wild-type	$125 \pm 20$	$10 \pm 1$
Glu	$219 \pm 38$	$3 \pm 1$
His	$101 \pm 12$	$10.2 \pm 0.7$
Met	$14 \pm 4$	$1.41 \pm 0.06$
Gln	$12 \pm 1$	$1.53 \pm 0.06$
Tyr	$10 \pm 4$	$0.9 \pm 0.4$
Ala	$8 \pm 1$	$1.1 \pm 0.2$
$\Delta$ NarGHI vesicles		$2.2 \pm 0.2$

**Table 5.2: The rate constants,  $k_{\text{fast}}$  and  $k_{\text{slow}}$ , for heme reduction of NarGHI<sup>Lys86</sup> variants by 0.35 mM menadiol.** The rate constants are reported as mean  $\pm$  standard deviation for  $n \geq 4$ . The negative control data was adequately fit by a single exponential component.

kinetic parameters similar to those of the wild-type.

Based on the behavior of the His and Glu variants of Lys86, we investigated the pH dependence of the pre-steady state kinetics of heme reduction by menadiol over a pH range of 5.5 to 9.5. We also investigated the effect of pH on the  $k_{\text{fast}}$  of the NarGHI<sup>K86A</sup> variant between pH 6 and pH 9, and confirmed that its  $k_{\text{fast}}$  remained negligible compared to that of the wild-type ( $k_{\text{fast}} < 10 \text{ s}^{-1}$ ). For comparison, we evaluated quinol-dependent heme reduction in membranes lacking NarGHI, yielding a kinetic trace that can be fitted to a single exponential with  $k < 5 \text{ s}^{-1}$ . Representative kinetic traces for wild-type, NarGHI<sup>K86H</sup> and NarGHI<sup>K86E</sup> at pH 6.0, 7.0, 8.0 and 9.0 are shown in **Figure 5.3**. **Figure 5.4** and **Supplementary Figure 5.2** respectively show  $k_{\text{fast}}$  and  $k_{\text{slow}}$  values plotted *versus* pH and the data was fitted to **equation 5.3** where activity of the fully protonated and deprotonated forms of the Q-site,  $L_{\text{H2A}}$  and  $L_{\text{A2-}}$  respectively, are set to  $0 \text{ s}^{-1}$ .

Considering the  $k_{\text{fast}}$  kinetics, across all three samples assayed the low  $\text{p}K_{\text{a}}$  ( $\sim 5.8$ ) was unperturbed across the active variants, while the high  $\text{p}K_{\text{a}}$  was significantly modified in the NarGHI<sup>K86E</sup> variant, going from  $\text{p}K_{\text{a}} > 10$  for wild-type NarGHI and NarGHI<sup>K86H</sup> to  $8.9 \pm 0.2$ . Interestingly, NarGHI<sup>K86E</sup> supported a higher maximum  $k_{\text{fast}}$

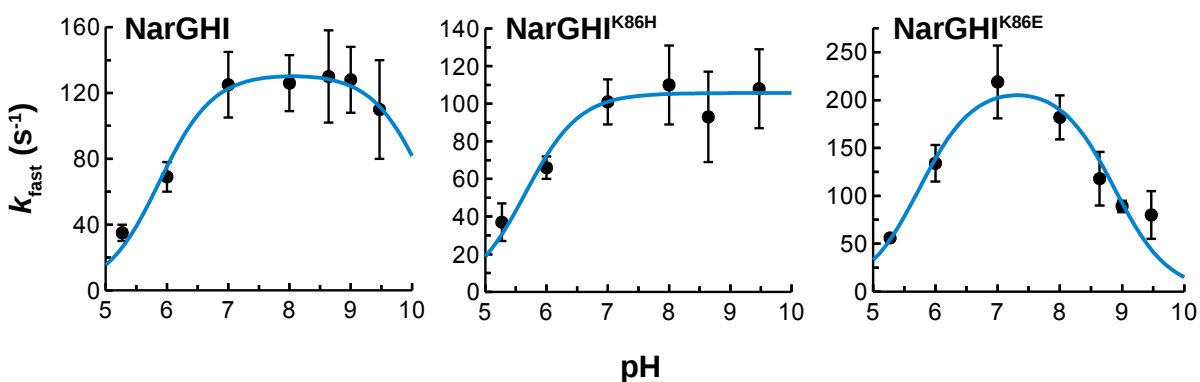


**Figure 5.4:  $k_{\text{fast}}$  pH dependence of heme reduction by 0.35 mM menadiol.**

**Equation 5.3** was used to model the pH dependence of  $k_{\text{fast}}$ , the results of which are (mean standard  $\pm$  error): wild-type ( $\text{p}K_{\text{a}1} = 5.9 \pm 0.1$ ;  $\text{p}K_{\text{a}2} = 10.2 \pm 0.3$ ;  $\text{LHA}^- = 132 \pm 14 \text{ s}^{-1}$ ), NarGHI<sup>K86H</sup> ( $\text{p}K_{\text{a}1} = 5.7 \pm 0.2$ ;  $\text{p}K_{\text{a}2} > 10$ ;  $\text{LHA}^- = 106 \pm 5 \text{ s}^{-1}$ ) and NarGHI<sup>K86E</sup> ( $\text{p}K_{\text{a}1} = 5.8 \pm 0.3$ ;  $\text{p}K_{\text{a}2} = 8.9 \pm 0.2$ ;  $\text{LHA}^- = 217 \pm 32 \text{ s}^{-1}$ ). Error bars denote the standard deviation among  $n \geq 4$  replicates.

( $L_{\text{HA}^-, \text{fast}} = 217 \pm 32 \text{ s}^{-1}$ ) than wild-type ( $L_{\text{HA}^-, \text{fast}} = 132 \pm 14 \text{ s}^{-1}$ ) or NarGHI<sup>K86H</sup> ( $L_{\text{HA}^-, \text{fast}} = 106 \pm 5 \text{ s}^{-1}$ ) though exhibited a lower maximum  $k_{\text{slow}}$ : NarGHI<sup>K86E</sup>  $L_{\text{HA}^-, \text{slow}} = 7.7 \pm 0.7 \text{ s}^{-1}$  versus  $L_{\text{HA}^-, \text{slow}} = 13.8 \pm 0.9 \text{ s}^{-1}$  and  $9.8 \pm 0.8 \text{ s}^{-1}$  for wild-type and NarGHI<sup>K86H</sup> respectively. The wild-type  $k_{\text{fast, pH7}}$  of  $125 \text{ s}^{-1}$  is consistent with the turnover number of  $105 \text{ s}^{-1}$  calculated from the PBH<sub>2</sub>:NO<sub>3</sub><sup>-</sup> oxidoreductase specific activity in **Table 5.1**. These values are also in agreement with the previously published value of  $120 \text{ s}^{-1}$  for PBH<sub>2</sub>:NO<sub>3</sub><sup>-</sup> turnover<sup>277</sup> and is broadly similar to the reported menadiol:nitrate  $k_{\text{cat}}$  values of  $31.9 \text{ s}^{-1}$  and  $41 \text{ s}^{-1}$ <sup>45,265</sup>. The specific activity numbers for PBH<sub>2</sub>:NO<sub>3</sub><sup>-</sup> activity for the NarI<sup>Lys86</sup> variants correlate with the  $k_{\text{fast}}$  numbers except NarGHI<sup>K86E</sup> which exhibits a reduced  $k_{\text{slow}}$ .

## 5.4. Discussion

Quinol oxidation in NarGHI is an electrogenic process, where the two quinol protons are guided by NarI to the periplasmic space. Proton transfer from the quinol O1 is facilitated by the heme  $b_D$  propionates, where propionate D acts as a direct H-bonding partner to the bound quinol, and an associated proton transfer pathway<sup>19</sup>. We have demonstrated a functional need of the residue at position 86 in NarI to be ionizable and thus be directly responsible for proton transfer from the quinol O4. *In vivo* and *in vitro* quinol analog:nitrate reductase activity demonstrates that by far the most functional variants are NarI<sup>K86D/E</sup> and NarI<sup>K86H</sup>. Since NarI<sup>K86R</sup> was only moderately active and the acidic variants were among the most active, this rules out the possible role of Lys86 as a positive counter-charge for the semiquinone, in agreement with our previous finding that the semiquinone is protonated ( $\text{p}K_{\text{a}1} = 8.7$ )<sup>359</sup>. There does seem to be a structural role for Lys86 because the bulky and flexible variants NarGHI<sup>K86R</sup> and NarGHI<sup>K86M</sup> exhibit intermediate levels of activity. However, NarI<sup>Lys86</sup> does not appear to have a purely structural role since all variants of NarI<sup>Lys86</sup> expressed well and the crystal structure of NarGHI<sup>K86A</sup> shows minimal structural deviation from the wild-type enzyme<sup>183</sup>. We propose that the primary function of

NarI<sup>Lys86</sup> is as a general base to directly deprotonate the C4 hydroxyl of quinol.

The stopped flow  $k_{\text{fast}}$  pH profile is characterized by two  $pK_a$  values, where we attribute the  $pK_{a2}$  of  $> 10$  to Lys86. Not only does this value agree with what one expects for a Lys residue, which has a generally accepted  $pK_a$  of  $\sim 10.5$ <sup>360</sup>, but upon mutation to Glu the  $pK_{a2}$  drops to 8.9, indicating that the residue at this position must function as a base and the local protein environment disfavors formation of negative charges. This high  $pK_a$  is also in line with what is required to deprotonate the quinol, which exhibits a  $pK_{a2}$  of 7.3<sup>359</sup>. The main contributing factor to the elevated apparent  $pK_a$  of NarGHI<sup>K86H</sup> and NarGHI<sup>K86E</sup> is likely the proximity of this functional group to the negative dipole of transmembrane helix II and the absence of adjacent Arg/Lys residues. The high  $pK_a$  of NarI<sup>Lys86</sup> and NarI<sup>K86H/E</sup> is indicative of a role in initial deprotonation of the quinol ( $\text{QH}_2 \rightarrow \text{QH}^- + \text{H}^+$ ), which is expected to have a  $pK_a$  of 9-10 based on previous studies of the semiquinones of *E. coli* cytochrome *bd* and *bo*<sub>3</sub><sup>166,167</sup>. The intriguingly high  $k_{\text{fast}}$  for NarGHI<sup>K86E</sup> is indicative of its significantly raised  $pK_a$  and that it is likely functioning through an intermediary water molecule.

The assignment of the  $pK_{a1}$  of 5.8 is less clear, though it is likely attributed to either His66 or heme *b*<sub>D</sub> propionate D. Both are known to interact with PCP, and thus the native quinone substrate, based on crystal structures and ESEEM and HYSCORE spectroscopy<sup>19,170</sup>. There are examples where heme propionates and axial coordinating histidine residues exhibit  $pK_a$  values near 7<sup>316,318,345,346</sup>. However, heme axial histidines are theoretically expected to have  $pK_a$  values  $\sim 4$  pH units lower than the histidine-histidinate transition ( $pK_a \sim 14$ ), and therefore without positive counter charges proximal to His66, the expected  $pK_a$  is in the 8-10 range<sup>361,362</sup>. This is the case observed for the axial histidine in met-myoglobin ( $pK_a$  10.45)<sup>361</sup>, adrenal cytochrome *b*<sub>561</sub> ( $pK_a \sim 8$ )<sup>344</sup> and *E. coli* cytochrome *b*<sub>562</sub> ( $pK_a$  9)<sup>343</sup>. With the proton channel of NarI including propionates A and D of heme *b*<sub>D</sub>, it is more likely that the  $pK_a$  of 5.8 characterizes propionate D. Also, we have previously assigned the  $pK_a$  Nar for Q-site occupancy of 7 to propionate D, which is similar to the value we report here. The difference likely arises from the different methodologies used (thermodynamic versus kinetic) and the state of the sample in the two studies<sup>359</sup>. Regardless, this

propionate  $pK_a$  is in line with its putative function of deprotonating the quinone/semiquinone at O1, efficiently transferring the proton to the heme  $b_D$  proton pathway.

We have demonstrated the need for an ionizable residue at NarI<sup>86</sup>, ideally a Lys, for quinol oxidation to occur and that this residue functions as a base to abstract the O4 proton from the bound quinol/semiquinone. HYSCORE spectra of the menaquinone indicates that only O1 is H-bonded to the protein, where O4 is not protonated nor does it H-bond to anything else<sup>168</sup>, therefore the substrate of NarI<sup>Lys86</sup> is the quinol, not the semiquinone. Following proton abstraction and transfer of the first electron from quinol, Lys86 must alter its conformation which would likely be determined by the oxidation state of the quinol and/or heme  $b_D$  as well as the ionization state of Lys86 itself. The Q-site, which constitutes the C-terminus of helix II, the N-terminus of helix III and the connecting loop (NarI<sup>64-93</sup>), is known to be inherently flexible<sup>19,183</sup> – exhibiting an average temperature (B) factor of 39 Å<sup>2</sup> whereas NarI has an average B-factor of 26 Å<sup>2</sup> (PDB ID 1Q16)<sup>19</sup>. NarI<sup>Lys86</sup> is expected to be particularly flexible, exhibiting an average B-factor of the amino terminus of Lys86 is 48 Å<sup>2</sup>. Such a mechanism for proton uptake from the quinol followed by a conformational change and deprotonation to the aqueous milieu has been proposed for Glu272 of cytochrome  $bc_1$ <sup>363</sup>. The conformational change of Lys86 and the one sided hydrogen bonding of the semiquinone has significant functional implications, primarily it decreases the reduction potential of the semiquinone/quinol transition and thus drives the oxidation of quinol to completion<sup>168,364,365</sup>.

We therefore propose the following mechanism for quinol oxidation by NarGHI (see **Figure 5.5**) :

- 1) Menaquinol binds, Lys86 ( $pK_a \geq 10$ ) is able to abstract the first quinol proton ( $pK_{a2} = 7.3$ <sup>359</sup>) concurrent with electron transfer along the H-bonds to propionate D/His66 to heme  $b_D$ .
- 2) The neutral semiquinone ( $pK_{a1} = 8.7$ <sup>359</sup>) is stabilized by a one-sided H-bond to His66 and likely also propionate D while Lys86 undergoes a conformational

change in order to transfer the proton to the periplasm <sup>170,183</sup>.

- 3) The final electron is transferred to heme  $b_D$  and a reconfiguration of the H-bond with propionate D ( $pK_a \approx 6-7$  <sup>359</sup>) facilitates proton transfer.
- 4) Quinone unbinds and proton transfer from propionate D to the periplasm occurs along the proton channel.

In conclusion, we demonstrate that quinol deprotonation at the O4 position ( $pK_a = 7.3$  <sup>359</sup>) is facilitated by NarI<sup>Lys86</sup> which exhibits a  $pK_a > 10$ . Along with a concurrent electron transfer, a neutral semiquinone with a  $pK_a$  of 8.7 results <sup>359</sup>. We also find that proton transfer away from the quinone O1 is facilitated by an acidic group with an  $pK_a$  of  $\sim 6$ , which is most likely heme  $b_D$  propionate D. Through a likely change in conformation of NarI<sup>Lys86</sup> as well as a H-bonding network adjacent heme  $b_D$ , the two quinol protons are transferred into the periplasm thus contributing to the proton motive force.

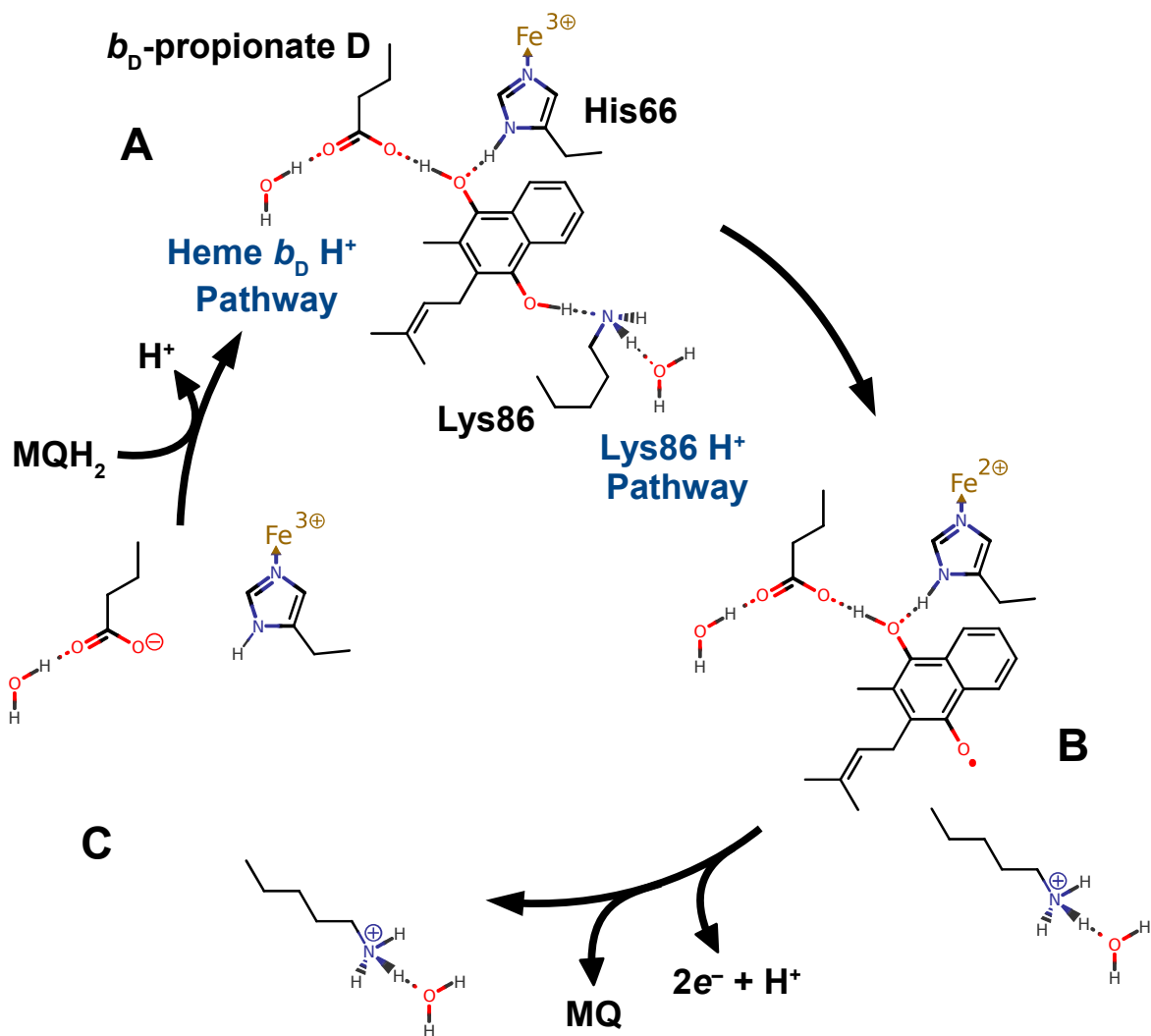
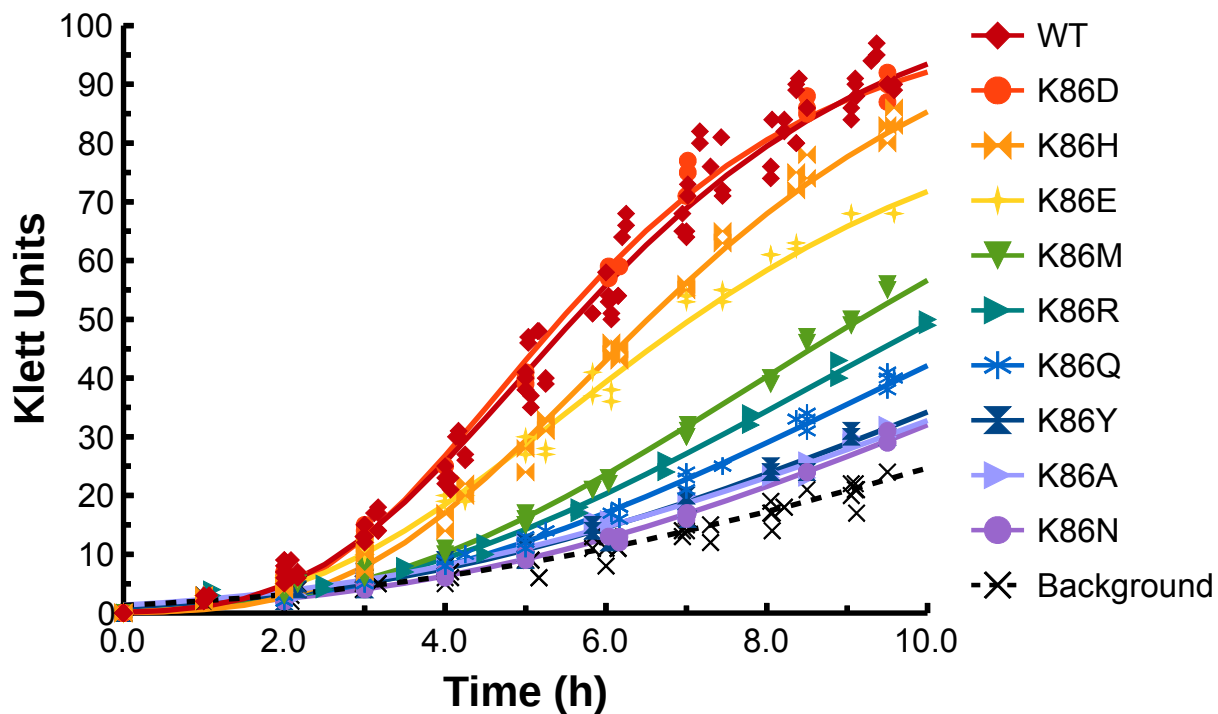


**Figure 5.5: Proposed mechanism of menaquinol oxidation by NarI.** (A) Following initial binding of menaquinol to the Q-site, Lys86 abstracts a proton from O4 and concomitantly the first electron is transferred to heme  $b_D$ . Lys86 adopts an extended conformation where no interaction with the semiquinone occurs, which is likely linked to the heme  $b_D$  oxidation state. (B) The semiquinone reduces heme  $b_D$  following its reoxidation, concurrent with, or followed by abstraction of the second proton on O1 by heme  $b_D$  propionate D. (C) Regeneration of the active site requires menaquinone unbinding and deprotonation of heme  $b_D$  propionate D via the associated proton egress pathway. Atom colors according to CPK convention.

## 5.5. Supplementary Material

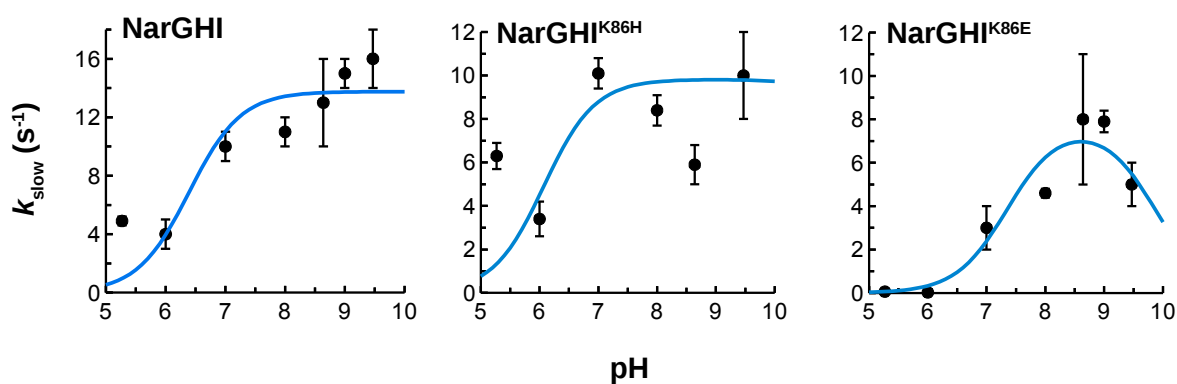
Below are the anaerobic growth curves and  $k_{\text{slow}}$  pH dependence figures referred to in the text as **Supplementary Figures 5.1** and **5.2**.



**Supplementary Figure 5.1: A representative anaerobic growth assay of *E. coli* strain LCB79 complemented with pVA700 encoding NarGHI variants on glycerol:nitrate media.** Using sealed-side arm flasks and a Klett Sommerson colorimeter. The growth curves are fit with a modified Gompertz equation (**equation 5.1**)<sup>354</sup> and the values for maximal growth rate ( $\mu_m$ ) are given in **Table 5.1**.

Variant		$A_{fast}$	$k_{fast}$ (S <sup>-1</sup> )	$A_{slow}$	$k_{slow}$ (S <sup>-1</sup> )	P
WT	pH 6	-0.0141 ± 5e-4	79 ± 5	-0.0202 ± 3e-4	5.2 ± 0.3	0.0378 ± 4e-4
	pH 7	-0.0226 ± 7e-4	142 ± 8	-0.0172 ± 5e-4	10.2 ± 0.08	0.0457 ± 3e-4
	pH 8	-0.0260 ± 7e-4	141 ± 7	-0.0172 ± 5e-4	12.3 ± 0.5	0.0483 ± 1e-4
	pH 9	-0.0239 ± 6e-4	104 ± 4	-0.0250 ± 5e-4	14.2 ± 0.3	0.05336 ± 8e-5
K86H	pH 6	-0.0900 ± 4e-4	63 ± 6	-0.0151 ± 3e-4	4.8 ± 0.3	0.0263 ± 4e-4
	pH 7	-0.014 ± 1e-3	100 ± 12	-0.0151 ± 8e-4	10 ± 1	0.0332 ± 4e-4
	pH 8	-0.0144 ± 6e-4	144 ± 12	-0.0191 ± 4e-4	9.6 ± 0.4	0.0374 ± 2e-4
	pH 9*	-0.0124 ± 3e-4	227 ± 12	-0.0221 ± 2e-4	11.5 ± 0.2	0.03853 ± 7e-5
K86E	pH 6	-0.0098 ± 3e-4	120 ± 8	-1 ± 6	0.03 ± 0.21	1 ± 6
	pH 7	-0.0132 ± 4e-4	189 ± 11	-0.030 ± 3e-3	1.7 ± 0.3	0.046 ± 3e-3
	pH 8	-0.0153 ± 3e-4	187 ± 8	-0.0218 ± 2e-4	4.9 ± 0.1	0.0404 ± 2e-4
	pH 9	-0.0102 ± 3e-4	90 ± 5	-0.0270 ± 2e-4	7.6 ± 0.1	0.0385 ± 1e-4

**Supplementary Table 5.1: Fitting parameters for pre-steady state heme reduction by menadiol of NarGHI-enriched vesicles of wild-type, K86H, and K86E as depicted in Figure 5.3.** The parameters correspond to those in *equation 5.2*. Values are reported as mean ± standard error of fitting over a 0.5 s time range. \*K86H pH9 was eliminated as an outlier in subsequent pH dependence analysis.



**Supplementary Figure 5.2:  $k_{\text{slow}}$  pH dependence of heme reduction by 0.35 mM menadiol.** Equation 5.3 was used to model the pH dependence of  $k_{\text{slow}}$ , the results of which are (mean standard  $\pm$  error): wild-type ( $pK_{a1} = 6.4 \pm 0.1$ ;  $pK_{a2} > 10$ ;  $\text{LHA}^- = 13.8 \pm 0.8 \text{ s}^{-1}$ ), NarGHI<sup>K86H</sup> ( $pK_{a1} = 6.1 \pm 0.2$ ;  $pK_{a2} > 10$ ;  $\text{LHA}^- = 9.8 \pm 0.8 \text{ s}^{-1}$ ) and NarGHI<sup>K86E</sup> ( $pK_{a1} = 7.4 \pm 0.1$ ;  $pK_{a2} = 9.9 \pm 0.3$ ;  $\text{LHA}^- = 7.7 \pm 0.7 \text{ s}^{-1}$ ). Error bars denote the standard deviation among  $n \geq 4$  replicates.

## 6. A NarI<sup>Met156Lys</sup> Variant of *E. coli* NarGHI Restores Quinol Oxidase Activity of a NarI<sup>Lys86Ala</sup> Mutation

**A version of this chapter has been submitted for publication:**

Justin G. Fedor, Richard A. Rothery and Joel H. Weiner. A NarI<sup>Met156Lys</sup> variant of *Escherichia coli* nitrate reductase A restores quinol oxidase activity of a NarI<sup>Lys86Ala</sup> mutation. *FEBS Journal*

**Acknowledgements:**

We would like to thank Shannon Murphy for technical assistance.

## 6.1. Introduction

*Escherichia coli* (*E. coli*) is a facultative anaerobe which exhibits biochemical flexibility by coupling a diverse set of reductants ( $H_2$ , NADH, succinate, formate, lactate, glycerol-3-phosphate) to an equally broad set of oxidants ( $O_2$ , fumarate, nitrate, nitrite, dimethyl sulfoxide, trimethylamine N-oxide)<sup>2,21</sup>. Each of these oxidants and reductants are metabolized by their respective membrane-associated oxidoreductase complexes, which in turn communicate via the ubiquinone and menaquinone pool (Q-pool). The  $2e^-/2H^+$  redox chemistry of quinones is exploited by many respiratory enzymes to generate the proton motive force (PMF) via scalar proton chemistry, where protons are consumed on the cytoplasmic face and deposited on the periplasmic face via 'Mitchell loops'<sup>15,21</sup>. The first 'Mitchell loop' to be resolved at the atomic level comprises formate dehydrogenase N and nitrate reductase A (NarGHI), which is primarily responsible for generating the PMF in *E. coli* under anaerobic and high nitrate conditions<sup>18,19</sup>. NarGHI faces the cytoplasm and functions as a dimer of heterotrimers which is anchored to the plasma membrane via NarI<sup>17,225–227</sup>. NarI oxidizes quinols ( $QH_2$ ) and coordinates two *b*-type hemes<sup>269</sup> identified as being proximal ( $b_P$ ) or distal ( $b_D$ ) to NarGH, where the Q-site is adjacent to  $b_D$ <sup>19</sup>. NarG binds a molybdo-bis(pyranopterin guanine dinucleotide) (Mo-bisPGD) cofactor, which is the site of nitrate reduction, as well as a [4Fe-4S] cluster. NarH, with its [3Fe-4S] and three [4Fe-4S] clusters, mediates electron transfer between NarI and NarG. An important functional feature of NarI is the existence of two proton egress pathways that lead from the Q-site to the periplasm, thereby coupling the oxidation of quinol to the contribution to PMF<sup>20,267</sup>. Our current hypothesis is that the quinol O1 proton is transferred to the periplasm via the heme  $b_D$  proton egress pathway, which consists of a number of highly conserved polar/ionizable residues ( $b_D$  propionates A and D, Thr143, Ser147, His150, Ser154, Gln87, Asp152) and several crystallographically conserved waters<sup>183,331</sup>. Proton transfer pathways like this are present in cytochrome oxidase<sup>366,367</sup>, NADH:ubiquinone oxidoreductase<sup>368,369</sup>, quinone:fumarate oxidoreductase<sup>370</sup> and cytochrome  $bc_1$  and  $b_6f$ <sup>187</sup>. The O4 proton,

on the other hand, takes the Lys86 proton egress pathway, depicted in **Figure 6.1**, which is less well defined and consists of fewer conserved waters. The reason this pathway is less clearly defined is likely due to its dynamic nature, as evident by a consistently less well resolved helix II-III loop (Q-loop) of NarI<sup>71-83</sup> in the existing NarGHI structures<sup>19,183,244</sup>. Furthermore, Lys86 has been demonstrated to be critical in quinol oxidation<sup>183,284</sup> where it deprotonates the quinol at O4<sup>331</sup>. Paradoxically, Lys86 has only been observed in an extended conformation such that N $\zeta$  is ~6 Å away from the quinol O4<sup>19,183</sup>, yet it has been ruled out by HYSORE and ESEEM that Lys86, nor any waters, interact with the semiquinone O4<sup>168,170</sup>. It has therefore been proposed that Lys86 adopts a bent conformation for quinol deprotonation and an extended conformation for proton transfer to the periplasm<sup>170,183,331</sup>. Such dynamical proton transfer pathways have been observed in other systems where critical ionizable residues adopt two conformations, for instance Lys227 of the Q<sub>i</sub> and Glu272 of the Q<sub>o</sub> sites of cytochrome *bc*<sub>1</sub><sup>371,372</sup>, Glu78 of the H<sup>+</sup> exit and Lys24 H<sup>+</sup> uptake sites of cytochrome *b*<sub>6f</sub><sup>187</sup>, Glu180 of fumarate reductase<sup>370</sup>.

In this work we provide experimental evidence that supports the hypothesis that Lys86 must adopt a conformation appropriate for abstraction of the O4 quinol proton. Mutation of Lys86 to Ala results in a significantly reduced ability of NarGHI to oxidize menaquinol and ubiquinol, stabilize semiquinone, and bind the Q-site inhibitors pentachlorophenol (PCP) and HOQNO (2-*n*-heptyl hydroxyquinoline-N-oxide)<sup>183,284</sup>. Lys86 can, however, be functionally replaced with alternative ionizable residues Glu, Asp or His<sup>331</sup>. Herein, we have used CAVER to better characterize the Lys86 proton egress pathway and consequently chose Met156, a partially conserved residue that points towards the quinol O4, as a subject for site directed mutagenesis studies. We demonstrate that Met156Lys partially restores activity of the Lys86Ala variant and interpret this as providing evidence for an alternative conformation of Lys86 for quinol deprotonation.

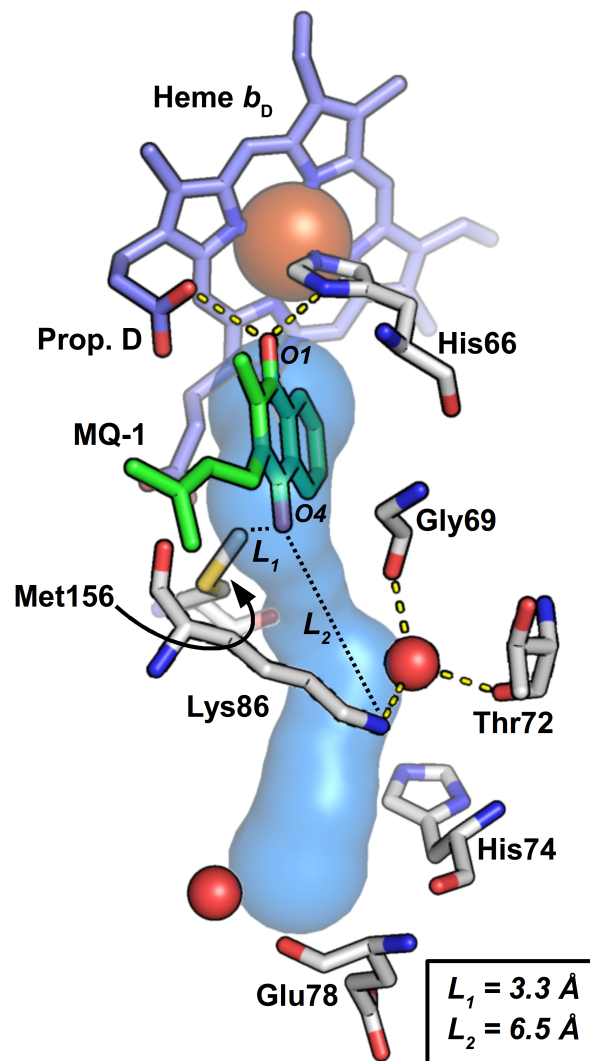


**Figure 6.1: The quinol binding site and Lys86 proton egress pathway within the NarI subunit of *E. coli* NarGHI.** The CAVER generated Lys86 proton egress pathway is depicted as a blue surface <sup>373</sup>. The image was generated using PyMOL based on the wild-type crystal structure with the Q-site inhibitor pentachlorophenol (PCP) bound (PDB ID 1Y4Z) but with MQ-1 (green) modeled in its place and PyWater to determine crystallographically conserved waters (80%) <sup>1803 353, 374</sup>. Heme  $b_D$  and its propionate D (Prop. D) are indicated as are the MQ-1 oxygens O1 and O4. Crystallographically conserved waters are depicted as red spheres and H-bonding interactions are depicted as dashed yellow lines. Residues critical in forming the H-bonding networks are represented as sticks and labelled.

## 6.2. Materials and Methods

*CAVER analysis of NarI* – CAVER PyMol plugin (version 3.0.1)<sup>373</sup> and PyMol (version 1.7.0.0)<sup>374</sup> were used to find any channels leading from the Q-site to the periplasm in the structure PDB ID 3EGW. This structure was modified in PyMol to include the sidechains of NarI Tyr77 and Glu78, choosing rotamers with the least steric clashes. The start point used was water-850, situated where quinol O1 would be in the Q-site, with a probe radius of 1.0 Å, shell radius and depth of 4.0 Å, 20 approximating balls and a clustering threshold of 3.5.

*Materials* – Plumbagin (5-hydroxy-2-methyl-1,4-naphthoquinol), menadiol (2-methyl-1,4-naphthoquinone) and low catalase glucose oxidase from *Aspergillus niger* (Sigma-Aldrich G0543) were obtained from Sigma Aldrich. Thesit<sup>R</sup> (Polyoxyethylene 9-dodocyl ether) was purchased from Fluka, diluted to 10% (w/v), rigorously degassed and stored at -80 °C.

*Bacterial strains, plasmids, and mutagenesis* – Wild-type NarGHI was overexpressed in the *E. coli* strain LCB79 (*araD139*  $\Delta$ (*lacI*-POZYA-*argF*) *rpsL*, *thi*,  $\Phi$ 79(*nar-lac*))<sup>298</sup>, which is deficient in *narGHJI*, and transformed with the plasmid pVA700 (*tacP*, *rrnB*, *lacI*<sup>q</sup>, *amp*<sup>r</sup>, *narGHJI*) (12 484 bp), including the mutated versions pVA700-NarI<sup>Lys86Ala</sup><sup>183</sup>, pVA700-NarI<sup>Met156Lys</sup>, and pVA700-NarI<sup>Met156Lys/Lys86Ala</sup><sup>268</sup>. Mutagenesis was conducted using two rounds of PCR, and four different primers: a forward primer that binds upstream of the mutation site, a reverse primer that binds downstream of the mutation site, and the overlapping forward and reverse mutagenic primers. In PCR A, forward and mutagenic-reverse primers are used; in PCR B, mutagenic-forward and reverse primers are used. The template DNA used for PCR A and B is pVA700 or pVA700-NarI<sup>Lys86Ala</sup>. Following the reaction, products were gel-purified using a TruIn Science gel purification kit (TruIn Science, Edmonton, AB), and the combined eluent was diluted 1:2 to 1:10 with 10 mM Tris-HCl, pH 8.5. Then, 1  $\mu$ L of the pooled, diluted, and purified PCR A and B was used as a template in the final round of PCR. In PCR C, the forward and reverse primers were used and the product (2188 bp) is PCR

purified with a TruIn Science PCR purification kit. The master mix for all PCR reactions consisted of 1x Q5 reaction buffer, 0.2 mM dNTPs, 0.5  $\mu\text{M}$  of each primer, and 0.02 U  $\mu\text{L}^{-1}$  of Q5<sup>TM</sup> High-Fidelity DNA polymerase from New England Biolabs. PCR A and B were 25  $\mu\text{L}$  final volume and PCR C was 50  $\mu\text{L}$ . The primers used were: forward primer (flanks the AatII cutsite in pVA700): 5'-GGGTAGCAACGGCATTCTGCC, reverse primer (flanks the XbaI cutsite in pVA700): 5'-CTTCTCTCATCCGCCAAAACAGCC, NarI<sup>M156K</sup> forward: 5'-GGTAGCGAGAAGATGAAACTGGTTGGC, NarI<sup>M156K</sup> reverse: 5'-CCAGTTTCATCTTCTCGCTACCGTCCATATGC. The cycles used were: 30 s 98°C, 29x[ 10 s 98°C, 15 s 65°C, 40-60 s 72°C] 5 min 72°C.

T4 DNA ligase (400 000 U  $\text{mL}^{-1}$ ) and all restriction enzymes (20 000 U  $\text{mL}^{-1}$ ) were acquired from New England Biolabs. pVA700 and purified PCR C products were digested with AatII and XbaI at final concentrations of 0.4 U  $\mu\text{L}^{-1}$  (pVA700) and 0.8 U  $\mu\text{L}^{-1}$  (PCR C) at 37°C for  $\geq 2$  hours. XhoI (0.4 U  $\mu\text{L}^{-1}$ ) was also added to the pVA700 digestion to help prevent religation of any partially digested plasmid; XhoI cuts between AatII and XbaI, producing three cleavage products. The pVA700 backbone was then gel purified and the digested PCR C was heat treated to denature the enzymes (80°C for 20 min). Ligation of the insert to the backbone was accomplished with 400 units of T4 DNA ligase in a 15  $\mu\text{L}$  reaction, including 1  $\mu\text{L}$  of the backbone, 2  $\mu\text{L}$  of insert and 1X T4 DNA ligase buffer (~1 fmol backbone to 3 fmol insert). The reaction was left to sit for 30 min at 23°C. 5  $\mu\text{L}$  of the ligation reaction and 60  $\mu\text{L}$  of RbCl competent LCB79 cells were gently combined and incubated on ice for  $\geq 30$  min. Following heat shock at 42°C for 60 s, then incubation on ice for 2 min, 750  $\mu\text{L}$  of SOC broth was added to the tube and the cells were left to recover for 1 h at 37°C on a rotator wheel<sup>301</sup>. Transformants were selected by plating 100  $\mu\text{L}$  of cells onto LB plates supplemented with 1% (w/v) thiamine hydrochloride, 0.1 mg  $\text{mL}^{-1}$  Ampicillin and Streptomycin and incubating overnight at 37°C. Successful mutants were screened by sequencing the purified (TruIn Science miniprep kit) transformant colonies (Eurofins MWG Operon LLC, Huntsville, AL) using 100-200 ng  $\mu\text{L}^{-1}$  of DNA and 3.33  $\mu\text{M}$  of the primer: 5'-CTTTGCCGGTGCCGTCG.

*Cell culturing and preparation of membrane vesicles* – Membranes enriched in NarGHI were obtained by culturing 2 L batches of LCB79/pVA700 in 6 L non-baffled flasks. The flasks contained Terrific Broth <sup>301</sup> supplemented with 100 mg L<sup>-1</sup> ampicillin, 100 mg L<sup>-1</sup> streptomycin and a 10% inoculum of an overnight stationary culture. The cultures were grown under nearly anaerobic conditions (100 rpm shaking) at 30°C overnight. Induction of protein expression was achieved by addition of 1 mM IPTG <sup>301</sup>. NarGHI-enriched membranes were harvested, as detailed previously <sup>270,321,331</sup>, by differential centrifugation including a 55%(w/v) sucrose bed. The buffer system used throughout was 100 mM MOPS and 5 mM EDTA pH 7.0. Initial harvesting included the serine protease inhibitor phenylmethanesulfonyl fluoride (PMSF) at a final concentration of 0.2 mM. Membranes were stored in ~30 mg mL<sup>-1</sup> aliquots at -70°C.

*Determination of protein and heme concentration* – Protein concentrations of NarGHI-enriched inner membrane vesicles was determined by a modified Lowry method, which includes 1% (w/v) of sodium dodecyl sulfate for solubilization of membrane proteins <sup>306</sup>. Heme optical spectroscopy was used to determine the heme concentration, where intensity was taken as the difference between the absorbance in reduced-*minus*-oxidized spectra of the  $\alpha$ -band at 559 nm *minus* the absorbance at 575 nm. Heme concentration was calculated using the  $\epsilon_{559-575}$  of 14.8 mM<sup>-1</sup> cm<sup>-1</sup> <sup>331</sup>.

*Anaerobic growth assays* – LCB79 was the host *E. coli* strain used and the cells were grown at 37°C in tightly sealed 125 mL Klett flasks, with stirring by a magnetic plate, on glycerol-nitrate (GN) media supplemented with 100 mg L<sup>-1</sup> ampicillin, 100 mg L<sup>-1</sup> streptomycin, 0.003% (w/v) leucine and threonine, as previously described <sup>331</sup>. Time dependent absorbance readings were taken with a Klett spectrophotometer equipped with a red filter. Growth assays were conducted with at least four replicates and the ensemble of data was fit with a modified Gompertz model (**equation 6.1**) <sup>354</sup>.

$$y = A \exp\left(-\exp\left(\frac{\mu_m e}{A}(\lambda - t) + 1\right)\right) \quad (6.1)$$

A is the stationary phase absorbance,  $\mu_m$  is the maximal specific growth rate (h<sup>-1</sup>) and

$\lambda$  is the lag phase duration (h).

*In vitro activity assays* – Quinol:nitrate activity was determined using the menaquinol analog plumbagin. Assays were carried out as previously described using an HP 8453 UV/Vis spectrophotometer equipped with an HP89090A Peltier temperature controller/cuvette stirrer<sup>277,321,331</sup>. The buffer used consisted of vacuum degassed 100 mM MOPS, 5 mM EDTA, 4 mM KNO<sub>3</sub>, 30 mM glucose and 0.01% (w/v) Thesit. Stock ethanolic solutions of 20 mM plumbagin were reduced in the presence of ~70 mg of Zn<sup>0</sup> and 190 mM HCl<sub>(aq)</sub> in sealed 2 mL HPLC vials, which were protected from light. Reactions were carried out at 25°C and included 5  $\mu$ L of a  $\geq 200$  U mg<sup>-1</sup> low catalase ( $\leq 0.1$  U mg<sup>-1</sup>) glucose oxidase (24.1 mg mL<sup>-1</sup>) and 50  $\mu$ L of plumbagin solution ( $C_f = 336$   $\mu$ M). The reactions included 0.01 – 0.05 mg mL<sup>-1</sup> of vesicles per cuvette or about 0.4 mg mL<sup>-1</sup> in the case of NarGHI-devoid control vesicles. Plumbagin  $\lambda_{\max} = 419$  nm,  $\epsilon_{419} = 3.95$  mM<sup>-1</sup> cm<sup>-1</sup><sup>277</sup>.

*Pre-steady state kinetics of heme reduction assays* – Stopped-flow kinetics assays were performed using a photodiode array-equipped Applied Photophysics SX-18MV stopped-flow spectrophotometer, using Xscan software (Applied Photophysics Ltd. Leatherhead, UK), as previously described<sup>331</sup>. A 1 cm pathlength was used and the measured instrument dead time was  $1.12 \pm 0.04$  ms. The buffer systems used consisted of 100 mM 100 mM MES (pH 6.0), 100 mM MOPS (pH 7.0), 100 mM Tricine (pH 8.0) or 100 mM CHES (pH 9.0) and 5 mM EDTA, 30 mM glucose, 0.01% Thesit. The buffer was first degassed for several hours on a vacuum line and 50 mL batches were further deoxygenated by addition of 0.5  $\mu$ L low catalase glucose oxidase per mL of degassed buffer. Stock 20 mM ethanolic menadiol was reduced by HCl/Zn<sup>0</sup>, as described in Materials and Methods. The deoxygenated buffer was used to flush the system thoroughly prior to the experiments, as well as to dilute the NarGHI-enriched vesicle samples to 2 mg mL<sup>-1</sup> and menadiol ( $E_{m,7} = -13$  mV) to 0.7 mM<sup>357</sup>. With a mixing ratio of 1:1 the final concentrations of protein and menadiol were 1 mg mL<sup>-1</sup> and 0.35 mM, respectively. Heme reduction kinetics was measured at 10 s or 100 s using logarithmic sampling at 23°C by using the intensity at 558 nm

*minus* that at 575 nm, utilizing the oxidized sample as a time zero reference. The first 3-4 ms of data was discarded due to mixing artifacts and a (-0.0012 s, 0.0) data point was added to account for the fact that fully oxidized NarGHI was used as the blank. Matlab (version 2014b, The MathWorks Inc., Natick, MA) was used to fit the signal traces to a two-component exponential decay, as in **equation 6.2**, while a single component was sufficient for the  $\Delta$ NarGHI and pH 6 NarGHI<sup>Lys86Ala</sup> membranes.

$$A_{559-575} = A_1 \exp(-k_{fast} t) + A_2 \exp(-k_{slow} t) + P \quad (6.2)$$

Where  $A_1$  and  $A_2$  are initial points and  $P$  is final plateau reached, both in absorbance units, and  $k_{fast}$  and  $k_{slow}$  are rate constants ( $s^{-1}$ )<sup>279,283</sup>.

## 6.3. Results and Discussion

### CAVER Analysis of the NarI Q-site

Proton egress from the Q-site of NarI to the periplasm appears to follow two distinct routes<sup>331</sup>. The heme  $b_D$  pathway allows for proton transfer from quinol O1 to the periplasm via the heme  $b_D$  propionate D and a defined hydrogen bonding network<sup>183,331</sup>. Proton egress from the quinol O4 involves deprotonation by Lys86 and proton transfer via a less well defined pathway. In order to gain insight into how the proton from quinol O4 is guided to the periplasm we submitted NarI to CAVER analysis<sup>373</sup>. The NarGHI structure PDB ID 3EGW is of the NarH<sup>C16A</sup> variant<sup>296,375</sup> and is the highest resolution structure of NarGHI (1.9 Å) where the Q-site is best resolved and modeled. However, the side chains of NarI Tyr77 and Glu78 are not resolved so the correct amino acid side chains were modeled in using PyMol, choosing rotamers with the least steric clashes. The 3EGW NarI aligns to wild-type NarI (PDB ID 1Q16)<sup>19</sup> with an RMSD of 0.067 Å (1572 to 1572 atoms) and therefore the NarH<sup>C16A</sup> mutation has no consequence on NarI structure.

Seven tunnels were clustered into three, two of which lead into the membrane thus denoting the Q-site entry (not shown) and one narrower tunnel (Lys86 proton

egress pathway) leading to the periplasm (**Figure 6.1**). This channel is bounded by several conserved residues, Lys86 being of utmost importance, but also Gly65, His66, Gly69, Ala90 and Met156. The channel is also bounded by the less well conserved residues His74, Glu78, Leu81, Ile83, Met157 and Val160. Thr72, Gly69 and Lys86 also appear important in stabilizing a conserved water molecule along the tunnel, as shown in **Figure 6.1**.

To probe whether Lys86 adopts a bent conformation in order to abstract the quinol O4 proton, we used site directed mutagenesis to introduce an amine functional group whose position would approximate that of Lys86 in this alternative conformation. When menaquinone-1 (MQ-1) is modeled in place of PCP<sup>183</sup> the methyl terminus of Met156 comes within 3.3 Å of the quinol O4, thus serving as an ideal residue for a Lys substitution. In fact, in an alignment of 475 sequences that share less than 90% identity, NarI<sup>156</sup> occurs as a Met 78% of the time or an Arg 15% of the time. While anaerobic growth experiments on nitrate demonstrated that NarGHI<sup>Met156Arg</sup> has nearly identical activity to wild-type ( $\mu_m = 14.5 \text{ h}^{-1}$  and  $15.4 \text{ h}^{-1}$ , respectively), we sought to specifically determine whether we could recover the activity lost in NarGHI<sup>Lys86Ala</sup> by substituting Met156 with Lys.

### Anaerobic growth assays

*In vivo* functionality of NarGHI variants was determined by monitoring anaerobic cell growth on a minimal glycerol-nitrate (GN) medium (**Figure 6.2**)<sup>298</sup>. *E. coli* LCB79 lacks the *narGHJI* operon and is unable to grow unless complemented with the plasmid pVA700, which encodes *narGHJI*. This ensures that the observed growth results from the expression of functional NarGHI. The negative control was LCB79/pVA700- $\Delta narI$ , which lacks NarI but expresses the soluble NarGH dimer, which is not coupled to the Q-pool and is unable to support growth. The residual growth that was observed in LCB79/pVA700- $\Delta narI$  is due to expression of periplasmic dissimilatory nitrate reductase, NapAB<sup>208</sup>. The growth curves were fit with a modified Gompertz equation, summarized in **Table 6.1** as maximal growth rates ( $\mu_m$ ). As

expected, wild-type NarGHI supports optimal growth whereas NarGHI<sup>Lys86Ala</sup> only supports minimal growth. The incorporation of an additional Lys into NarI, NarGHI<sup>Met156Lys</sup>, does not alter the wild-type growth rate. Importantly, the double variant NarGHI<sup>Met156Lys/Lys86Ala</sup> largely restores the growth rate of NarGHI<sup>Lys86Ala</sup> to near wild-type levels. This indicates that under physiological conditions, loss of a Lys residue at NarI<sup>86</sup> can be overcome by introducing a Lys at NarI<sup>156</sup>, thereby lending support to the hypothesis of multiple conformations for Lys86 and to the existence of the Lys86 proton transfer pathway.

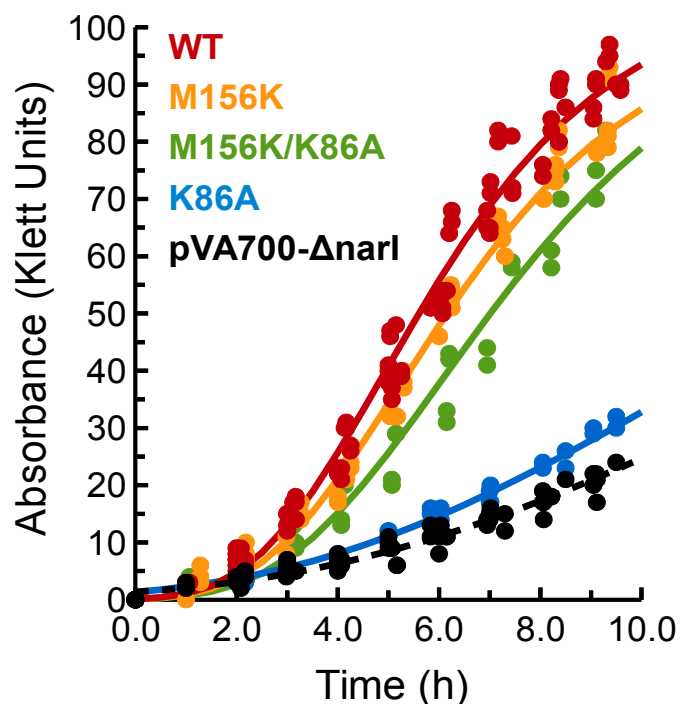


**Figure 6.2: Anaerobic growth assay on glycerol:nitrate media of *E. coli* LCB79 complemented with pVA700 encoding NarGHI variants.** The growth curves are fit with a modified Gompertz equation (**equation 6.1**)<sup>354</sup> and the values for maximal growth rate ( $\mu_m$ ) are given in **Table 6.1**.

### ***In vivo* and *in vitro* activity of Lys86 variants**

Based on SDS-PAGE, Lowry and heme optical assays, the protein expression of the variants, as well as heme incorporation, was similar to the wild-type enzyme. *In vitro* steady-state enzyme activity was monitored using the hydroxylated naphthoquinone plumbagin (PBH<sub>2</sub>) ( $E_{m,7} = -40$  mV), which has been shown to be an appropriate *in vitro* substrate for NarGHI<sup>277</sup>. Heme content was used to quantify NarGHI as well as to calculate the PBH<sub>2</sub>:NO<sub>3</sub><sup>-</sup> activity (**Table 6.1**). Membrane vesicles prepared from *E. coli* LCB79 were used as a negative control ( $\Delta$ NarGHI). In

agreement with the *in vivo* growth assays, these vesicles were incapable of oxidizing PBH<sub>2</sub> in the presence of nitrate (2% wild-type). Vesicles prepared from *E. coli* LCB79/pVA700 supported maximal activity. As previously reported, the variant NarGHI<sup>Lys86Ala</sup> exhibits greatly diminished PBH<sub>2</sub>:NO<sub>3</sub><sup>-</sup> activity (6% of wild-type)<sup>183</sup>. Incorporation of an additional Lys residue into wild-type NarI proximal to heme b<sub>D</sub> (NarIMet156Lys) has minimal effects on PBH<sub>2</sub>:NO<sub>3</sub><sup>-</sup> activity (69% wild-type). Importantly, the double variant NarGHI<sup>Met156Lys/Lys86Ala</sup> largely rescued the NarI<sup>Lys86Ala</sup> variant (72% wild-type). This again supports our hypothesis that in order for quinol oxidation to occur, a Lys must be in hydrogen bonding distance of the quinol. However, the reduced activity of NarGHI<sup>Met156Lys/Lys86Ala</sup> relative to wild-type is likely indicative of non-ideal bonding geometry, perturbed pK<sub>a</sub> values, and/or diminished kinetics of subsequent proton transfer steps.

### Pre-steady state kinetics of heme reduction

Variant	Growth Assay <sup>a</sup> $\mu_m$ (h <sup>-1</sup> )	Plumbagin:NO <sub>3</sub> <sup>-</sup> <sup>b</sup> $\mu\text{mol min}^{-1} \text{nmol heme}^{-1}$
NarGHI	15.4 ± 0.3	3.2 ± 0.1
NarGHI <sup>M156K</sup>	13.8 ± 0.4	2.1 ± 0.1
NarGHI <sup>M156K/K86A</sup>	12.3 ± 0.6	2.3 ± 0.1
NarGHI <sup>K86A</sup>	5.0 ± 0.1	0.190 ± 0.005
ΔNarGHI	4.2 ± 0.1	0.073 ± 0.006

**Table 6.1: The *in vivo* and *in vitro* activity of NarGHI Lys86 and Met156 variants.** The maximal growth rates ( $\mu_m$ ) and specific activity for PBH<sub>2</sub>:NO<sub>3</sub><sup>-</sup> oxidoreductase activity. The background in the growth assays was LCB79/pVA700-Δ*narl*, while the background in the PBH<sub>2</sub>:NO<sub>3</sub><sup>-</sup> activity assays is the activity of membrane vesicles prepared from untransformed LCB79. There is ≥ 4 replicates and at least biological duplicates of each variant in the growth assay. The PBH<sub>2</sub>:NO<sub>3</sub><sup>-</sup> reductase activity assays were performed in at least triplicate. **a** – The mean ± standard error of fitting the Gompertz model to the aggregated data points. **b** – The mean ± standard deviation.

In order to examine the pre-steady state kinetics of quinol oxidation by NarGHI and to gain further insight into possible perturbation of quinol oxidation-associated  $pK_a$ s, menadiol mediated heme reduction of NarGHI in vesicles prepared from *E. coli* LCB79/pVA700 was monitored using a stopped flow apparatus coupled to a diode array spectrophotometer<sup>279,283,331</sup>. A time zero blank was determined using oxidized NarGHI at 1 mg mL<sup>-1</sup> and the absorbance of the  $\alpha$  peak of hemes  $b_D$  and  $b_P$  (559 nm) *minus* that of the background at 575 nm was measured with respect to time. **Figure 6.3** depicts representative pH 7

kinetic traces of vesicles containing wild-type NarGHI and the variants, where fitting to a double exponential equation yields two kinetic constants,  $k_{fast}$  and  $k_{slow}$  (see **equation 6.2**); the fitting parameters are given in **Supplementary Table 6.1**. Pre-steady state activity was measured at pH values 6, 7, 8 and 9 and the  $k_{fast}$  and  $k_{slow}$  parameters are summarized in **Figure 6.4**. The heme reduction kinetics of vesicles lacking functional NarGHI prepared from *E. coli* LCB79 vesicles at all pH values tested, and from NarGHI<sup>Lys86Ala</sup> at pH 6, were satisfactorily fit with single components. We interpreted the kinetic data such that  $k_{fast}$  represents the initial reduction by the first reducing equivalents of menadiol:  $menadiol \rightarrow menadione + 2H^+ + 2e^-$ <sup>331</sup>.  $k_{slow}$  interpretation is complicated

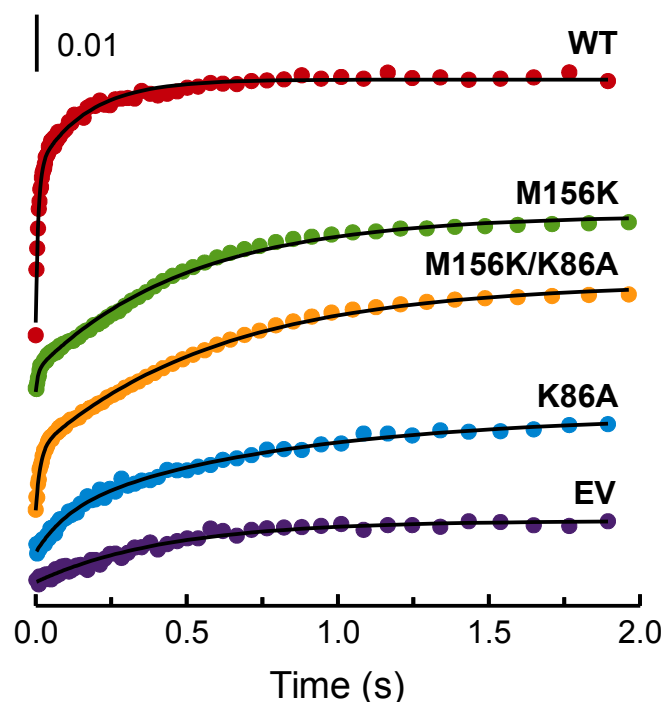


**Figure 6.3: Pre-steady state kinetics of heme reduction of 1 mg mL<sup>-1</sup> NarGHI with 0.35 mM menadiol at pH 7.0.** The kinetic traces represent reduced minus oxidized heme spectra taken at  $A_{559}-A_{570}$  and shifted up for clarity, initial points are all (-0.0012 s, 0.0). The traces are fit with a two-component exponential decay (**equation 6.2**), the NarGHI-devoid membrane vesicle control is fit with a single component exponential decay. Fitting parameters used are given in **Supplementary Table 6.1**.

not only by subsequent electron transfer through NarGHI but also by interference of background cytochromes<sup>332</sup> and photo-reduction of the hemes<sup>358</sup>.

In agreement with the *in vivo* and *in vitro* activity assays, wild-type and NarGHI<sup>Met156Lys</sup> vesicles exhibit maximal  $k_{fast}$  activity, whereas  $k_{fast}$  of NarGHI<sup>Lys86Ala</sup> is

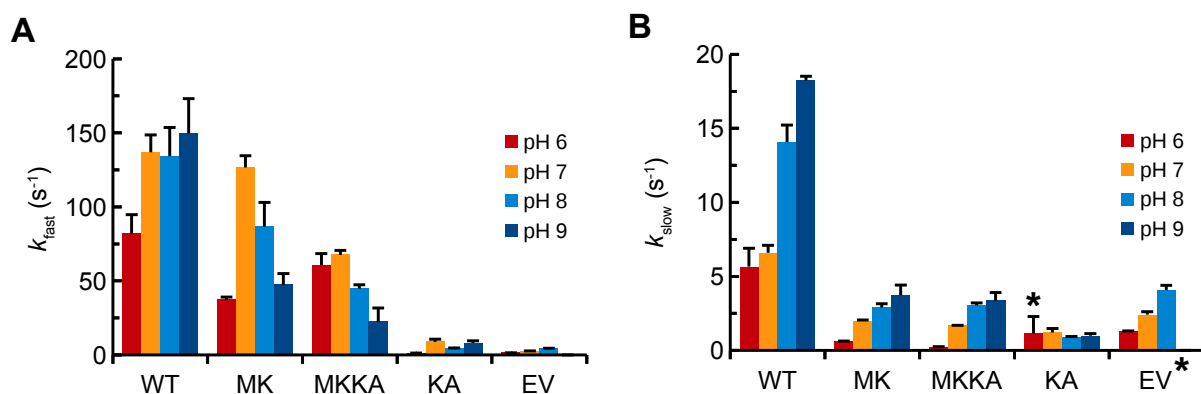


**Figure 6.4: pH dependence of (A)  $k_{fast}$  and (B)  $k_{slow}$  parameters for pre-steady state heme reduction of NarGHI by menadiol.** Intensity of bars represent mean values of  $\geq 4$  replicates with error bars representing the standard deviation. \*K86A pH 6 and all NarGHI-devoid membrane vesicle control traces were fit to a single component, therefore the same values for these samples are displayed in the  $k_{fast}$  and  $k_{slow}$  charts for comparison.

only marginally greater than background levels. NarGHI<sup>Met156Lys/Lys86Ala</sup>  $k_{fast}$  levels are intermediate (**Figure 6.4A**). The  $k_{slow}$  rates of all variants (**Figure 6.4B**), however, are drastically reduced compared to wild-type and are indistinguishable from background rates, indicating that subsequent reactions, *i.e.* active site regeneration via proton transfer and/or electron transfer, have become slowed. We noted that the double variant did not exhibit near wild-type activity as expected from the growth assays. This is likely reflects the use of high substrate levels of a non-physiological quinol analog (menadiol). Further, the *in vitro* activity and growth assays report on steady state activity, while **Figure 6.4** reports pre-steady state kinetics. Therefore, the largest effects on activity for NarGHI<sup>Met156Lys</sup> and NarGHI<sup>Met156Lys/Lys86Ala</sup> are seen in the earliest, non-rate limiting, stages of turnover, likely the initial proton and electron transfer.

It is apparent from the trends in  $k_{fast}$  that the electrostatic environment within NarI has been changed upon mutation of Met156 to Lys. Specifically, the  $pK_a$  of  $>10$

previously attributed to Lys86 by pre-steady state kinetics appears decreased by 1-2 pH units<sup>331</sup>. The double variant is more significantly affected, as wild-type activity is not achieved at any pH. PROPKA 3.1 analysis of NarI (PDB ID 3EGW) is roughly correct in predicting a Lys86  $pK_a$  of 9.63<sup>341</sup>. The NarGHI<sup>Met156Lys</sup> variant is predicted to exhibit  $pK_a$ s for Lys86 and Lys156 of 9.62 and 7.58, respectively. The double mutant NarGHI<sup>Met156Lys/Lys86Ala</sup> has a similarly predicted NarGHI<sup>Met156Lys</sup>  $pK_a$  of 7.88, in agreement with the pH profile observed for  $k_{fast}$ . As the PROPKA predictions are based on NarI out of a membrane environment, these  $pK_a$  values are only approximations. This drastic difference in predicted  $pK_a$  for the two positions of Lys indicates that in the position approximated by having a Lys at NarI<sup>156</sup>, the terminal amine is in a more hydrophobic environment and more likely to be reversibly protonated<sup>340</sup>, a key feature if it is to take up a proton from quinol O4. That is, the  $pK_a$  of Lys86 in wild-type NarGHI can be modulated based on its conformation and therefore function in proton transfer from the quinol O4 to the periplasm.

A functional feature of many membrane bound oxidoreductases is the presence of a proton transfer network or pathway<sup>363,367,370,376</sup>. As a component of these proton transfer pathways, there are crucial ionizable residues that in many cases are conformationally flexible, going between two or more conformational states in order to accomplish proton transfer between the quinone/quinol and aqueous milieu, or simply to gate proton transfer through a proton transfer pathway. One example is His201 and Lys227 of the  $Q_i$  site of cytochrome  $bc_1$ , where both adopt two conformations as observed in crystal structures of the yeast and bovine complexes<sup>372</sup>. Upon quinone reduction and proton transfer, Lys227 and His201 move away from the substrate where Lys227 specifically rotates  $\sim 180^\circ$  to accept a matrix proton<sup>372</sup>. Similarly, function of the  $Q_o$  site of cytochrome  $bc_1$  involves movement of Glu272 such that it can aid in deprotonation of the quinol then rotate  $\sim 180^\circ$  to interact with heme  $b_L$  to facilitate proton transfer<sup>363,371</sup>. The origins for such conformational changes lie in protonation state of the residue and oxidation state of the protein.

In NarGHI we only observe one oxidation state of the enzyme (oxidized) in the

crystal structures, and the Q-site is either unoccupied or has PCP bound but no other quinone substrates or analogs<sup>19,183,244</sup>. In these structures, Lys86 adopts an extended conformation whereby N $\zeta$  is ~6 Å from the quinol O4. Yet Lys86 is critical for Q-site function and the defective variant NarI<sup>Lys86Ala</sup> can be rescued by incorporating a Lys at NarI<sup>156</sup>. In this variant the N $\zeta$  of Lys156 is within hydrogen bonding distance of the quinol O4 and thus explains the recovery of activity. Lys86 therefore does appear to direct proton transfer from the Q-site to the periplasm<sup>331</sup>. Following initial H<sup>+</sup>+e<sup>-</sup> transfer from the quinol, the neutral semiquinone is bound via a one-sided hydrogen bond to His66<sup>168,170,359</sup> and possibly *b<sub>D</sub>* propionate D as Lys86 moves out of interaction with the semiquinone. This one-sided hydrogen bond is expected to decrease the SQ/QH<sub>2</sub> couple thereby preventing back-flow of electrons in NarI<sup>168,364,377</sup>. What would drive the conformational changes of Lys86 is not known, however it is likely linked to the oxidation states of heme *b<sub>D</sub>* (and possibly *b<sub>P</sub>*), and the quinone. A possibility is that, with the semiquinone being neutral, Lys86 will be stabilized in the extended conformation due to its intrinsic affinity for the negative dipole of NarI helix II. The changes in conformation, as well as Q-site occupancy, would in turn be associated with changes in p*K<sub>a</sub>*.

## 6.4. Conclusion

In conclusion, we have demonstrated that a secondary variant, NarGHI<sup>Met156Lys/Lys86Ala</sup>, is able to functionally restore activity of the NarGHI<sup>Lys86Ala</sup> variant. We interpret this as evidence that Lys86 adopts two conformations, one in which quinol O4 proton abstraction is allowed and one observed in crystal structures where Lys86 is elongated and hydrogen bonded to a conserved water. This not only has implications in PMF generation, but also semiquinone stability and the flow of electrons through NarGHI.

## 6.5. Supplementary Material

Variant	$A_{\text{fast}}$	$k_{\text{fast}} (\text{s}^{-1})$	$A_{\text{slow}}$	$k_{\text{slow}} (\text{s}^{-1})$	$P$
NarGHI	$-0.0253 \pm 7e-4$	$116 \pm 6$	$-0.0169 \pm 4e-4$	$6.0 \pm 0.4$	$0.0483 \pm 2e-4$
NarGHI <sup>M156K</sup>	$-0.0037 \pm 4e-4$	$126 \pm 32$	$-0.0293 \pm 3e-4$	$1.98 \pm 0.06$	$0.0327 \pm 3e-4$
NarGHI <sup>M156K/K86A</sup>	$-0.0105 \pm 3e-4$	$68 \pm 4$	$-0.0315 \pm 2e-4$	$1.65 \pm 0.04$	$0.0428 \pm 3e-4$
NarGHI <sup>K86A</sup>	$-0.007 \pm 1e-3$	$10 \pm 2$	$-0.0187 \pm 8e-4$	$1.3 \pm 0.2$	$0.0249 \pm 9e-4$
$\Delta$ NarGHI	$-0.0116 \pm 2e-4$	$2.3 \pm 0.1$		N.A.	$0.0149 \pm 2e-4$

**Supplementary Table 6.1: Fitting parameters for pre-steady state heme reduction by menadiol** Heme reduction of NarGHI-enriched vesicles of NarGHI, NarGHI<sup>M156K</sup>, NarGHI<sup>K86A</sup>, NarGHI<sup>M156K/K86A</sup> and NarGHI-devoid vesicles as depicted in **Figure 6.3**. The parameters correspond to those in **equation 6.2**. Values are reported as mean  $\pm$  standard error of fitting over a 2 s time range. N.A. = Not Applicable (single component fitting).

## 7. Conclusions and Future Directions

Over the last several years I have worked to gain a more intimate understanding of *E. coli* nitrate reductase (NarGHI), and in particular its membrane subunit, NarI. The work included in this thesis focuses on two related aspects of NarI. The first is the electrochemical and biophysical properties of the two hemes and the energetics of transmembrane electron transfer. The second major theme of my work has been on characterizing the Q-site through site-directed mutagenesis, EPR spectroscopy of the SQ, and enzyme kinetics. That quinol oxidation involves heme  $b_D$ , and quinone binding influences the electrochemical and biophysical properties of heme  $b_D$ , unites the two themes.

So why did I study nitrate reductase? First, it is representative of a broad family bacterial respiratory proteins, the DMSO reductase family of molybdoenzymes<sup>378</sup>, and also shares common elements of enzymes in mitochondrial oxidative phosphorylation. For instance, the transmembrane electron transfer between hemes  $b_D$  and  $b_P$  of NarI is similar to the same process in the cytochrome subunit of complex III<sup>22,379</sup>. Furthermore, the Q-cycle within complex III involves the same quinone chemistry as in nitrate reductase, or any other quinone oxidoreductases<sup>179,380,381</sup>. The better we understand the processes of specific enzymes, the better able we are to rationalize the processes in similar but distinct systems. The second reason *E. coli* nitrate reductase is an ideal subject to study is the ease by which it can be highly over expressed, and its stability *in vitro*<sup>19,258,286,296,382</sup>. This has allowed NarGHI to be highly characterized by various techniques, such as crystallography, x-ray absorption spectroscopy, protein film voltammetry and EPR, where enriched vesicles are near spectroscopic purity<sup>19,153,183,239,240,258,321</sup>.

## 7.1. Heme Electrochemical and Biophysical Characteristics

In the first section of this thesis, comprising **Chapter 2** and **Chapter 3**, I primarily sought to better characterize the thermodynamics of transmembrane electron transfer through the NarI redox system:  $b_D$ ,  $b_P$ , and FS4. EPR is the method of choice for this characterization since the hemes of NarI are well resolved from each

other and from the other redox cofactors of NarGH (i.e. FS4). The nature of the EPR signal position ( $g_z$ -value) of hemes  $b_D$  and  $b_P$  largely reports on the coordination geometry by their two axial histidine ligands<sup>268,273</sup>. Perturbation of the interplanar His dihedral angle changes the position of the  $g_z$  value reported by EPR. For instance, the heme  $b_D$   $g_z$  spectral feature is much more broad than that of  $b_P$ , a reflection of its greater structural variability compared to  $b_P$  because of its proximity to the Q-site. Furthermore, binding of Q-site inhibitors alters the peak position of the  $b_D$  EPR signal, as the binding slightly alters the axial His ligand (His66) angle with respect to the second His (His187)<sup>183,268,275</sup>. In as-is prepared NarGHI, heme  $b_D$  exhibits heterogeneity in its  $g_z$  EPR feature, where in **Chapter 2** I showed that the degree of heterogeneity can be correlated with the degree of aeration by which overexpression occurred<sup>321</sup>. Specifically, I demonstrated that one of the heme conformations ( $g_z = 3.34$ ) is associated with a quinone-bound state, and the other ( $g_z = 3.18$ ) is a result of a Q-site devoid of quinone. Even more significantly, I demonstrated that the binding of quinone influences the heme  $b_D$  redox characteristics, such as  $E_m$  and pH dependence. In the quinone-free state, heme  $b_D$  exhibits an  $E_{m,8}$  of +25 mV and a pH dependence of -59 mV pH<sup>-1</sup>. When quinone is bound, the  $E_{m,8}$  shifts to -35 mV and the pH dependence drops to -40 mV pH<sup>-1</sup>. The presence of the quinone clearly modulates the heme  $b_D$  properties and this therefore serves to caution future studies – to account for both components when looking at heme  $b_D$  redox properties.

With the issue of heme  $b_D$  heterogeneity clarified, it was possible to more thoroughly characterize the energetics of transmembrane electron transfer. In **Chapter 3** I addressed some issues of the “redox weirdness” of the  $b_D$ ,  $b_P$  and FS4 system. The hemes either require two ideal components in redox titration fitting or electron stoichiometries ( $n$ ) of < 1; and FS4 also requires two ideal components<sup>132,213,278</sup>. Also, the binding of Q-site inhibitors, HOQNO in particular, drastically modulates the redox characteristics of both hemes, despite HOQNO only binding adjacent heme  $b_D$ <sup>132,183,270</sup>. I developed a model whereby the electrostatic interactions between redox cofactors is accounted for and this not only yielded improved fits, but also revealed a more reasonable origin for the redox behaviour of HOQNO-bound

NarGHI<sup>132</sup>. The interaction between FS4 and heme  $b_P$  was found to be strongest, being approximately -50 mV, and while it seems likely that a similar interaction between the two hemes occurs in as-is NarGHI, the separation of their  $E_m$  values precluded my elucidation of their interaction. Also as a result of this model, are revised microscopic  $E_m$  values for  $b_D$ ,  $b_P$  and FS4. This results in a new perspective on the thermodynamics of transmembrane electron transfer through NarGHI as well as the effect of Q-site inhibitor binding to NarI. The main functional feature of this revised model is that upon becoming increasingly reduced, electron flow across the membrane is expected to slow, and electron equilibration between the two hemes ensures a greater extent of heme  $b_D$  reduction. This in turn ensures enhanced stabilization of SQ intermediate. This has implications in *E. coli* respiratory control and NarGHI activity.

With regards to this section there are two main aspects that require future work. First, in order to better understand the thermodynamics and kinetics of electron transfer through the entire NarGHI system, an extended redox interaction model will need to be applied to every other cofactor, including Moco and quinone transitions. For instance, data now shown in this thesis indicates that the oxidation state of the quinone has significant effects on the heme  $b_D$  redox properties. Furthermore, the presence of very low potential FeS clusters along electron transfer relays is a common feature of integral membrane oxidoreductases<sup>2</sup>. Is the very low potential of NarGHI FS2 ( $E_{m,8} = -420$  mV) just a consequence of redox anti-cooperativity<sup>213</sup>, or is the  $E_m$  of FS2 deliberately tuned that low by the protein environment<sup>258,265,296,375</sup>? In either case, what is the physiological effect of having such low potential FeS clusters along an electron transfer relay, in general? A similar question is why do electron transfer relays have to be so long? Could not Nature just couple the quinone subunit and the catalytic subunit directly, or is long distance separation a requirement for optimal activity of such enzymes?

## 7.2. Quinol Oxidation by NarI

In **Chapters 4-6**, I sought to determine the mechanism by which NarI catalyses quinol oxidation. Quinol is a  $2e^-/2H^+$  carrier, and as such there are two separate electron transfer steps and two deprotonation events, which may or may not be concurrent with the electron transfers. Generally, quinol oxidation proceeds through an anionic SQ intermediate, where the first step involves double deprotonation and a one electron oxidation<sup>2,383,384</sup>. However, there are examples where a neutral SQ is the intermediate<sup>329</sup>, where only one proton and one electron are transferred in the first step. I needed to determine which was the case for NarGHI, and also determine what role conserved residues play in quinol oxidation, and how the protons get from the quinol to the periplasm.

In **Chapter 4**, redox titrations of the SQ, by EPR, over a range of pH values revealed that the MSQ bound to NarGHI is neutral (protonated), with a  $pK_a$  of  $\sim 8.7$ . This work also determined that Q-site occupancy is pH dependent, where maximal occupancy is at high pH ( $pK_a$  Nar  $\sim 7$ ). This agrees with a similar finding for the pH dependence of heme heterogeneity in **Chapter 2**, where I observed that the Q-bound form of heme  $b_D$  is favoured at high pH<sup>321</sup>. I reasoned that  $pK_a$  Nar is likely attributable to heme  $b_D$  propionate D, and His66 is expected to have a higher  $pK_a$ , and so does not undergo deprotonation during turnover. The model used to determine these values agrees with previously published  $E_m$  values for MSQ and indicates that, while NarGHI preferentially binds MQH<sub>2</sub> over MQ, this preference is marginal ( $K_{red}/K_{ox} = 0.5$ )<sup>45</sup>. We also found that, contrary to previous findings, the stability of the MSQ is actually in line with similar enzymes ( $K_{stab} \sim 2.3$ )<sup>45</sup>. Less physiologically relevant, we also probed the SQ bound to NarI( $\Delta$ GH) and determined that the bound DMSQ exhibits similar, but different, electrochemical properties to MSQ bound to NarGHI. This is likely due to the combined effect of NarI being in an altered conformation in the absence of NarGH, and that DMQ and MQ have slightly different intrinsic properties<sup>38</sup>. Importantly, however, I found that the pH dependence of Q-site occupancy is the same in the two systems ( $pK_a$  Nar  $\sim 7$ ). Thus, the two major findings of this chapter

were that quinol oxidation progresses through a protonated SQ intermediate, and that quinone binding is pH dependent.

In **Chapter 5**, the focus was on what role the Q-site residue Lys86 plays in quinol oxidation and binding. That Lys86 is critical for these processes has been known for several years now <sup>183,284</sup>. However, it was not previously determined what role Lys86 played exactly. It does not interact with the SQ, and in crystal structures its orientation seems inappropriate for interacting with the quinol <sup>170,183</sup>. It had been suggested that Lys86 was involved in the initial stages of quinol binding and deprotonation, but there was no experimental evidence to support this claim <sup>183</sup>. By using a variety of NarI<sup>86</sup> variants, I was able to show that as long as NarI<sup>86</sup> is an ionizable residue (Lys, Asp, Glu, His), quinol oxidation is catalysed. Thus, Lys86 is indeed involved in quinol deprotonation, exhibiting a  $pK_a$  of  $\geq 10$ , and that changing this residue to His or Glu modified this  $pK_a$  ( $>10$  and 8.9, respectively). It was also found that the pH dependence of heme reduction by menadiol follows a bell-shaped curve, where the second  $pK_a$  of  $\sim 6$  is attributed to heme  $b_D$  propionate D. In the first section of this thesis I suggested that heme  $b_D$  propionate D is likely responsible for the pH dependent binding of quinone to NarI, which is further supported here. However, in **Chapter 4** the  $pK_a$ Nar determined is 7, and in **Chapter 5** it is 6. This moderate discrepancy is due to the different methodologies used, especially that  $pK_a$ Nar of 7 is thermodynamically derived, while the  $pK_a$  of 6 is kinetically derived. In either case,  $b_D$  propionate D is suited to maintaining a neutral SQ and only deprotonating the oxidized quinone. Taking together these data has allowed me to assemble a mechanism for quinol oxidation (see **Figure 5.5**), where Lys86 abstracts the first proton from the menaquinol O4, followed by a conformational change where Lys86 swings away from the SQ and points towards the periplasm. Heme  $b_D$  propionate D is a component of a hydrogen bonding network leading from the Q-site to the periplasm, and thus transfer of the second proton from quinone to propionate D, facilitates proton transfer to the periplasm.

**Chapter 6** built on the work in **Chapter 5** by further probing proton transfer from quinol O4 by Lys86 to the periplasm. Using software (Caver) to map any

channels leading from the Q-site <sup>373</sup>, the Lys86 proton transfer pathway was indeed found. A residue that shares similar conservation to Lys86, Met156, also lines this pathway and so mutagenesis studies on it were conducted. Importantly, mutation of Met156 to Lys significantly restored activity of the inactive NarI<sup>K86A</sup> variant, though the pH dependence was effected – likely tied to changes in heme *b<sub>D</sub>* *E<sub>m</sub>*. I suggest that this is evidence for an alternative conformation of Lys86, or at least further evidence in support of the Lys86 proton pathway.

The work conducted in Section 2 has contributed greatly to our understanding of quinol oxidation and binding in NarGHI. The mechanism proposed is consistent with previous observations and is similar to that of other quinol oxidases. The findings reported here can be applied to further increasing our understanding of NarI function and also to other quinone-binding proteins. Though, I completely neglected UQ in these studies, so future work will need to be done on USQ and UQH<sub>2</sub> oxidation to determine if it is similar to MQ. Moreover, in order to confirm the protonation states and *pK<sub>a</sub>* values for the various residues involved in quinol oxidation requires other biophysical methods. Fourier Transform Infrared (FTIR) spectroscopy has previously been used to determine the protonation states of acidic residues and heme propionates <sup>186,385–387</sup>. It would be wise to do similar studies on NarI to determine the protonation states of heme *b<sub>D</sub>* propionate D, His66 and Lys86 under various conditions (pH and *E<sub>h</sub>*). Similar studies using FTIR can be conducted on the SQ to confirm its protonation <sup>388</sup>. EPR studies on the heme and SQ properties of the various NarI variants also needs to be conducted, though these experiments are expensive. Further biophysical work and QM/MM simulations should also be conducted on NarI to determine the validity of Lys86 undergoing conformational flexing during quinol binding and oxidation, as well as to determine the likely routes for proton egress <sup>369,389,390</sup>. These simulations would also be valuable in determining whether QH<sub>2</sub>/SQ/Q exhibit alternative binding modes. Though, this is unlikely given the near identical *K<sub>d</sub>*s for the reduced and oxidized forms of quinone. Finally, much more detailed thermodynamic and kinetic analysis should be conducted on quinol binding and oxidation. Temperature dependence of quinol oxidation can provide insight into

transition state energies, for instance <sup>6,334</sup>. Also, I had intended to look at what role the isoprenoid tail of quinol plays in binding to NarI. Such experiments would also help clarify the origin of the splittings in the DMSQ EPR signal, which I hypothesize is due to the isoprenoid tail C $\beta$  hydrogens.

In conclusion, this thesis has shed light on the complexity of NarGHI, specifically with regards to the mechanisms of transmembrane electron transfer and quinol oxidation in NarI. While much work needs to be done on the molecular details, we also need to think more about NarGHI in the context of the cell. Does it comprise respiratory supercomplexes <sup>29</sup>? Is NarGHI spatio-temporally regulated, as recently proposed <sup>29</sup>? What are the exact mechanisms by which it matures <sup>244,290,391</sup>? But for me, the holy grail of NarGHI would be a full kinetic and thermodynamic model for quinol oxidation, electron transfer, and nitrate reduction. Much more characterization of the entire enzyme will need to be done, but the shear intellectual rewards of this highly difficult and laborious endeavour would be supremely satisfying.

## 8. References

- (1) Schrodinger, E. (2012) *What is Life?: With Mind and Matter and Autobiographical Sketches* Reprint edition. Cambridge University Press.
- (2) Nicholls, D. G., and Ferguson, S. J. (2013) *Bioenergetics* 4th ed. Academic Press, London.
- (3) Tran, Q. H., and Uden, G. (1998) Changes in the proton potential and the cellular energetics of *Escherichia coli* during growth by aerobic and anaerobic respiration or by fermentation. *Eur. J. Biochem.* 251, 538–543.
- (4) Mitchell, P. (1961) Coupling of phosphorylation to electron and hydrogen transfer by a chemiosmotic type of mechanism. *Nature* 191, 144–148.
- (5) Peter Mitchell - Nobel Lecture: David Keilin's respiratory chain concept and its chemiosmotic consequences.
- (6) Atkins, P., and De Paula, J. (2009) *Physical Chemistry* 9th ed. W. H. Freeman, New York.
- (7) Nicholls, D. G., and Ward, M. W. (2000) Mitochondrial membrane potential and neuronal glutamate excitotoxicity: mortality and millivolts. *Trends Neurosci.* 23, 166–174.
- (8) Kim, N., Ripple, M. O., and Springett, R. (2012) Measurement of the mitochondrial membrane potential and pH gradient from the redox poise of the hemes of the *bc<sub>1</sub>* complex. *Biophys. J.* 102, 1194–1203.
- (9) Porcelli, A. M., Ghelli, A., Zanna, C., Pinton, P., Rizzuto, R., and Rugolo, M. (2005) pH difference across the outer mitochondrial membrane measured with a green fluorescent protein mutant. *Biochem. Biophys. Res. Commun.* 326, 799–804.
- (10) Cammack, R. (1996) Redox states and potentials, in *Bioenergetics: A Practical Approach*, pp 85–105. Oxford University Press.
- (11) Nelson, D. L., and Cox, M. M. (2012) *Lehninger Principles of Biochemistry* 6th ed. W H Freeman & Co, New York.
- (12) Wickstrand, C., Dods, R., Royant, A., and Neutze, R. (2015) Bacteriorhodopsin: Would the real structural intermediates please stand up? *Biochim. Biophys. Acta BBA - Gen. Subj.* 1850, 536–553.

- (13) Sazanov, L. A. (2014) The mechanism of coupling between electron transfer and proton translocation in respiratory complex I. *J. Bioenerg. Biomembr.* *46*, 247–253.
- (14) Sharma, V., Belevich, G., Gamiz-Hernandez, A. P., Róg, T., Vattulainen, I., Verkhovskaya, M. L., Wikström, M., Hummer, G., and Kaila, V. R. I. (2015) Redox-induced activation of the proton pump in the respiratory complex I. *Proc. Natl. Acad. Sci. U. S. A.* *112*, 11571–11576.
- (15) Simon, J., van Spanning, R. J. M., and Richardson, D. J. (2008) The organisation of proton motive and non-proton motive redox loops in prokaryotic respiratory systems. *Biochim. Biophys. Acta* *1777*, 1480–1490.
- (16) Lester, R. L., and DeMoss, J. A. (1971) Effects of molybdate and selenite on formate and nitrate metabolism in *Escherichia coli*. *J. Bacteriol.* *105*, 1006–1014.
- (17) Enoch, H. G., and Lester, R. L. (1975) The purification and properties of formate dehydrogenase and nitrate reductase from *Escherichia coli*. *J. Biol. Chem.* *250*, 6693–6705.
- (18) Jormakka, M., Törnroth, S., Byrne, B., and Iwata, S. (2002) Molecular basis of proton motive force generation: structure of formate dehydrogenase-N. *Science* *295*, 1863–1868.
- (19) Bertero, M. G., Rothery, R. A., Palak, M., Hou, C., Lim, D., Blasco, F., Weiner, J. H., and Strynadka, N. C. (2003) Insights into the respiratory electron transfer pathway from the structure of nitrate reductase A. *Nat. Struct. Biol.* *10*, 681–687.
- (20) Jones, R. W., Lamont, A., and Garland, P. B. (1980) The mechanism of proton translocation driven by the respiratory nitrate reductase complex of *Escherichia coli*. *Biochem. J.* *190*, 79–94.
- (21) Uden, G., and Bongaerts, J. (1997) Alternative respiratory pathways of *Escherichia coli*: energetics and transcriptional regulation in response to electron acceptors. *Biochim. Biophys. Acta* *1320*, 217–234.
- (22) Crofts, A. R. (2004) The cytochrome *bc<sub>1</sub>* complex: Function in the context of structure. *Annu. Rev. Physiol.* *66*, 689–733.
- (23) Richardson, D. J. (2000) Bacterial respiration: a flexible process for a changing environment. *Microbiol. Read. Engl.* *146 (Pt 3)*, 551–571.
- (24) Sargent, F. (2007) Constructing the wonders of the bacterial world: biosynthesis of complex enzymes. *Microbiology* *153*, 633–651.

- (25) Kumar, R., and Shimizu, K. (2011) Transcriptional regulation of main metabolic pathways of *cyoA*, *cydB*, *fnr*, and *fur* gene knockout *Escherichia coli* in C-limited and N-limited aerobic continuous cultures. *Microb. Cell Factories* 10, 3.
- (26) Gunsalus, R. P., and Park, S.-J. (1994) Aerobic-anaerobic gene regulation in *Escherichia coli*: control by the ArcAB and Fnr regulons. *Res. Microbiol.* 145, 437–450.
- (27) Sousa, P. M. F., Videira, M. A. M., Bohn, A., Hood, B. L., Conrads, T. P., Goulao, L. F., and Melo, A. M. P. (2012) The aerobic respiratory chain of *Escherichia coli*: from genes to supercomplexes. *Microbiology* 158, 2408–2418.
- (28) Sousa, P. M. F., Silva, S. T. N., Hood, B. L., Charro, N., Carita, J. N., Vaz, F., Penque, D., Conrads, T. P., and Melo, A. M. P. (2011) Supramolecular organizations in the aerobic respiratory chain of *Escherichia coli*. *Biochimie* 93, 418–425.
- (29) Lenn, T., Leake, M. C., and Mullineaux, C. W. (2008) Are *Escherichia coli* OxPhos complexes concentrated in specialized zones within the plasma membrane? *Biochem. Soc. Trans.* 36, 1032.
- (30) Alberge, F., Espinosa, L., Seduk, F., Sylvi, L., Toci, R., Walburger, A., and Magalon, A. (2015) Dynamic subcellular localization of a respiratory complex controls bacterial respiration. *eLife* 4.
- (31) Toya, Y., Nakahigashi, K., Tomita, M., and Shimizu, K. (2012) Metabolic regulation analysis of wild-type and *arcA* mutant *Escherichia coli* under nitrate conditions using different levels of omics data. *Mol. Biosyst.* 8, 2593–2604.
- (32) Lü, W., Du, J., Schwarzer, N. J., Wacker, T., Andrade, S. L. A., and Einsle, O. (2013) The formate/nitrite transporter family of anion channels. *Biol. Chem.* 394, 715–727.
- (33) Leonhartsberger, S., Korsá, I., and Böck, A. (2002) The molecular biology of formate metabolism in enterobacteria. *J. Mol. Microbiol. Biotechnol.* 4, 269–276.
- (34) Pecher, A., Zinoni, F., Jatisatienr, C., Wirth, R., Hennecke, H., and Böck, A. (1983) On the redox control of synthesis of anaerobically induced enzymes in *Enterobacteriaceae*. *Arch. Microbiol.* 136, 131–136.
- (35) Gunsalus, R. P. (1992) Control of electron flow in *Escherichia coli*: coordinated transcription of respiratory pathway genes. *J. Bacteriol.* 174, 7069–7074.
- (36) Calhoun, M. W., Oden, K. L., Gennis, R. B., Mattos, M. J. de, and Neijssel, O. M. (1993) Energetic efficiency of *Escherichia coli*: effects of mutations in components of

the aerobic respiratory chain. *J. Bacteriol.* 175, 3020–3025.

(37) Puustinen, A., Finel, M., Haltia, T., Gennis, R. B., and Wikstrom, M. (1991) Properties of the two terminal oxidases of *Escherichia coli*. *Biochemistry* 30, 3936–3942.

(38) Holländer, R. (1976) Correlation of the function of demethylmenaquinone in bacterial electron transport with its redox potential. *FEBS Lett.* 72, 98–100.

(39) Søballe, B., and Poole, R. K. (1999) Microbial ubiquinones: multiple roles in respiration, gene regulation and oxidative stress management. *Microbiol. Read. Engl.* 145 (Pt 8), 1817–1830.

(40) Wallace, B. J., and Young, I. G. (1977) Role of quinones in electron transport to oxygen and nitrate in *Escherichia coli*. Studies with a *ubiA<sup>-</sup> menA<sup>-</sup>* double quinone mutant. *Biochim. Biophys. Acta BBA - Bioenerg.* 461, 84–100.

(41) Shestopalov, A. I., Bogachev, A. V., Murtazina, R. A., Viryasov, M. B., and Skulachev, V. P. (1997) Aeration-dependent changes in composition of the quinone pool in *Escherichia coli*: Evidence of post-transcriptional regulation of the quinone biosynthesis. *FEBS Lett.* 404, 272–274.

(42) Wissenbach, U., Kröger, A., and Uden, G. (1990) The specific functions of menaquinone and demethylmenaquinone in anaerobic respiration with fumarate, dimethylsulfoxide, trimethylamine N-oxide and nitrate by *Escherichia coli*. *Arch. Microbiol.* 154, 60–66.

(43) Wissenbach, U., Ternes, D., and Uden, G. (1992) An *Escherichia coli* mutant containing only demethylmenaquinone, but no menaquinone: effects on fumarate, dimethylsulfoxide, trimethylamine N-oxide and nitrate respiration. *Arch. Microbiol.* 158, 68–73.

(44) Sharma, P., Teixeira de Mattos, M. J., Hellingwerf, K. J., and Bekker, M. (2012) On the function of the various quinone species in *Escherichia coli*. *FEBS J.* 279, 3364–3373.

(45) Rendon, J., Pilet, E., Fahs, Z., Seduk, F., Sylvi, L., Hajj Chehade, M., Pierrel, F., Guigliarelli, B., Magalon, A., and Grimaldi, S. (2015) Demethylmenaquinol is a substrate of *Escherichia coli* nitrate reductase A (NarGHI) and forms a stable semiquinone intermediate at the NarGHI quinol oxidation site. *Biochim. Biophys. Acta BBA - Bioenerg.* 1847, 739–747.

(46) Tseng, C. P., Albrecht, J., and Gunsalus, R. P. (1996) Effect of microaerophilic cell growth conditions on expression of the aerobic (*cyoABCDE* and *cydAB*) and

anaerobic (*narGHJI*, *frdABCD*, and *dmsABC*) respiratory pathway genes in *Escherichia coli*. *J. Bacteriol.* 178, 1094–1098.

(47) Henkel, S. G., Beek, A. T., Steinsiek, S., Stagge, S., Bettenbrock, K., de Mattos, M. J. T., Sauter, T., Sawodny, O., and Ederer, M. (2014) Basic regulatory principles of *Escherichia coli*'s electron transport chain for varying oxygen conditions. *PLoS ONE* 9, e107640.

(48) Spiro, S., and Guest, J. R. (1990) FNR and its role in oxygen-regulated gene expression in *Escherichia coli*. *FEMS Microbiol. Rev.* 6, 399–428.

(49) Green, J., Scott, C., and Guest, J. R. (2001) Functional versatility in the CRP-FNR superfamily of transcription factors: FNR and FLP (Physiology, B.-A. in M., Ed.), pp 1–34. Academic Press.

(50) Crack, J., Green, J., and Thomson, A. J. (2004) Mechanism of oxygen sensing by the bacterial transcription factor fumarate-nitrate reduction (FNR). *J. Biol. Chem.* 279, 9278–9286.

(51) Bettenbrock, K., Bai, H., Ederer, M., Green, J., Hellingwerf, K. J., Holcombe, M., Kunz, S., Rolfe, M. D., Sanguinetti, G., Sawodny, O., Sharma, P., Steinsiek, S., and Poole, R. K. (2014) Chapter Two - Towards a Systems Level Understanding of the Oxygen Response of *Escherichia coli*, in *Advances in Microbial Physiology* (Poole, R. K., Ed.), pp 65–114. Academic Press.

(52) Lazazzera, B. A., Bates, D. M., and Kiley, P. J. (1993) The activity of the *Escherichia coli* transcription factor FNR is regulated by a change in oligomeric state. *Genes Dev.* 7, 1993–2005.

(53) Zhang, B., Crack, J. C., Subramanian, S., Green, J., Thomson, A. J., Le Brun, N. E., and Johnson, M. K. (2012) Reversible cycling between cysteine persulfide-ligated [2Fe-2S] and cysteine-ligated [4Fe-4S] clusters in the FNR regulatory protein. *Proc. Natl. Acad. Sci. U. S. A.* 109, 15734–15739.

(54) Noriega, C. E., Lin, H.-Y., Chen, L.-L., Williams, S. B., and Stewart, V. (2010) Asymmetric cross-regulation between the nitrate-responsive NarX–NarL and NarQ–NarP two-component regulatory systems from *Escherichia coli* K-12. *Mol. Microbiol.* 75, 394–412.

(55) Rabin, R. S., and Stewart, V. (1993) Dual response regulators (NarL and NarP) interact with dual sensors (NarX and NarQ) to control nitrate- and nitrite-regulated gene expression in *Escherichia coli* K-12. *J. Bacteriol.* 175, 3259–3268.

(56) Goh, E.-B., Bledsoe, P. J., Chen, L.-L., Gyaneshwar, P., Stewart, V., and Igo, M.

M. (2005) Hierarchical control of anaerobic gene expression in *Escherichia coli* K-12: The nitrate-responsive NarX-NarL regulatory system represses synthesis of the fumarate-responsive DcuS-DcuR regulatory system. *J. Bacteriol.* 187, 4890–4899.

(57) Stewart, V., and Bledsoe, P. J. (2003) Synthetic lac operator substitutions for studying the nitrate- and nitrite-responsive NarX-NarL and NarQ-NarP two-component regulatory systems of *Escherichia coli* K-12. *J. Bacteriol.* 185, 2104–2111.

(58) Darwin, A. J., Li, J., and Stewart, V. (1996) Analysis of nitrate regulatory protein NarL-binding sites in the *fdnG* and *narG* operon control regions of *Escherichia coli* K-12. *Mol. Microbiol.* 20, 621–632.

(59) Magalon, A., Fedor, J. G., Walburger, A., and Weiner, J. H. (2011) Molybdenum enzymes in bacteria and their maturation. *Coord. Chem. Rev.* 255, 1159–1178.

(60) Anderson, L. A., McNairn, E., Leubke, T., Pau, R. N., and Boxer, D. H. (2000) ModE-dependent molybdate regulation of the molybdenum cofactor operon *moa* in *Escherichia coli*. *J. Bacteriol.* 182, 7035–7043.

(61) Uden, G., and Guest, J. R. (1985) Isolation and characterization of the Fnr protein, the transcriptional regulator of anaerobic electron transport in *Escherichia coli*. *Eur. J. Biochem. FEBS* 146, 193–199.

(62) Hille, R., Hall, J., and Basu, P. (2014) The mononuclear molybdenum enzymes. *Chem. Rev.* 114, 3963–4038.

(63) Self, W. T., Grunden, A. M., Hasona, A., and Shanmugam, K. T. (1999) Transcriptional regulation of molybdoenzyme synthesis in *Escherichia coli* in response to molybdenum: ModE-molybdate, a repressor of the *modABCD* (molybdate transport) operon is a secondary transcriptional activator for the *hyc* and *nar* operons. *Microbiology* 145, 41–55.

(64) Regulski, E. E., Moy, R. H., Weinberg, Z., Barrick, J. E., Yao, Z., Ruzzo, W. L., and Breaker, R. R. (2008) A widespread riboswitch candidate that controls bacterial genes involved in molybdenum cofactor and tungsten cofactor metabolism. *Mol. Microbiol.* 68, 918–932.

(65) Edwards, A. N., Patterson-Fortin, L. M., Vakulskas, C. A., Mercante, J. W., Potrykus, K., Vinella, D., Camacho, M. I., Fields, J. A., Thompson, S. A., Georgellis, D., Cashel, M., Babitzke, P., and Romeo, T. (2011) Circuitry linking the Csr and stringent response global regulatory systems. *Mol. Microbiol.* 80, 1561–1580.

(66) Page, C. C., Moser, C. C., Chen, X., and Dutton, P. L. (1999) Natural engineering principles of electron tunnelling in biological oxidation-reduction. *Nature* 402, 47–52.

- (67) DeVault, D., and Chance, B. (1966) Studies of photosynthesis using a pulsed laser. I. Temperature dependence of cytochrome oxidation rate in *chromatium*. Evidence for tunneling. *Biophys. J.* 6, 825–847.
- (68) Marcus, R. A., and Sutin, N. (1985) Electron transfers in chemistry and biology. *Biochim. Biophys. Acta BBA - Rev. Bioenerg.* 811, 265–322.
- (69) Dick, L. A., Malfant, I., Kuila, D., Nebolsky, S., Nocek, J. M., Hoffman, B. M., and Ratner, M. A. (1998) Cryogenic electron tunneling within mixed-metal hemoglobin hybrids: Protein glassing and electron-transfer energetics. *J. Am. Chem. Soc.* 120, 11401–11407.
- (70) Winkler, J. R., and Gray, H. B. (2014) Electron flow through metalloproteins. *Chem. Rev.* 114, 3369–3380.
- (71) Moser, C. C., Keske, J. M., Warncke, K., Farid, R. S., and Dutton, P. L. (1992) Nature of biological electron transfer. *Nature* 355, 796–802.
- (72) Moser, C. C., Chobot, S. E., Page, C. C., and Dutton, P. L. (2008) Distance metrics for heme protein electron tunneling. *Biochim. Biophys. Acta BBA - Bioenerg.* 1777, 1032–1037.
- (73) Moore, G. R., Pettigrew, G. W., and Rogers, N. K. (1986) Factors influencing redox potentials of electron transfer proteins. *Proc. Natl. Acad. Sci. U. S. A.* 83, 4998–4999.
- (74) Louro, R. O., Catarino, T., Paquete, C. M., and Turner, D. L. (2004) Distance dependence of interactions between charged centres in proteins with common structural features. *FEBS Lett.* 576, 77–80.
- (75) Sharp, K. A. (1998) Calculation of electron transfer reorganization energies using the finite difference Poisson-Boltzmann model. *Biophys. J.* 74, 1241–1250.
- (76) Page, C. C., Moser, C. C., and Dutton, P. L. (2003) Mechanism for electron transfer within and between proteins. *Curr. Opin. Chem. Biol.* 7, 551–556.
- (77) Marcus, R. A. (1997) Electron transfer reactions in chemistry theory and experiment. *J. Electroanal. Chem.* 438, 251–259.
- (78) Rudolph A. Marcus - Nobel Lecture: Electron transfer reactions in chemistry: Theory and experiment.
- (79) Moser, C. C., and Dutton, P. L. (1992) Engineering protein structure for electron transfer function in photosynthetic reaction centers. *Biochim. Biophys. Acta* 1101,

171–176.

(80) Hampel, A., and Cowan, J. A. (1997) A unique mechanism for RNA catalysis: the role of metal cofactors in hairpin ribozyme cleavage. *Chem. Biol.* **4**, 513–517.

(81) Gray, H. B., Stiefel, E. I., Valentine, J. S., and Bertini, I. (2006) *Biological Inorganic Chemistry: Structure and Reactivity* 1st ed. University Science Book.

(82) Perera, L., Freudenthal, B. D., Beard, W. A., Shock, D. D., Pedersen, L. G., and Wilson, S. H. (2015) Requirement for transient metal ions revealed through computational analysis for DNA polymerase going in reverse. *Proc. Natl. Acad. Sci.* **112**, E5228–E5236.

(83) Beinert, H. (2000) Iron-sulfur proteins: ancient structures, still full of surprises. *JBIC J. Biol. Inorg. Chem.* **5**, 2–15.

(84) Cheng, V. W., Ma, E., Zhao, Z., Rothery, R. A., and Weiner, J. H. (2006) The iron-sulfur clusters in *Escherichia coli* succinate dehydrogenase direct electron flow. *J. Biol. Chem.* **281**, 27662–27668.

(85) Johnson, M. K., Bennett, D. E., Morningstar, J. E., Adams, M. W., and Mortenson, L. E. (1985) The iron-sulfur cluster composition of *Escherichia coli* nitrate reductase. *J. Biol. Chem.* **260**, 5456–5463.

(86) Althoff, T., Mills, D. J., Popot, J.-L., and Kühlbrandt, W. (2011) Arrangement of electron transport chain components in bovine mitochondrial supercomplex I<sub>1</sub>III<sub>2</sub>IV<sub>1</sub>. *EMBO J.* **30**, 4652–4664.

(87) Berry, E. A., and Huang, L.-S. (2011) Conformationally linked interaction in the cytochrome *bc*<sub>1</sub> complex between inhibitors of the Q<sub>o</sub> site and the Rieske iron–sulfur protein. *Biochim. Biophys. Acta BBA - Bioenerg.* **1807**, 1349–1363.

(88) Robbins, A. H., and Stout, C. D. (1985) Iron-sulfur cluster in aconitase. Crystallographic evidence for a three-iron center. *J. Biol. Chem.* **260**, 2328–2333.

(89) Ciurli, S., and Musiani, F. (2005) High potential iron-sulfur proteins and their role as soluble electron carriers in bacterial photosynthesis: Tale of a discovery. *Photosynth. Res.* **85**, 115–131.

(90) Giel, J. L., Nesbit, A. D., Mettert, E. L., Fleischhacker, A. S., Wanta, B. T., and Kiley, P. J. (2013) Regulation of iron–sulphur cluster homeostasis through transcriptional control of the *Isc* pathway by [2Fe–2S]–*IscR* in *Escherichia coli*. *Mol. Microbiol.* **87**, 478–492.

- (91) Hentze, M. W., Muckenthaler, M. U., Galy, B., and Camaschella, C. (2010) Two to tango: Regulation of mammalian iron metabolism. *Cell* 142, 24–38.
- (92) Yarunin, A., Panse, V. G., Petfalski, E., Dez, C., Tollervey, D., and Hurt, E. (2005) Functional link between ribosome formation and biogenesis of iron–sulfur proteins. *EMBO J.* 24, 580–588.
- (93) Dong, J., Lai, R., Nielsen, K., Fekete, C. A., Qiu, H., and Hinnebusch, A. G. (2004) The essential ATP-binding cassette protein RLI1 functions in translation by promoting preinitiation complex assembly. *J. Biol. Chem.* 279, 42157–42168.
- (94) Khoshnevis, S., Gross, T., Rotte, C., Baierlein, C., Ficner, R., and Krebber, H. (2010) The iron-sulphur protein RNase L inhibitor functions in translation termination. *EMBO Rep.* 11, 214–219.
- (95) Netz, D. J. A., Stith, C. M., Stümpfig, M., Köpf, G., Vogel, D., Genau, H. M., Stodola, J. L., Lill, R., Burgers, P. M. J., and Pierik, A. J. (2012) Eukaryotic DNA polymerases require an iron-sulfur cluster for the formation of active complexes. *Nat. Chem. Biol.* 8, 125–132.
- (96) Rudolf, J., Makrantonis, V., Ingledew, W. J., Stark, M. J. R., and White, M. F. (2006) The DNA repair helicases XPD and FancJ have essential iron-sulfur domains. *Mol. Cell* 23, 801–808.
- (97) Liu, J., Chakraborty, S., Hosseinzadeh, P., Yu, Y., Tian, S., Petrik, I., Bhagi, A., and Lu, Y. (2014) Metalloproteins containing cytochrome, iron–sulfur, or copper redox centers. *Chem. Rev.* 114, 4366–4469.
- (98) Rieske, J. S., MacLennan, D. H., and Coleman, R. (1964) Isolation and properties of an iron-protein from the (reduced coenzyme Q)-cytochrome c reductase complex of the respiratory chain. *Biochem. Biophys. Res. Commun.* 15, 338–344.
- (99) Iismaa, S. E., Vázquez, A. E., Jensen, G. M., Stephens, P. J., Butt, J. N., Armstrong, F. A., and Burgess, B. K. (1991) Site-directed mutagenesis of *Azotobacter vinelandii* ferredoxin I. Changes in [4Fe-4S] cluster reduction potential and reactivity. *J. Biol. Chem.* 266, 21563–21571.
- (100) Hochkoepler, A., Kofod, P., Ferro, G., and Ciurli, S. (1995) Isolation, characterization, and functional role of the high-potential iron-sulfur protein (HiPIP) from *Rhodospirillum rubrum*. *Arch. Biochem. Biophys.* 322, 313–318.
- (101) Hosseinzadeh, P., and Lu, Y. Design and fine-tuning redox potentials of metalloproteins involved in electron transfer in bioenergetics. *Biochim. Biophys. Acta BBA - Bioenerg.*

- (102) Imlay, J. A. (2006) Iron-sulphur clusters and the problem with oxygen. *Mol. Microbiol.* 59, 1073–1082.
- (103) Jang, S., and Imlay, J. A. (2007) Micromolar intracellular hydrogen peroxide disrupts metabolism by damaging iron-sulfur enzymes. *J. Biol. Chem.* 282, 929–937.
- (104) Blanc, B., Gerez, C., and Ollagnier de Choudens, S. (2015) Assembly of Fe/S proteins in bacterial systems: Biochemistry of the bacterial ISC system. *Biochim. Biophys. Acta BBA - Mol. Cell Res.* 1853, 1436–1447.
- (105) Maio, N., and Rouault, T. A. (2015) Iron –sulfur cluster biogenesis in mammalian cells: New insights into the molecular mechanisms of cluster delivery. *Biochim. Biophys. Acta BBA - Mol. Cell Res.* 1853, 1493–1512.
- (106) Jacobson, M. R., Cash, V. L., Weiss, M. C., Laird, N. F., Newton, W. E., and Dean, D. R. (1989) Biochemical and genetic analysis of the *nifUSVWZM* cluster from *Azotobacter vinelandii*. *Mol. Gen. Genet. MGG* 219, 49–57.
- (107) Frazzon, J., and Dean, D. R. (2003) Formation of iron–sulfur clusters in bacteria: an emerging field in bioinorganic chemistry. *Curr. Opin. Chem. Biol.* 7, 166–173.
- (108) Zheng, L., Cash, V. L., Flint, D. H., and Dean, D. R. (1998) Assembly of iron-sulfur clusters. Identification of an *iscSUA-hscBA-fdx* gene cluster from *Azotobacter vinelandii*. *J. Biol. Chem.* 273, 13264–13272.
- (109) Nachin, L., Loiseau, L., Expert, D., and Barras, F. (2003) SufC: an unorthodox cytoplasmic ABC/ATPase required for [Fe-S] biogenesis under oxidative stress. *EMBO J.* 22, 427–437.
- (110) Takahashi, Y., and Tokumoto, U. (2002) A third bacterial system for the assembly of iron-sulfur clusters with homologs in archaea and plastids. *J. Biol. Chem.* 277, 28380–28383.
- (111) Ali, V., Shigeta, Y., Tokumoto, U., Takahashi, Y., and Nozaki, T. (2004) An intestinal parasitic protist, *Entamoeba histolytica*, possesses a non-redundant nitrogen fixation-like system for iron-sulfur cluster assembly under anaerobic conditions. *J. Biol. Chem.* 279, 16863–16874.
- (112) Kispal, G., Csere, P., Prohl, C., and Lill, R. (1999) The mitochondrial proteins Atm1p and Nfs1p are essential for biogenesis of cytosolic Fe/S proteins. *EMBO J.* 18, 3981–3989.
- (113) Lill, R., and Mühlenhoff, U. (2005) Iron–sulfur-protein biogenesis in eukaryotes.

*Trends Biochem. Sci.* 30, 133–141.

(114) Kim, H. J., Khalimonchuk, O., Smith, P. M., and Winge, D. R. (2012) Structure, function, and assembly of heme centers in mitochondrial respiratory complexes. *Biochim. Biophys. Acta BBA - Mol. Cell Res.* 1823, 1604–1616.

(115) Teichmann, L. T. S. (1853) Concerning the crystallization of organic components of blood. *Z Ration Med* 3, 8.

(116) MacMunn, C. A. (1883) Observations on the colouring-matters of the so-called bile of invertebrates, on those of the bile of vertebrates, and on some unusual urine pigments. *Proc. R. Soc. Lond.* 35, 132–134.

(117) Keilin, D. (1925) On cytochrome, a respiratory pigment, common to animals, yeast, and higher plants. *Proc. R. Soc. Lond. Ser. B Contain. Pap. Biol. Character* 98, 312–339.

(118) Takaichi, S., and Morita, S. (1981) Procedures and conditions for application of the pyridine hemochrome method to photosynthetically grown cells of *Rhodospseudomonas sphaeroides*. *J. Biochem. (Tokyo)* 89, 1513–1519.

(119) Burmester, T., and Hankeln, T. (2014) Function and evolution of vertebrate globins. *Acta Physiol.* 211, 501–514.

(120) Antonini, E., and Brunori, M. (1971) Hemoglobin and myoglobin in their reactions with ligands. North-Holland Pub. Co., Amsterdam.

(121) Gray, H. B., and Winkler, J. R. (2009) Electron flow through proteins. *Chem. Phys. Lett.* 483, 1–9.

(122) Shimizu, T., Huang, D., Yan, F., Stranova, M., Bartosova, M., Fojtíková, V., and Martínková, M. (2015) Gaseous O<sub>2</sub>, NO, and CO in signal transduction: structure and function relationships of heme-based gas sensors and heme-redox sensors. *Chem. Rev.* 115, 6491–6533.

(123) Mense, S. M., and Zhang, L. (2006) Heme: a versatile signalling molecule controlling the activities of diverse regulators ranging from transcription factors to MAP kinases. *Cell Res.* 16, 681–692.

(124) Hu, R.-G., Wang, H., Xia, Z., and Varshavsky, A. (2008) The N-end rule pathway is a sensor of heme. *Proc. Natl. Acad. Sci. U. S. A.* 105, 76–81.

(125) McLean, K. J., Luciakova, D., Belcher, J., Tee, K. L., and Munro, A. W. (2015) Biological diversity of cytochrome P450 redox partner systems. *Adv. Exp. Med. Biol.*

851, 299–317.

(126) Reedy, C. J., and Gibney, B. R. (2004) Heme protein assemblies. *Chem. Rev.* 104, 617–650.

(127) Smith, L. J., Kahraman, A., and Thornton, J. M. (2010) Heme proteins--diversity in structural characteristics, function, and folding. *Proteins* 78, 2349–2368.

(128) Liptak, M. D., Wen, X., and Bren, K. L. (2010) NMR and DFT investigation of heme ruffling: functional implications for cytochrome *c*. *J. Am. Chem. Soc.* 132, 9753–9763.

(129) Dolla, A., Blanchard, L., Guerlesquin, F., and Bruschi, M. (1994) The protein moiety modulates the redox potential in cytochromes *c*. *Biochimie* 76, 471–479.

(130) Zheng, Z., and Gunner, M. R. (2009) Analysis of the electrochemistry of hemes with  $E_m$ s spanning 800 mV. *Proteins Struct. Funct. Bioinforma.* 75, 719–734.

(131) Hendler, R. W., and Westerhoff, H. V. (1992) Redox interactions in cytochrome *c* oxidase: from the “neoclassical” toward “modern” models. *Biophys. J.* 63, 1586–1604.

(132) Fedor, J. G., Rothery, R. A., and Weiner, J. H. (2014) A new paradigm for electron transfer through *Escherichia coli* nitrate reductase A. *Biochemistry* 53, 4549–4556.

(133) Tezcan, F. A., Winkler, J. R., and Gray, H. B. (1998) Effects of ligation and folding on reduction potentials of heme proteins. *J. Am. Chem. Soc.* 120, 13383–13388.

(134) Fonseca, B. M., Paquete, C. M., Salgueiro, C. A., and Louro, R. O. (2012) The role of intramolecular interactions in the functional control of multiheme cytochromes *c*. *FEBS Lett.* 586, 504–509.

(135) Olea, C., Jr, Kuriyan, J., and Marletta, M. A. (2010) Modulating heme redox potential through protein-induced porphyrin distortion. *J. Am. Chem. Soc.* 132, 12794–12795.

(136) Reedy, C. J., Elvekrog, M. M., and Gibney, B. R. (2008) Development of a heme protein structure-electrochemical function database. *Nucleic Acids Res.* 36, D307–313.

(137) Johansson, M. P., Blomberg, M. R. A., Sundholm, D., and Wikström, M. (2002) Change in electron and spin density upon electron transfer to haem. *Biochim.*

*Biophys. Acta BBA - Bioenerg.* 1553, 183–187.

(138) Takano, Y., and Nakamura, H. (2010) Electronic structures of heme *a* of cytochrome *c* oxidase in the redox states—Charge density migration to the propionate groups of heme *a*. *J. Comput. Chem.* 31, 954–962.

(139) Kamiya, K., Yamamoto, S., Shiraishi, K., and Oshiyama, A. (2009) Significant change in electronic structures of heme upon reduction by strong coulomb repulsion between Fe *d*-electrons. *J. Phys. Chem. B* 113, 6866–6872.

(140) Baniulis, D., Yamashita, E., Zhang, H., Hasan, S. S., and Cramer, W. A. (2008) Structure–function of the cytochrome *b<sub>6</sub>f* complex. *Photochem. Photobiol.* 84, 1349–1358.

(141) Paquete, C. M., and Louro, R. O. (2010) Molecular details of multielectron transfer: the case of multiheme cytochromes from metal respiring organisms. *Dalton Trans.* 39, 4259–4266.

(142) Heinemann, I. U., Jahn, M., and Jahn, D. (2008) The biochemistry of heme biosynthesis. *Arch. Biochem. Biophys.* 474, 238–251.

(143) Hamza, I., and Dailey, H. A. (2012) One ring to rule them all: Trafficking of heme and heme synthesis intermediates in the metazoans. *Biochim. Biophys. Acta BBA - Mol. Cell Res.* 1823, 1617–1632.

(144) Zhang, Y., and Gladyshev, V. N. (2008) Molybdoproteomes and evolution of molybdenum utilization. *J. Mol. Biol.* 379, 881–899.

(145) Reiss, J., and Hahnewald, R. (2011) Molybdenum cofactor deficiency: Mutations in GPHN, MOCS1, and MOCS2. *Hum. Mutat.* 32, 10–18.

(146) Schwarz, G., Mendel, R. R., and Ribbe, M. W. (2009) Molybdenum cofactors, enzymes and pathways. *Nature* 460, 839–847.

(147) Einsle, O., Tezcan, F. A., Andrade, S. L. A., Schmid, B., Yoshida, M., Howard, J. B., and Rees, D. C. (2002) Nitrogenase MoFe-protein at 1.16 Å resolution: a central ligand in the FeMo-cofactor. *Science* 297, 1696–1700.

(148) Carepo, M. S. P., Pauleta, S. R., Wedd, A. G., Moura, J. J. G., and Moura, I. (2014) Mo–Cu metal cluster formation and binding in an orange protein isolated from *Desulfovibrio gigas*. *JBIC J. Biol. Inorg. Chem.* 19, 605–614.

(149) Leimkühler, S., and Iobbi-Nivol, C. (2015) Bacterial molybdoenzymes: old enzymes for new purposes. *FEMS Microbiol. Rev.* fuv043.

- (150) Havemeyer, A., Lang, J., and Clement, B. (2011) The fourth mammalian molybdenum enzyme mARC: current state of research. *Drug Metab. Rev.* 43, 524–539.
- (151) Rothery, R. A., Workun, G. J., and Weiner, J. H. (2008) The prokaryotic complex iron-sulfur molybdoenzyme family. *Biochim. Biophys. Acta* 1778, 1897–1929.
- (152) Jormakka, M., Richardson, D., Byrne, B., and Iwata, S. (2004) Architecture of NarGH reveals a structural classification of Mo-bisMGD enzymes. *Structure* 12, 95–104.
- (153) George, G. N., Turner, N. A., Bray, R. C., Morpeth, F. F., Boxer, D. H., and Cramer, S. P. (1989) X-ray-absorption and electron-paramagnetic-resonance spectroscopic studies of the environment of molybdenum in high-pH and low-pH forms of *Escherichia coli* nitrate reductase. *Biochem. J.* 259, 693–700.
- (154) Kloer, D. P., Hagel, C., Heider, J., and Schulz, G. E. (2006) Crystal structure of ethylbenzene dehydrogenase from *Aromatoleum aromaticum*. *Struct. Lond. Engl.* 1993 14, 1377–1388.
- (155) Shanmugam, K. T., Stewart, V., Gunsalus, R. P., Boxer, D. H., Cole, J. A., Chippaux, M., DeMoss, J. A., Giordano, G., Lin, E. C., and Rajagopalan, K. V. (1992) Proposed nomenclature for the genes involved in molybdenum metabolism in *Escherichia coli* and *Salmonella typhimurium*. *Mol. Microbiol.* 6, 3452–3454.
- (156) Bay, D. C., Chan, C. S., and Turner, R. J. (2015) NarJ subfamily system specific chaperone diversity and evolution is directed by respiratory enzyme associations. *BMC Evol. Biol.* 15, 110.
- (157) Collins, M. D., and Jones, D. (1981) Distribution of isoprenoid quinone structural types in bacteria and their taxonomic implication. *Microbiol. Rev.* 45, 316–354.
- (158) Nowicka, B., and Kruk, J. (2010) Occurrence, biosynthesis and function of isoprenoid quinones. *Biochim. Biophys. Acta BBA - Bioenerg.* 1797, 1587–1605.
- (159) Galassi, V. V., and Arantes, G. M. (2015) Partition, orientation and mobility of ubiquinones in a lipid bilayer. *Biochim. Biophys. Acta BBA - Bioenerg.* 1847, 1560–1573.
- (160) Lenaz, G., and Genova, M. L. (2009) Mobility and function of coenzyme Q (ubiquinone) in the mitochondrial respiratory chain. *Biochim. Biophys. Acta* 1787, 563–573.
- (161) Nasiri, H. R., Panisch, R., Madej, M. G., Bats, J. W., Lancaster, C. R. D., and

Schwalbe, H. (2009) The correlation of cathodic peak potentials of vitamin K<sub>3</sub> derivatives and their calculated electron affinities: The role of hydrogen bonding and conformational changes. *Biochim. Biophys. Acta BBA - Bioenerg.* 1787, 601–608.

(162) Brunmark, A., and Cadenas, E. (1989) Redox and addition chemistry of quinoid compounds and its biological implications. *Free Radic. Biol. Med.* 7, 435–477.

(163) Uchimiya, M., and Stone, A. T. (2009) Reversible redox chemistry of quinones: impact on biogeochemical cycles. *Chemosphere* 77, 451–458.

(164) Robinson, H. H., and Kahn, S. D. (1990) Interplay of substituent conformation and electron affinity in quinone models of quinone reductases. *J. Am. Chem. Soc.* 112, 4728–4731.

(165) Zhang, H., Chobot, S. E., Osyczka, A., Wraight, C. A., Dutton, P. L., and Moser, C. C. (2008) Quinone and non-quinone redox couples in complex III. *J. Bioenerg. Biomembr.* 40, 493–499.

(166) Ingledew, W. J., Ohnishi, T., and Salerno, J. C. (1995) Studies on a stabilisation of ubisemiquinone by *Escherichia coli* quinol oxidase, cytochrome *bo*. *Eur. J. Biochem.* 227, 903–908.

(167) Hastings, S. F., Kaysser, T. M., Jiang, F., Salerno, J. C., Gennis, R. B., and Ingledew, W. J. (1998) Identification of a stable semiquinone intermediate in the purified and membrane bound ubiquinol oxidase-cytochrome *bd* from *Escherichia coli*. *Eur. J. Biochem. FEBS* 255, 317–323.

(168) Grimaldi, S., Arias-Cartin, R., Lanciano, P., Lyubenova, S., Szenes, R., Endeward, B., Prisner, T. F., Guigliarelli, B., and Magalon, A. (2012) Determination of the proton environment of high stability menasemiquinone intermediate in *Escherichia coli* nitrate reductase A by pulsed EPR. *J. Biol. Chem.* 287, 4662–4670.

(169) Flores, M., Okamura, M. Y., Niklas, J., Pandelia, M.-E., and Lubitz, W. (2012) Pulse Q-Band EPR and ENDOR spectroscopies of the photochemically generated monoprotinated benzosemiquinone radical in frozen alcoholic solution. *J. Phys. Chem. B* 116, 8890–8900.

(170) Grimaldi, S., Arias-Cartin, R., Lanciano, P., Lyubenova, S., Endeward, B., Prisner, T. F., Magalon, A., and Guigliarelli, B. (2010) Direct evidence for nitrogen ligation to the high stability semiquinone intermediate in *Escherichia coli* nitrate reductase A. *J. Biol. Chem.* 285, 179–187.

(171) Hellwig, P., Yano, T., Ohnishi, T., and Gennis, R. B. (2002) Identification of the residues involved in stabilization of the semiquinone radical in the high-affinity

ubiquinone binding site in cytochrome *bo*<sub>3</sub> from *Escherichia coli* by site-directed mutagenesis and EPR spectroscopy. *Biochemistry* 41, 10675–10679.

(172) Paddock, M. L., Flores, M., Isaacson, R., Shepherd, J. N., and Okamura, M. Y. (2009) EPR and ENDOR investigation of rhodosemiquinone in bacterial reaction centers formed by B-branch electron transfer. *Appl. Magn. Reson.* 37, 39–48.

(173) Fisher, N., and Rich, P. R. (2000) A motif for quinone binding sites in respiratory and photosynthetic systems. *J. Mol. Biol.* 296, 1153–1162.

(174) Osyczka, A., Zhang, H., Mathé, C., Rich, P. R., Moser, C. C., and Dutton, P. L. (2006) Role of the PEWY glutamate in hydroquinone–quinone oxidation–reduction catalysis in the Q<sub>o</sub> site of cytochrome *bc*<sub>1</sub>. *Biochemistry* 45, 10492–10503.

(175) Rodrigues, M. L., Scott, K. A., Sansom, M. S. P., Pereira, I. A. C., and Archer, M. (2008) Quinol oxidation by *c*-type cytochromes: Structural characterization of the menaquinol binding site of NrfHA. *J. Mol. Biol.* 381, 341–350.

(176) Taguchi, A. T., O'Malley, P. J., Wraight, C. A., and Dikanov, S. A. (2014) Hyperfine and nuclear quadrupole tensors of nitrogen donors in the Q<sub>A</sub> site of bacterial reaction centers: Correlation of the histidine Nδ tensors with hydrogen bond strength. *J. Phys. Chem. B* 118, 9225–9237.

(177) Rothery, R. A., Seime, A. M., Spiers, A. M., Maklashina, E., Schroder, I., Gunsalus, R. P., Cecchini, G., and Weiner, J. H. (2005) Defining the Q-site of *Escherichia coli* fumarate reductase by site-directed mutagenesis, fluorescence quench titrations and EPR spectroscopy. *FEBS J.* 272, 313–326.

(178) Iverson, T. M., Luna-Chavez, C., Cecchini, G., and Rees, D. C. (1999) Structure of the *Escherichia coli* fumarate reductase respiratory complex. *Science* 284, 1961–1966.

(179) Barragan, A. M., Crofts, A. R., Schulten, K., and Solov'yov, I. A. (2015) Identification of ubiquinol binding motifs at the Q<sub>o</sub>-site of the cytochrome *bc*<sub>1</sub> complex. *J. Phys. Chem. B* 119, 433–447.

(180) Saito, K., Rutherford, A. W., and Ishikita, H. (2013) Mechanism of proton-coupled quinone reduction in Photosystem II. *Proc. Natl. Acad. Sci.* 110, 954–959.

(181) Jormakka, M., Yokoyama, K., Yano, T., Tamakoshi, M., Akimoto, S., Shimamura, T., Curmi, P., and Iwata, S. (2008) Molecular mechanism of energy conservation in polysulfide respiration. *Nat. Struct. Mol. Biol.* 15, 730–737.

(182) Postila, P. A., Kaszuba, K., Sarewicz, M., Osyczka, A., Vattulainen, I., and Róg,

T. (2013) Key role of water in proton transfer at the Q<sub>o</sub>-site of the cytochrome *bc*<sub>1</sub> complex predicted by atomistic molecular dynamics simulations. *Biochim. Biophys. Acta BBA - Bioenerg.* 1827, 761–768.

(183) Bertero, M. G., Rothery, R. A., Boroumand, N., Palak, M., Blasco, F., Ginet, N., Weiner, J. H., and Strynadka, N. C. (2005) Structural and biochemical characterization of a quinol binding site of *Escherichia coli* nitrate reductase A. *J. Biol. Chem.* 280, 14836–14843.

(184) da Silva, G. F. Z., Shinkarev, V. P., Kamensky, Y. A., and Palmer, G. (2012) Spectroscopic evidence of the role of an axial ligand histidinate in the mechanism of adrenal cytochrome *b*<sub>561</sub>. *Biochemistry* 51, 8730–8742.

(185) Shinkarev, V. P., Kolling, D. R. J., Miller, T. J., and Crofts, A. R. (2002) Modulation of the midpoint potential of the [2Fe–2S] Rieske iron sulfur center by Q<sub>o</sub> occupants in the *bc*<sub>1</sub> complex. *Biochemistry* 41, 14372–14382.

(186) Mileni, M., Haas, A. H., Mäntele, W., Simon, J., and Lancaster, C. R. D. (2005) Probing heme propionate involvement in transmembrane proton transfer coupled to electron transfer in dihemic quinol:fumarate reductase by <sup>13</sup>C-labeling and FTIR difference spectroscopy. *Biochemistry* 44, 16718–16728.

(187) Hasan, S. S., Yamashita, E., Baniulis, D., and Cramer, W. A. (2013) Quinone-dependent proton transfer pathways in the photosynthetic cytochrome *b*<sub>6f</sub> complex. *Proc. Natl. Acad. Sci.* 110, 4297–4302.

(188) Mulkidjanian, A. Y. (2005) Ubiquinol oxidation in the cytochrome *bc*<sub>1</sub> complex: Reaction mechanism and prevention of short-circuiting. *Biochim. Biophys. Acta BBA - Bioenerg.* 1709, 5–34.

(189) Nabedryk, E., and Breton, J. (2008) Coupling of electron transfer to proton uptake at the Q<sub>B</sub> site of the bacterial reaction center: a perspective from FTIR difference spectroscopy. *Biochim. Biophys. Acta* 1777, 1229–1248.

(190) Fujimoto, N., Yamada, M., and Kosaka, T. (2012) Menaquinone as well as ubiquinone as a crucial component in the *Escherichia coli* respiratory chain (Ekinici, Deniz, Ed.). InTech.

(191) Lee, P. T., Hsu, A. Y., Ha, H. T., and Clarke, C. F. (1997) A C-methyltransferase involved in both ubiquinone and menaquinone biosynthesis: isolation and identification of the *Escherichia coli ubiE* gene. *J. Bacteriol.* 179, 1748–1754.

(192) Bekker, M., Kramer, G., Hartog, A. F., Wagner, M. J., Koster, C. G. de, Hellingwerf, K. J., and Mattos, M. J. T. de. (2007) Changes in the redox state and

composition of the quinone pool of *Escherichia coli* during aerobic batch-culture growth. *Microbiology* 153, 1974–1980.

(193) Sterner, R. W., Elser, J. J., and Vitousek, P. M. (2002) Ecological Stoichiometry: The Biology of Elements from Molecules to the Biosphere. Princeton University Press, Princeton.

(194) Canfield, D. E., Glazer, A. N., and Falkowski, P. G. (2010) The evolution and future of Earth's nitrogen cycle. *Science* 330, 192–196.

(195) Fowler, D., Coyle, M., Skiba, U., Sutton, M. A., Cape, J. N., Reis, S., Sheppard, L. J., Jenkins, A., Grizzetti, B., Galloway, J. N., Vitousek, P., Leach, A., Bouwman, A. F., Butterbach-Bahl, K., Dentener, F., Stevenson, D., Amann, M., and Voss, M. (2013) The global nitrogen cycle in the twenty-first century. *Philos. Trans. R. Soc. Lond. B. Biol. Sci.* 368, 20130164.

(196) Howard, J. B., and Rees, D. C. (2006) How many metals does it take to fix N<sub>2</sub>? A mechanistic overview of biological nitrogen fixation. *Proc. Natl. Acad. Sci.* 103, 17088–17093.

(197) Demanèche, S., Philippot, L., David, M. M., Navarro, E., Vogel, T. M., and Simonet, P. (2009) Characterization of denitrification gene clusters of soil bacteria via a metagenomic approach. *Appl. Environ. Microbiol.* 75, 534–537.

(198) Dore, J. E., Popp, B. N., Karl, D. M., and Sansone, F. J. (1998) A large source of atmospheric nitrous oxide from subtropical North Pacific surface waters. *Nature* 396, 63–66.

(199) Piña-Ochoa, E., Høgslund, S., Geslin, E., Cedhagen, T., Revsbech, N. P., Nielsen, L. P., Schweizer, M., Jorissen, F., Rysgaard, S., and Risgaard-Petersen, N. (2010) Widespread occurrence of nitrate storage and denitrification among Foraminifera and Gromiida. *Proc. Natl. Acad. Sci. U. S. A.* 107, 1148–1153.

(200) Kraft, B., Tegetmeyer, H. E., Sharma, R., Klotz, M. G., Ferdelman, T. G., Hettich, R. L., Geelhoed, J. S., and Strous, M. (2014) The environmental controls that govern the end product of bacterial nitrate respiration. *Science* 345, 676–679.

(201) Strous, M., Pelletier, E., Mangenot, S., Rattai, T., Lehner, A., Taylor, M. W., Horn, M., Daims, H., Bartol-Mavel, D., Wincker, P., Barbe, V., Fonknechten, N., Vallenet, D., Segurens, B., Schenowitz-Truong, C., Médigue, C., Collingro, A., Snel, B., Dutilh, B. E., Op den Camp, H. J. M., van der Drift, C., Cirpus, I., van de Pas-Schoonen, K. T., Harhangi, H. R., van Niftrik, L., Schmid, M., Keltjens, J., van de Vossenberg, J., Kartal, B., Meier, H., Frishman, D., Huynen, M. A., Mewes, H.-W., Weissenbach, J., Jetten, M. S. M., Wagner, M., and Le Paslier, D. (2006) Deciphering

the evolution and metabolism of an anammox bacterium from a community genome. *Nature* 440, 790–794.

(202) Moreno-Vivián, C., Cabello, P., Martínez-Luque, M., Blasco, R., and Castillo, F. (1999) Prokaryotic nitrate reduction: molecular properties and functional distinction among bacterial nitrate reductases. *J. Bacteriol.* 181, 6573–6584.

(203) Campbell, W. H. (2001) Structure and function of eukaryotic NAD(P)H:nitrate reductase. *Cell. Mol. Life Sci. CMLS* 58, 194–204.

(204) González, P. J., Correia, C., Moura, I., Brondino, C. D., and Moura, J. J. G. (2006) Bacterial nitrate reductases: Molecular and biological aspects of nitrate reduction. *J. Inorg. Biochem.* 100, 1015–1023.

(205) Richardson, D. J., Berks, B. C., Russell, D. A., Spiro, S., and Taylor, C. J. (2001) Functional, biochemical and genetic diversity of prokaryotic nitrate reductases. *Cell. Mol. Life Sci. CMLS* 58, 165–178.

(206) Vázquez-Torres, A., and Bäumler, A. J. (2015) Nitrate, nitrite and nitric oxide reductases: from the last universal common ancestor to modern bacterial pathogens. *Curr. Opin. Microbiol.* 29, 1–8.

(207) Sparacino-Watkins, C., Stolz, J. F., and Basu, P. (2013) Nitrate and periplasmic nitrate reductases. *Chem. Soc. Rev.* 43, 676–706.

(208) Potter, L. C., Millington, P., Griffiths, L., Thomas, G. H., and Cole, J. A. (1999) Competition between *Escherichia coli* strains expressing either a periplasmic or a membrane-bound nitrate reductase: does Nap confer a selective advantage during nitrate-limited growth? *Biochem. J.* 344 Pt 1, 77–84.

(209) Brondijk, T. H. C., Fiegen, D., Richardson, D. J., and Cole, J. A. (2002) Roles of NapF, NapG and NapH, subunits of the *Escherichia coli* periplasmic nitrate reductase, in ubiquinol oxidation. *Mol. Microbiol.* 44, 245–255.

(210) Potter, L. C., and Cole, J. A. (1999) Essential roles for the products of the *napABCD* genes, but not *napFGH*, in periplasmic nitrate reduction by *Escherichia coli* K-12. *Biochem. J.* 344 Pt 1, 69–76.

(211) Huang, Y., Kittichotirat, W., Mayer, M. p. a., Hall, R., Bumgarner, R., and Chen, C. (2013) Comparative genomic hybridization and transcriptome analysis with a pan-genome microarray reveal distinctions between JP2 and non-JP2 genotypes of *Aggregatibacter actinomycetemcomitans*. *Mol. Oral Microbiol.* 28, 1–17.

(212) Blasco, F., Iobbi, C., Ratouchniak, J., Bonnefoy, V., and Chippaux, M. (1990)

Nitrate reductases of *Escherichia coli*: Sequence of the second nitrate reductase and comparison with that encoded by the *narGHJI* operon. *Mol. Gen. Genet. MGG* 222, 104–111.

(213) Guigliarelli, B., Asso, M., More, C., Augier, V., Blasco, F., Pommier, J., Giordano, G., and Bertrand, P. (1992) EPR and redox characterization of iron-sulfur centers in nitrate reductases A and Z from *Escherichia coli*. Evidence for a high-potential and a low-potential class and their relevance in the electron-transfer mechanism. *Eur. J. Biochem. FEBS* 207, 61–68.

(214) Iobbi, C., Santini, C., Bonnefoy, V., and Giordano, G. (1987) Biochemical and immunological evidence for a second nitrate reductase in *Escherichia coli* K12. *Eur. J. Biochem.* 168, 451–459.

(215) Iobbi-Nivol, C., Santini, C. L., Blasco, F., and Giordano, G. (1990) Purification and further characterization of the second nitrate reductase of *Escherichia coli* K12. *Eur. J. Biochem. FEBS* 188, 679–687.

(216) Chang, L., Wei, L. I.-C., Audia, J. P., Morton, R. A., and Schellhorn, H. E. (1999) Expression of the *Escherichia coli* NRZ nitrate reductase is highly growth phase dependent and is controlled by RpoS, the alternative vegetative sigma factor. *Mol. Microbiol.* 34, 756–766.

(217) Zhu, L., Gunn, C., and Beckman, J. S. (1992) Bactericidal activity of peroxynitrite. *Arch. Biochem. Biophys.* 298, 452–457.

(218) Winter, S. E., Winter, M. G., Xavier, M. N., Thiennimitr, P., Poon, V., Keestra, A. M., Laughlin, R. C., Gomez, G., Wu, J., Lawhon, S. D., Popova, I. E., Parikh, S. J., Adams, L. G., Tsois, R. M., Stewart, V. J., and Bäumlner, A. J. (2013) Host-derived nitrate boosts growth of *E. coli* in the inflamed gut. *Science* 339, 708–711.

(219) Jones, S. A., Gibson, T., Maltby, R. C., Chowdhury, F. Z., Stewart, V., Cohen, P. S., and Conway, T. (2011) Anaerobic respiration of *Escherichia coli* in the mouse intestine. *Infect. Immun.* 79, 4218–4226.

(220) Cunningham-Bussel, A., Zhang, T., and Nathan, C. F. (2013) Nitrite produced by *Mycobacterium tuberculosis* in human macrophages in physiologic oxygen impacts bacterial ATP consumption and gene expression. *Proc. Natl. Acad. Sci.* 110, E4256–E4265.

(221) Weber, I., Fritz, C., Ruttkowski, S., Kreft, A., and Bange, F.-C. (2000) Anaerobic nitrate reductase (*narGHJI*) activity of *Mycobacterium bovis* BCG in vitro and its contribution to virulence in immunodeficient mice. *Mol. Microbiol.* 35, 1017–1025.

- (222) Akhtar, S., Khan, A., Sohaskey, C. D., Jagannath, C., and Sarkar, D. (2013) Nitrite reductase NirBD is induced and plays an important role during in vitro dormancy of *Mycobacterium tuberculosis*. *J. Bacteriol.* 195, 4592–4599.
- (223) Jung, J.-Y., Madan-Lala, R., Georgieva, M., Rengarajan, J., Sohaskey, C. D., Bange, F.-C., and Robinson, C. M. (2013) The intracellular environment of human macrophages that produce nitric oxide promotes growth of *Mycobacteria*. *Infect. Immun.* 81, 3198–3209.
- (224) Forget, P. (1974) The bacterial nitrate reductases. *Eur. J. Biochem.* 42, 325–332.
- (225) Jones, R. W., Ingledew, W. J., Graham, A., and Garland, P. B. (1978) Topography of nitrate reductase of the cytoplasmic membrane of *Escherichia coli*: The nitrate-reducing site. *Biochem. Soc. Trans.* 6, 1287–1289.
- (226) Graham, A., and Boxer, D. H. (1980) Arrangement of respiratory nitrate reductase in the cytoplasmic membrane of *Escherichia coli*: Location of  $\beta$  subunit. *FEBS Lett.* 113, 15–20.
- (227) Kristjansson, J. K., and Hollocher, T. C. (1979) Substrate binding site for nitrate reductase of *Escherichia coli* is on the inner aspect of the membrane. *J. Bacteriol.* 137, 1227–1233.
- (228) Lund, K., and DeMoss, J. A. (1976) Association-dissociation behavior and subunit structure of heat-released nitrate reductase from *Escherichia coli*. *J. Biol. Chem.* 251, 2207–2216.
- (229) Arias-Cartin, R., Grimaldi, S., Arnoux, P., Guigliarelli, B., and Magalon, A. (2012) Cardiolipin binding in bacterial respiratory complexes: Structural and functional implications. *Biochim. Biophys. Acta BBA - Bioenerg.* 1817, 1937–1949.
- (230) Magalon, A., Asso, M., Guigliarelli, B., Rothery, R. A., Bertrand, P., Giordano, G., and Blasco, F. (1998) Molybdenum cofactor properties and [Fe-S] cluster coordination in *Escherichia coli* nitrate reductase A: investigation by site-directed mutagenesis of the conserved his-50 residue in the NarG subunit. *Biochemistry* 37, 7363–7370.
- (231) Lanciano, P., Savoyant, A., Grimaldi, S., Magalon, A., Guigliarelli, B., and Bertrand, P. (2007) New method for the spin quantitation of [4Fe-4S]<sup>+</sup> clusters with S = 3/2. Application to the FS0 center of the NarGHI nitrate reductase from *Escherichia coli*. *J. Phys. Chem. B* 111, 13632–13637.
- (232) Rothery, R. A., Magalon, A., Giordano, G., Guigliarelli, B., Blasco, F., and

Weiner, J. H. (1998) The molybdenum cofactor of *Escherichia coli* nitrate reductase A (NarGHI). Effect of a *mobAB* mutation and interactions with [Fe-S] clusters. *J. Biol. Chem.* 273, 7462–7469.

(233) Jepson, B. J. N., Mohan, S., Clarke, T. A., Gates, A. J., Cole, J. A., Butler, C. S., Butt, J. N., Hemmings, A. M., and Richardson, D. J. (2007) Spectropotentiometric and structural analysis of the periplasmic nitrate reductase from *Escherichia coli*. *J. Biol. Chem.* 282, 6425–6437.

(234) Dias, J. M., Than, M. E., Humm, A., Huber, R., Bourenkov, G. P., Bartunik, H. D., Bursakov, S., Calvete, J., Caldeira, J., Carneiro, C., Moura, J. J., Moura, I., and Romão, M. J. (1999) Crystal structure of the first dissimilatory nitrate reductase at 1.9 Å solved by MAD methods. *Struct. Lond. Engl.* 1993 7, 65–79.

(235) Coelho, C., and Romão, M. J. (2015) Structural and mechanistic insights on nitrate reductases. *Protein Sci.* n/a–n/a.

(236) Johnson, J. L., Hainline, B. E., Rajagopalan, K. V., and Arison, B. H. (1984) The pterin component of the molybdenum cofactor. Structural characterization of two fluorescent derivatives. *J. Biol. Chem.* 259, 5414–5422.

(237) George, G. N., Bray, R. C., Morpeth, F. F., and Boxer, D. H. (1985) Complexes with halide and other anions of the molybdenum centre of nitrate reductase from *Escherichia coli*. *Biochem. J.* 227, 925–931.

(238) Morpeth, F. F., and Boxer, D. H. (1985) Kinetic analysis of respiratory nitrate reductase from *Escherichia coli* K12. *Biochemistry* 24, 40–46.

(239) Elliott, S. J., Hoke, K. R., Heffron, K., Palak, M., Rothery, R. A., Weiner, J. H., and Armstrong, F. A. (2004) Voltammetric studies of the catalytic mechanism of the respiratory nitrate reductase from *Escherichia coli*: how nitrate reduction and inhibition depend on the oxidation state of the active site. *Biochemistry* 43, 799–807.

(240) Wu, S.-Y., Rothery, R. A., and Weiner, J. H. (2015) Pyranopterin coordination controls molybdenum electrochemistry in *Escherichia coli* nitrate reductase. *J. Biol. Chem.* 290, 25164–25173.

(241) Rothery, R. A., and Weiner, J. H. (2014) Shifting the metallocentric molybdoenzyme paradigm: the importance of pyranopterin coordination. *JBIC J. Biol. Inorg. Chem.* 20, 349–372.

(242) Enemark, J. H., and Garner, C. D. (1997) The coordination chemistry and function of the molybdenum centres of the oxomolybdoenzymes. *JBIC J. Biol. Inorg. Chem.* 2, 817–822.

- (243) Rothery, R. A., Stein, B., Solomonson, M., Kirk, M. L., and Weiner, J. H. (2012) Pyranopterin conformation defines the function of molybdenum and tungsten enzymes. *Proc. Natl. Acad. Sci.* *109*, 14773–14778.
- (244) Rothery, R. A., Bertero, M. G., Spreter, T., Bouromand, N., Strynadka, N. C. J., and Weiner, J. H. (2010) Protein crystallography reveals a role for the FS0 cluster of *Escherichia coli* nitrate reductase A (NarGHI) in enzyme maturation. *J. Biol. Chem.* *285*, 8801–8807.
- (245) Beitlich, T., Kühnel, K., Schulze-Briese, C., Shoeman, R. L., and Schlichting, I. (2007) Cryoradiolytic reduction of crystalline heme proteins: analysis by UV-Vis spectroscopy and X-ray crystallography. *J. Synchrotron Radiat.* *14*, 11–23.
- (246) Vincent, S. P., and Bray, R. C. (1978) Electron-paramagnetic-resonance studies on nitrate reductase from *Escherichia coli* K12. *Biochem. J.* *171*, 639–647.
- (247) Anderson, L. J., Richardson, D. J., and Butt, J. N. (2001) Catalytic protein film voltammetry from a respiratory nitrate reductase provides evidence for complex electrochemical modulation of enzyme activity. *Biochemistry* *40*, 11294–11307.
- (248) Fourmond, V., Burlat, B., Dementin, S., Arnoux, P., Sabaty, M., Boiry, S., Guigliarelli, B., Bertrand, P., Pignol, D., and Leger, C. (2008) Major Mo(V) EPR signature of *Rhodobacter sphaeroides* periplasmic nitrate reductase arising from a dead-end species that activates upon reduction. Relation to other molybdoenzymes from the DMSO reductase family. *J. Phys. Chem. B* *112*, 15478–15486.
- (249) Cerqueira, N. M. F. S. A., Fernandes, P. A., Gonzalez, P. J., Moura, J. J. G., and Ramos, M. J. (2013) The sulfur shift: an activation mechanism for periplasmic nitrate reductase and formate dehydrogenase. *Inorg. Chem.* *52*, 10766–10772.
- (250) Hofmann, M. (2009) Density functional theory study of model complexes for the revised nitrate reductase active site in *Desulfovibrio desulfuricans* NapA. *J. Biol. Inorg. Chem. JBIC Publ. Soc. Biol. Inorg. Chem.* *14*, 1023–1035.
- (251) Rothery, R. A., Bertero, M. G., Cammack, R., Palak, M., Blasco, F., Strynadka, N. C., and Weiner, J. H. (2004) The catalytic subunit of *Escherichia coli* nitrate reductase A contains a novel [4Fe-4S] cluster with a high-spin ground state. *Biochemistry* *43*, 5324–5333.
- (252) Lanciano, P., Vergnes, A., Grimaldi, S., Guigliarelli, B., and Magalon, A. (2007) Biogenesis of a respiratory complex is orchestrated by a single accessory protein. *J. Biol. Chem.* *282*, 17468–17474.
- (253) Vergnes, A., Gouffi-Belhabich, K., Blasco, F., Giordano, G., and Magalon, A.

(2004) Involvement of the molybdenum cofactor biosynthetic machinery in the maturation of the *Escherichia coli* nitrate reductase A. *J. Biol. Chem.* 279, 41398–41403.

(254) Ceccaldi, P., Rendon, J., Léger, C., Toci, R., Guigliarelli, B., Magalon, A., Grimaldi, S., and Fourmond, V. (2015) Reductive activation of *E. coli* respiratory nitrate reductase. *Biochim. Biophys. Acta BBA - Bioenerg.* 1847, 1055–1063.

(255) Bennett, B., and Bray, R. C. (1994) Further studies on redox-related activation and deactivation of *E. coli* nitrate reductase: a possible physiologically relevant role for the low potential [4Fe-4S] centres. *Biochem. Soc. Trans.* 22, 283S.

(256) Bennett, B., and Bray, R. C. (1994) Redox-related activation and deactivation of *E. coli* nitrate reductase: kinetic and spectroscopic studies. *Biochem. Soc. Trans.* 22, 78S.

(257) Field, S. J., Thornton, N. P., Anderson, L. J., Gates, A. J., Reilly, A., Jepson, B. J. N., Richardson, D. J., George, S. J., Cheesman, M. R., and Butt, J. N. (2005) Reductive activation of nitrate reductases. *Dalton Trans.* 3580–3586.

(258) Guigliarelli, B., Magalon, A., Asso, M., Bertrand, P., Frixon, C., Giordano, G., and Blasco, F. (1996) Complete coordination of the four Fe-S centers of the  $\beta$  subunit from *Escherichia coli* nitrate reductase. Physiological, biochemical, and EPR characterization of site-directed mutants lacking the highest or lowest potential [4Fe-4S] clusters. *Biochemistry* 35, 4828–4836.

(259) Darimont, B., and Sterner, R. (1994) Sequence, assembly and evolution of a primordial ferredoxin from *Thermotoga maritima*. *EMBO J.* 13, 1772–1781.

(260) Condon, C., Cammack, R., Patil, D. S., and Owen, P. (1985) The succinate dehydrogenase of *Escherichia coli*. Immunochemical resolution and biophysical characterization of a 4-subunit enzyme complex. *J. Biol. Chem.* 260, 9427–9434.

(261) Cheng, V. W., Rothery, R. A., Bertero, M. G., Strynadka, N. C., and Weiner, J. H. (2005) Investigation of the environment surrounding iron-sulfur cluster 4 of *Escherichia coli* dimethylsulfoxide reductase. *Biochemistry* 44, 8068–8077.

(262) Deaton, J. C., Solomon, E. I., Watt, G. D., Wetherbee, P. J., and Durfor, C. N. (1987) Electron paramagnetic resonance studies of the tungsten-containing formate dehydrogenase from *Clostridium thermoaceticum*. *Biochem. Biophys. Res. Commun.* 149, 424–430.

(263) Hudson, J. M., Heffron, K., Kotlyar, V., Sher, Y., Maklashina, E., Cecchini, G., and Armstrong, F. A. (2005) Electron transfer and catalytic control by the iron-sulfur

clusters in a respiratory enzyme, *E. coli* fumarate reductase. *J. Am. Chem. Soc.* 127, 6977–6989.

(264) Cammack, R., and Weiner, J. H. (1990) Electron paramagnetic resonance spectroscopic characterization of dimethyl sulfoxide reductase of *Escherichia coli*. *Biochemistry* 29, 8410–8416.

(265) Giordani, R., Buc, J., Cornish-Bowden, A., and Cárdenas, M. L. (1997) Kinetics of membrane-bound nitrate reductase A from *Escherichia coli* with analogues of physiological electron donors--different reaction sites for menadiol and duroquinol. *Eur. J. Biochem. FEBS* 250, 567–577.

(266) Sodergren, E. J., Hsu, P. Y., and DeMoss, J. A. (1988) Roles of the *narJ* and *narI* gene products in the expression of nitrate reductase in *Escherichia coli*. *J. Biol. Chem.* 263, 16156–16162.

(267) Berks, B. C., Page, M. D., Richardson, D. J., Reilly, A., Cavill, A., Outen, F., and Ferguson, S. J. (1995) Sequence analysis of subunits of the membrane-bound nitrate reductase from a denitrifying bacterium: the integral membrane subunit provides a prototype for the dihaem electron-carrying arm of a redox loop. *Mol. Microbiol.* 15, 319–331.

(268) Magalon, A., Lemesle-Meunier, D., Rothery, R. A., Frixon, C., Weiner, J. H., and Blasco, F. (1997) Heme axial ligation by the highly conserved His residues in helix II of cytochrome *b* (NarI) of *Escherichia coli* nitrate reductase A. *J. Biol. Chem.* 272, 25652–25658.

(269) Hackett, N. R., and Bragg, P. D. (1982) The association of two distinct *b* cytochromes with the respiratory nitrate reductase of *Escherichia coli*. *FEMS Microbiol. Lett.* 13, 213–217.

(270) Rothery, R. A., Blasco, F., Magalon, A., Asso, M., and Weiner, J. H. (1999) The hemes of *Escherichia coli* nitrate reductase A (NarGHI): Potentiometric effects of inhibitor binding to NarI. *Biochemistry* 38, 12747–12757.

(271) Rothery, R. A., Blasco, F., Magalon, A., and Weiner, J. H. (2001) The diheme cytochrome *b* subunit (NarI) of *Escherichia coli* nitrate reductase A (NarGHI): structure, function, and interaction with quinols. *J. Mol. Microbiol. Biotechnol.* 3, 273–283.

(272) Palmer, G. (1985) The electron paramagnetic resonance of metalloproteins. *Biochem. Soc. Trans.* 13, 548–560.

(273) Astashkin, A. V., and Walker, F. A. (2013) Determination of the principal *g*-values

of type I or highly-anisotropic low spin (HALS) ferriheme centers in frozen solutions. *J. Magn. Reson.* 231, 15–21.

(274) Walker, F. A., Huynh, B.H., B., Scheidt, W. R., and Osvath, S. R. (1986) Models of the cytochromes *b*. 6. The effect of axial ligand plane orientation on the EPR and Mössbauer spectra of low-spin ferrihemes. *J Am Chem Soc* 108, 5288–5297.

(275) Magalon, A., Rothery, R. A., Lemesle-Meunier, D., Frixon, C., Weiner, J. H., and Blasco, F. (1998) Inhibitor binding within the NarI subunit (cytochrome *b<sub>nr</sub>*) of *Escherichia coli* nitrate reductase A. *J. Biol. Chem.* 273, 10851–10856.

(276) Giordani, R., and Buc, J. (2004) Evidence for two different electron transfer pathways in the same enzyme, nitrate reductase A from *Escherichia coli*. *Eur. J. Biochem.* 271, 2400–2407.

(277) Rothery, R. A., Chatterjee, I., Kiema, G., McDermott, M. T., and Weiner, J. H. (1998) Hydroxylated naphthoquinones as substrates for *Escherichia coli* anaerobic reductases. *Biochem. J.* 332 (Pt 1), 35–41.

(278) Rothery, R. A., Blasco, F., and Weiner, J. H. (2001) Electron transfer from heme *b<sub>L</sub>* to the [3Fe-4S] cluster of *Escherichia coli* nitrate reductase A (NarGHI). *Biochemistry* 40, 5260–5268.

(279) Zhao, Z., Rothery, R. A., and Weiner, J. H. (2003) Transient kinetic studies of heme reduction in *Escherichia coli* nitrate reductase A (NarGHI) by menaquinol. *Biochemistry* 42, 5403–5413.

(280) Zhao, Z., Rothery, R. A., and Weiner, J. H. (2006) Effects of site-directed mutations in *Escherichia coli* succinate dehydrogenase on the enzyme activity and production of superoxide radicals. *Biochem. Cell Biol. Biochim. Biol. Cell.* 84, 1013–1021.

(281) Grimaldi, S., Lanciano, P., Bertrand, P., Blasco, F., and Guigliarelli, B. (2005) Evidence for an EPR-detectable semiquinone intermediate stabilized in the membrane-bound subunit NarI of nitrate reductase A (NarGHI) from *Escherichia coli*. *Biochemistry* 44, 1300–1308.

(282) Arias-Cartin, R., Lyubenova, S., Ceccaldi, P., Prisner, T., Magalon, A., Guigliarelli, B., and Grimaldi, S. (2010) HYSCORE evidence that endogenous mena- and ubisemiquinone bind at the same Q Site (Q<sub>D</sub>) of *Escherichia coli* nitrate reductase A. *J. Am. Chem. Soc.* 132, 5942–5943.

(283) Zhao, Z., Rothery, R. A., and Weiner, J. H. (2003) Effects of site-directed mutations on heme reduction in *Escherichia coli* nitrate reductase A by menaquinol: A

stopped-flow study. *Biochemistry* 42, 14225–14233.

(284) Lanciano, P., Magalon, A., Bertrand, P., Guigliarelli, B., and Grimaldi, S. (2007) High-stability semiquinone intermediate in nitrate reductase A (NarGHI) from *Escherichia coli* is located in a quinol oxidation site close to heme b<sub>D</sub>. *Biochemistry* 46, 5323–5329.

(285) Vergnes, A., Pommier, J., Toci, R., Blasco, F., Giordano, G., and Magalon, A. (2006) NarJ chaperone binds on two distinct sites of the aponitrate reductase of *Escherichia coli* to coordinate molybdenum cofactor insertion and assembly. *J. Biol. Chem.* 281, 2170–2176.

(286) Liu, X., and DeMoss, J. A. (1997) Characterization of NarJ, a system-specific chaperone required for nitrate reductase biogenesis in *Escherichia coli*. *J. Biol. Chem.* 272, 24266–24271.

(287) Dubourdieu, M., and DeMoss, J. A. (1992) The *narJ* gene product is required for biogenesis of respiratory nitrate reductase in *Escherichia coli*. *J. Bacteriol.* 174, 867–872.

(288) Chan, C. S., Chang, L., Rommens, K. L., and Turner, R. J. (2009) Differential Interactions between Tat-specific redox enzyme peptides and their chaperones. *J. Bacteriol.* 191, 2091–2101.

(289) Lorenzi, M., Sylvi, L., Gerbaud, G., Mileo, E., Halgand, F., Walburger, A., Vezin, H., Belle, V., Guigliarelli, B., and Magalon, A. (2012) Conformational selection underlies recognition of a molybdoenzyme by its dedicated chaperone. *PloS One* 7, e49523.

(290) Zakian, S., Lafitte, D., Vergnes, A., Pimentel, C., Sebban-Kreuzer, C., Toci, R., Claude, J.-B., Guerlesquin, F., and Magalon, A. (2010) Basis of recognition between the NarJ chaperone and the N-terminus of the NarG subunit from *Escherichia coli* nitrate reductase. *FEBS J.* 277, 1886–1895.

(291) Pinske, C., and Sawers, R. G. (2012) A-type carrier protein ErpA is essential for formation of an active formate-nitrate respiratory pathway in *Escherichia coli* K-12. *J. Bacteriol.* 194, 346–353.

(292) Facey, S. J., and Kuhn, A. (2010) Biogenesis of bacterial inner-membrane proteins. *Cell. Mol. Life Sci.* 67, 2343–2362.

(293) Wimpenny, J. W. T., and Cole, J. A. (1967) The regulation of metabolism in facultative bacteria III. The effect of nitrate. *Biochim. Biophys. Acta BBA - Gen. Subj.* 148, 233–242.

- (294) Richardson, D. J., and Watmough, N. J. (1999) Inorganic nitrogen metabolism in bacteria. *Curr. Opin. Chem. Biol.* 3, 207–219.
- (295) Blasco, F., Guigliarelli, B., Magalon, A., Asso, M., Giordano, G., and Rothery, R. A. (2001) The coordination and function of the redox centres of the membrane-bound nitrate reductases. *Cell. Mol. Life Sci. CMLS* 58, 179–193.
- (296) Magalon, A., Rothery, R. A., Giordano, G., Blasco, F., and Weiner, J. H. (1997) Characterization by electron paramagnetic resonance of the role of the *Escherichia coli* nitrate reductase (NarGHI) iron-sulfur clusters in electron transfer to nitrate and identification of a semiquinone radical intermediate. *J. Bacteriol.* 179, 5037–5045.
- (297) Arias-Cartin, R., Grimaldi, S., Pommier, J., Lanciano, P., Schaefer, C., Arnoux, P., Giordano, G., Guigliarelli, B., and Magalon, A. (2011) Cardiolipin-based respiratory complex activation in bacteria. *Proc. Natl. Acad. Sci.* 108, 7781–7786.
- (298) Pascal, M. C., Burini, J. F., Ratouchniak, J., and Chippaux, M. (1982) Regulation of the nitrate reductase operon: effect of mutations in *chiA*, *B*, *D* and *E* genes. *Mol. Gen. Genet. MGG* 188, 103–106.
- (299) Kikuchi, S., Shibuya, I., and Matsumoto, K. (2000) Viability of an *Escherichia coli* *pgsA* null mutant lacking detectable phosphatidylglycerol and cardiolipin. *J. Bacteriol.* 182, 371–376.
- (300) Baba, T., Ara, T., Hasegawa, M., Takai, Y., Okumura, Y., Baba, M., Datsenko, K. A., Tomita, M., Wanner, B. L., and Mori, H. (2006) Construction of *Escherichia coli* K-12 in-frame, single-gene knockout mutants: the Keio collection. *Mol. Syst. Biol.* 2, 2006.0008.
- (301) Sambrook, J., and Russell, D. W. (2001) *Molecular Cloning: A Laboratory Manual* 3rd ed. CSHL Press.
- (302) Bilous, P. T., and Weiner, J. H. (1985) Dimethyl sulfoxide reductase activity by anaerobically grown *Escherichia coli* HB101. *J. Bacteriol.* 162, 1151–1155.
- (303) Rothery, R. A., and Weiner, J. H. (1996) Interaction of an engineered [3Fe-4S] cluster with a menaquinol binding site of *Escherichia coli* DMSO reductase. *Biochemistry* 35, 3247–3257.
- (304) Weil, J. A. J. A. (2007) *Electron Paramagnetic Resonance: Elementary Theory and Practical Applications*. Wiley-Interscience.
- (305) Bou-Abdallah, F., and Chasteen, N. D. (2008) Spin concentration measurements of high-spin ( $g' = 4.3$ ) rhombic iron(III) ions in biological samples:

theory and application. *J. Biol. Inorg. Chem. JBIC Publ. Soc. Biol. Inorg. Chem.* 13, 15–24.

(306) Markwell, M. A., Haas, S. M., Bieber, L. L., and Tolbert, N. E. (1978) A modification of the Lowry procedure to simplify protein determination in membrane and lipoprotein samples. *Anal. Biochem.* 87, 206–210.

(307) Lowry, O. H., Rosebrough, N. J., Farr, A. L., and Randall, R. J. (1951) Protein measurement with the Folin phenol reagent. *J. Biol. Chem.* 193, 265–275.

(308) Ingledew, W. J., and Poole, R. K. (1984) The respiratory chains of *Escherichia coli*. *Microbiol. Rev.* 48, 222–271.

(309) Polglase, W. J., Pun, W. T., and Withaar, J. (1966) Lipoquinones of *Escherichia coli*. *Biochim. Biophys. Acta* 118, 425–426.

(310) Lacapère, J.-J., Pebay-Peyroula, E., Neumann, J.-M., and Etchebest, C. (2007) Determining membrane protein structures: still a challenge! *Trends Biochem. Sci.* 32, 259–270.

(311) Kühlbrandt, W. (1988) Three-dimensional crystallization of membrane proteins. *Q. Rev. Biophys.* 21, 429–477.

(312) Vinothkumar, K. R., and Henderson, R. (2010) Structures of membrane proteins. *Q. Rev. Biophys.* 43, 65–158.

(313) Unden, G. (1988) Differential roles for menaquinone and demethylmenaquinone in anaerobic electron transport of *E. coli* and their *fnr*-independent expression. *Arch. Microbiol.* 150, 499–503.

(314) Maklashina, E., and Cecchini, G. (2010) The quinone-binding and catalytic site of complex II. *Biochim. Biophys. Acta* 1797, 1877–1882.

(315) Kong, M. K., and Lee, P. C. (2011) Metabolic engineering of menaquinone-8 pathway of *Escherichia coli* as a microbial platform for vitamin K production. *Biotechnol. Bioeng.* 108, 1997–2002.

(316) Mikami, S., Tai, H., and Yamamoto, Y. (2009) Effect of the redox-dependent ionization state of the heme propionic acid side chain on the entropic contribution to the redox potential of *Pseudomonas aeruginosa* cytochrome *c*<sub>551</sub>. *Biochemistry* 48, 8062–8069.

(317) Takayama, S. J., Mikami, S., Terui, N., Mita, H., Hasegawa, J., Sambongi, Y., and Yamamoto, Y. (2005) Control of the redox potential of *Pseudomonas aeruginosa*

cytochrome  $c_{551}$  through the Fe–Met coordination bond strength and  $pK_a$  of a buried heme propionic acid side chain. *Biochemistry* 44, 5488–5494.

(318) Das, D. K., and Medhi, O. K. (1998) The role of heme propionate in controlling the redox potential of heme: Square wave voltammetry of protoporphyrinato IX iron(III) in aqueous surfactant micelles. *J. Inorg. Biochem.* 70, 83–90.

(319) Augier, V., Guigliarelli, B., Asso, M., Bertrand, P., Frixon, C., Giordano, G., Chippaux, M., and Blasco, F. (1993) Site-directed mutagenesis of conserved cysteine residues within the beta subunit of *Escherichia coli* nitrate reductase. Physiological, biochemical, and EPR characterization of the mutated enzymes. *Biochemistry* 32, 2013–2023.

(320) Bloch, D. A., Borisov, V. B., Mogi, T., and Verkhovsky, M. I. (2009) Heme/heme redox interaction and resolution of individual optical absorption spectra of the hemes in cytochrome *bd* from *Escherichia coli*. *Biochim. Biophys. Acta BBA - Bioenerg.* 1787, 1246–1253.

(321) Fedor, J. G., Rothery, R. A., Giraldi, K. S., and Weiner, J. H. (2014) Q-Site occupancy defines heme heterogeneity in *Escherichia coli* nitrate reductase A (NarGHI). *Biochemistry* 53, 1733–1741.

(322) Rothery, R. A., and Ingledew, W. J. (1989) The cytochromes of anaerobically grown *Escherichia coli*. An electron-paramagnetic-resonance study of the cytochrome *bd* complex in situ. *Biochem. J.* 261, 437–443.

(323) Ullmann, G. M., and Knapp, E. W. (1999) Electrostatic models for computing protonation and redox equilibria in proteins. *Eur. Biophys. J. EBJ* 28, 533–551.

(324) Quinlan, C. L., Gerencser, A. A., Treberg, J. R., and Brand, M. D. (2011) The mechanism of superoxide production by the antimycin-inhibited mitochondrial Q-cycle. *J. Biol. Chem.* 286, 31361–31372.

(325) Infossi, P., Lojou, E., Chauvin, J.-P., Herbette, G., Brugna, M., and Giudici-Ortoni, M.-T. (2010) Aquifex aeolicus membrane hydrogenase for hydrogen biooxidation: Role of lipids and physiological partners in enzyme stability and activity. *Int. J. Hydrog. Energy* 35, 10778–10789.

(326) Robertson, D. E., Prince, R. C., Bowyer, J. R., Matsuura, K., Dutton, P. L., and Ohnishi, T. (1984) Thermodynamic properties of the semiquinone and its binding site in the ubiquinol-cytochrome *c* ( $c_2$ ) oxidoreductase of respiratory and photosynthetic systems. *J. Biol. Chem.* 259, 1758–1763.

(327) Hong, S., de Almeida, W. B., Taguchi, A. T., Samoiloova, R. I., Gennis, R. B.,

O'Malley, P. J., Dikanov, S. A., and Crofts, A. R. (2014) The semiquinone at the Q<sub>i</sub> site of the bc<sub>1</sub> complex explored using HYSCORE spectroscopy and specific isotopic labeling of ubiquinone in *Rhodobacter sphaeroides* via <sup>13</sup>C methionine and construction of a methionine auxotroph. *Biochemistry* 53, 6022–6031.

(328) Yap, L. L., Samoilova, R. I., Gennis, R. B., and Dikanov, S. A. (2007) Characterization of mutants that change the hydrogen bonding of the semiquinone radical at the Q<sub>H</sub> site of the cytochrome bo<sub>3</sub> from *Escherichia coli*. *J. Biol. Chem.* 282, 8777–8785.

(329) Graige, M. S., Paddock, M. L., Feher, G., and Okamura, M. Y. (1999) Observation of the protonated semiquinone intermediate in isolated reaction centers from *Rhodobacter sphaeroides*: Implications for the mechanism of electron and proton transfer in proteins. *Biochemistry* 38, 11465–11473.

(330) Gardiner, A. T., Zech, S. G., MacMillan, F., Käss, H., Bittl, R., Schlodder, E., Lenzian, F., and Lubitz, W. (1999) Electron paramagnetic resonance studies of zinc-substituted reaction centers from *Rhodospseudomonas viridis*. *Biochemistry* 38, 11773–11787.

(331) Fedor, J. G., Ma, Y. K., Giraldi, K. S., Rothery, R. A., and Weiner, J. H. A mechanism for menaquinol deprotonation in *E. coli* nitrate reductase A. *Biochim. Biophys. Acta BBA - Bioenerg.* Submitted (BBABIO–15–235).

(332) Hata, A., Kirino, Y., Matsuura, K., Itoh, S., Hiyama, T., Konishi, K., Kita, K., and Anraku, Y. (1985) Assignment of ESR signals of *Escherichia coli* terminal oxidase complexes. *Biochim. Biophys. Acta* 810, 62–72.

(333) Kooser, R. G., Kirchmann, E., and Matkov, T. (1992) Measurements of spin concentration in electron paramagnetic resonance spectroscopy preparation of standard solutions from optical absorption. *Concepts Magn. Reson.* 4, 145–152.

(334) Fersht, A. (1998) Structure and Mechanism in Protein Science: A Guide to Enzyme Catalysis and Protein Folding 1st edition. W. H. Freeman, New York.

(335) Zheng, M., and Dismukes, G. C. (1996) The conformation of the isoprenyl chain relative to the semiquinone head in the primary electron acceptor (Q<sub>A</sub>) of higher plant PSII (plastosemiquinone) differs from that in bacterial reaction centers (ubisemiquinone or menasemiquinone) by ~90°. *Biochemistry* 35, 8955–8963.

(336) Himo, F., Babcock, G. T., and Eriksson, L. A. (1999) Conformational analysis of quinone anion radicals in photosystem II and photosynthetic bacteria. *J. Phys. Chem. A* 103, 3745–3749.

- (337) McLachlan, A. D. (1958) Hyperconjugation in the electron resonance spectra of free radicals. *Mol. Phys.* 1, 233–240.
- (338) Verkhovsky, M., Bloch, D. A., and Verkhovskaya, M. (2012) Tightly-bound ubiquinone in the *Escherichia coli* respiratory Complex I. *Biochim. Biophys. Acta BBA - Bioenerg.* 1817, 1550–1556.
- (339) Maklashina, E., Hellwig, P., Rothery, R. A., Kotlyar, V., Sher, Y., Weiner, J. H., and Cecchini, G. (2006) Differences in protonation of ubiquinone and menaquinone in fumarate reductase from *Escherichia coli*. *J. Biol. Chem.* 281, 26655–26664.
- (340) Isom, D. G., Castañeda, C. A., Cannon, B. R., and García-Moreno, B. (2011) Large shifts in pK<sub>a</sub> values of lysine residues buried inside a protein. *Proc. Natl. Acad. Sci. U. S. A.* 108, 5260–5265.
- (341) Olsson, M. H. M., Søndergaard, C. R., Rostkowski, M., and Jensen, J. H. (2011) PROPKA3: Consistent treatment of internal and surface residues in empirical pK<sub>a</sub> predictions. *J. Chem. Theory Comput.* 7, 525–537.
- (342) Søndergaard, C. R., Olsson, M. H. M., Rostkowski, M., and Jensen, J. H. (2011) Improved treatment of ligands and coupling effects in empirical calculation and rationalization of pK<sub>a</sub> values. *J. Chem. Theory Comput.* 7, 2284–2295.
- (343) Moore, G. R., Williams, R. J. P., Peterson, J., Thomson, A. J., and Matthews, F. S. (1985) A spectroscopic investigation of the structure and redox properties of *Escherichia coli* cytochrome *b*<sub>562</sub>. *Biochim. Biophys. Acta BBA - Protein Struct. Mol. Enzymol.* 829, 83–96.
- (344) Arnesano, F., Banci, L., Bertini, I., Ciofi-Baffoni, S., Woodyear, T. de L., Johnson, C. M., and Barker, P. D. (2000) Structural consequences of *b*- to *c*-type heme conversion in oxidized *Escherichia coli* cytochrome *b*<sub>562</sub>. *Biochemistry* 39, 1499–1514.
- (345) Brändén, G., Brändén, M., Schmidt, B., Mills, D. A., Ferguson-Miller, S., and Brzezinski, P. (2005) The protonation state of a heme propionate controls electron transfer in cytochrome *c* oxidase. *Biochemistry* 44, 10466–10474.
- (346) Roncel, M., Ortega, J. M., and Losada, M. (2001) Factors determining the special redox properties of photosynthetic cytochrome *b*<sub>559</sub>. *Eur. J. Biochem.* 268, 4961–4968.
- (347) Fernandes, A. S., Pereira, M. M., and Teixeira, M. (2001) The succinate dehydrogenase from the thermohalophilic bacterium *Rhodothermus marinus*: Redox–Bohr effect on heme *b*<sub>L</sub>. *J. Bioenerg. Biomembr.* 33, 343–352.

- (348) Desbois, A., and Lutz, M. (1992) Redox control of proton transfers in membrane *b*-type cytochromes: an absorption and resonance Raman study on bis(imidazole) and bis(imidazolate) model complexes of iron-protoporphyrin. *Eur. Biophys. J.* 20, 321–335.
- (349) Jones, S. A., Chowdhury, F. Z., Fabich, A. J., Anderson, A., Schreiner, D. M., House, A. L., Autieri, S. M., Leatham, M. P., Lins, J. J., Jorgensen, M., Cohen, P. S., and Conway, T. (2007) Respiration of *Escherichia coli* in the mouse intestine. *Infect. Immun.* 75, 4891–4899.
- (350) Huang, Q., Abdalla, A. E., and Xie, J. (2015) Phylogenomics of *Mycobacterium* nitrate reductase operon. *Curr. Microbiol.* 71, 121–128.
- (351) Malm, S., Tiffert, Y., Micklinghoff, J., Schultze, S., Joost, I., Weber, I., Horst, S., Ackermann, B., Schmidt, M., Wohlleben, W., Ehlers, S., Geffers, R., Reuther, J., and Bange, F.-C. (2009) The roles of the nitrate reductase NarGHJ, the nitrite reductase NirBD and the response regulator GlnR in nitrate assimilation of *Mycobacterium tuberculosis*. *Microbiol. Read. Engl.* 155, 1332–1339.
- (352) Kemp, M. B., Haddock, B. A., and Garland, P. B. (1975) Synthesis and sidedness of membrane-bound respiratory nitrate reductase (EC 1.7.99.4) in *Escherichia coli* lacking cytochromes. *Biochem. J.* 148, 329–333.
- (353) Patel, H., Grüning, B. A., Günther, S., and Merfort, I. (2014) PyWATER: a PyMOL plug-in to find conserved water molecules in proteins by clustering. *Bioinforma. Oxf. Engl.* 30, 2978–2980.
- (354) Zwietering, M. H., Jongenburger, I., Rombouts, F. M., and van 't Riet, K. (1990) Modeling of the bacterial growth curve. *Appl. Environ. Microbiol.* 56, 1875–1881.
- (355) Katoh, K., and Standley, D. M. (2013) MAFFT multiple sequence alignment software version 7: Improvements in performance and usability. *Mol. Biol. Evol.* 30, 772–780.
- (356) Consortium, T. U. (2015) UniProt: a hub for protein information. *Nucleic Acids Res.* 43, D204–D212.
- (357) Denke, E., Merbitz-Zahradnik, T., Hatzfeld, O. M., Snyder, C. H., Link, T. A., and Trumppower, B. L. (1998) Alteration of the midpoint potential and catalytic activity of the Rieske iron-sulfur protein by changes of amino acids forming hydrogen bonds to the iron-sulfur cluster. *J. Biol. Chem.* 273, 9085–9093.
- (358) Gu, Y., Li, P., Sage, J. T., and Champion, P. M. (1993) Photoreduction of heme proteins: spectroscopic studies and cross-section measurements. *J. Am. Chem. Soc.*

115, 4993–5004.

(359) Fedor, J. G., Rothery, R. A., and Weiner, J. H. Quinol oxidation progresses through a neutral semiquinone in *E. coli* nitrate reductase A. *Biochim. Biophys. Acta BBA - Bioenerg.* Submitted (BBABIO–15–258).

(360) Kyte, J. (2006) Structure in Protein Chemistry 2 edition. Garland Science, New York.

(361) Gadsby, P. M. A., and Thomson, A. J. (1982) Identification of the imidazolate anion as a ligand in metmyoglobin by near-infrared magnetic circular dichroism spectroscopy. *FEBS Lett.* 150, 59–63.

(362) Sundberg, R. J., and Martin, R. B. (1974) Interactions of histidine and other imidazole derivatives with transition metal ions in chemical and biological systems. *Chem. Rev.* 74, 471–517.

(363) Hunte, C., Palsdottir, H., and Trumpower, B. L. (2003) Protonmotive pathways and mechanisms in the cytochrome *bc*<sub>1</sub> complex. *FEBS Lett.* 545, 39–46.

(364) Sinnecker, S., Flores, M., and Lubitz, W. (2006) Protein–cofactor interactions in bacterial reaction centers from *Rhodobacter sphaeroides* R-26: Effect of hydrogen bonding on the electronic and geometric structure of the primary quinone. A density functional theory study. *Phys. Chem. Chem. Phys.* 8, 5659–5670.

(365) Lin, M. T., Baldansuren, A., Hart, R., Samoilova, R. I., Narasimhulu, K. V., Yap, L. L., Choi, S. K., O'Malley, P. J., Gennis, R. B., and Dikanov, S. A. (2012) Interactions of intermediate semiquinone with surrounding protein residues at the Q<sub>H</sub> site of wild-type and D75H mutant cytochrome *bo*<sub>3</sub> from *Escherichia coli*. *Biochemistry* 51, 3827–3838.

(366) Lyons, J. A., Aragão, D., Slattery, O., Pisiakov, A. V., Soulimane, T., and Caffrey, M. (2012) Structural insights into electron transfer in *caa*<sub>3</sub>-type cytochrome oxidase. *Nature* 487, 514–518.

(367) Koepke, J., Olkhova, E., Angerer, H., Müller, H., Peng, G., and Michel, H. (2009) High resolution crystal structure of *Paracoccus denitrificans* cytochrome *c* oxidase: New insights into the active site and the proton transfer pathways. *Biochim. Biophys. Acta BBA - Bioenerg.* 1787, 635–645.

(368) Baradaran, R., Berrisford, J. M., Minhas, G. S., and Sazanov, L. A. (2013) Crystal structure of the entire respiratory complex I. *Nature* 494, 443–448.

(369) Tan, P., Feng, Z., Zhang, L., Hou, T., and Li, Y. (2014) The mechanism of proton

translocation in respiratory complex I from molecular dynamics. *J. Recept. Signal Transduct.* 1–10.

(370) Madej, M. G., Nasiri, H. R., Hilgendorff, N. S., Schwalbe, H., and Lancaster, C. R. D. (2006) Evidence for transmembrane proton transfer in a dihaem-containing membrane protein complex. *EMBO J.* 25, 4963–4970.

(371) Covian, R., and Trumppower, B. L. (2009) The rate-limiting step in the cytochrome *bc*<sub>1</sub> complex (ubiquinol-cytochrome *c* oxidoreductase) is not changed by inhibition of cytochrome *b*-dependent deprotonation implications for the mechanism of ubiquinol oxidation at center P of the *bc*<sub>1</sub> complex. *J. Biol. Chem.* 284, 14359–14367.

(372) Gao, X., Wen, X., Esser, L., Quinn, B., Yu, L., Yu, C.-A., and Xia, D. (2003) Structural basis for the quinone reduction in the *bc*<sub>1</sub> complex: A comparative analysis of crystal structures of mitochondrial cytochrome *bc*<sub>1</sub> with bound substrate and inhibitors at the Q<sub>i</sub> site. *Biochemistry* 42, 9067–9080.

(373) Chovancova, E., Pavelka, A., Benes, P., Strnad, O., Brezovsky, J., Kozlikova, B., Gora, A., Sustr, V., Klvana, M., Medek, P., Biedermannova, L., Sochor, J., and Damborsky, J. (2012) CAVER 3.0: a tool for the analysis of transport pathways in dynamic protein structures. *PLoS Comput. Biol.* 8, e1002708.

(374) DeLano, W. L. (2002) The PyMOL molecular graphics system. Schrödinger, LLC.

(375) Augier, V., Asso, M., Guigliarelli, B., More, C., Bertrand, P., Santini, C.-L., Blasco, F., Chippaux, M., and Giordano, G. (1993) Removal of the high-potential iron-sulfur [4Fe-4S] center of the beta-subunit from *Escherichia coli* nitrate reductase. Physiological, biochemical, and EPR characterization of site-directed mutated enzymes. *Biochemistry* 32, 5099–5108.

(376) Hasan, S. S., Proctor, E. A., Yamashita, E., Dokholyan, N. V., and Cramer, W. A. (2014) Traffic within the cytochrome *b*<sub>6</sub>*f* lipoprotein complex: Gating of the quinone portal. *Biophys. J.* 107, 1620–1628.

(377) Lin, T.-J., and O'Malley, P. J. (2011) Binding site influence on the electronic structure and electron paramagnetic resonance properties of the phyllosemiquinone free radical of photosystem I. *J Phys Chem B* 115, 9311–9319.

(378) Rothery, R. A., Workun, G. J., and Weiner, J. H. (2008) The prokaryotic complex iron-sulfur molybdoenzyme family. *Biochim. Biophys. Acta BBA - Biomembr.* 1778, 1897–1929.

(379) Gong, X., Yu, L., Xia, D., and Yu, C.-A. (2005) Evidence for electron equilibrium

between the two hemes  $b_L$  in the dimeric cytochrome  $bc_1$  complex. *J. Biol. Chem.* 280, 9251–9257.

(380) Bossis, F., De Grassi, A., Palese, L. L., and Pierri, C. L. (2014) Prediction of high- and low-affinity quinol-analogue-binding sites in the  $aa_3$  and  $bo_3$  terminal oxidases from *Bacillus subtilis* and *Escherichia coli*. *Biochem. J.* 461, 305–314.

(381) Coates, C. S., Ziegler, J., Manz, K., Good, J., Kang, B., Milikisiyants, S., Chatterjee, R., Hao, S., Golbeck, J. H., and Lakshmi, K. V. (2013) The structure and function of quinones in biological solar energy transduction: A cyclic voltammetry, EPR, and hyperfine sub-level correlation (HYSCORE) spectroscopy study of model naphthoquinones. *J. Phys. Chem. B* 117, 7210–7220.

(382) Chippaux, M., Bonnefoy-Orth, V., Ratouchniak, J., and Pascal, M.-C. (1981) Operon fusions in the nitrate reductase operon and study of the control gene *nirR* in *Escherichia coli*. *Mol. Gen. Genet. MGG* 182, 477–479.

(383) Rich, P. R. (1985) Mechanisms of quinol oxidation in photosynthesis. *Photosynth. Res.* 6, 335–348.

(384) Hales, B. J., and Case, E. E. (1981) Immobilized radicals. IV. Biological semiquinone anions and neutral semiquinones. *Biochim. Biophys. Acta BBA - Bioenerg.* 637, 291–302.

(385) Hellwig, P., Gomes, C. M., and Teixeira, M. (2003) FTIR spectroscopic characterization of the cytochrome  $aa_3$  from *Acidianus ambivalens*: Evidence for the involvement of acidic residues in redox coupled proton translocation. *Biochemistry* 42, 6179–6184.

(386) Zhang, J., Oettmeier, W., Gennis, R. B., and Hellwig, P. (2002) FTIR spectroscopic evidence for the involvement of an acidic residue in quinone binding in cytochrome *bd* from *Escherichia coli*. *Biochemistry* 41, 4612–4617.

(387) Nicolaidis, A., Soulimane, T., and Varotsis, C. (2015) Detection of functional hydrogen-bonded water molecules with protonated/deprotonated key carboxyl side chains in the respiratory enzyme  $ba_3$ -oxidoreductase. *Phys. Chem. Chem. Phys. PCCP* 17, 8113–8119.

(388) Burie, J.-R., Boussac, A., Boullais, C., Berger, G., Mattioli, T., Mioskowski, C., Nabedryk, E., and Breton, J. (1995) FTIR spectroscopy of UV-generated quinone radicals: Evidence for an intramolecular hydrogen atom transfer in ubiquinone, naphthoquinone, and plastoquinone. *J. Phys. Chem.* 99, 4059–4070.

(389) Pisljakov, A. V., Hino, T., Shiro, Y., and Sugita, Y. (2012) Molecular dynamics

simulations reveal proton transfer pathways in cytochrome *c*-dependent nitric oxide reductase. *PLoS Comput. Biol.* 8, e1002674.

(390) Guallar, V., and Wallrapp, F. H. (2010) QM/MM methods: looking inside heme proteins biochemistry. *Biophys. Chem.* 149, 1–11.

(391) Chan, C. S., Howell, J. M., Workentine, M. L., and Turner, R. J. (2006) Twin-arginine translocase may have a role in the chaperone function of NarJ from *Escherichia coli*. *Biochem. Biophys. Res. Commun.* 343, 244–251.